Étude des caloducs cryogéniques pulsés diphasiques d'un mètre de longueur

María Asunción Barba Higueras

université PARIS-SACLAY

UNIVERSITÉ PARIS SUD
Comprendre le monde, construire l'avenir

NNT : 2019SACLS224

Thèse de doctorat

Study of Meter-scale Horizontal Cryogenic Pulsating Heat Pipes

Thèse de doctorat de l'Université Paris-Saclay
préparée à l'Université Paris-Sud

Ecole doctorale n°576 Particules, Hadrons, Énergie, Noyau, Instrumentation, Imagerie, Cosmos, et Simulation (PHENIICS)
Spécialité de doctorat : Physique des accélérateurs

Thèse présentée et soutenue à Saclay, le 18 Septembre 2019, par

MARÍA ASUNCIÓN BARBA HIGUERAS

Composition du Jury :

F. Lusseyran Docteur, Directeur de recherche, Laboratoire LIMSI	Président
M. Marengo Professeur, University of Brighton	Rapporteur
F. Lefèvre Professeur, INSA de Lyon	Rapporteur
M. Breschi Professeur, Università di Bologna	Examinateur
P. Védrine Docteur, CEA de Saclay	Examinateur
P. Brédy Docteur, CEA de Saclay	Examinateur
B. Baudouy Docteur, Directeur de recherche, CEA de Saclay	Directeur de thèse
R. Bruce Docteur, CEA de Saclay	Co-encadrant

A mis familiares, maestros y amigos, gracias por su tiempo.

Remerciements

Cet écrit est le résultat de trois années de travail de recherche réalisée au sein du Laboratoire de Cryogénie et Stations d'Essais (LCSE) du Département des Accélérateurs, Cryogénie et Magnétisme (DACM) appartenant à l'Institut de Recherche sur Lois Fondamentales de l'Univers (IRFU) du Commissariat à l'Énergie Atomique et aux Énergies Alternatives (CEA) de Paris - Saclay. Avant d'aborder cet ouvrage, je tiens à remercier dans ces quelques lignes toutes les personnes qui m'ont accompagnées tout au long de ce travail de doctorat.

Je voudrais tout d'abord remercier la direction de l'IRFU qui a entièrement financé mes travaux de thèse. De même, je voudrais remercier la direction du DACM et du LCSE, Messieurs Pierre Védrine, Philippe Brédy, Christophe Mayri et Madame Roser Vallcorba, pour leur accueil et leur disponibilité de tous les instants ainsi que pour avoir financé ma participation aux différentes formations et conférences qui m'ont permis d'approfondir mes connaissances et de m'intégrer dans la communauté de la cryogénie et la supraconductivité.

De plus, c'est un honneur pour moi d'avoir compté dans mon jury de thèse des experts reconnus dans les domaines de la mécanique des fluides, des transferts thermiques et de la supraconductivité: M. Lusseyran, M. Marengo, M. Lefèvre, M. Breschi, M. Védrine et M. Brédy. Je les remercie énormément pour l'intérêt qu'ils ont porté pour mon sujet, pour leurs corrections, suggestions et conseils, qui ont contribué à la qualité de l'écrit et à un échange très enrichissant lors de la soutenance.

Concernant les personnes qui ont travaillé plus directement avec moi durant cette thèse, je voudrais remercier tout d'abord mon directeur de thèse, Bertrand Baudouy, pour son encadrement, son soutien, sa disponibilité constante, son savoir-faire scientifique, la rigueur de ses corrections et ses conseils (scientifiques et humains). Tout cela a été un pilier essentiel de la réussite de ce travail.

De même, je remercie Romain Bruce, pour son soutien et dynamisme, pour avoir cru en mes capacités plus que moi-même, pour ses conseils qui m'ont guidé vers les bons chemins dans l'analyse des phénomènes physiques et le développement des systèmes numériques. Sa passion pour la science a été une véritable source de motivation pour l'aboutissement de mes recherches. Cela été un plaisir de continuer les travaux initiés lors de son postdoctorat.

Un grand merci aussi à Florent Bouchet, stagiaire avec lequel j'ai eu le plaisir de travailler pendant cette thèse. Avec son travail et effort il a énormément contribué à la grande base de données expérimentales de cette thèse, en plus d'être un excellent collègue et ami.

Je souhaiterais aussi remercier très fortement tous les membres du laboratoire LCSE, avec une spéciale mention à Clément Hilaire, Antoine Bonelli, Gilles Authelet, Jean-Marc Gheller, Vadim Stepanov, Charles Mailleret, Antoine Caisson, Andrea Vitrano, Romain Boy, Denis Bouziat et les nombreuses personnes que j'ai croisées durant ces trois années. Je voudrais les remercier pour leurs conseils et leurs apprentissages qui ont été très utiles pour la réalisation des expériences et, surtout, pour les bons moments passés ensemble. Ils ont été des véritables rayons de soleil chaque jour!

Ajouté à cela, je tiens aussi à remercier les membres du personnel administratif, Séverine Candau et Armelle Le Noa, l'ingénieur de sécurité, Olivier Kuster et les ingénieurs informatique

pour leur disponibilité et leur amabilité. Merci aussi à tous les membres du laboratoire LEAS pour les conseils et discussions enrichissantes ainsi que les bons moments passés ensemble, avec une mention spéciale à François-Paul Juster, les conseils des plus sages sont toujours les meilleurs.

Pour finir, je tiens à exprimer ma gratitude à mes parents, mon frère et le reste de ma famille et proches pour leur soutien incontournable durant tout mon doctorat, voire depuis toujours, étant un de mes piliers fondamentaux. Merci infiniment.

Contents

List of Figures

List of Tables

Nomenclature

Roman letters

$\dot{m}_{lv}$	rate of mass transfer during the evaporation process	$kg/(m^3.s)$
$\dot{m}_{vl}$	rate of mass transfer during the condensation process	$kg/(m^3.s)$
Bc	critical magnetic field	T
Cp	specific heat	$kJ/(kg.K)$
E	energy	J
F	external force	$(kg.m)/s^2$
Jc	critical current density	A/m^2
Lv	latent heat	kJ/kg
M	molar mass	kg/mol
P	pressure	Pa
p	pressure	Pa
R	radius	m
R	resistance	Ω
S	source term	
T	temperature	K
Tc	critical temperature	K
U_f	volume flux through the face	m^3/s
V	volume	m^3
v	velocity	m/s

Greek letters

α	volume fraction
ϵ	emissivity

λ	thermal conductivity	$W/(m.K)$
ρ	density	kg/m^3
μ	dynamic viscosity	$Pa.s$
σ	surface tension	N/m
σ_b	Boltzmann constant	$W/(m^2.K^4)$

Dimensionless numbers

Cou	Courant number; $Cou = \frac{v\Delta t}{\Delta x}$
$Eö$	Eötvös number; $Eö = D^2 g(\rho_l - \rho_v)/\sigma$
Fr	Froude number; $Fr = \frac{V\mu_l}{gD^2\rho_l}$
Ja	Jacob number; $Ja = \frac{Cp \cdot \Delta T}{Lv}$
Ps	Poiseuille number; $Ps = \frac{V^2}{gD}$

Subscripts and superscripts

0	related to resistance at 0°C
1	related to phase one
2	related to phase two
ec	related to evaporator and condenser temperatures
l	related to liquid phase
lg	related to liquid-gas interface
p	related to one fluid phase
php	related to the volume of the PHP
q	related to one fluid phase
RTD	related to platinum resistance thermometers
sat	related to saturation conditions
sg	related to solid-gas interface
sl	related to solid-liquid interface
v	related to vapor phase

Physical constants

g	acceleration of gravity	$\approx 9.81\ m/s^2$

R	gas constant	$8.314472 J/(mol.K)$

Acronyms

APT	Absolute Pressure Transducer
BV	Buffer Volume
CFD	Computational Fluid Dynamics
FFT	Fast Fourier Transform
FR	Filling Ratio %
MLI	Multi-Layer Insulation
NHMFL	National High Magnetic Field Laboratory
NTC	Negative Temperature Coefficient
CEA	Atomic Energy Commission
DACM	Accelerators, Cryogenics and Magnetism Department
HTS	High Temperature Superconductors
MRI	Magnetic Resonance Imaging
PHP	Pulsating Heat Pipe
PHPs	Pulsating Heat Pipes
PTC	Positive Temperature Coefficient
SR2S	Space Radiation Superconductive Shield
VOF	Volume of Fluid
UDF	User-Defined Function
VP	Vacuum Pump

Introduction

Cryogenics is the area of physics covering the production of low temperature environment and study of physical effects at these temperatures. Its use cover a wide range of applications in electronics, medicine, physics, rocketry, levitation and high magnetic field production. It is indispensable for revealing in certain materials their superconducting state, only attainable at cryogenic temperatures. In fact, below a certain critical temperature (T_c), the superconductivity phenomenon appears in materials (known as superconductors), allowing the circulation of electrical current without any resistance or energy loss. Consequently, in the case of superconducting magnets, this lack of electrical resistance allows the generation of huge magnetic fields used, for example, in Magnetic Resonance Imaging (MRI) for medical applications or to deviate and focalize particles in accelerators.

Nowadays, research efforts on superconductivity focus on developing new materials with high critical temperature, known as High Temperature Superconductors (HTS), avoiding the use of helium as cryogenic cooling fluids. This allows to deal with repetitive helium scarcities by using other cryogenic fluids more affordable existing in large quantities on earth.

In addition, the interest in superconducting technologies for space applications is demanding new cryogenic technologies able to work without gravity, as studied in the project Space Radiation Superconductive Shield (SR2S) [3, 4]. Funded by the European Commission, the objective of this scientific project was to develop technologies to protect the astronauts during deep space travel missions from overexposure to harmful radiation, which increases the probability of developing serious diseases, such as cancer. During this project, active shielding solutions have been studied involving superconducting magnets surrounding the space shuttles and using the magnetic field to deflect particles by changing their trajectory as the geomagnetic field does on earth. The project succeeded in demonstrating the potential of key technologies needed for the development of such an active magnetic shield. As a member of this project, the Accelerators, Cryogenics and Magnetism Department (DACM) of the CEA Paris - Saclay, worked on the cryogenic cooling technology for this superconducting space magnet. The DACM developed meter-scale cryogenic Pulsating Heat Pipes (PHPs), one of the longest created so far, as a novel technology for space applications.

Invented by Akachi in the 90's, pulsating heat pipes have been widely studied at room temperature by Khandekar [5], for example, and developed in multiple sizes for different applications, such as electronics cooling [6] or thermal storage [7, 8]. In the cryogenic field, pulsating heat pipes have been mostly studied for cooling superconducting magnets. For example, a PHP of a few centimeters long has been tested by Mito et Natsume [9–12] using different cryogenic working fluids. At the same time, in the meter-scale, a 1 m long vertical cryogenic PHP has been studied by Fonseca [13] using helium as working fluid. The literature reveals that pulsating heat pipes working in no-gravity conditions are comparable to the ones working in horizontal position on earth [14]. However, no horizontal meter-scale cryogenic PHP able to work with different fluids has been developed until now. Concerning numerical simulations related to the physical phenomena occurring in pulsating heat pipes, the main numerical codes have been developed in one dimension by Shafii et Zhang [15, 16] and later by Mameli et al. [17] and Nikolayev et al. [18–20]. Nowadays, there is no effective method to predict PHPs behavior and a completed numerical model of a PHP would be a step towards a predictive tool for future PHPs designs. The development of 2D numerical models would represent the first step for a future simulation of an entire PHP. To summarize, the chaotic behavior of the pulsating heat pipes makes them unpredictable and a more fundamental comprehension, guided by experimental and numerical tests, is needed for the development of future cryogenic pulsating heat pipes design applications.

For these reasons, the objective of the present work consists in characterizing the thermohydraulic behavior of the meter-scale horizontal cryogenic PHPs as a cooling solution for superconducting magnets.

In chapter 1 the role of cryogenics and the superconductivity phenomenon are defined. The main existing superconducting magnet cooling techniques are exposed and a detailed definition followed by a literature review on pulsating heat pipes is given. Finally, the motivation and contribution of this work are provided.

Chapter 2 is dedicated to the description of the cryogenic experimental facility, composed of three horizontal one-meter long pulsating heat pipes.

The following chapters focus on the experimental and numerical results collected during the present research project. In chapter 3, experimental results obtained using nitrogen as working fluid during a progressive heat load test are presented. The thermodynamic characteristics of the fluid are defined based on the temperature and pressure evolution of the evaporator, adiabatic and condenser parts. Thermal performance and circulation modes are also provided. This test will be considered as the "reference" to compare with other experimental results in the following chapters.

Chapter 4 is dedicated to a comparison of the experimental results from progressive heat load and fixed heat load tests using three different working fluids, which are nitrogen,

neon and argon. Physical parameters of the different working fluid are compared to understand differences in the fluid's behavior. Moreover, the influence of the buffer volume connection to the PHP during experimental tests is analyzed.

Specific tests to determine the influence in the thermal performance of the start-up conditions and the temperature of the condenser have also been performed. These experimental results are presented in chapter 5. This chapter also focuses on the influence of the number of turns in the thermal performance of the system. Finally, results of tests of a sudden increase of heat load are discussed. These tests are supposed to simulate the heat load submitted during the quench of a superconducting magnet to help comprehend the transient behavior of such heat pipes.

Chapter 6 is dedicated to the numerical work developed during the present research project. Firstly, the experimental reference model of a single-branch cryogenic PHP is defined. Secondly, the 2D axisymmetric numerical model with assumptions and limiting conditions is presented. Then, the numerical results are shown and explained with respect to the literature findings.

Finally, the last part of this document reviews the findings of this work and identifies potential investigations to solve new questions concerning the operating mode of pulsating heat pipes.

Chapter 1

Cryogenic cooling for superconducting magnets

1.1 Scientific and technical background

1.1.1 Cryogenics

Cryogenics is the area of physics related to the phenomena and processes at low temperatures, usually defined as below 120 K [21]. The specific phenomena that occur at cryogenic temperatures refers to the characteristics of fluids and materials such as liquefaction and solidification of ambient gases, ductility of structural materials, heat transfer capacities of fluids and materials, or even the appearance of quantum effects like superconductivity and superfluidity.

In this context, numerous cryogenic technologies have been developed for a huge range of applications, from cryopreservation systems in biology conservation to cryogenics fuels as propellants for space rockets (liquid hydrogen is the most common example) or cooling of superconductors (including magnets, wires and electronic components).

The present research work focuses on the cryogenic technology allowing the appearance of the superconductivity phenomena in superconducting magnets.

1.1.2 Superconductivity

Discovered by H. Kamerlingh Onnes in 1911, the superconductivity is the physical phenomenon corresponding to zero electrical resistance. A *superconductor* is a material able to conduct electrical current without resistance and, consequently, any heat dissipation by Joule effect. It is actually the prerequisite for most applications, such as high-current transmission lines or high-field magnets, reducing dramatically operation costs [22]. Nev-

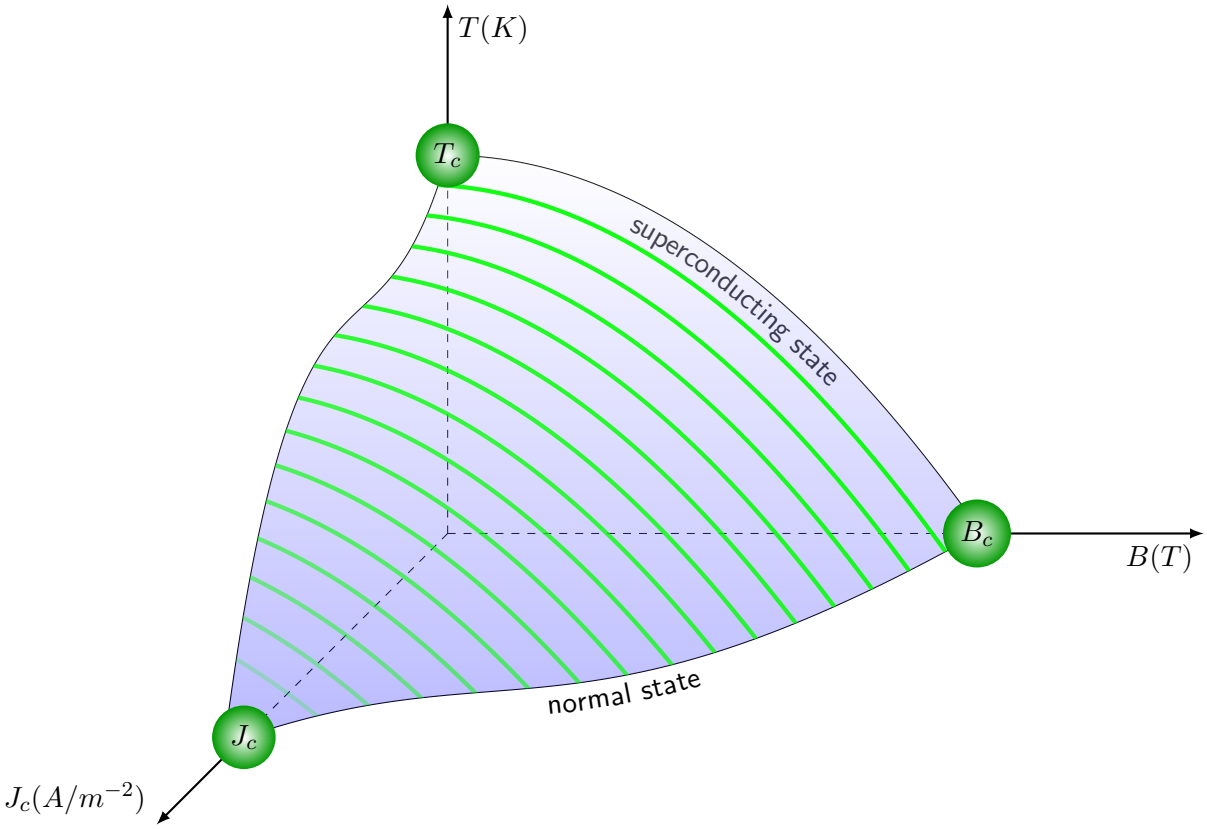

Figure 1.1: Critical surface of a superconductor.

ertheless, this superconducting state is reached only below a certain temperature (in the cryogenic range), called *critical temperature* (Tc), achieved using cryogenic cooling techniques.

This temperature requirement can be reduced in the presence of magnetic field (B) and/or electrical current density (J) in the bulk of the material. As a result, a "superconducting region" can be represented graphically relating the critical current density, the critical magnetic field and the critical temperature (Jc, Bc and Tc respectively) in what is known as the *critical surface*, shown in Fig. 1.1. Out of this region, the material is not in superconducting state. Consequently, if one of the three parameters is increased, the superconducting region on the plane defined by the other two is necessarily reduced. Thus, fixing one parameter, the evolution of the other two parameters can be represented in what is known as the *critical curve*. As an example, critical curves at fixed temperature of some superconductors are presented in Fig. 1.2.

High magnetic fields can be generated by superconducting magnets by using significantly high current densities. Considering the characteristics described previously, the working temperature (T) will be reduced from the maximum critical temperature (Tc) of the superconductor material ($T < Tc$ at $B = 0$ and $J = 0$). Due to this, the choice of a appropriate cooling system with its cryogenic working fluid is crucial to maintain the superconductor in its superconducting state and therefore generate the desired mag-

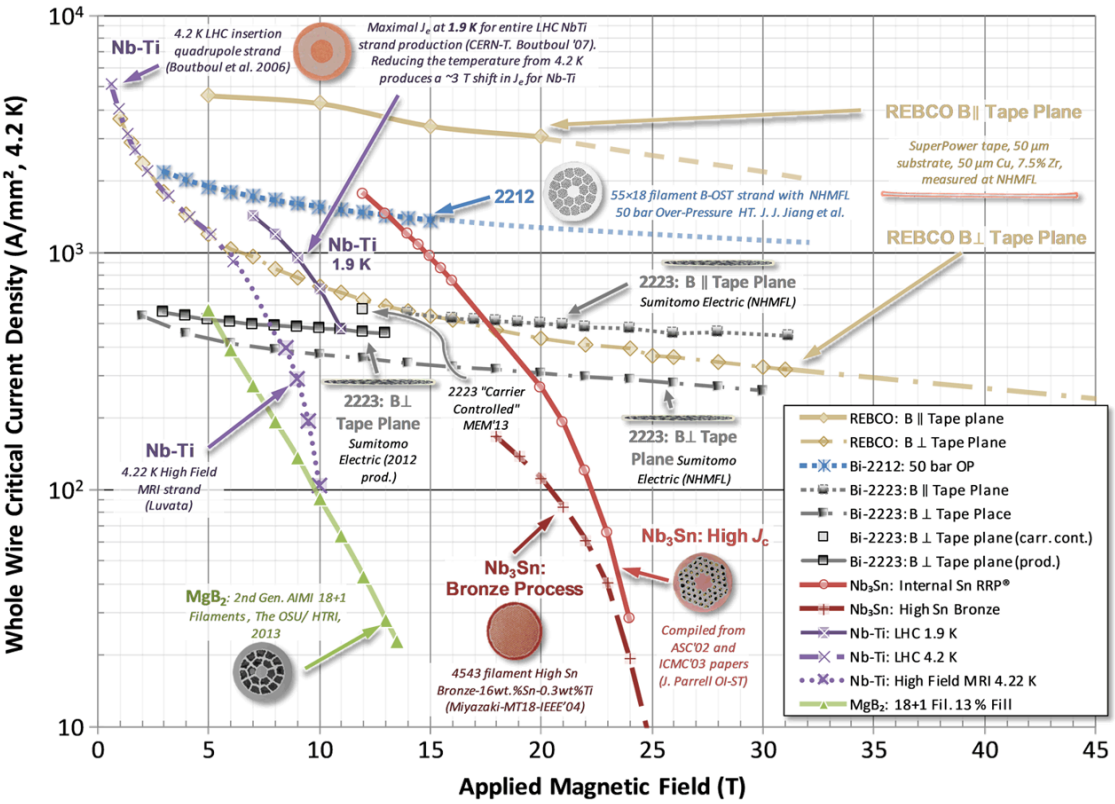

Figure 1.2: Critical characteristics of some superconductors. Courtesy of P. Lee (NHMFL)

netic field. It can be seen in Fig. 1.3, the range of working temperatures of the available cryogenic fluids and the critical temperatures of some superconductors. For example of the most used superconductors, the NbTi, has a critical temperature of 9 K. It has been always associated with helium which practical temperature range is around 1.8 to 4.2 K. This is to have a sufficient temperature margin to ensure stable working conditions.

In this section, a simplified definition of the superconductivity is given to understand the relation in the present research project between superconducting magnets and cryogenics. Nevertheless, it is important to mention that superconductivity is also characterized by another phenomena which is the expulsion of the magnetic field from the material (known as the Meissner effect), and that there are other factors which can affect the superconducting state, such as the microstructures, which alter magnetic vortex dynamics [22].

1.1.3 Magnet cooling techniques

There exist two main categories for cooling superconducting magnets: the "direct method" and the "indirect method". The first one uses a cryogenic fluid in direct contact with the superconductor, the magnets is then considered as a "wet" magnet. The second method uses a cryogenic fluid or a cooling system through intermediate thermal components. In this case, the magnet is considered as a "dry" magnet. Both cooling methods can be

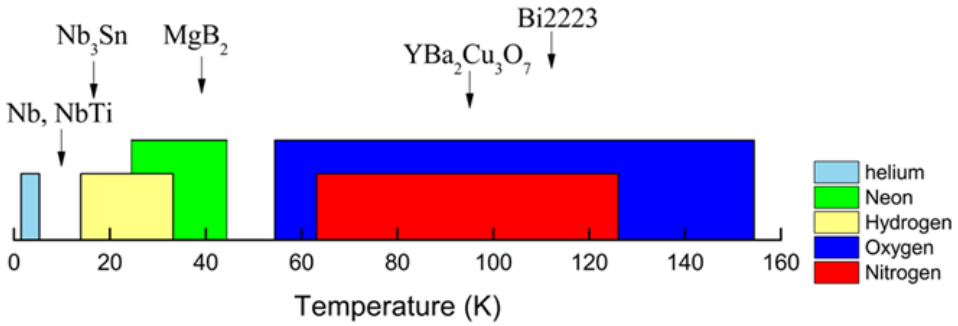

Figure 1.3: Range of working temperatures of cryogenic cooling fluids and critical temperatures of some superconductors.

used through different configurations, as can be seen in Fig. 1.4 and can be divided into subcategories depending on the physical phenomena employed to cool, such as pool boiling convection (cooling baths), forced convection, natural circulation and pure solid conduction.

The choice of the cooling system mainly depends on the superconductor type (and its critical temperature), the geometric configurations, the heat load to evacuate and its time distribution. Consequently, the working fluid or materials will be selected to meet the demands.

Each method has its own advantages, the "direct" cooling method ensures a perfect contact between the cryogenic fluid and the magnet, giving a large heat transfer rate and an enthalpy reserve. The "indirect" method consumes considerably less cryogenic fluid, and offers a larger number of possible configurations, often combining a copper thermal link connected to a heat exchanger using a cryogenic fluid and linked to a cryocooler. Pulsating heat pipes are an example of thermal links that can be used in this indirect method and will be defined below in section 1.2.

1.1.4 The need of developing new cryogenic technologies

Nowadays, helium prices are unstable and subject to scarcities around the globe. At the beginning of the 20th century, the US Federal Reserve ensured stable helium supply offering low prices. After several crisis and the privatization of the organization, helium production these days is provided by a small group of countries, such as Algeria, Russia, Poland, Qatar and also the US [24]. Political instability, technical problems and the desire of certain countries to fill their reserves have generated a market crisis increasing the prices.

The development of low consumption cooling technologies using other cryogenic fluids seems to be a solution to avoid helium price dependence. Since other cryogenic fluids liquefy at higher temperatures than helium, in the case of superconducting magnets, the mentioned new technologies could be used to cool superconductors with relatively high

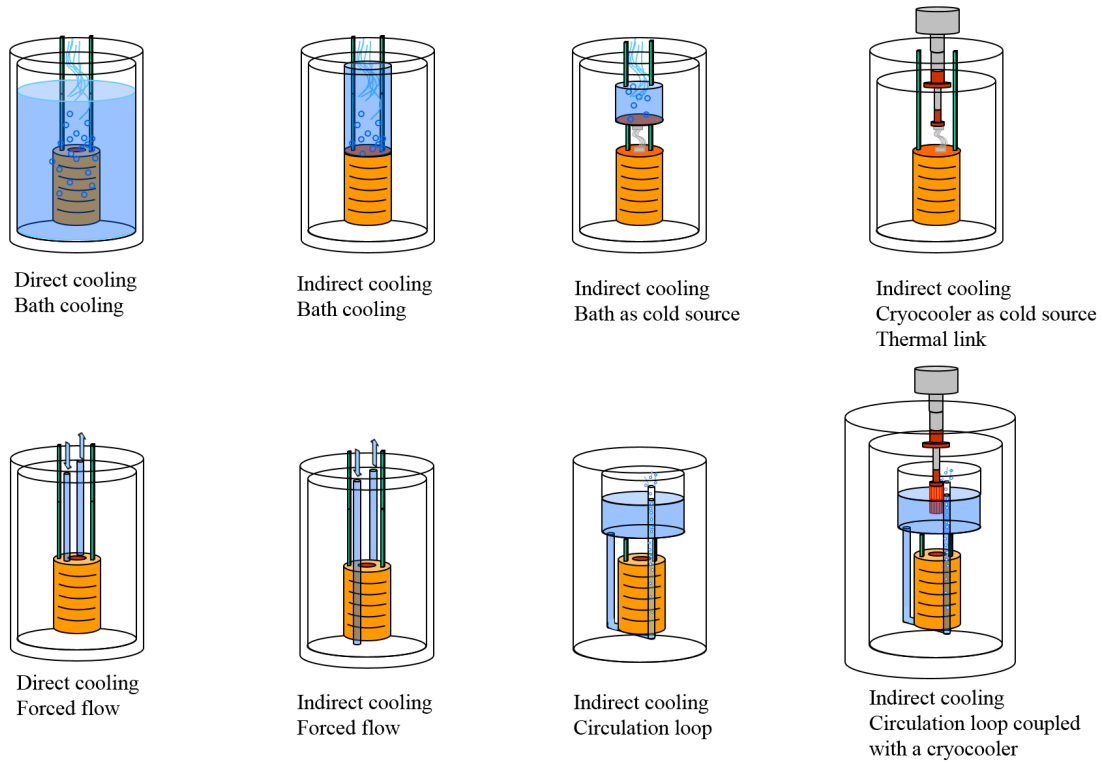

Figure 1.4: Example of various cooling methods [23].

critical temperature, known as High Temperature Superconductors (HTS).

In addition to that, the strong interest of the space industry in using superconducting devices, such as magnets for physics detectors, will lead to new cryogenic cooling technologies, because of the weight and gravity dependence of the existing ones described in section 1.1.3.

For all of these reasons, the development of new cryogenics cooling techniques for HTS characterized by lightness, low consumption and gravity independence, seems to be necessary in the years to come. In order to contribute to this area of research, the Accelerators, Cryogenics and Magnetism Department (DACM) is developing large-scale cryogenic Pulsating Heat Pipes (PHPs) as a novel cooling solution for high temperature superconducting magnets.

1.2 On the definition of Pulsating Heat Pipes

The pulsating (or oscillating) heat pipes take their name from the "pulsating" (or "oscillating") flow that the working fluid adopts in operating conditions. In fact, a pulsating heat pipe (PHP) is a heat transfer device composed of a single capillary tube (or pipe) bent in many U-turns, connecting an evaporator to a condenser separated by an adiabatic part (see Fig. 2.4 a)). The temperature and pressure conditions of the fluid are close to phase-change conditions. Due to this and to the capillary dimensions of the tube, the

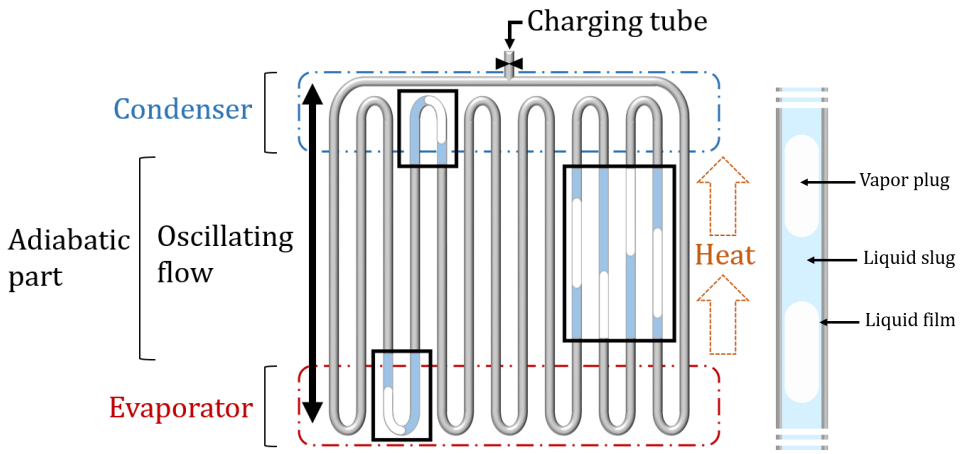

(a) Pulsating Heat Pipe.

(b) Zoom in a capillary tube.

Figure 1.5: Schematic of the structure of a PHP.

fluid is distributed in alternating liquid slugs and vapor plugs generally surrounded by a thin liquid film (see Fig. 2.4 b)). This liquid film enables circulation of the vapor plugs sliding through the tube. Permanent thermal instabilities in the PHP create the oscillating flow which allows the transfer of heat from one end (the evaporator) to the other (the condenser).

More precisely, when a liquid slug and an adjacent vapor plug approach the evaporator, the heat input received generates a temperature increase and several processes occur: firstly evaporation takes place in the liquid film and also in the liquid slug at the edge in contact with the vapor plug, where phase-change conditions are reached. Secondly, the vapor plug increases its pressure considerably (vapor expansion) creating a small pressure disruption. Also, new vapor bubbles can appear in the liquid slug due to boiling. On the other side, when a liquid slug and an adjacent vapor plug approach the condenser, inverse processes occur: the heat is transmitted to the condenser decreasing the temperature of the fluid, the vapor plug is then liquefied (vapor contraction and condensation), increasing the size of the adjacent liquid slug and contributing also to a pressure disturbance. Then, if we consider these phenomena several times in a larger scale, these thermally induced two-phase instabilities create several pressure instabilities that causes the pulsating or oscillating motion.

The heat is mainly carried out through two different ways: on one hand by sensible heat, mainly through the liquid parts which have a higher density and heat capacity. The heat transport from the evaporator to the condenser takes place by advection of these liquid parts. On the other hand by latent heat, due to all the phase-changes occurring simultaneously. Until now, it is not clear which of them plays the key role in the overall heat transfer [25]. The movement is mainly due to compression and expansions of the vapor plugs that push the adjacent liquid slugs.

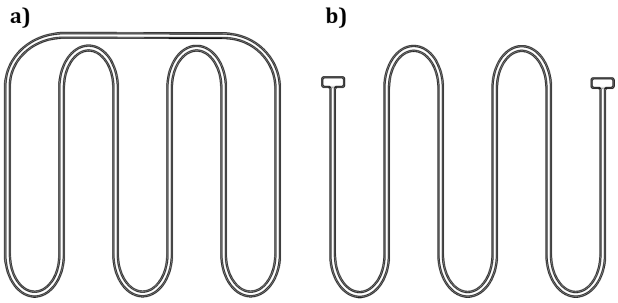

Figure 1.6: Configurations of pulsating heat pipes. a) Closed-loop configuration b) Open-loop configuration.

Concerning the amount of fluid inside the PHP, the *liquid filling ratio* (FR) is generally used to indicate the proportion of liquid and vapor in the PHP. This latter compares the volume of liquid inside the PHP over the volume of the PHP, and is defined as follows:

$$FR = \frac{V_l}{V_{php}} \cdot 100. \tag{1.1}$$

The pulsating heat pipes can be in a "closed-loop" configuration (or "looped" configuration), where the ends of the capillary tube are connected to one another, or on the contrary, in an "open-loop" configuration (or "unlooped" configuration), as illustrated in Fig. 1.6. Occasionally, some PHPs may also use a check valve to join both ends of the tube, forcing a fluid direction [26]. It is generally agreed by researchers that the closed-loop PHP configuration has better heat transfer performance [27].

In addition, the pulsating heat pipes can operate in different orientations, from vertical to horizontal position. In vertical position, where they are gravity assisted, they can operate in "bottom heating mode" (with the evaporator located at the bottom) or in "top heating mode" (with the evaporator located at the top). They can also have several heating configurations, with more than one evaporator [13].

The definition of the inner diameter of the capillary tube is derived from theoretical analysis and experimental results using the Eötvös dimensionless number (Eö) which considers the equilibrium between gravitational and capillary forces. The slug/plug circulation is maintained when capillary forces overcome gravitational forces. According to the literature, it is generally accepted that the maximum value of the inner diameter is defined by:

$$D \leq A\sqrt{\frac{\sigma}{g(\rho_l - \rho_v)}}, \tag{1.2}$$

where $A = \sqrt{E\ddot{o}}$ and generally equal to 2 [25] or 1.84 [28].

Nevertheless, other researchers have suggested different values of the Eötvös number, ranging from 0.88 to $2\pi^2$ [29] and consequently, other limiting diameters. This means that the limiting values to calculate the maximum diameter are not definitive and are still under research.

The working fluid in pulsating heat pipes can adopt in some cases flow patterns other than the oscillating flow. At low heat fluxes, the oscillating flow can be slow enough to stop in certain parts of the PHP creating what is known as "local dry-out", where a vapor plug without liquid film acts as a real plug and locally stops the flow [30–32]. Nevertheless, if the PHP has enough parallel tubes between the evaporator and the condenser, it will continue to work even with a blocked tubing part. In addition, when the heat input of the evaporator exceeds a certain limit, the standard oscillating flow switches to a semi-annular or annular flow following a single direction of circulation. This transition has been visualized in transparent PHPs [5, 27, 33] but cannot be confirmed in other PHPs using opaque materials, especially in horizontal pulsating heat pipes. Finally, beyond a certain value of heat input at the evaporator, the working limit of the PHP can be reached. In that case, the amount of liquid in the evaporator is too small to evacuate the heat because of a strong evaporation mass flow rate, and the temperature of the evaporator increases permanently unless the heat load is reduced, this event is known as "dry-out".

Moreover, global heat transfer performance is also affected by the properties of the materials of the different components, such as the thermal conductivity and effusivity of the tube [34], as well as by the size of the evaporator and the condenser and the length of the adiabatic part [35].

The concept of "Pulsating Heat Pipe" was introduced by Hisateru Akachi with the publication of two patents "Structure of a heat pipe" [36] and "Structure of a micro-heat pipe" [37] in 1990 and 1993 respectively. In this patents, more than 30 different pipe configurations where described, all of them having at least one heating part and one cooling part. A variety of tube cross sections, pipe configurations and orientations, as well as a non-condensable gas storage tank used as a control system were defined. Since then, the study of the thermohydraulic behavior of pulsating heat pipes have been developed for numerous applications that will be detailed in next section 1.3.

1.3 Literature Review on Pulsating Heat Pipes

1.3.1 Cryogenic Pulsating Heat Pipes

In the cryogenic field, pulsating heat pipes have mainly been studied to cool superconducting magnets [11, 30, 38, 39], but there exist other applications such as cell preservation in cryobiology [40]. The working fluids tested in cryogenic PHPs are generally helium (4.2 K

at 1 bar), nitrogen (77.3 K at 1 bar), neon (27.1 K at 1 bar), hydrogen (20.3 K at 1 bar), and oxygen (90.1 K at 1 bar) and argon (87.2 K at 1 bar) to a lesser extent. It can be found on open literature that experimental setups often use copper blocks as evaporator and condenser parts, to reproduce the magnet to cool and to ensure the thermal contact with the cold source. Generally, a cryocooler is used as a cold source and the capillary tubes are made of stainless steel having a poor thermal conduction for being sure that the heat is mainly transferred due to the pulsating heat pipe mode. Moreover, vertical pulsating heat pipes are studied in the "bottom heating mode" with the evaporator located at the bottom, benefiting from gravity assistance.

Experimental results from different cryogenic pulsating heat pipes using a variety of working fluids have been reported in scientific literature. The main studies on the cryogenic PHPs are presented below focusing on the lengths of the devices and their thermal performances.

As a reference, T. Mito and K. Natsume et al. [9–11, 41] have been working on two similar PHPs having a length between 16 and 20 cm, including the evaporator, the condenser and the adiabatic part. They have tested neon, nitrogen and hydrogen at different filling ratios and inclinations. The effective (or equivalent) thermal conductivities (defined below in chapter 3) were between 5100 and 19500 W/(m.K) for Ne, 2200 and 11500 W/(m.K) for H_2 and 5000 and 18000 W/(m.K) for N_2. The maximum heat load transferred was 1.5 W using Ne, 1.2 W using H_2 and 7 W using N_2. It can also be noticed that they obtained excellent thermal performances using neon as working fluid even when the inner diameter of the capillary tubes was larger than the maximum theoretical one [41] given by eq. 1.2.

Concerning cryogenic pulsating heat pipes using helium, L.D. Fonseca et al. [13] have been working on three one-meter long vertical pulsating heat pipes all three connected through the condenser part and having each two evaporators at the bottom. It can be observed that the temperatures of the three evaporating parts oscillate with the same amplitude and frequency but with a time lag, showing the influence of each PHP into the other [42]. The maximum effective thermal conductivity was 50000 W/(m.K) with a heat load of 0.258 W per heater. In addition, D. Xu [43] and M. Li [44] tested shorter helium cryogenic PHPs (about 20 cm long) transferring a maximum heat load of 1.29 W in both cases. The first author tested different inclinations and filling ratios attaining a maximum effective thermal conductivity close to 16000 W/(m.K) in vertical position. The second author tested the influence of the number of turns in vertical position, achieving 15652 W/(m.K).

Furthermore, Liang et al. [45–48] have studied several vertical pulsating heat pipes using mainly neon as working fluid. Firstly, a 16.5 cm long PHP has been evaluated at different filling ratios, achieving a maximum effective thermal conductivity of

22180 W/(m.K). The maximum heat load transferred was 4.93 W before the dry-out. Two other longer PHPs, exceptionally made of copper capillary tubes, have been studied at different filling ratios and condenser operating temperatures, achieving the maximum performance at the highest condenser's temperature: on the one hand, a 70 cm long pulsating heat pipe with a curving adiabatic part reached an effective thermal conductivity between 3466 and 30854 W/(m.K) being able to transfer 35.6 W of heat load; on the other hand, a 48 cm long PHP has been tested using neon and nitrogen as working fluids, attaining effective thermal conductivities between 13000 and 34000 W/(m.K) for Ne and 6000 and 18000 W/(m.K) for N_2, and transferring 12.24 and 35.92 W of heat load respectively.

Using also nitrogen as working fluid, other PHPs with similar lengths have been characterized. As a reference, Jiao et al. [49] have developed a PHP with a length of 20 cm. Cooled with a nitrogen bath and working in horizontal position, the PHP was able to achieve a minimum thermal resistance of 0.11 K/W and to transfer 381.2 W of heat load. In addition, Y. Li et al. [44] have tested a 17 cm long PHP also cooled in a nitrogen bath. They tested different orientations and heating configurations transferring a maximum heat load of 19 W. The maximum effective thermal conductivity was 16000 W/(m.K). In their results, it can be seen that a minimal temperature difference between the evaporator and the condenser is necessary to start the working oscillating motion and that the evaporator was unable to recover its performance after a dry-out. Furthermore, Fonseca et al. [50] have developed a cylindrical 22 cm long PHP able to attain effective thermal conductivities between 16000 and 50000 W/(m.K) in vertical position and 35000 and 62500 W/(m.K) in horizontal position. The maximum heat load transferred was 3.5 W in vertical position.

As mentioned before, certain cryogenic fluids are less common in cryogenic PHPs. Nevertheless, X. Sun et al. [51] have tested a 60 cm long vertical PHP using H_2 at different filling ratios and condenser's temperatures, achieving an effective thermal conductivity between 30000 and 70000 W/(m.K) and transferring up to 10 W before the dry-out. They observed local stopovers at low heat load and a better thermal performance at higher condenser's temperature. In this case the material of the tubing parts was different in the adiabatic part (stainless steel) than in the evaporator and condenser sections (copper), ensuring a better heat exchange. Another example is the single capillary horizontal tube tested by Gully et al. [52] using O_2 as working fluid and transferring 1.5 W of heat load.

Other cryogenic PHPs have also being developed in the last years, such as [12, 38, 53–55], but will not be detailed in this literature review because considerable differences in experimental setups and working conditions make the results difficult to compare with the experimental results of this research project.

Finally, the CEA of Paris - Saclay has developed and tested meter-scale long horizontal pulsating heat pipes working with N_2, Ne and Ar as working fluids. Experimental

results are part of the present research project and will be exposed in the following chapters 3, 4 and 5.

1.3.2 Microgravity conditions and horizontal inclination

Pulsating Heat Pipes have also been studied under microgravity conditions. Several results can be gather from experimental and numerical investigations. Generally, to attain microgravity conditions, the PHPs have been tested during parabolic flights and the working fluids used are fluids having a phase-change transition close to ambient temperature. Among the scientific works in microgravity we can highlight the following results:

Two aluminum 25 cm long PHPs using refrigerant R-114 as working fluid have been tested by Gu et al. [56, 57]. Both PHPs showed better heat transfer performance under reduced gravity ($\approx 0.02g$) than normal or hypergravity ($\approx 2g$) conditions. In horizontal orientation the performance was not affected by the gravity variations and a steady pulsating flow was achieved.

Exceptionally, De Pavia et al. [58] were able to test a PHP in a sounding rocket, achieving microgravity conditions during several minutes. Even if it was a 10 cm long copper flat-plate PHP, where the heat transfer by conduction was not negligible, the device transferred almost 35 W in stable conditions using water as working fluid.

Furthermore, Mameli et al. have collaborated in several numerical and experimental researches. Mameli et al. [59] and Manzoni et al. [60] have developed and validated a 1D numerical code comparing their numerical results with experimental results obtained during parabolic flights. In this case, the PHP was more gravity dependent, showing an increase of evaporator's temperature during microgravity conditions. Moreover, they tested two other types of PHPs in parabolic flights. The PHPs were about 20 cm long and FC-72 was used as working fluid. In the first experiment [14], the PHP was made of 32 copper channels. The variation of the acceleration field had no measurable effect on thermal operations of the PHP in horizontal position and results on ground were also very similar to results in microgravity conditions. In the second experiment [61, 62], the PHP was made of ten aluminum parallel channels and the inner diameter was larger than the capillary threshold. Due to this, the PHP worked as a thermosiphon on ground but adopted an oscillating flow in microgravity conditions, even during non-uniform heating configurations. A similar aluminum PHP with 14 parallel channels was also tested [63] showing that the microgravity periods contributed to start and maintain the oscillating flow.

Finally, in the most recent scientific publications, we can also find numerical 1D simulations from Sun et al. [64] investigating the oscillating motion of the working fluid under microgravity conditions, experimental results of Ayel et al. [65, 66] in a flat-plate

PHP submitted to different gravity conditions.

In addition to the particular results found in microgravity conditions and their similarities with horizontal PHPs on ground, several researches have also been working on the influence of the number of turns (or parallel tubing parts) in horizontal PHPs. Since the beginning of the PHPs, the inventor Akachi [67] suggested a minimum number of 80 turns for horizontal PHPs to work. This minimum number was later reduced to 40 by Lin et al. [68] and Cai et al. [69], showing the same thermal performance in horizontal and vertical inclination. Later on, Mameli et al. [17] proved numerically the existence of this minimum number. Finally, results from Charoensawan et al. [70, 71] showed the influence of several parameters to define the minimum number of turns in horizontal PHPs, such as the working fluid, the inner diameter and the evaporation section.

It can be concluded from this section that, even if during parabolic flights the microgravity conditions last only a few seconds and working stable conditions cannot be reached during long periods, there are similarities between microgravity conditions and the horizontal position on ground. Also, the number of turns has a strong influence in the performance of horizontal pulsating heat pipes. Due to this, in the present research project, three horizontal pulsating heat pipes having different number of turns have been tested for possible space applications in the context of the SR2S project mentioned in the introduction. The experimental setup will be detailed in chapter 2.

1.3.3 Influence of the working fluid

It is generally agreed by researchers that the physical properties of the working fluid have a strong influence in the global PHP behavior. Nevertheless, it is difficult to quantify the role of each property in the overall heat transfer process, especially considering that some properties have opposite effects in the fluid behavior. The surface tension (σ) and the dynamic viscosity (μ) are related to the movement of the fluid, while the specific heat (Cp) and the thermal conductivity (λ) are responsible of "carrying" the heat in the transfer process. Other properties, such as the latent heat (Lv) and the density (ρ) also play an important role. In addition, the boiling point and the rate dp/dT at saturation conditions determine at which point the properties change and how important is this change. More details about the effects of the mentioned physical properties are given as follows:

- Surface tension. The surface tension has a dual effect. On one hand, larger surface tension creates larger capillary resistance and additional pressure drop. So, smaller surface tension is more favorable to the fluid movement [5]. On the other hand, if we consider the calculation of the inner diameter as defined in 1.2, higher surface tension gives a higher critical diameter. In this case, the cross-sectional area is higher improving the heat transfer [15].

- Latent heat. This physical property also has a dual effect [72, 73]. Firstly, a lower latent heat contributes to the generation of bubbles, accelerating the boiling process (especially during start-up process) and increasing the fluid oscillating velocities. Due to this, at low heat fluxes a lower latent heat is therefore desirable. But, at higher heat fluxes, a fluid with a higher latent heat can absorb more heat before boiling, avoiding the dry-out, more energy can then be adsorbed or released during the phase change. It is important to note that nowadays it is not clear if the latent heat or the sensible heat plays the key role in the overall heat transfer. Some studies [73] support the importance of the fluid movement and its dependence on the latent heat, and other studies defend the theory that the sensible heat plays the key role [15, 74].

- Specific heat. This property is related to the sensible heat transfer. Normally, a higher specific heat is desirable because it could bring more energy within each degree of temperature difference, as the fluid has a larger enthalpy reserve [72].

- Dynamic viscosity. Similarly to the surface tension, a lower dynamic viscosity is responsible of lower friction forces and easier fluid motion. In fact, reducing the shear stress and the pressure drop, the heat input required to start or maintain the oscillations is lower, the fluid can move easily and with a higher velocity [72, 75].

- Thermal conductivity. The thermal conductivity and, consequently, the thermal diffusivity ($k/(\rho Cp)$), are responsible of the temperature distribution in the fluid and the thermal response time. A larger thermal conductivity ensures a faster heat transfer reducing the temperature difference between the evaporator and the condenser, as concluded in [76].

- The rate of dp/dT at saturation conditions. At a higher value of $(dp/dT)_{sat}$, the difference of vapor pressure between the evaporator and condenser will increase with temperature. This pressure difference represents the primary driving force that causes the fluid motion. Due to this, a higher value of $(dp/dT)_{sat}$ contributes to a better global performance improving the oscillatory motion of the liquid slugs [25, 77].

Before concluding about the role of each property in the overall heat transfer, further investigations need to be performed to determine precisely the weight of each property in the overall heat transfer. In addition, parameters related to the wettability, such as the dynamic contact angle, could also be investigated, as well as fluid mixtures for modifying those properties.

1.3.4 Fluid circulation in Pulsating Heat Pipes

As mentioned in section 1.2, pressure instabilities due to the temperature difference between the evaporator and the condenser generate the characteristic oscillating flow in pulsating heat pipes. Nevertheless, several studies on PHPs have shown that the fluid can adopt different flow patterns depending on the operating conditions. The movement of the fluid in pulsating heat pipes has been generally studied in visualization experiments using infrared or high speed video cameras in vertical PHPs with fluids working near the room temperature.

In the first visualization studies [27, 78–80] boiling phenomena, growth and coalescence of vapor bubbles, random fluid circulation and evaporation of liquid film were observed.

In addition, Khandekar has extensively studied pulsating heat pipes at room temperature, defining the evolution of the flow patterns with increasing heat flux [5]. He performed two visualization experiments. In the first one, the PHP was made of 10 parallel tubes in glass at the adiabatic part and copper turns at the evaporator and condenser parts. The PHP was tested at different orientations and filling ratios (between 20 and 80 %) using ethanol and water as working fluids. The device did not work properly in horizontal position (probably due to the low number of turns as suggested by the author) and the main visual observations were performed with the PHP in vertical position. In the second experiment, the PHP was a single vertical loop also with glass tubes.

First of all, is was observed that a minimum heat flux is needed to create flow instabilities and start the movement of the fluid, otherwise bubbles remain stagnant at their respective positions. Then, when the heat flux surpasses a critical value, the flow pattern remains an oscillating flow. The amplitude of these oscillations increase with the input power. Above a certain heat input, the flow direction tends to be fixed (reversals become rare) meaning that the transition from oscillating to annular flow has started. Finally, when the heat flux is increased even higher, an annular flow is clearly established. At this point, the thermal performance of the PHP is maximal. Several images of the evolution of the flow pattern with the heat flux are represented in Fig. 1.7.

Later on, other researchers have confirmed these different flow patterns and discovered more specific details about fluid circulation in PHPs. Visualization work performed by Spinato et al. [81] in a vertical capillary tube using R245fa as working fluid confirmed the existence of flow reversals which tend to disappear increasing the heat load. Specific frequencies of oscillations were detected during slug and annular flows. Recently, Xue et al. [82] filmed the coalescence of bubbles and measured different fluid velocities depending on the applied heat load (between 0.1 and 0.6 m/s for oscillating flow and between 0.4 and 0.9 m/s for annular flow) in a PHP working with ammonia. Ayel et al. [65] observed

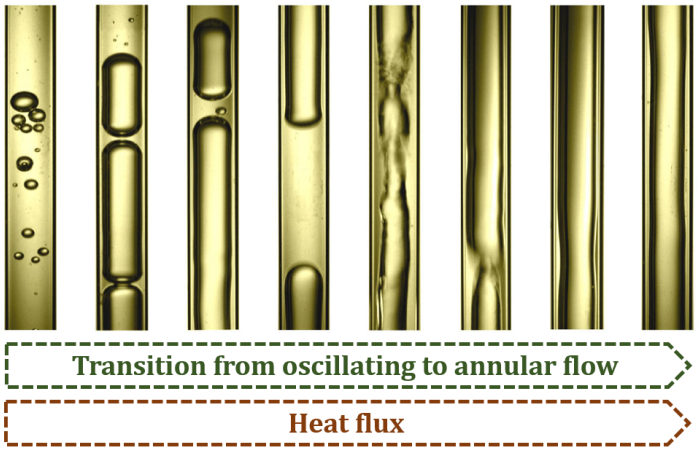

Figure 1.7: Flow patterns observed in closed-loop pulsating heat pipes by Khandekar [5].

the flow patterns in a vertical flat-plate PHP with ethanol always having an annular flow. Furthermore, Sun et al. [64] observed the generation and growth of small bubbles in capillary tubes with ethanol. The size of the bubbles was inversely proportional to the heat load and the filling ratio. A single loop tested with ethanol and FC-72 was also studied by Ilinca et al. [83]. They observed a clockwise and anticlockwise fluid circulation, depending on the heating configuration.

Apart from visualization results, other experimental results have also shown specific characteristics of the fluid circulation. For example, stopovers of the working fluid have also been noticed by Manzoni et al. [60] at zero-g conditions in their numerical model and by Mangini et al. [62] experimentally in microgravity conditions. Moreover, local temperature increase in specific locations at the outer surface of the tubes of the adiabatic part have been measured by Cui et al. [84] and Bruce et al. [30].

Furthermore, results concerning specific oscillation frequencies do not always match. On the one hand, experimental and numerical results from Mameli et al. [85], Pouryoussefi et al. [86] and Manzoni et al. [87] do not show any specific frequency after performing Fast Fourier Transform (FFT) of the temperature and pressure evolution, concluding on the chaotic behavior of the PHP fluid system. On the other hand, some experimental results [35, 42, 88, 89] reveal the existence of specific temperature and pressure frequencies depending on the heat load, the filling ratio and the heating configurations. In addition, numerical results from Pouryoussefi et al. [90] show dominant frequencies decaying with time towards to a chaotic system.

1.3.5 Working conditions in Pulsating Heat Pipes

To understand the thermodynamics of pulsating heat pipes is a key point to control and predict their thermal behavior. However, it is one of the least understood aspects. To solve this, some studies have focused on the definition of the thermodynamic state of the

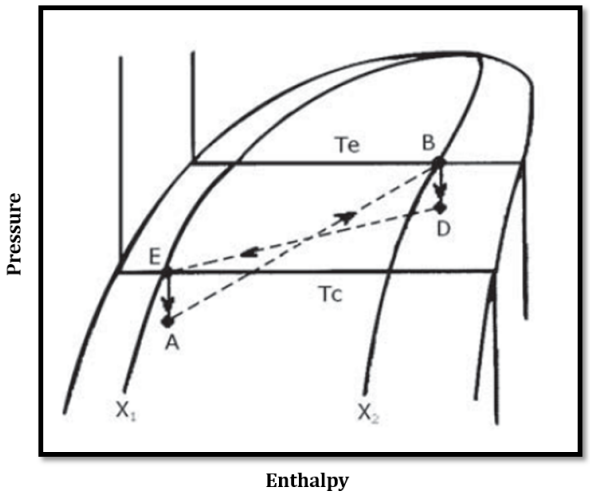

Figure 1.8: Thermodynamics of a PHP [33].

fluid in different cases, from stable working conditions to dry-out conditions.

As a reference, Groll et al. [33] defined a thermodynamic cycle of the fluid in PHPs using an enthalpy diagram as seen in Fig. 1.8. In the P-h diagram, even if exact positions are unknown, relative (and instantaneous) locations of the state of fluid at condenser and evaporator outlet can be assumed based on their vapor quality. When the fluid passes through the evaporator, from point A to point B in the diagram, the process is simplified to heat input at a constant pressure combined with isentropic pressure increase due to bubble expansion. When the fluid passes through the condenser, from point D to point E in the diagram, the process is simplified to constant pressure condensation with negative isentropic work. Isenthalpic pressure drop in the adiabatic section completes the cycle.

Other authors have concluded experimentally [62, 91] and numerically [31] about the subcooled state of the liquid parts and saturated or superheated state of the vapor parts during operating working conditions. It has also been noticed by [52] and [30] that sometimes a vapor plug in the adiabatic part can reach a higher temperature than the evaporator, what is known as "piston effect", a local adiabatic compression defined by [92]. Conversely, other authors [42, 55] have made the hypothesis that both phases are at saturation conditions.

In addition, when the heat flux becomes too important, the total amount of heat cannot be transferred to the condenser by the working fluid. The amount of liquid arriving into the evaporator is too small to evacuate the heat because of a strong evaporation mass flow rate, the temperature of the evaporator increases [45] and ends up drying, full of superheated vapor [30, 91]. It has also been noticed by Khandekar et al. [32] in a single loop PHP that in dry-out situations, a single liquid plug hangs in the condenser zone while the evaporator section is covered up by one vapor bubble, the fluid is then divided into two distinct parts. Furthermore, in some cases the PHP is not affected by its heating history and, after a dry-out process, stable operating working conditions can be re-established

again if the heat input is reduced [93]. In some other cases, after a dry-out, even if the input power is decreased, the temperature and pressure conditions are higher than before the dry-out at same input power [44].

Apart from the thermodynamic state of the fluid, it is also important to consider the amount of liquid and vapor in the PHP, what is known as the filling ratio, defined in section 1.2. Some researchers have determined an optimum filling ratio where stable conditions and maximum thermal performance are reached. This optimum filling ratio seems to vary considerably depending on the fluid and the PHP configuration [94]. For example, Fonseca [42] found an optimum filling ratio at 69% using helium as working fluid, Pouryoussefi et al. [86] at 60% with water and ethanol, Zhao et al. [8] around 40% also with water and ethanol and Mameli et al. [93] at 50% with FC-72. In addition, Liang et al. found different optimum filling ratios for low and high heat fluxes [47] using neon as working fluid.

Moreover, some other authors have also studied the start-up process to find optimum start-up conditions. As a reference, Wang et al. [95] concluded about the necessity of a minimum input power to start-up the oscillations, Liu et al. [96] noticed a faster start-up at higher input powers and Han et al. concluded that the initial random distribution of the fluid has a strong influence on the start-up process [72]. Moreover, a minimum temperature difference between the evaporator and condenser generates a pressure difference that contributes to start-up the oscillating flow in PHPs [44, 94].

1.3.6 Geometric parameters

In pulsating heat pipes, the most important geometrical parameter is the inner tube diameter. As mentioned in section 1.2, the inner diameter of the capillary tubes is calculated from the Eötvös dimensionless number, which takes into account the equilibrium between the surface tension and the gravity forces. The maximum value of this inner diameter ensures the surface tension domination to maintain the vapor plugs.

The maximum limit of this inner diameter was defined for the first time by White and Beardmore [97] after analyzing, with many different fluids, the evolution of a property number (Y) that compares the surface tension forces (Eötvös number), the viscous forces (Poiseuille number) and the inertial forces (Froude number) and is defined as:

$$Y = \frac{g\mu_l^4}{\rho_l \sigma^3} = \frac{Ps^4 E\ddot{o}^3}{Fr^2}. \tag{1.3}$$

The authors found that the surface tension force dominates when $E\ddot{o} \leq 4$, as it can be seen in Fig. 1.9, which shows the evolution of the Froude number versus the Eötvös number related by the property number. It is worthwhile to note that the corresponding

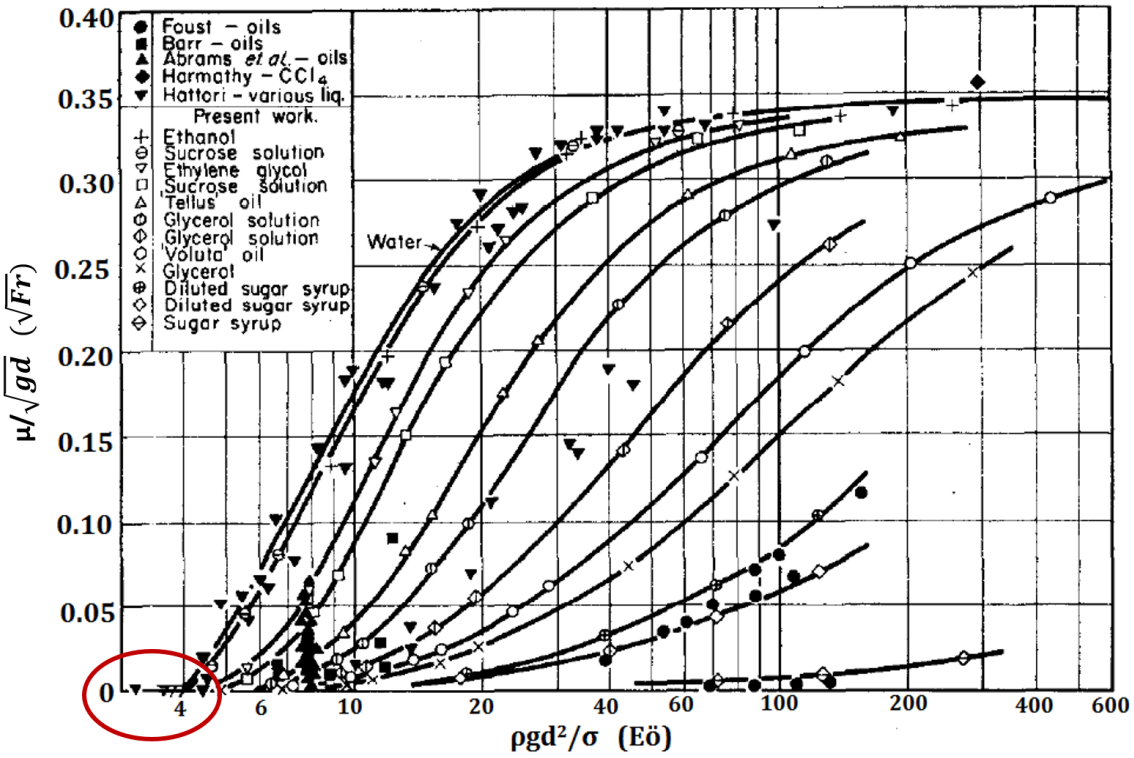

Figure 1.9: Results of cylindrical air bubbles rising in vertical tubes by [97]. Froude number versus Eötvös number.

experiments have been performed in vertical tubes, where the motion of the fluid is highly influenced by the gravity.

Later on, Khandkear [5] concluded that rather than a certain fixed critical diameter for PHP operation, there is a finite transition zone between PHP and thermosiphon operations where the inner diameter can be slightly larger. Furthermore, Gu et al. [56] defined the maximum inner diameter for microgravity conditions based on the comparison of the kinetic energy and the surface energy. Moreover, Hosoda et al. [98] developed an analytical model to predict the minimum inner diameter concluding that this latter depends on more parameters than just the Eötvös number.

It can also be found in other scientific works that PHPs have been able to work with larger diameters (around 1.2 times larger) [10, 41], especially under microgravity conditions (around 1.5 and 1.7 times larger) [14, 61, 63] and in horizontal position (around 1.2 times larger) [91].

Other geometric parameters such as the length and shape of the adiabatic part [6, 99], the sizes of the evaporator and condenser [100] or the shape of the capillary tubes [101] have also been tested recently but further investigations need to be performed to draw firm conclusions.

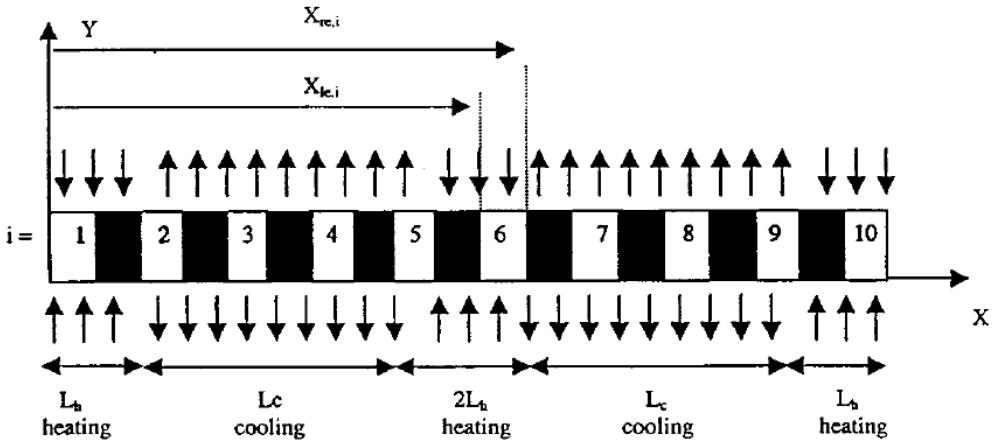

Figure 1.10: Alternating cooling and heating parts in the 1D thermal model developed by Y. Zhang and A. Faghri et al. [15].

1.3.7 Modelling of Pulsating Heat Pipes

In the numerical field several authors have been working on simulations of pulsating heat pipes, developing models to predict the behavior of the working fluid and the heat transfer phenomena. As a reference, the group of Y. Zhang and A. Faghri have developed one of the first consistent 1D numerical models. In their thermal model for looped and unlooped PHPs in [15], they simulate oscillatory phenomena solving the mass, momentum and energy equations for each liquid slug and vapor plug in a straight tube with alternating cooling and heating parts representing the turns of the evaporator and condenser parts, as shown in 1.10. To simplify, the heat transfer coefficients are fixed, the liquid is considered incompressible and the vapor follows the ideal gas law. As a result, they achieved to simulate the propagation of a pressure wave in the different plugs and slugs as in a PHP, but at the end of the simulation the total number of vapor plugs is reduced to the total number of heating sections, no matter how many vapor plugs were initially in the system. In addition, they conclude that the sensible heat plays a more important role than the latent heat in the overall heat transfer. Later on, they performed a similar study modifying the number of turns [16]. As a result, above five turns, the amplitude and frequency of oscillations and the lengths of plugs and slugs vary with the number of turns. Similar work was developed to analyze the liquid film evaporation and condensation processes in [74], and varying the diameter of the capillary tube in [102].

Based on the work started by the group mentioned previously, Mameli et al. have also developed a 1D numerical code for pulsating heat pipes [17, 59]. In this case, the tube wall and the liquid parts are subdivided into control volumes. Liquid slugs can merge or split creating a new vapor plug. In addition, the calculation of pressure also considers pressure drop due to meanderings. This constitutes a key point because, for the first time, it was numerically proved the influence of the number of turns in the fluid motion of a PHP and the similarities between zero-gravity conditions and horizontal position. The

model has also been modified and tested by [60, 87] in normal and hypergravity conditions considering this time the vapor as a real gas.

Another reference in the simulation field on pulsating heat pipes is the work developed by V. Nikolayev et al. In the thermal 1D model presented in [19], the geometry consists of a single capillary tube with one liquid part and one vapor part where the oscillations of the liquid-vapor interface are thermally induced. In this case, vapor is considered in superheated state following the ideal gas law and liquid is considered in subcooled state, ensuring thermal instabilities. The model has been tested in two different cases: without considering the liquid film and considering it with a variable length. The strong effect of the liquid film in the amplitude of the oscillations is proved. In [18], a multi-branch horizontal PHP is simulated, including effects of the tube heat conduction and bubble generation phenomenon. The results showed the contribution of bubble generation in stable oscillations with large amplitudes. Recently, simulations performed using CASCO software have demonstrated the impact of the inclination on PHPs [20], showing that thermal results in horizontal inclination are equivalent to microgravity conditions, thermal performance is highly conditioned by the fluid distribution due to inclination and latent heat plays a more important role than sensible heat in the overall heat transfer. It is therefore worthwhile to note that in horizontal position, a minimum temperature difference between the evaporator and condenser is necessary to start the oscillating movement and flow stopovers can occur at low heat flux. These authors have also worked on the simulation of thermodynamics of working fluid in PHPs. In [31] they present the results from calculations considering two different vapor states (saturated and superheated) and they analyze the influence of physical properties of four different fluids in the global PHP performance.

In order to name but a few other examples of 1D numerical models for PHPs, we can find the work developed by D. Yin et al. [103] where the transition from slug to annular flow is studied considering in the momentum equation the penetration of vapor plugs into liquid slugs. Also, in simulations performed by T. Daimaru et al. [104], pressure and energy propagation are related and vapor plugs received or exerted energy according to the direction of propagation. Senjaya et al. [105] have also developed a model to simulate the dry-out phenomena associated to a complete evaporation of the liquid film.

In addition, Rao et al. [34, 106] have also compare their numerical simulations with experimental results of a single vertical capillary tube. In their model the vapor is also considered as superheated following the ideal gas law and the liquid film has a variable thickness. In their results they obtain a double oscillation of the menisci before re-entering in the evaporator due to the small overpressure generated by the evaporation of the liquid film.

Concerning 2D and 3D numerical models, one of the few numerical works that can

be found on open literature has been developed by Pouryoussefi et al. [86] in 3D and [90] in 2D, where the two-phase fluid is simulated using the Volume of Fluid method (VOF). This method will be detailed in chapter 6. Their results show a chaotic behavior fluid oscillations during operating conditions.

Other existing numerical methods have also been used to predict the behavior of pulsating heat pipes. The Artificial Neural Network (ANN) has been used by [107] and [5] as a statistical technique to identify recurring phenomena in PHPs. Furthermore some authors have developed numerical correlations after processing experimental data from experiments at room temperature [108–112] and with cryogenic PHPs [11, 47]. Moreover, numerical simulations considering the PHP as a spring-mass-damper system have also been developed by [113] and [114], for example. In the present project we will not focus on the approaches defined in this latest paragraph.

1.3.8 Applications

Apart from cryogenic applications described in 1.3.1, pulsating heat pipes are also being developed nowadays as cooling systems for electronic devices, such as CPUs [115] or LED chips [99] for example, as solar collectors and heating systems [7, 116], for heat recovery [117], to generate electromagnetic induction for electric power production [118] or even to cool fuel cells [119].

1.4 The contribution of this work

Pulsating Heat Pipes are considered these days as a very promising solution for multiple cooling applications, from electronic devices at ambient temperatures to superconducting magnets at cryogenic temperatures. As can be concluded from the literature review discussed in the previous section 1.3, since the 90's, several characteristics of PHPs have been discovered, such as their high thermal efficiency, as well as the influence of inclination (from horizontal to vertical) and the heating configuration (bottom or top heating modes) in thermal performance. Concerning the geometry, the closed-loop configuration is the most studied configuration for efficiency and simplicity reasons. It has also been demonstrated that, depending on the heat load, the working fluid can adopt different flow patterns (from slug to annular flow). In addition, the influence of the number of turns in the PHPs has also been confirmed, especially in horizontal inclination. Regarding the numerical simulations, the most complete existing models are 1D models. Based on strong assumptions, they have been improved gradually by adding highly detailed equations representing physical phenomena. In 2D and 3D, only a very few models exist, all of them representing vertical pulsating heat pipes.

Nevertheless, the influence of many other parameters is still not clear, and sometimes, conclusions in literature are opposite, and several issues still remain unsolved [25]. As an example, the thermodynamic state of the fluid in working conditions or during dry-out processes is not perfectly clear. In addition, the role of the sensible and latent heats in overall heat transfer, as well as the influence of the physical properties of the working fluid in global behavior are both not perfectly understood. There exist some correlations to predict the thermal response of a PHP considering the properties of the fluid and the heat load applied [11, 108–112], but they are not generic enough to be used in every PHP case. In addition, horizontal pulsating heat pipes have been less developed than vertical because they are not gravity-assisted but, for space applications, the study of horizontal PHPs could be more appropriate. Furthermore, pulsating heat pipes at cryogenic temperatures have been studied less than at room temperatures. Moreover, the majority of the existing cryogenic PHPs have a length of a few centimeters (20 cm on average) so, the performance of a meter-scale cryogenic PHP has never been tested. Due to this, it becomes a key issue to develop and study longer cryogenic PHPs to cool meter-scale superconducting magnets. Separating the cryocooler from the magnet by using the PHP as a thermal link, the cryocooler is then located off the fringe field avoiding any performance degradation [120–122]. Finally, concerning the numerical simulations, there is an absolute lack of 2D or 3D models for horizontal pulsating heat pipes. The existence of 2D (or 3D) models is nonetheless necessary to study the influence of the inner diameter effect on capillarity phenomena.

Based on the facts stated above, we can identify the necessity of studying larger-scale pulsating heat pipes in the cryogenic field. Due to this, the main goal of this research project is to contribute to a better understanding of the thermohydraulic behavior and operating conditions of meter-scale cryogenic pulsating heat pipes working in horizontal position. The scientific and technical objectives are stated as follows:

- to identify the operating conditions of horizontal cryogenic PHPs, including the thermodynamic state and the thermal performance at different heat loads, as well as the dry-out phenomenon.
- to analyze and compare the physical properties of three cryogenic fluids (nitrogen, neon and argon) and their influence on the overall heat transfer of horizontal cryogenic PHPs during progressive heat load experiments and long stability experiments.
- to determine the operating conditions of the PHP system open or closed to a buffer volume.
- to confirm the influence of the number of turns in horizontal PHPs during operating conditions.
- to determine optimum initial test conditions.

- to analyze the influence of the temperature of the condenser in the PHP operating conditions.
- to evaluate the thermal response of horizontal cryogenic PHPs in case of sudden additional heat load, simulating the heat load submitted during the quench of a superconducting magnet.
- to contribute to future 2D simulations of PHPs, developing a 2D model of a single horizontal capillary tube.

Chapter 2

The experimental facility

In order to study the performance, limits and thermodynamic behavior of cryogenic pulsating heat pipes, experiments were conducted in a cryogenic facility. In this chapter, the experimental facility will be described detailing the PHP core composed of three horizontal pulsating heat pipes, the cryostat, the instrumentation and the associated precision and accuracy, the gas supply system and the data acquisition system. Schematic drawings and pictures of the different components support the descriptions. The experimental protocols and the start-up procedures will also be defined.

2.1 The cryostat

To perform cryogenic experiments, cryostats are used as a cavity to isolate the experimental facility from external heat inputs. In this case, the cryostat used as a test bench is in horizontal position and made of stainless steel. It measures 6.4 m in length and has a diameter of 1 m. An additional extension, represented in blue in Fig. 2.1, has been added for this project with openings for the cold head and the different connections, which will be described in sections 2.2 and 2.3. Inside the cryostat, several thermal shields combined with a high vacuum level allows to protect the PHP core from external heat sources.

The first thermal barrier consists of a thermal shield cooled by liquid nitrogen circulation loop at 77 K. The loop extends to the length of the cryostat and is fixed to an aluminum (1050A) structure which is thermalized. As a result, the space containing the PHP core is maintained at around 85 K (see Fig. 2.2). All of this requires a permanent consumption of liquid nitrogen, for this reason, the liquid nitrogen circulation was only open a few hours before and during the experimental tests.

A second aluminum (1050A) structure surrounds the first one. This second one is a floating aluminum thermal shield surrounded by sixteen sheets of thermal superinsulation (MLI) at each side to reduce radiative heat fluxes (see Fig. 2.2 and Fig. 2.3).

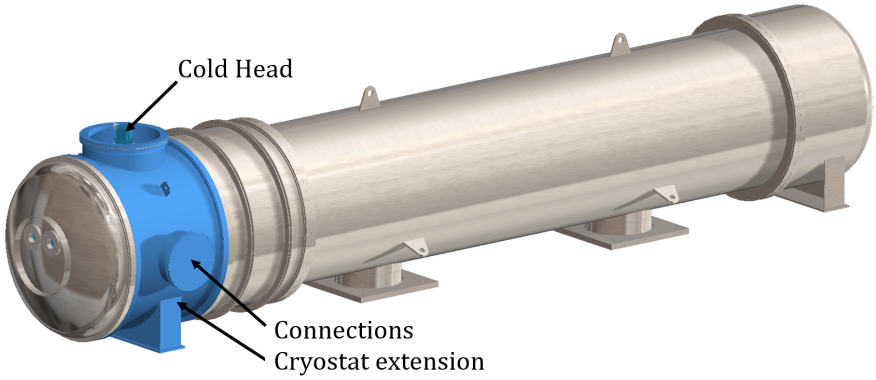

Figure 2.1: Schematic illustration of the cryostat.

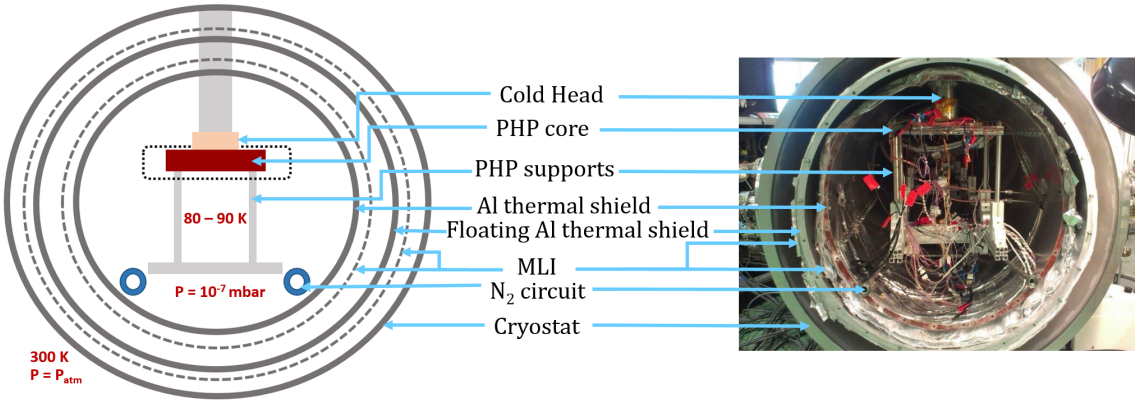

Figure 2.2: Thermal schematic of the experiment and picture of the interior view of the cryostat.

Furthermore, the cryostat is permanently connected to a pumping system composed of a primary pump and a turbopump. These pumps ensure a vacuum between 10^{-4} and 10^{-6} Pa avoiding any type of heat input by convection. This pumping system is connected to the cryostat through a pipe containing an automatic safety valve which closes in case of power blackout.

Additional undesirable heat inputs arriving into the PHP core have been estimated to be less than 1 W. This extra unwanted wattage comes from two main sources: radiative heat inputs coming from the aluminum thermal shields and conductive heat inputs arriving through the supporting aluminum structure of the PHP core. The calculation of this parasitic heat loads has been done assuming strong adverse hypotheses.

Radiative heat inputs from the aluminum structure are estimated to be 0.99 W, without considering any superinsulation surrounding the PHP core and using the Boltzmann law:

$$Q = G\sigma_b\epsilon(T_h^4 - T_c^4), \tag{2.1}$$

where Q is the heat transferred from the cold surface to the hot one, G is a geometric

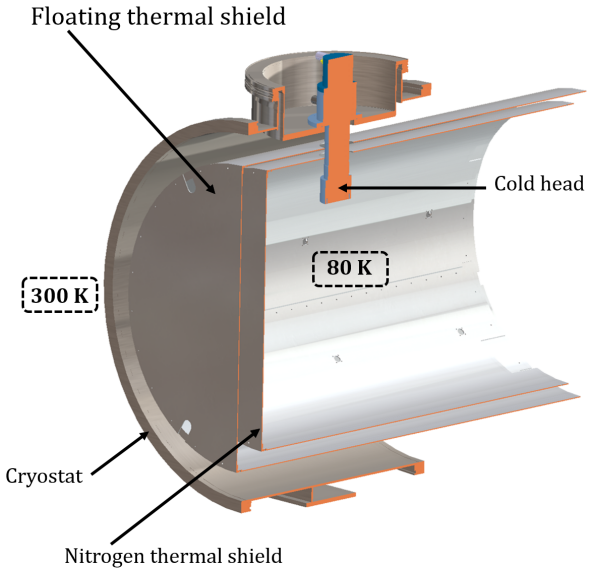

Figure 2.3: Aluminum structures inside the cryostat.

factor, σ_b is the Boltzmann constant, ϵ is the emissivity, estimated at 0.05 in this case, and T_h and T_c the temperatures of the hot and cold surfaces corresponding to the aluminum structure and the PHP core respectively.

Furthermore, heat inputs arriving through the aluminum supporting structure are estimated to be 0.025 W, assuming a perfect thermal contact with the PHP core. This calculation has been performed following a conduction law:

$$Q = \frac{\lambda \cdot A}{x}(T_1 - T_2), \tag{2.2}$$

where Q is the heat transferred through the supporting structure to the PHP core, A and x are geometric factors, λ is the thermal conductivity of aluminum and T_1 and T_2 are the temperatures of the supporting structure and the PHP core respectively.

2.2 The pulsating heat pipes

Figure 2.4 illustrates the main PHP core of the experimental facility composed of three horizontal pulsating heat pipes (PHP) with both ends connected to a T-junction in the condenser which is the inlet of the PHP (cf. Fig. 2.5). The capillary tubes have smooth surfaces (Ra. inner lower than 3.2 μm) and are made of stainless steel (304L). This material has been chosen due to its poor thermal conductivity, in order to be sure that the heat will mainly be transferred through the working fluid in a PHP mode. The inner and outer diameters are 1.5 and 2 mm respectively. The inner diameter has been determined considering nitrogen as the working fluid. The diameter is no larger than the critical diameter 1.7 mm, defined following the Bond criterion to maintain capillary forces

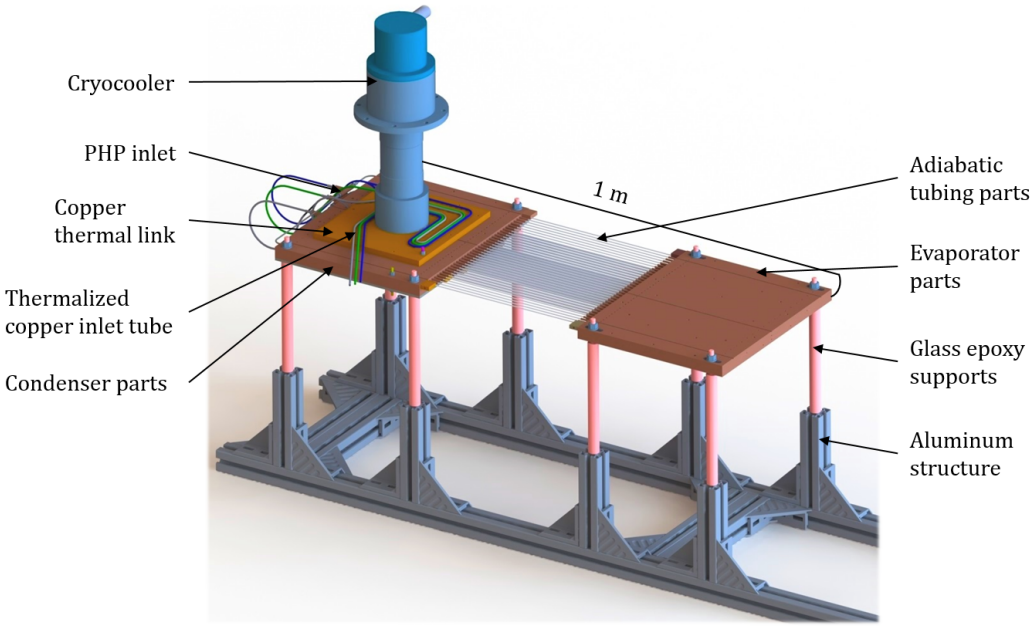

Figure 2.4: Schematic illustration of the experimental facility.

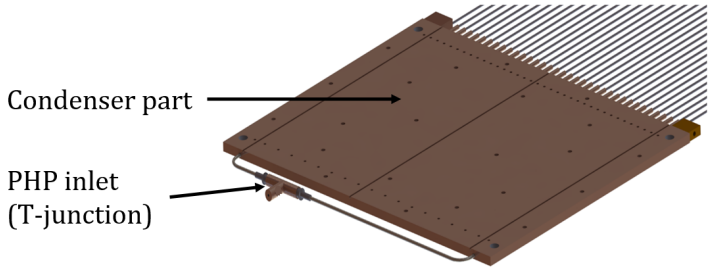

Figure 2.5: Schematic illustration of a condenser part with its PHP inlet.

necessary to the PHP operation. The only difference between each PHP is the number of parallel capillary tubes (or U-turns): one PHP has 36, one has 24 and one has 12. Each condenser, evaporator and adiabatic section is 330 mm long, giving a total length to each PHP of 1 m. The three PHP are positioned in a supporting aluminum structure and fixed by glass epoxy supports.

Each evaporator section is made of two copper plates (Cu-a1) surrounding the capillary tubing parts having a U-shape. In the bottom plate (400 mm × 300 mm × 4 mm) the tubes are inserted in machined grooves (cf. Fig. 2.6). The top plate (400 mm × 300 mm × 2 mm) has an Omega® Kapton flexible heater glued to the top surface. Details about the heaters and fixation procedures are given in section 2.3. The tubes inside are tin soldered to both copper plates. The copper plates have an identical size but heaters are proportionate to the number of turns of each PHP and cover strictly the area occupied by the tubes on each evaporator. This means that the mass of copper is the same for the three evaporators, but not the size of the heaters (cf. Fig. 2.7). The three evaporators are separated by sixteen sheets of thermal superinsulation (MLI).

Figure 2.6: Machined copper plate.

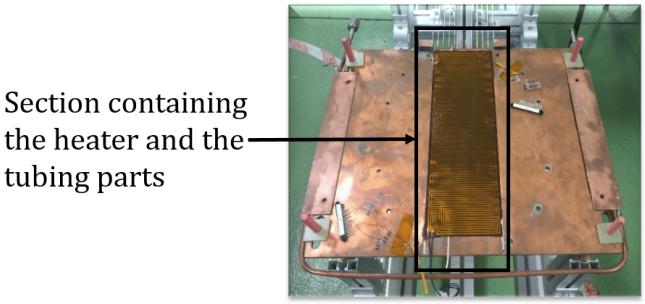

Figure 2.7: Evaporator part of the PHP having 12 parallel tubes.

The condensers are made in the same way: machined copper plates contain the tin soldered U-shaped capillary tubes. The three condensers are thermally connected with each other by indium threads. On the top of this pile of condensers, there is another tin soldered copper plate (Cu-a1), with a smaller area (26 cm × 24 cm × 1.2 cm), that ensures the thermal connection between the three condensers and the cold head of the cryocooler (see. Fig. 2.8). This copper thermal link has three copper tubes thermalized on its surface. Each copper tube is connected to the inlet of each PHP (T-junction) on one side and to the external gas supply system outside the cryostat on the other side. In this way, the copper thermal link accomplishes two functions: firstly, its square shape contributes to a better thermalization of the condensers from the cylindrical end of the cold head, secondly, the working fluid arriving from outside the cryostat is cooled down to cryogenic temperatures before being inserted into the PHP. Furthermore, Omega® Kapton flexible heaters are fixed around the cold head and the copper thermal link to regulate the temperature of the condensers block with a temperature controller that will be described in section 2.3. The cylinder of the cold head as well as the condensers block are covered with sixteen sheets of thermal superinsulation (MLI).

Each adiabatic part is composed of parallel tubing parts which are connected to the U-turns tubes of the evaporator and the condenser by copper sleeves (see. Fig. 2.9). The three adiabatic parts are also covered with sixteen sheets of thermal superinsulation (MLI).

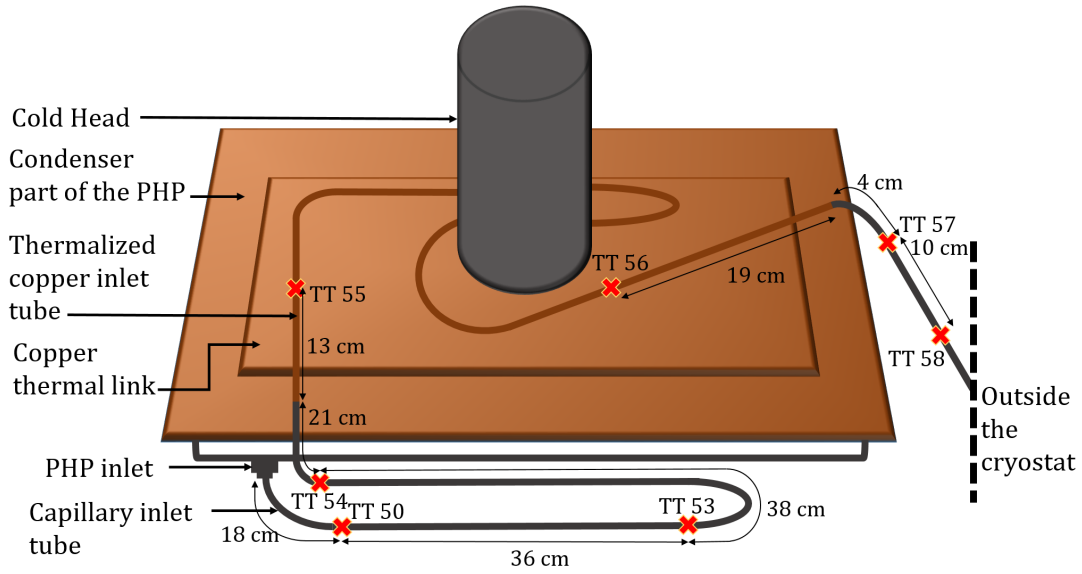

Figure 2.8: Schematic illustration of the copper thermal link and the thermalized inlet tube of a single PHP with the corresponding temperature sensors (✖).

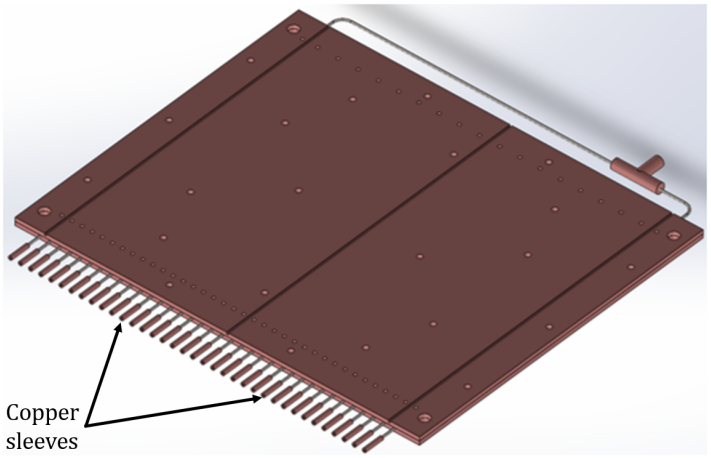

Figure 2.9: Schematic illustration of the copper sleeves.

The cold source is a single head cryocooler (Sumitomo® CH110). This type of cryocooler runs through a Gifford-McMahon cycle using helium as working fluid and has a range of working temperatures between 20 and 115 K. The cryocooler is connected to a compressor (Sumitomo® F-70) through helium lines flowing at 2.2×10^6 Pa in the supply line and at 5×10^5 Pa in the return line.

While the three condensers are thermally connected constituting a single block, the evaporators are separated by a 4 mm glass epoxy piece at each corner to place several sheets of thermal superinsulation (MLI) between each evaporator and reduce the thermal radiation from one to another. It is important to note that, due to this, the adiabatic parts of the 36-turn PHP and the 24-turn PHP are slightly inclined, at 1.4° and 0.7° respectively from the horizontal position. Nevertheless, such a slight inclination will be considered negligible.

2.3 Instrumentation and configurations

In order to characterize the thermal behavior of the three cryogenic PHP, a specific non-intrusive instrumentation has been chosen for data acquisition at low temperature. Furthermore, power supply technology as well as several heaters and a temperature controller have been used to perform tests at different temperatures and heat loads. In the following sections we will described the instrumentation, the type of heaters, the power supply technology and the temperature controller system.

2.3.1 Temperature sensors

There are two types of temperature sensors in the present experimental facility: calibrated Cernox® SD temperature sensors and platinum resistance thermometers, known as Omega® Pt100 temperature sensors.

Pt100 temperature sensors

The Pt100 temperature sensor is a resistance temperature detector (RTD). An image of this type of sensor is shown in Fig. 2.10. This type of sensor contains a resistor that changes electrical resistance value as its temperature changes. More precisely, the resistance increases with temperature, which is known as positive temperature coefficient (PTC). In this case, the sensor contains a platinum resistor with a ceramic protection and the evolution of the resistance with the temperature is almost linear and given by the Callendar-Van Dusen equation:

$$R_{RTD} = R_0(1 + AT + BT^2 + C(T - 100)T^3), \tag{2.3}$$

Figure 2.10: Pt100 temperature sensor.

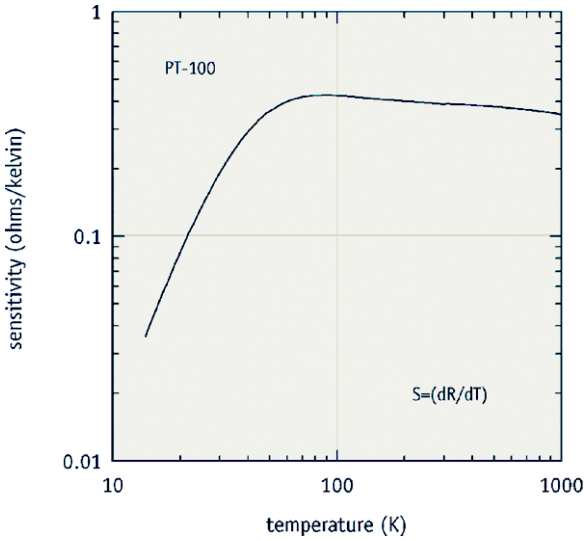

Figure 2.11: Sensitivity of Pt100 temperature sensor.

where R_0 is a 100 Ω resistance at 0°C (Pt100) and the coefficients are $A = 3.9083\times10^{3}$, B = -5.7759×10^{-7}, C = -4.186×10^{-12} (below 0°C), or $C = 0$ (above 0°C).

The low price of the Pt100 sensors make them affordable but, as it can be seen in Fig. 2.11, the sensitivity decreases considerably with temperature, especially below 60 K. For this reason, this facility has a second type of sensor, more expensive but with higher sensitivity in order to compare both sensors permanently and to adjust the Pt100 sensors re-calibrating them when we work at temperatures below 60 K. In appendix A the calibration procedure used below 60 K is described.

Cernox® SD temperature sensors

Cernox® SD temperature sensors are a thin film sensors with a hermetic ceramic packaging. An image of this type of sensor is given in Fig. 2.12. Each sensor has its own calibration curve given by the manufacturer. The evolution of the resistance with temperature follows a negative temperature coefficient (NTC) meaning that the resistance increases when temperature decreases, which make them highly accurate measuring variations at very low temperature. In the present experimental facility there are two type of Cernox® SD sensors: CX-1050-SD and CX-1070-SD. The only difference between each model is the calibration range: 1.4 - 325 K for 1050 and 4 - 325 K for 1070. Both calibrations are acceptable for the range of working temperatures operating in this facility (20 - 100 K). In addition, as it can be seen in Fig. 2.13, the sensitivity of both models is maximum for the range of working temperatures.

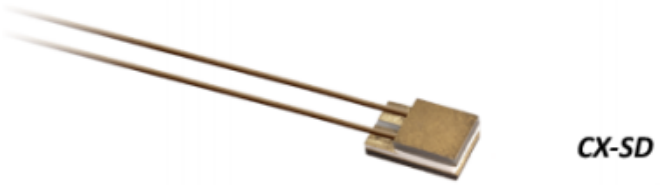

Figure 2.12: Cernox® SD temperature sensor.

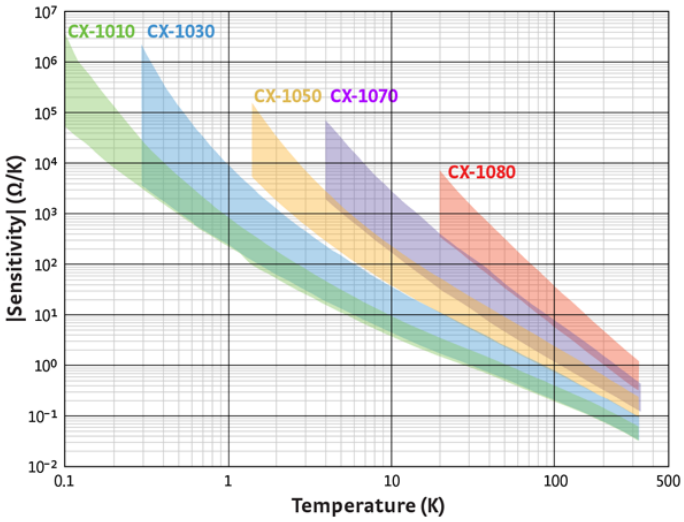

Figure 2.13: Sensitivity of Cernox® SD temperature sensor.

The present experimental facility contains 52 Pt100 temperature sensors and 4 Cernox® SD temperature sensors. All the temperature sensors are connected in a 4 twisted-wire configuration. This type of connection has two main advantages: first, the 4-wire connection allows to know the resistance of the device and the resistance of the wires separately, secondly, the twisted configuration allows to reduce considerably the voltages induced by the magnetic field produced by the circulation of current passing through each wire. At each twist, the sign of the voltage changes and, in a considerable length, the voltage self-induction is highly reduced. In this case, both types of temperature sensors have only two electric leads coming out of it. Due to this, the wires are soldered by pairs at the two contacts of the sensors. The sensors are fixed to the surfaces of the different components with copper powder charged epoxy resin (DP-190) to improve the thermal contact. All the wires are firstly thermalized closed to the measuring point and secondly at the surface of the nitrogen cooled thermal shield, described previously in section 2.1, using aluminum tape.

2.3.2 Pressure sensors

There are three types of pressure sensors in the present experimental facility: Kulite® Pressure Transducer for the PHP core, MKS Baratron® Absolute Pressure Transducer for

Figure 2.14: Kulite® Pressure Transducer.

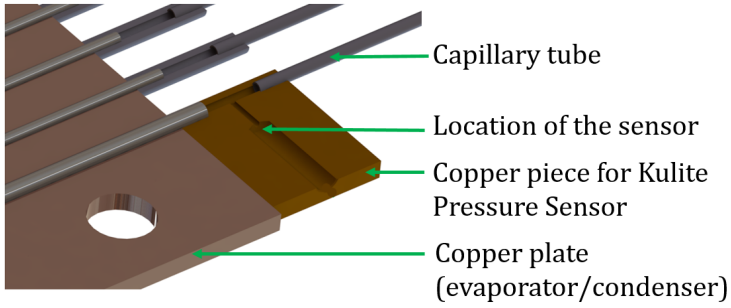

Figure 2.15: Section cut of the copper piece for a Kulite pressure sensor.

the external gas supply circuit, described in section 2.4, and MKS QuadMag® Transducer to measure the vacuum in the cryostat.

Kulite® Pressure Transducer

There are five pressure sensors in the PHP core, four in the PHP with 36 parallel tubes and one in the PHP with 24 parallel tubes. All of them are Kulite® pressure transducers (CT-190) connected in a 4-wire configuration. The principle of operation of those pressure sensors consists of measuring the deformation of a membrane by the force exerted by the fluid. Specifically, the Kulite sensors use a membrane of a conductive material with a variable resistance. An image of this type of sensor is shown in Fig. 2.14. Specific copper pieces have been designed to replace the sleeves and to connect mechanically the Kulite® pressure sensors to the tubing parts of the PHP, as it can be seen in Fig. 2.15. As well as for the temperature sensors, all the wires are thermalized at the surface of the nitrogen cooled thermal shield using aluminum tape. More details about their calibration are given in appendix B.

MKS Baratron® Absolute Pressure Transducer

A single MKS Baratron® absolute pressure transducer (Type 722B) is used to control the pressure of the gas supply system, described below in section 2.4. This sensor is a compact capacitance manometer also connected in a 4-wire configuration. The sensor capsule contains an Inconel® diaphragm and a metal-on-ceramic electrode structure. Pressure is determined by measuring the change in capacitance between the diaphragm and the electrode.

Table 2.1: Specific characteristics of sensors.

Temperature Sensor	Measuring range	Measurement error
Omega® Pt100	73 - 1124 K	±(0.15 + 0.002T)
Cernox® SD	0.10 - 420 K	±10 mK (30 K)
		±16 mK (77 K)
Pressure Sensor	**Measuring range**	**Measurement error**
Kulite®	0 - 7.10^5 Pa	±0.1 %
MKS Baratron®	100 - 7.10^5 Pa	±0.5 %
MKS QuadMag®	1.10^{-6} - 2.10^5 Pa	±30 % (7.10^{-6} - 0.1 Pa)
		±5 % (0.1 - 7.10^3 Pa)
		±1 % (7.10^3 - 1.10^5 Pa)

MKS QuadMag® vacuum transducer

A MKS QuadMag® vacuum transducer (Type 974B) is used to measure the vacuum in the cryostat. This type of sensor is divided in three separated parts. The first part, consists of a heated resistive element on a silicon chip where the gas passes through and the heat loss of the gas is measured. Then, the molecules are ionized by electrons accelerated by a cathode-anode system with a magnet. The ionization of the molecules creates an electric current as a function of the pressure. Furthermore, the mechanical deflection of a silicon membrane exposed to ambient pressure on one side and to vacuum on the other side is measured.

2.3.3 Locations and characteristics of sensors

The measuring ranges and accuracies of the pressure and temperature sensors previously described are presented in Table 2.1.

The locations of all of the different sensors in the three pulsating heat pipes are shown in Fig. 2.16. To this should be added the temperature sensors located in the copper thermal link represented in Fig. 2.8 as well as two other sensors located in the supporting aluminum structure of the PHP and the nitrogen circulation loop. Both of them are Pt100 temperature sensors.

2.3.4 Heaters

There are five Omega® rectangular Kapton flexible heaters in the experimental facility. Kapton has been chosen for its good degassing properties at high vacuum. As mentioned before, each evaporator has a heater fixed at the top of its surface. The dimensions of

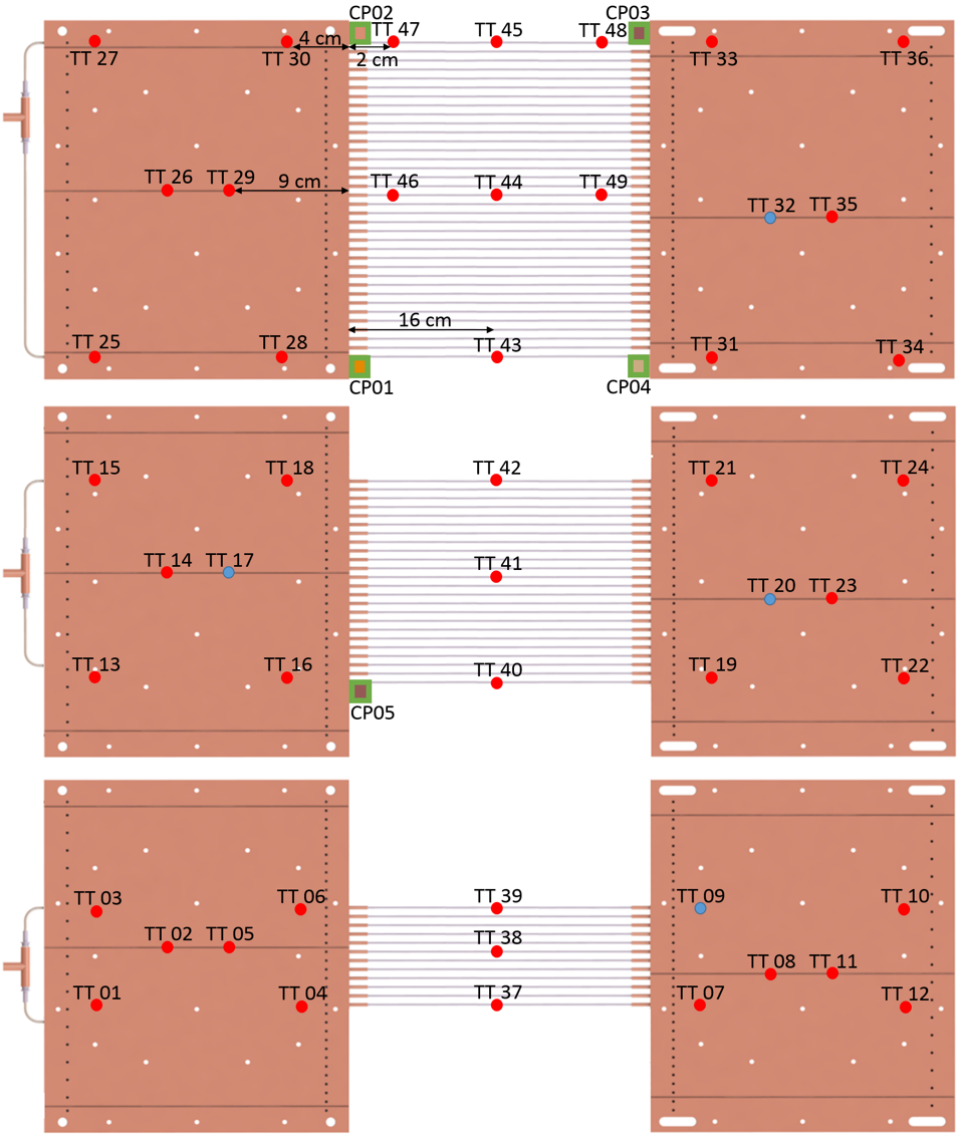

Figure 2.16: Locations of sensors in the three pulsating heat pipes. Type of sensors: ● Pt100 temperature sensor, ● Cernox® SD temperature sensor and ■ Kulite® pressure sensor.

Table 2.2: Specific characteristics of heaters.

Heater	Dimensions	Maximum power
CH1	30 cm × 10 cm	120 W at 115 V
CH2	30 cm × 20 cm	240 W at 115 V
CH3	30 cm × 30 cm	360 W at 115 V
CH4	20 cm × 3 cm	240 W at 120 V
CH5	7.5 cm × 1.5 cm	100 W at 115 V

the three heaters are proportionate in size to the number of turns, as indicated in section 2.2, and they are connected in a 4-wire configuration in order to make a real measurement independently of the impedance of the power supply, which can create errors. The heater of the evaporator of the PHP having 36 parallel tubes is called CH3, the heater of the evaporator of the PHP having 24 parallel tubes is called CH2 and the heater of the evaporator of the PHP having 12 parallel tubes is called CH1. There is another heater fixed at the surface of the copper thermal link called CH4 and a fifth heater fixed at the cold head called CH5. Specific characteristics of the heaters are given in table 2.2. All the heaters are fixed with copper powder charged epoxy resin (DP-190) to improve the thermal contact. It is important to fixe perfectly the entire surface of the heater in order to have a uniform surface heating and also because if the heat is not well evacuated it can easily burn in a vacuum environment where no convective flow will evacuate the heat. All the wires are also thermalized at the surface of the nitrogen cooled thermal shield using aluminum tape.

2.3.5 Power supply systems

The power supply is provided by two different electrical sources, both controlled by the Labview® program, described in section 2.5. First, an Agilent® 6655A DC power supply system which can deliver up to 480 W is connected to the heater CH4. The current corresponding to the desired power must be entered manually in the Labview® program. The other source is a LakeShore® Temperature Controller 336 that provides power to the heater CH5 and to the heater of the evaporator of the connected PHP, which can be the heater CH3, CH2 or CH1. The desired power value is translated into a current requirement to be provided by the power supply system. The maximum power that can be delivered to the heaters of the evaporators is 100 W, the value for the desired power must be entered in the Labview® program directly in watts. The power delivered to the heater CH5 is managed by a PID (Proportional Integral Derivative) linked to the Cernox® SD temperature sensor located in the condensers block, which determines the power needed to maintain the cold head temperature at the desired value. The coefficients of the PID and the desired working temperature of the cold head are entered in the Labview® program.

2.4 Gas supply system

The quantity of fluid inside the PHP is controlled by a specific gas supply system. This system connects the gas supply outside the cryostat to the PHP core. A detailed schematic illustration of the entire supply system is given in Fig. 2.17. The system is composed of three gas tanks of 0.05 m^3 each: a nitrogen (N_2) gas tank, a neon (Ne) gas tank and an argon (Ar) gas tank. Each gas tank has its own pressure regulator and buffer volume (BV) of 0.05 m^3. The buffer volume has two main roles, firstly, when a PHP is working connected to the buffer volume, the enormous difference between the volume of the buffer volume and the volume of the PHP (about a thousand times larger) allows the buffer volume to withstand any overpressure in the PHP, secondly, the buffer volume is an intermediate tool to calculate and control the amount of fluid inside the PHP as will be explained below in section 2.8. In the present gas supply system, there is also an absolute pressure transducer (APT) to measure the pressure of the circuit described in section 2.3, an Adixen® (ACP 15) dry vacuum pump (VP) to empty the PHP and the circuit before every test, and numerous Swagelok® valves completing the system.

2.5 Signal data acquisition

Only one PHP can be connected at a time. The analogical voltages coming from sensors are converted into digital signals by three different types of National Instruments® data acquisition cards. Five NI 9217 cards convert the analogical signal coming from the Pt100 temperature sensors, one NI 9239 card converts the analogical data coming from the Kulite® pressure sensors (each sensor uses a TDK Lambda® din rail power and a SCAIME® analog signal conditioner) and one NI 9229 card converts the analogical signal coming from the MKS Baratron® absolute pressure transducer and also reads the voltage of the evaporator's heater. All the digital signals are then integrated in a Labview® program running on a desktop computer where the raw data are interpreted on its visual interface.

The Labview® program has three different roles:

- Visualization of different signals from sensors.
- Sending instructions to the power sources to control the different heaters and the temperature controller.
- Saving row data to an Excel worksheet during acquisition periods.

A screenshot of the Labview® visualization program of one PHP is shown in Fig. 2.18. The different parts of the Labview® interface are marked with letters and listed below.

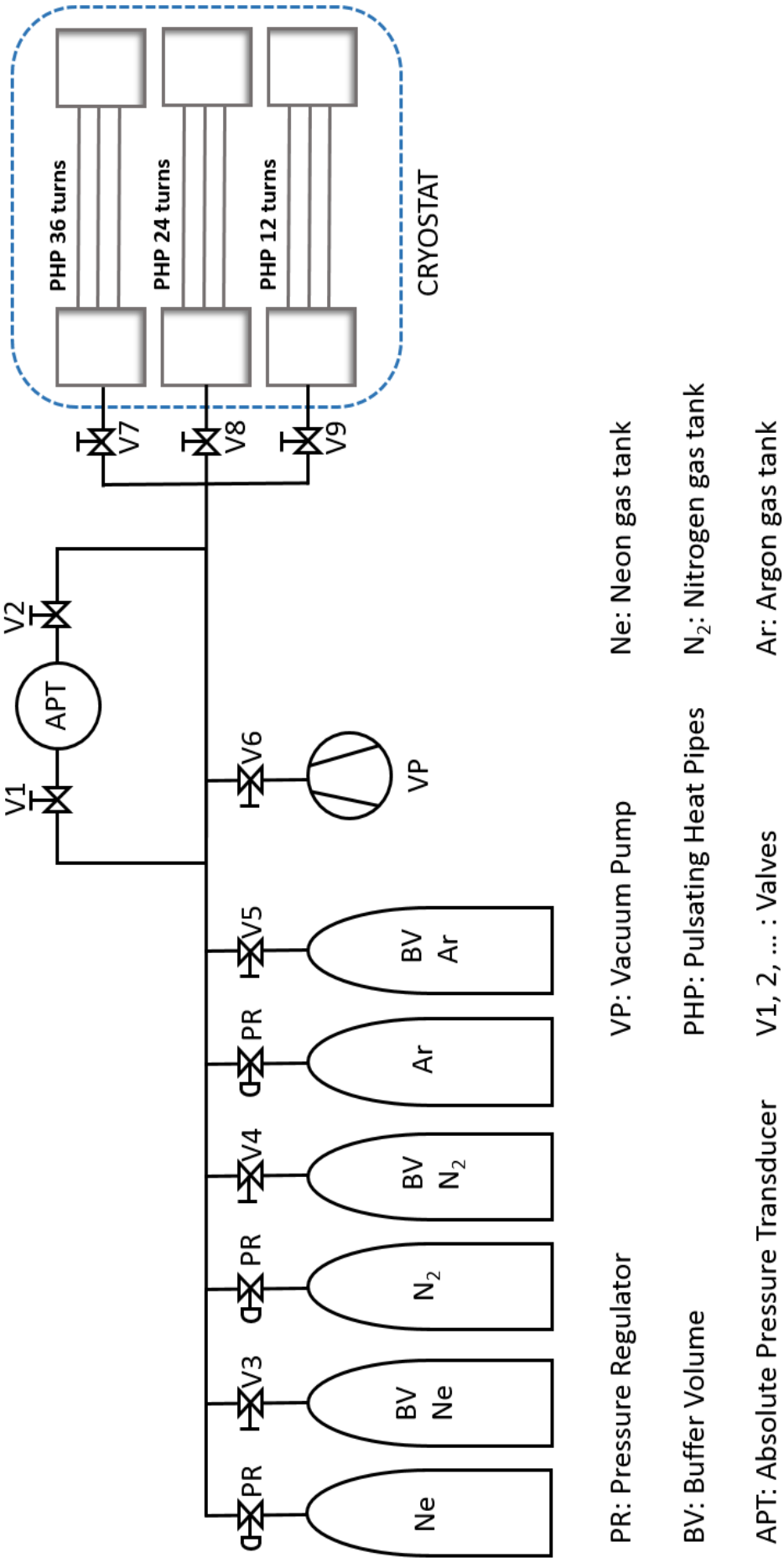

Figure 2.17: Gas supply system.

A. Schematic illustration of the PHP with locations and dynamic values of the temperature and pressure sensors.

B. Command window for the temperature, input power and temperature controller coefficients of the condenser part.

C. Command window for the temperature, input power and resistance of the heater of the evaporator part.

D. Scrolling graph representing the time evolution of the temperatures of the evaporator part.

E. Scrolling graph representing the time evolution of the temperatures of the adiabatic part.

F. Scrolling graph representing the time evolution of the temperatures of the condenser part.

G. Scrolling graph representing the time evolution of the input power of the evaporator part.

H. Scrolling graph representing the time evolution of the temperature of the inlet tube of the PHP.

I. Command window for the input current of the heater fixed at the copper thermal link.

J. Button to record data.

2.6 Data Processing

A Matlab code has been developed to read, filter and process experimental data obtained with the acquisition system. The code starts with the reading and filtering of the row data from the Excel worksheet created by the Labview® program. Then, using the NIST Refprop Database several thermodynamic properties are obtained to calculate the thermal properties and the filling ratio, described in section 2.8. Furthermore, other calculations are also computed such as Fast Fourier Transform on temperature and pressure measurements, dimensionless numbers relating thermohydraulic properties and other correlations. All the results are finally plotted and saved. A simplified structure of the data processing code is shown in Fig. 2.19.

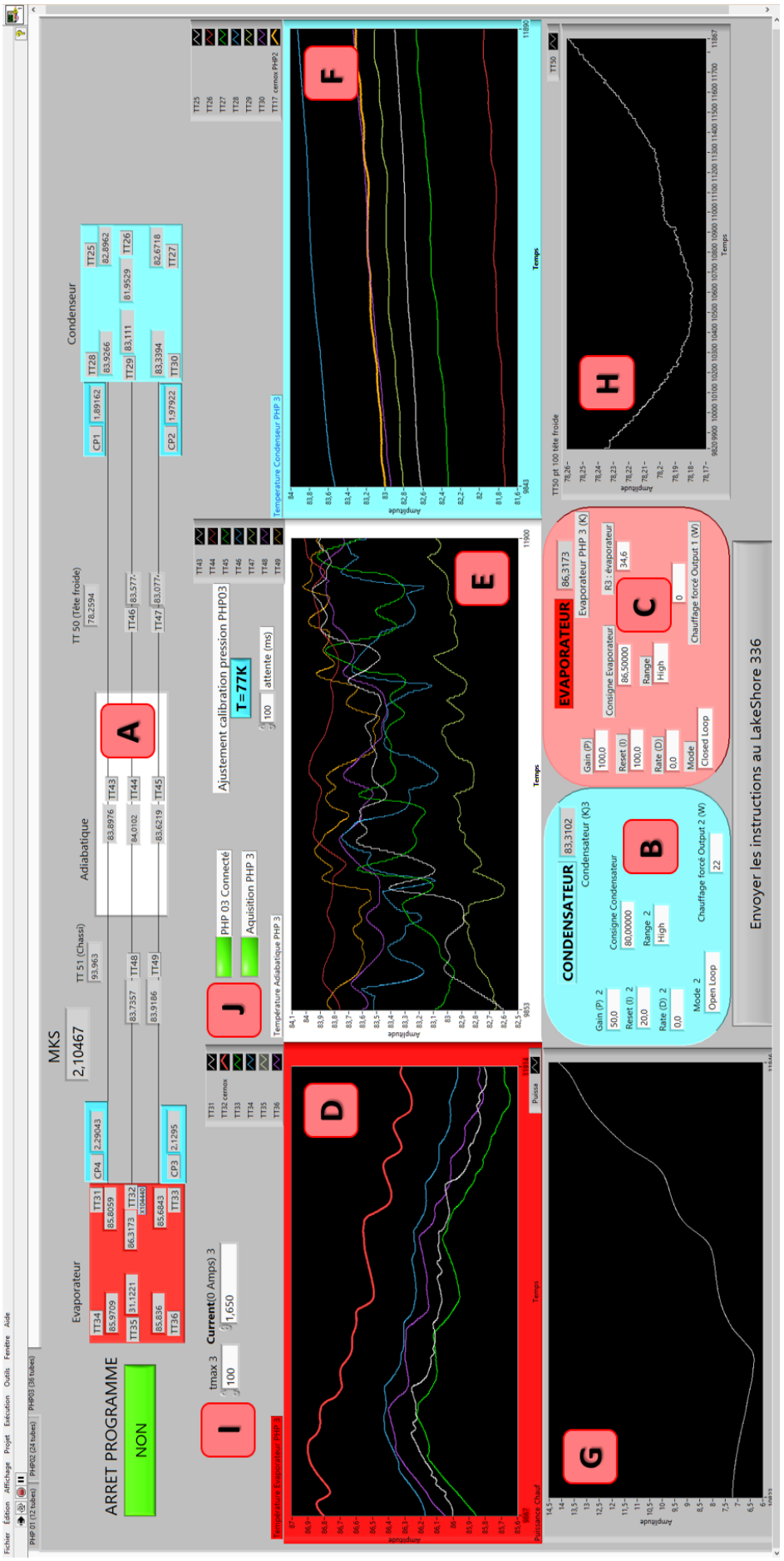

Figure 2.18: Screenshot of the Lavbiew visualization program.

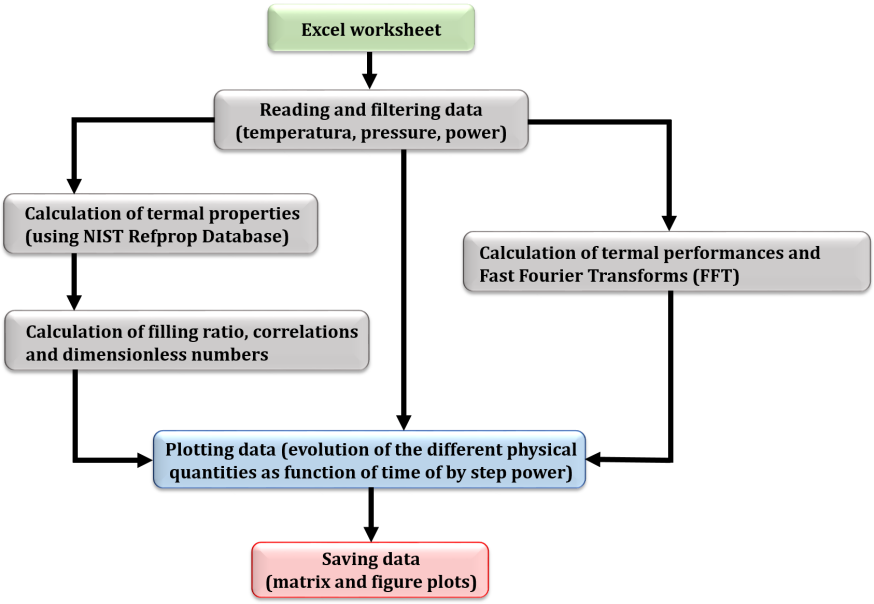

Figure 2.19: Simplified structure of the data processing code.

2.7 Preparation of experiments

Before every test period, several check-in tests are done. First of all, the electrical connections of every sensor are checked in the PHP core and outside the cryostat. For this, the resistance between each pair of wires is measured with a multimeter. Due to the 4-wire configuration, it becomes possible to determine the resistance of the sensor and the wires on one hand and the resistance only of the wires on the other hand by measuring the resistances on all possible pairs between the four wires. Secondly, a leak test is performed several times on every PHP. For this, the inlet (T-junction) of each PHP is connected to the leak detector, composed of a pumping system and a helium mass spectrometer. After this, the PHP is inserted into the cryostat. The inlet tubes of each PHP are connected to the gas supply circuit and a second series of leak tests are performed for this section. Then, the first aluminum shield and the nitrogen circulation loop are closed and another series of leak tests are performed for the nitrogen circulation loop. Finally, the cryostat closure is entirely sealed with vacuum grease and fasteners. The pumping procedure starts with the primary pump until a vacuum of 1 Pa is reached, then the turbopump is activated to achieve the desired vacuum for cryogenic experiments: between 10^{-4} and 10^{-6} mbar. The liquid nitrogen circulation starts and after the cold head is activated.

It should be noted that when the block of condensers achieves the cryogenic temperatures, the evaporators are still at a very high temperature because of the poor conduction of the stainless steel capillary tubes. In order to cool down the evaporators, the pulsating heat pipes are filled with a small amount of working fluid used for experiments, which can be nitrogen, neon or argon. In this way, the heat due to the temperature difference is transferred from the evaporators to the condensers in a PHP mode.

2.8 Start-Up procedure

Before starting every single test, the PHP and the gas supply circuit are pumped to avoid any impurity inside the PHP. Then, the filling process starts: the buffer volume (V_1) is filled with the gas tank at a certain pressure, called the insertion pressure. Then, after closing the gas tank, the empty PHP is filled with the working fluid coming from the buffer volume. The pressure difference in the buffer volume between the beginning and the end of this filling process determines the quantity of fluid injected into the PHP. The method to determine the filling ratio and the insertion pressure is explained as follows, considering a single PHP:

The liquid filling ratio $FR(\%)$, also known as filling ratio, is determined by:

$$FR = \frac{V_l}{V_{php}} \cdot 100, \tag{2.4}$$

where V_l is the volume of the liquid in the PHP and V_{php} is the volume of the PHP. It is obtained from the following mass conservation equation:

$$\rho_1 V_1 - \rho_2 V_1 = \rho_3 V_3 + \rho_4 V_4 + \rho_5 V_5 + \rho_l V_l + \rho_v V_v, \tag{2.5}$$

where $\rho_1 V_1$ is the mass in the buffer before insertion, $\rho_2 V_1$ is the mass left in the buffer volume after insertion, $\rho_3 V_3$ is the mass of the volume V_3 of the supply circuit (see Fig. 2.20), $\rho_4 V_4$ is the mass of the intermediate volume V_4 inside the cryostat (see Fig. 2.20) and $\rho_5 V_5$ is the mass of the volume V_5 of the tube thermalized at the surface of the thermal link. The inlet tube indicated also in Fig. 2.20 is included in the total volume of the PHP. The volume of the PHP can also be defined as

$$V_l + V_v = V_{php}. \tag{2.6}$$

Then, eq. 2.5 becomes

$$\rho_1 V_1 - \rho_2 V_1 = \rho_3 V_3 + \rho_4 V_4 + \rho_5 V_5 + \rho_v V_{php} + (\rho_l - \rho_v) V_l. \tag{2.7}$$

Then, the amount of liquid inside the PHP can be determined by

$$V_l = \frac{\rho_1 V_1 - \rho_2 V_1 - \rho_3 V_3 - \rho_4 V_4 - \rho_5 V_5 - \rho_v V_{php}}{\rho_l - \rho_v}, \tag{2.8}$$

where the corresponding volumes V_1, V_3, V_4 and V_5 of the gas supply system are indicated in Fig. 2.20. The volume of the inlet tube is included in the PHP volume. The different densities are obtained using the NIST Refprop Database knowing the corresponding

pressure and temperature at each section thanks to the numerous sensors.

Conversely, fixing the filling ratio (FR), the insertion pressure is obtained with NIST Refprop Database knowing the temperature and the density given by

$$\rho_1 = \frac{\rho_3 V_3 + \rho_4 V_4 + \rho_5 V_5 + \rho_l(\frac{FR}{100} V_{php}) + \rho_v(1 - \frac{FR}{100}) V_{php} + \rho_2 V_1}{V_1}. \tag{2.9}$$

Finally, it is important to note that the calculation is performed assuming that the entire PHP is at the temperature of the condenser (75 K). Nevertheless, the temperature of the adiabatic and the evaporator parts are higher than the condenser's one, so the real filling ratio remains slightly different (lower) than the theoretical one. The real filling ratio is later calculated by using the experimental data obtained during the test.

2.9 Final comments

This chapter has been focused on the description of the experimental set-up, where all the cryogenic tests have been performed. During long test periods, a huge number of parameters affecting the thermodynamic behavior of the pulsating heat pipes have been evaluated.

Three cryogenic fluids working at different temperatures have been tested: nitrogen (N_2), neon (Ne) and argon (Ar). Numerous progressive heat load experiments and constant heat load experiments have been performed at different liquid filling ratios. Some of them have even been repeated several times for different time durations to verify the repeatability of the experimental results. During these tests, different operating conditions and start-up parameters have been modified, evaluating their influence in the PHP thermal behavior. Finally, extreme high heat load tests have been done in order to emulate a quench situation of a superconducting magnet.

The study derived from the analysis of the experimental results will be presented in the following five chapters.

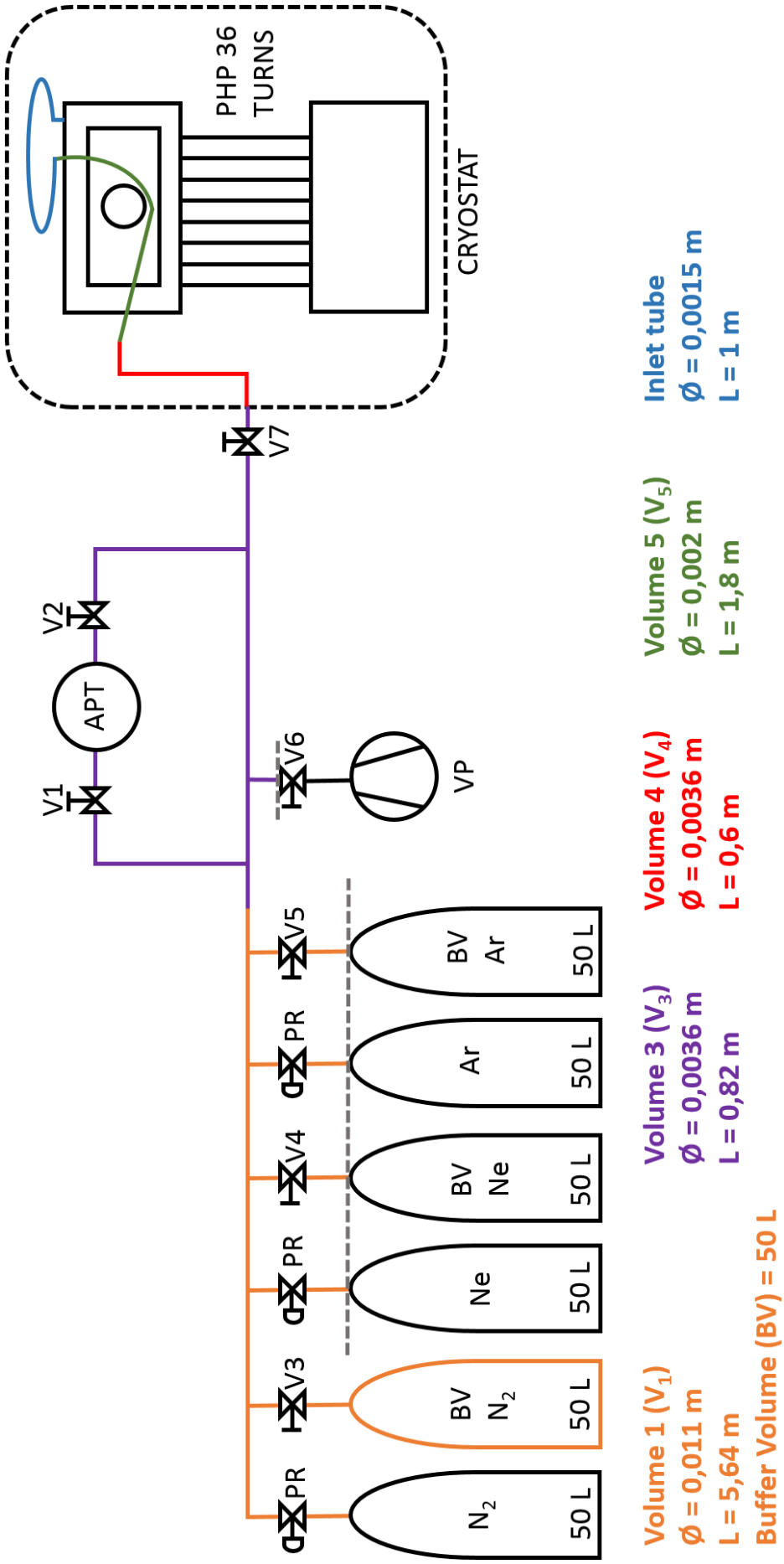

Figure 2.20: Schematic illustration of the gas supply circuit connected to the PHP with 36 turns with the corresponding lengths and diameters.

Chapter 3

Generic working conditions

In the following chapters 3, 4 and 5, the thermohydraulic behavior of cryogenic pulsating heat pipes will be explored by analyzing experimental test results. This contribution to the field seeks to better understand the drivers of heat transfer in long horizontal pulsating heat pipes.

3.1 Previous work

Before presenting the experimental results of the present research project, it is important to know, that the three pulsating heat pipes constituting the experimental facility described in chapter 2 have been operated in the past in a different configuration. In fact, a longer version having a total length of 3.66 m has been tested previously. This latter was composed of the same evaporators and condensers, being 33 cm long each, and adiabatic parts with a length of 3 m, as it can be shown in Fig. 3.1 and detailed in [39]. This configuration has been tested using only nitrogen as working fluid. It worked in stable conditions during only 35 minutes in a couple of experimental tests.

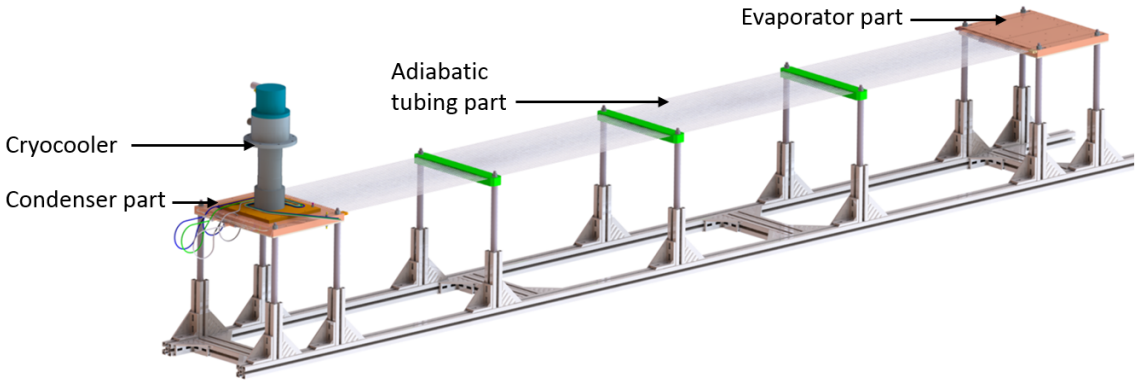

Figure 3.1: Schematic illustration of the 3.6 m long experimental facility.

It can be seen in Fig. 3.2 the evolution of the PHP global pressure and the tem-

peratures of the evaporator, condenser and adiabatic part during a test performed in the 3.6 m long version of the PHP with 36 turns. The PHP is completely closed and isolated from the buffer volume and the inlet gas system, and filled at a liquid filling ratio of 33 %. During the test, three different phases can be distinguished: the start-up, the oscillating phase and the dry-out. During the oscillating phase, the temperature of the evaporator oscillates and increases very slowly from 84 K to 85 K reaching an equivalent thermal conductivity (definition given in the next section) between 290 and 190 kW/(m.K) with a fixed power of 10 W. The oscillating phase lasts 35 minutes before suffering a spontaneous dry-out. At that point, the temperature of the evaporator increases continually, meaning that the heat is not being transferred anymore. This indicates the instability of the PHP system during long periods of time (more than 35 minutes) with this configuration.

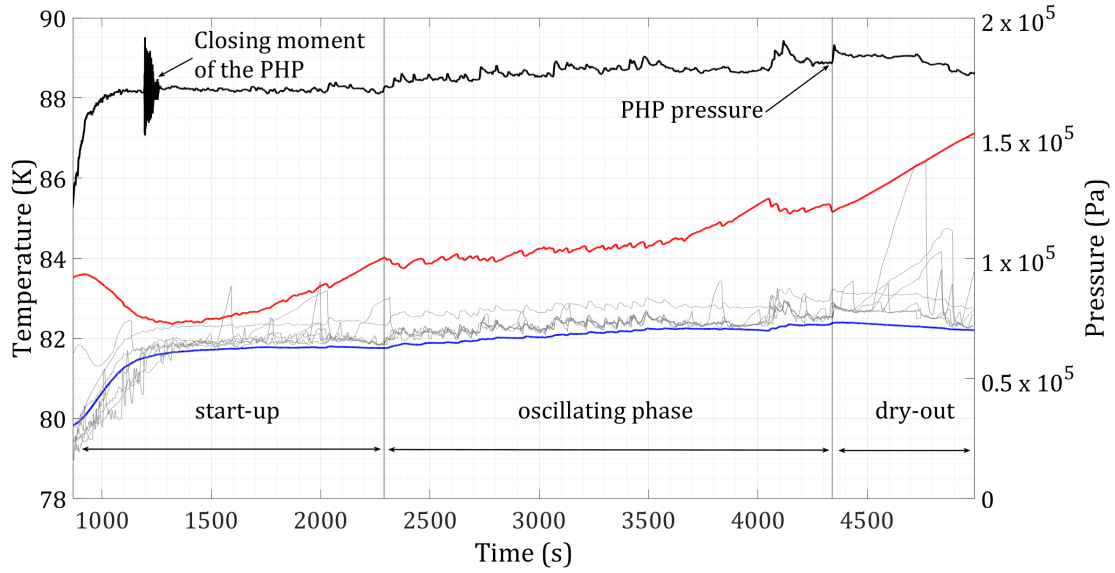

Figure 3.2: Evolution of the PHP global pressure (—), the average temperature of the evaporator (—) and the condenser (—) and the temperatures of the adiabatic part (—) of a test with a fixed heat load in the 3.6 m long PHP version.

Due to the impossibility to work in stable conditions with this PHP version and in order to obtain enough data to conclude about long PHPs thermal behavior, this longer version has been reduced to 1 m long, being anyway the longest horizontal cryogenic pulsating heat pipes operating nowadays. Neon and argon were supplied after the experimental setup modification. It is possible anyway to conclude that this PHP configuration was not able to attain stable operating conditions and transfer the heat properly from the evaporator to the condenser, at least using nitrogen as working fluid.

3.2 Reference test

3.2.1 Experimental procedure

Henceforth, only experimental results of the 1 m long version pulsating heat pipes will be presented. In this chapter, experimental results of a single test with the PHP with 36 turns will be and analyzed in detail. Additional experimental results in the following chapters will be compared to this reference test.

In this test, nitrogen is used as working fluid and the filling ratio is initially calculated to be at 50 %. Before starting the test, the PHP is completely evacuated down to 1 Pa with the vacuum pump, in order to avoid any impurity inside the system. Then, after closing all the valves, the evaporator is heated from 75 K to 80 K while the temperature of the condenser is maintained at 75 K using the temperature controller. Opening the pressure regulator (PR) of the nitrogen gas tank and the valve V3, the buffer volume (BV) can be filled to a desired pressure measured with the absolute pressure transducer (APT) opening the valve V1 (see Fig. 2.20 in chapter 2). After closing the pressure regulator (PR), valves V2 and V7 are opened in order to fill the PHP. The heater of the evaporator delivers 5 W during this filling process and, as soon as the temperature of the evaporator is stable, meaning that the PHP is filled enough and works in stable conditions, the valve V7 is closed isolating the PHP from the inlet system and the buffer volume.

This start-up phase characterized by an initial temperature difference of 5 K between the condenser and the evaporator and 5 W delivered at the evaporator facilitates the evaporation and condensation processes for the creation of the liquid slugs and vapor plugs and allows to generate a pressure difference between both parts when inserting the fluid to start the oscillating process. This contributes to the homogenization of liquid slugs and vapor plugs distribution, necessary for the PHP oscillations. This technique has been already used by other authors in a horizontal PHP [44].

3.2.2 General test description

The experiment is performed by increasing gradually the input power at the heater fixed on the surface of the evaporator in 5-watts steps from 5 to 30 W. Fig. 3.3 illustrates the evolution of the temperatures of the adiabatic section and the condenser and evaporator parts as well as the PHP pressure during the test. As explained above, during the start-up phase, the PHP is open to the buffer volume for the filling process. During this phase, the temperature of the evaporator decreases due to the arrival of the working fluid, which has been cooled down previously passing through the thermalized inlet tube described in Fig. 2.8 in chapter 2. After 21 minutes, when the temperature of the evaporator remains stable at 76.15 K, this connection is closed. Then, the input power is increased

gradually and the stable oscillating phases start. Each phase lasts between 40 and 60 minutes, in order to confirm the stable working conditions. It can be observed in Fig. 3.3 that the temperature of the evaporator increases at each power step attaining rapidly a stable value. Due to the temperature controller system, the temperature of the condenser oscillates around 75 K all along the test. Consequently, the temperature difference between the evaporator and the condenser is greater at each power step, going from 1 K at 5 W to 7 K at 25 W. Temperatures of the adiabatic part mainly oscillate between the evaporator and the condenser during the test. More details about their evolution will be given in the next sections. At 30 W, the temperature of the evaporator increases continually. The heat transfer between the fluid and the evaporator is not enough, a dry-out takes place then the experiment is stopped when the temperature attains 90 K in the evaporator, after 5.5 hours. Under these experimental conditions, the PHP is able to transfer a maximum of 25 W of heat load in stable conditions. Concerning the PHP pressure, this latter also oscillates around a stable value at each power step going from 8.5×10^4 Pa at 5 W to 1.13×10^5 Pa (on average) at 30 W, but it is important to note that the amplitude of oscillations become considerably more important from 25 W, indicating the beginning of instabilities concerning the temperature of the evaporator and the end of stable oscillating phases.

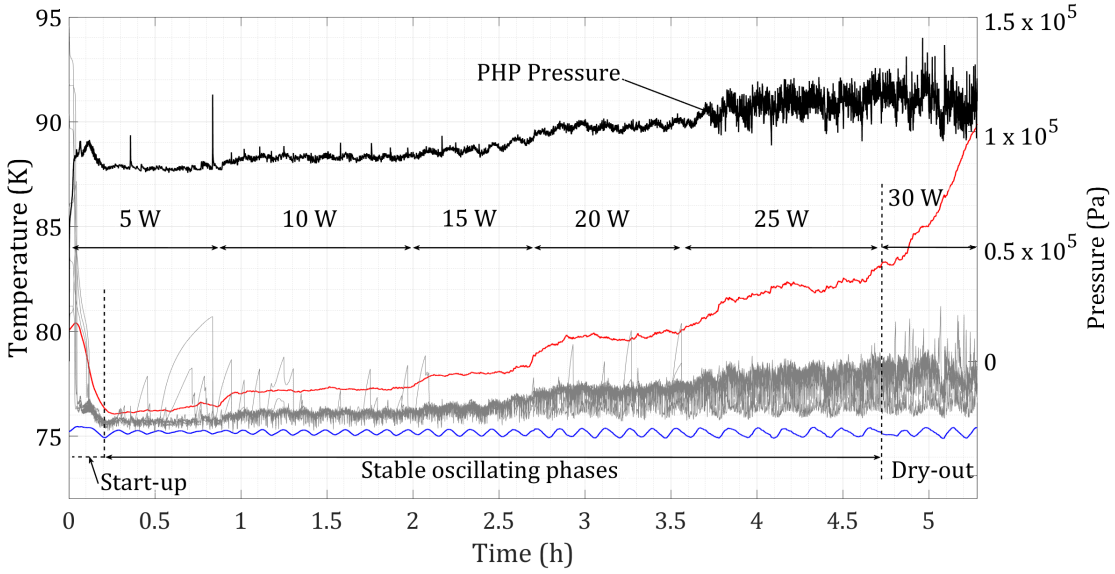

Figure 3.3: Evolution of the PHP global pressure (—), the average temperature of the evaporator (—) and the condenser (—) and the temperatures of the adiabatic part (—) of the reference test.

Remarks

- Several identical tests have been performed, within few months apart, to confirm the reproducibility of the experimental results.
- The evolution of the pressure inside the PHP is measured by four different pres-

sure sensors described in chapter 2. Nevertheless, only measurements given by one pressure sensor are plotted in the different graphs (always the same sensor). This is because during the test, all the pressure sensors present the same evolution (with differences lower than 5.10^3 Pa mainly due to measurement errors).

- Concerning the temperature controller, this latter is necessary to maintain the temperature of the condenser (and the cold head) at a desired value. Some tests have been done without the regulation, deactivating the temperature controller and imposing a constant input power at the condenser. Results showed that the temperature of the condenser, as well as the temperature of the evaporator and the pressure, increased with the input power, saturating the cold head of the cryocooler and evaporating the working fluid inside the PHP. This shows the need of a temperature controller system at the cold head when using cryocoolers instead of cryogenic cold baths. In the reference test, the temperature of the condenser oscillates around 75 K at a frequency of 2.10^{-3} Hz with an amplitude of 0.5 K. In addition to that, another progressive heat load test has been performed deactivating the temperature controller and changing manually the input power at the condenser, to maintain a stable temperature. Results showed a constant temperature at the condenser all along the test, a stable temperature at the evaporator at each power step and the same performances than in the reference test. From this, it is possible to conclude that the temperature oscillations in the condenser plate due to the temperature controller are not responsible for the PHP stable operating conditions. Nevertheless, the temperature controller is necessary for the automation of the system.

- As mentioned at the beginning of this section, the filling ratio described in chapter 2 is initially calculated to be theoretically 50 %. For this primary calculation, all the volumes of the inlet gas system are considered at the pressure of the PHP and at an intermediate temperatures between the condenser and 300 K. The properties of the fluid in the PHP are considered at saturation conditions at the temperature of the condenser: 75 K. Consequently, this initial filling ratio does not correspond with the reality because the entire PHP is not at the temperature of the condenser. Due to this, after performing every test, the real ratio is computed considering the properties of the fluid at the measured temperatures and pressure in all the different volumes of the inlet system thanks to the numerous sensors (see Fig. 2.8 in chapter 2). Inside the PHP, the filling ratio is calculated in two different ways in order to estimate the maximum uncertainty. On one hand, a filling ratio called FR_{sat}, is calculated considering all the vapor and liquid parts inside the PHP at saturation conditions at the measured pressure. On the other hand, a filling ratio called FR_{ec}, is calculated considering all the vapor and liquid parts inside the PHP at the temperature of the evaporator and the condenser respectively and at the measured pressure. In the PHP, the temperature of the vapor parts is necessarily between

the saturation temperature and the evaporator's temperature and the temperature of the liquid parts is necessarily between the saturation temperature and the condenser's temperature. Due to this, the two mentioned calculations give us the two possible limit values of the real filling ratio. Density values are obtained using NIST Refprop Database [2]. Results show that during the test, the filling ratio decreases slightly due to the increasing input power and the corresponding evaporation rate. In the first case, FR_{sat} decreases from 43.75 to 41.5% and, in the second case, FR_{ec} decreases from 43.6 to 40.9%. The maximum difference between both values goes from ±0.34% at the beginning of the test to ±1.46% at the end of the test. Due to the negligible differences and for simplicity reasons of calculation, since now, the filling ratio at saturation conditions (FR_{sat}) will be considered as the real filling ratio. Thus, the average filling ratio during this reference test is 42.6%.

3.2.3 Evolution of the thermal performance

Fig. 3.4 shows the evolution and the experimental standard deviation of the equivalent thermal conductivity during the test. The equivalent thermal conductivity λ_{eq} is determined by:

$$\lambda_{eq} = \frac{Q \cdot L}{A \cdot \Delta T},$$

where Q is the input power at the surface of the evaporator (W), L is the length of the tubing part (m), A is the cross-sectional area of all the tubes (m^2) and ΔT is the temperature difference between the evaporator and the condenser. This equivalent thermal conductivity is calculated when the temperature of the evaporator oscillates around a stable value, going from 72.5 kW/(m.K) at 5 W to 85 kW/(m.K) at 15 W (maximum value) and decreasing to 63 kW/(m.K) at 25 W. At 30 W, the temperature of the evaporator is unstable, the equivalent thermal conductivity decreases from 63 to 35 kW/(m.K) and it has not been plotted. It can also be observed that the higher standard deviations correspond to 5 and 25 W, when the system is less stable, being close to the start-up and dry-out phases respectively.

3.2.4 Thermodynamics and fluid distribution

The different locations of the temperature and pressure sensors and the position of the external tube (the tube closer to the PHP inlet) are given in Fig. 3.5. This scheme will be a useful reference for the following analysis.

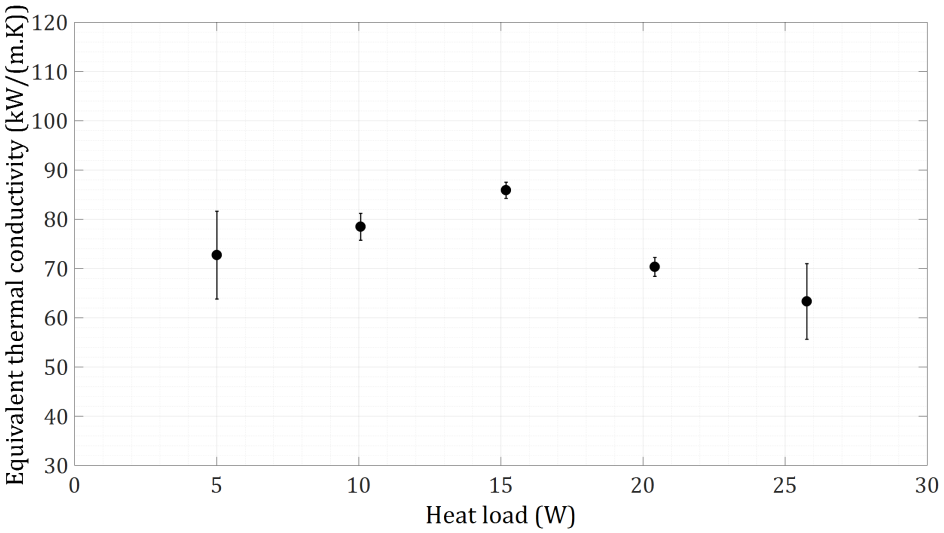

Figure 3.4: Evolution of the equivalent thermal conductivity.

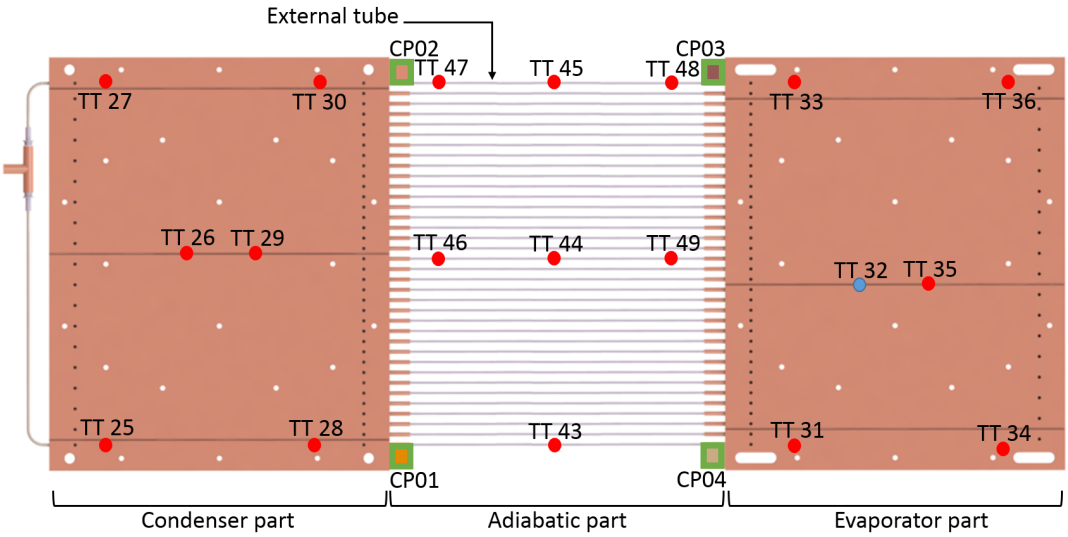

Figure 3.5: Locations of temperature (● , ●) and pressure (■) sensors of the 36-turns PHP.

General thermodynamic behavior

As mentioned before, all the pressure sensors present the same evolution. From this finding and according to the literature, we make the assumption that the mean pressure is identical within the entire PHP [85] and represents the pressure of the fluid at saturation conditions [52]. In this way, the saturation temperature is calculated and plotted using the NIST Refprop Database [2]. Fig. 3.6 shows the evolution of the PHP pressure, the corresponding saturation temperature, the average temperatures of the evaporator and the condenser, and the temperatures of the adiabatic part of the reference test. In the evaporator and the condenser, sensors are fixed on the surface of the copper plates and, consequently, local fluid oscillations in the tubes cannot be estimated precisely. On the contrary, in the adiabatic section, sensors are fixed directly to the surfaces of the tubing

parts with copper powder charged epoxy resin, ensuring a good thermal contact. Due to this, it becomes possible to measure precisely temperature oscillations of the fluid. In order to confirm the accuracy of these temperature measurements in the adiabatic part, a transient thermal 3D simulation have been performed with COMSOL Multiphysics® to estimate the thermal response throughout temperature changes of the fluid. Specific details and results of this simulation are given in appendix C. Numerical results of the mentioned simulation have shown a temperature difference between the inner surface of the capillary tube and a temperature sensor lower than 0.1 K after a temperature increase of 2 K in the liquid nitrogen which is in contact with the inner surface of the capillary tube. In addition, the temperature difference between the liquid nitrogen and a temperature sensor was lower than 0.2 K after 5 s, which is shorter in time than the temperature peaks' duration measured experimentally. Furthermore, it can observed in Fig. 3.6 that temperatures measured by the sensors of the adiabatic part are often below the saturation temperature (1 K lower at maximum). This could indicate the liquid state of the fluid or the presence of vapor at low temperature due to a strong adiabatic relaxation, but an adiabatic relaxation can only occur when the gas is not surrounded by a liquid film, so the first option (fluid in liquid state) seems more appropriate in this case. All of this indicates that the temperature of the fluid at the adiabatic part can be measured with acceptable accuracy, when liquid is present at the sensor's location.

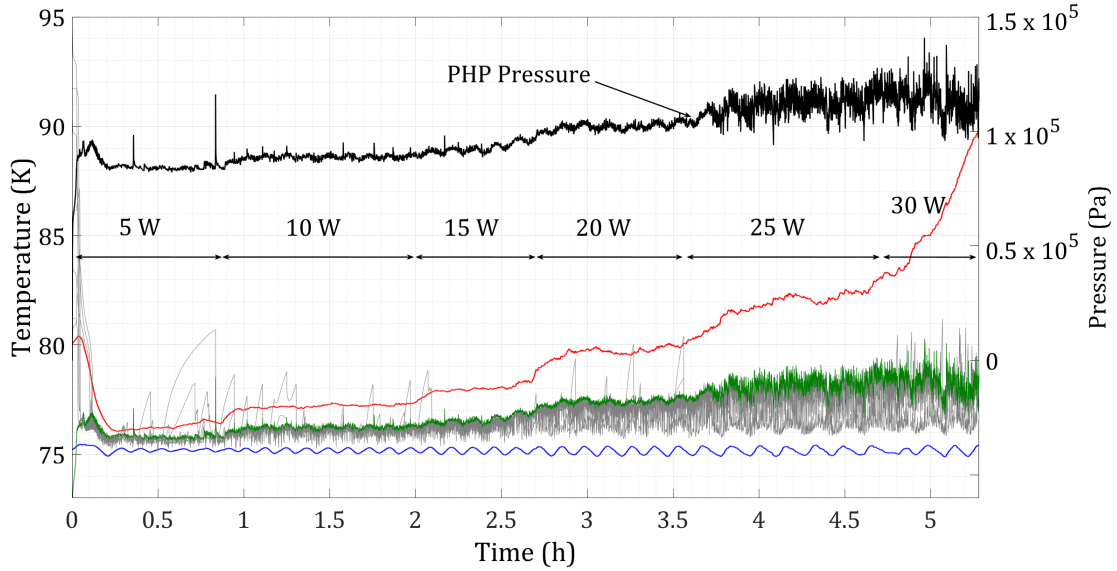

Figure 3.6: Evolution of the PHP pressure (—), the saturation temperature (—), the average temperature of the evaporator (—) and the condenser (—) and the temperatures of the adiabatic part (—) of the reference test.

It can be observed in Fig. 3.6 that temperatures of the adiabatic part are mainly lower than the calculated saturation temperature. This finding indicates the subcooled state of the liquid parts (including liquid slugs and surrounding liquid films of vapor plugs), as suggested by other authors [31, 62]. Therefore, the vapor parts remain at saturated or superheated state [106], depending on the location in the PHP. In addition,

intermittent temperature peaks at the adiabatic part can be observed. These temperature peaks exceeds the saturation temperature, indicating the superheated state of the fluid at this spot, which seems to correspond to a superheated vapor part without a surrounding liquid film (previously evaporated), as indicated by [18]. During these "local dry-outs", temperatures peaks exceed between 0.2 and 4.8 K the saturation temperature and can even reach higher temperature than the evaporator's one. This phenomena could be explained by local adiabatic compressions in vapor plugs exerted by surrounding liquid slugs. It has also been noticed by [52] and defined as the "piston effect" by [92]. In this case, pressure peaks can be considered as a consequence of a pressure compression and relaxation at the end of the event. These temperature peaks are more frequent at low heat fluxes. At 15 W no temperature peak is measured while at 20 W they occur again. When the thermal performance is maximal (at 15 W), adiabatic compressions are less frequent or even nonexistent indicating an optimum fluid distribution of the oscillating flow.

Fluid distribution: analysis of a single capillary tube

In this section, the temperature evolution and distribution of one tube of the adiabatic part is analyzed in detail. In order to avoid possible influence of the inlet of the PHP on the fluid distribution, the tube located in the middle of the adiabatic part has been chosen for this analysis (see Fig. 3.5).

Fig. 3.7 represents the evolution of the temperatures of the fluid inside the capillary tube located in the center of the PHP (sensors TT46, TT44 and TT49) as well as the calculated saturation temperature at 5 W and 10 W respectively. In both cases it can be observed that the saturation temperature is higher than or equal to the temperatures measured by the three sensors. It can also be observed that the evolution of these temperatures is quite chaotic, the lowest temperature is measured sometimes by sensor TT44 (located in the middle of the adiabatic part) and sometimes by sensor TT46 (located close to the condenser). Considering this, subcooled liquid slugs can be noticed in the middle of the adiabatic part surrounded by vapor bubbles (this is exemplified by the temperature of the sensor TT44 lower than the temperature of the sensor TT46). Also, subcooled liquid slugs can be noticed close to the condenser (when the temperature of sensor TT46 is lower than the temperature of sensor TT44). In addition, temperature peaks exceeding the saturation temperature measured by sensor TT49 can also be observed and are indicated by red circles. All of this shows the chaotic and uneven liquid/vapor distribution in the PHP at 5 and 10 W.

Fig. 3.8 represents the evolution of the temperatures of the fluid inside the capillary tube located in the center of the PHP (sensors TT46, TT44 and TT49) as well as the calculated saturation temperature at 15 W of input power. In this case, where the maximum equivalent thermal conductivity is achieved, no temperature peak exceeding the

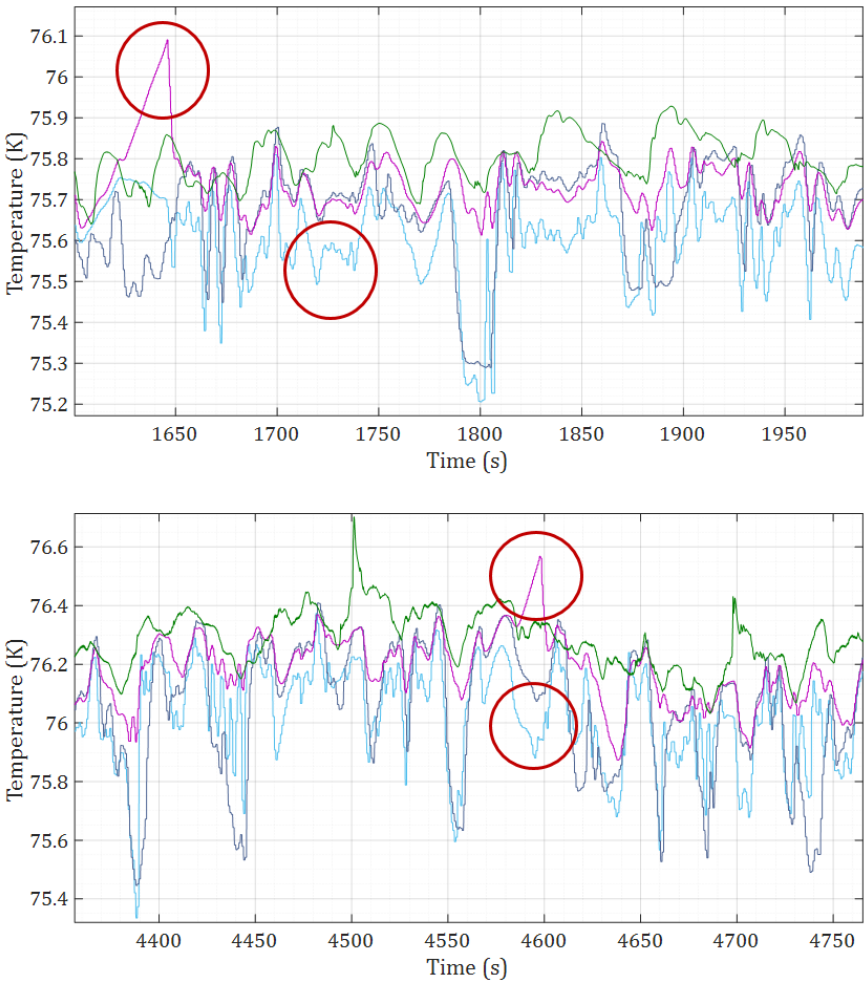

Figure 3.7: Evolution of the temperatures of the fluid inside the capillary tube located in the center of the PHP (sensors TT46 (—), TT44 (—) and TT49 (—)) and the saturation temperature (—) at 5 and 10 W of input power respectively.

saturation temperature can be observed. Nevertheless, the lowest temperatures continue to be measured alternatively by sensors TT44 and TT46.

Fig. 3.9 represents the evolution of the temperatures of the fluid inside the capillary tube located in the center of the PHP (sensors TT46, TT44 and TT49) as well as the calculated saturation temperature at 20 W and 25 W respectively. In both cases it can be observed that the highest temperature below the saturation one is generally measured by sensor TT49 (close to the evaporator). The lowest temperature is most of the time measured by the sensor TT46 (close to the condenser) followed by sensor TT44 (in the middle). In addition, it can also be seen that the temperature difference between sensors TT46 and TT44 is higher than in the previous power steps, revealing the considerable temperature differences all along the tube, due to the increasing temperature difference between the evaporator and condenser. Furthermore, temperature peaks measured by sensor TT49 exceeding the saturation temperature re-appear (indicated by a red circle). At this point, the tubing part seems to be composed of subcooled liquid slugs close to

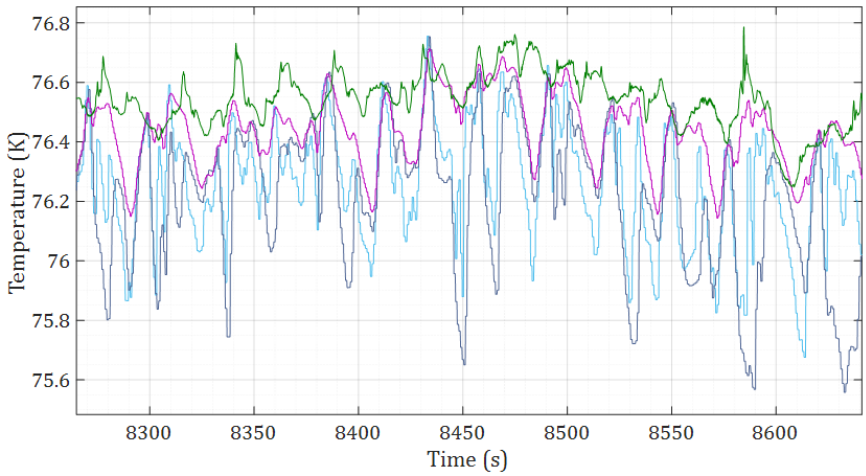

Figure 3.8: Evolution of the temperatures of the fluid inside the capillary tube located in the center of the PHP (sensors TT46 (—), TT44 (—) and TT49 (—)) and the saturation temperature (—) at 15 W of input power.

the condenser part and the distribution of alternating liquid slugs and vapor plugs tends to disappear. Nevertheless, a single-direction circulation of the fluid cannot be confirmed due to the permanent temperature oscillations in all the sensors.

Fig. 3.10 represents the evolution of the temperatures of the fluid inside the capillary tube located in the center of the PHP (sensors TT46, TT44 and TT49) as well as the calculated saturation temperature at 30 W of input power. At this point, temperature peaks measured by TT49 become more frequent (indicated by red ellipses), while temperatures measured by TT44 and TT46 oscillate closer, still lower but closer, to the saturation temperature compared to previous power-steps. This indicates important temperature differences along the tube and reveals the instability of the system due to the beginning of the dry-out process occurring at the evaporator. More details about the dry-out phase will be given in section 3.2.5.

Comparison of the adiabatic tubing parts

In this section, temperature evolutions of the three monitored adiabatic tubing parts are analyzed and compared, considering their respective positions in the PHP.

The evolution of the temperatures of the adiabatic part of the external tube, the central tube and the other external tube, indicated in Fig. 3.11, are given in Fig. 3.12, 3.13 and 3.14 respectively. In the three figures are included the evolution of the average temperatures of the evaporator and the condenser as well as the calculated saturation temperature.

Comparing the three figures, it can be noticed that most of the temperature peaks (local dry-outs) mentioned above, occur in the external tube of the PHP, especially at low

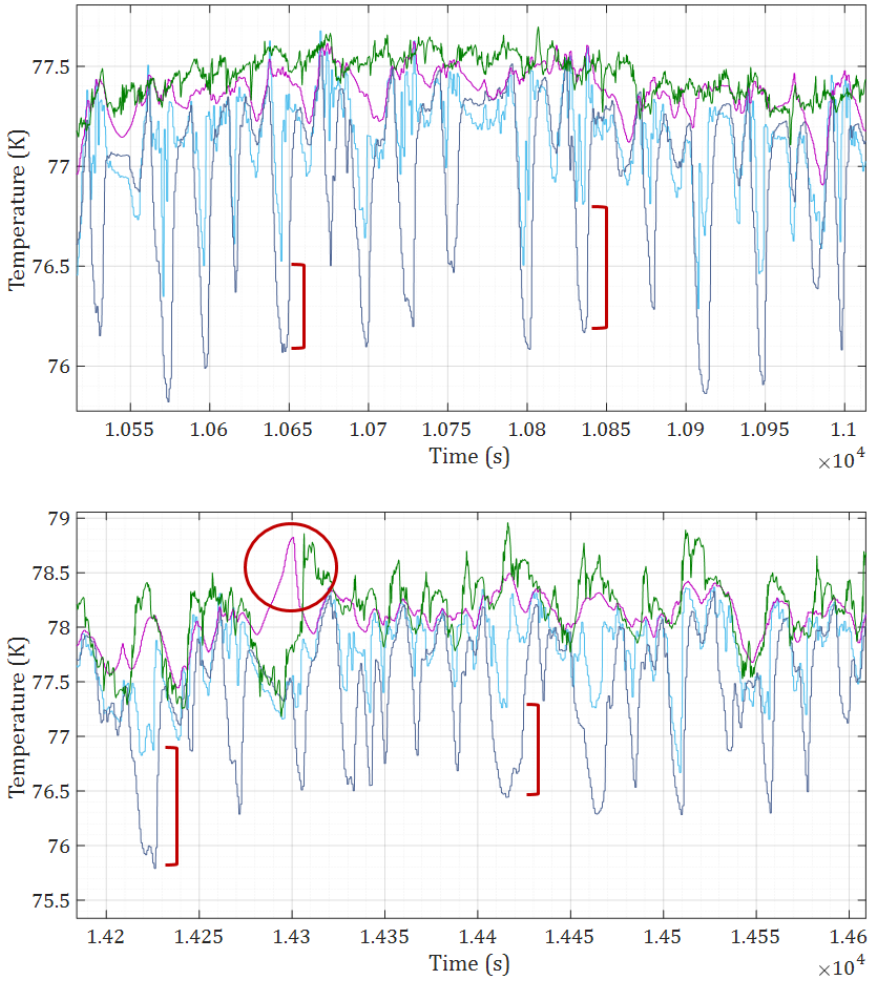

Figure 3.9: Evolution of the temperatures of the fluid inside the capillary tube located in the center of the PHP (sensors TT46 (—), TT44 (—) and TT49 (—)) and the saturation temperature (—) at 20 and 25 W of input power respectively.

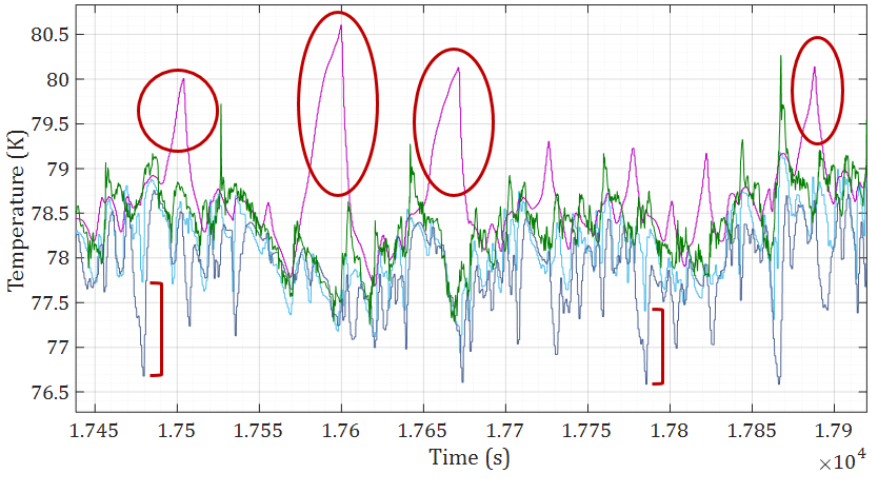

Figure 3.10: Evolution of the temperatures of the fluid inside the capillary tube located in the center of the PHP (sensors TT46 (—), TT44 (—) and TT49 (—)) and the saturation temperature (—) at 30 W of input power.

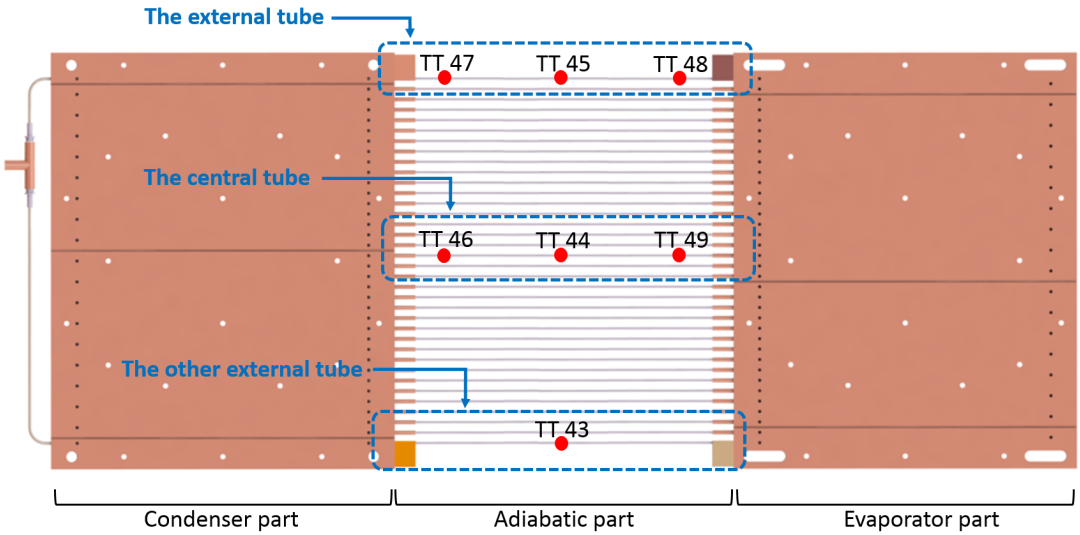

Figure 3.11: Locations of the three monitored tubes of the adiabatic part.

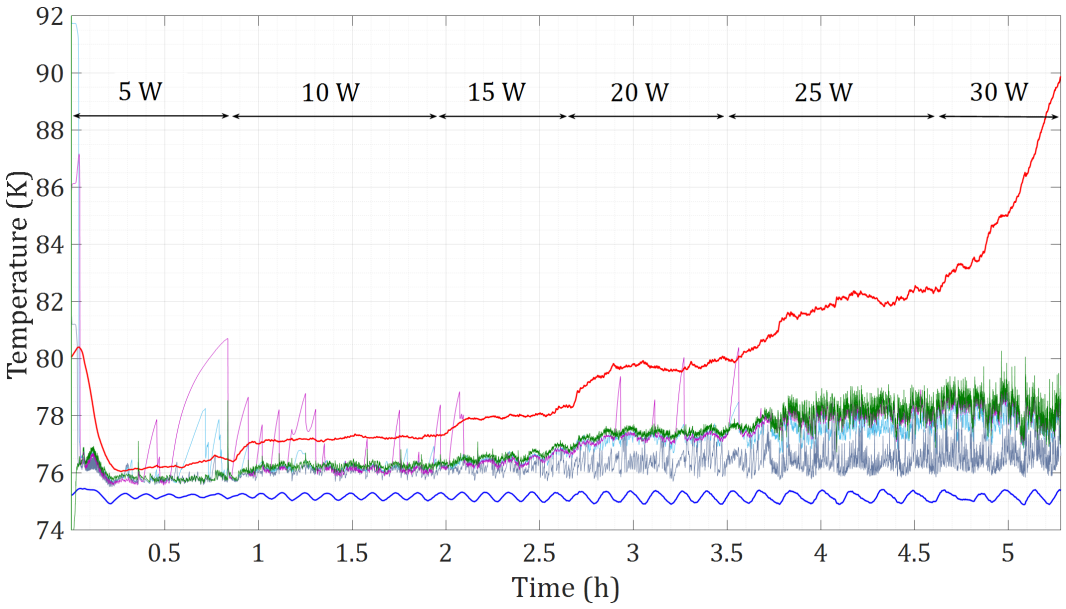

Figure 3.12: Evolution of the average temperature of the evaporator (—) and the condenser (—), the saturation temperature (—) and the temperatures of the adiabatic part (sensors TT45 (—), TT47 (—) and TT48 (—)) of the external tube.

heat fluxes. In addition, it can be seen on Fig. 3.12 that the highest peaks are measured by the sensor TT48 (close to the evaporator) and some other are also detected by the sensor TT45 (in the middle of the tube). In most cases, temperature peaks are even higher than the temperature of the evaporator. This could be explained as follows: When the PHP is being filled, the external tube is the first part of the PHP where the fluid flows through after being liquefied at the inlet thermal link described in chapter 2. In addition, at the end of the filling process, the fluid inside this tube has never pass through any U-turn of the evaporator. Consequently, large liquid slugs flowing slowly due to a higher pressure drop can act as stoppers and adiabatic compressions of the few vapor plugs become more

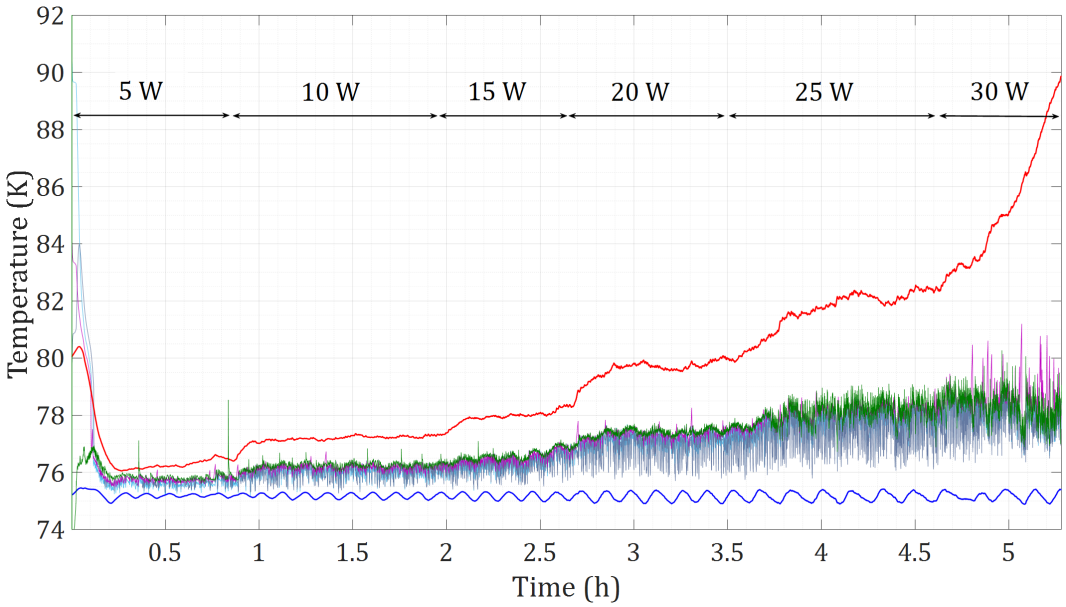

Figure 3.13: Evolution of the average temperature of the evaporator (—) and the condenser (—), the saturation temperature (—) and the temperatures of the adiabatic part (sensors TT44 (—), TT46 (—) and TT49 (—)) of the central tube.

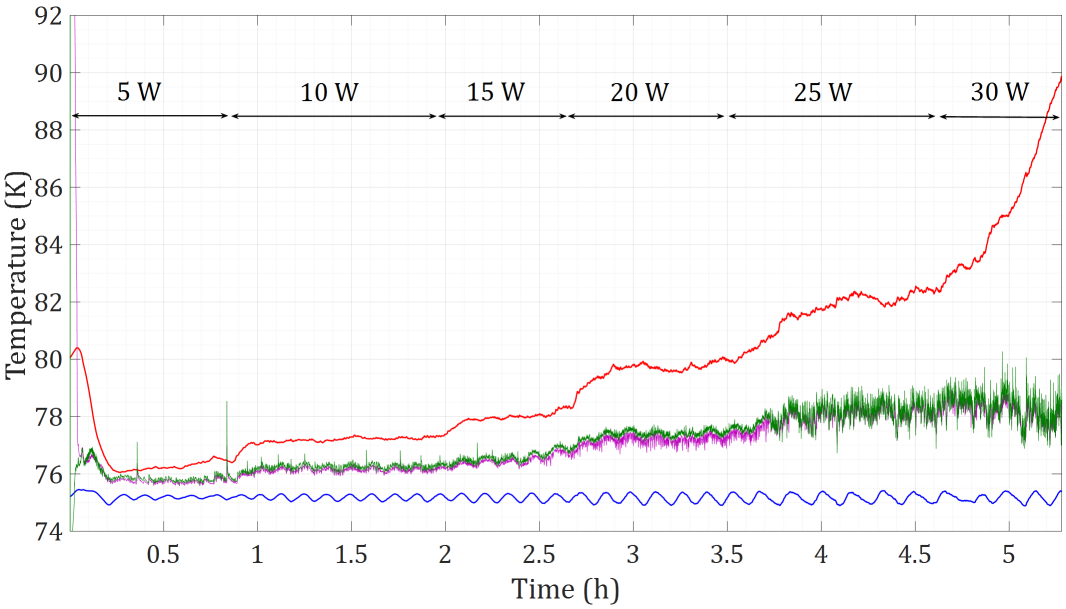

Figure 3.14: Evolution of the average temperature of the evaporator (—) and the condenser (—), the saturation temperature (—) and the temperatures of the adiabatic part (sensor TT43 (—)) of the external other tube.

important than in the other tubes of the PHP, generating temperature peaks that can even exceed the temperature of the evaporator. It could also have an influence of the asymmetric PHP inlet, but to verify this it would be necessary to add more sensors in the opposite external tube (the other external tube) and compare temperature evolutions.

Furthermore, it can also be noticed that, above 15 W, the curve of the average temperatures of the adiabatic part of this external tube splits into two different values

and the oscillation amplitudes become more important. Sensor TT47 oscillates around an average value considerably lower (between 0.8 and 1.4 K lower) than the two other sensors. This indicates, once again, a temperature distribution along the tube heading to a remarkable uneven liquid/vapor distribution, with more liquid slugs close to the condenser, or at least, with liquid slugs "more subcooled" close to the condenser.

Concerning the central and the other external tube, it can be seen in Fig. 3.13 and Fig. 3.14 that temperatures of the adiabatic part oscillate permanently between the evaporator and the condenser temperatures. However, in the case of the central tube, punctual temperature peaks exceeding the saturation temperature can be noticed at 5, 10 and 20 W, showing that local dry-outs can occur and be measured in different tubes of the adiabatic part. In the case of the other external tube, this latter has less temperature sensors, which makes more difficult to conclude about the presence or not of local dry-out spots.

In the three tubes, the amplitudes of temperature and pressure oscillations of the adiabatic part increase with the input power. Generally speaking, on the first half of the test, the increasing input power leads to increasing temperature and pressure oscillations. This has the effect of increasing the fluid distribution in alternating liquid slugs and vapor plugs, leading to improved thermal performance. On the second half of the test (after 15 W), the temperature distribution contributes to a uneven fluid re-distribution, with more liquid parts close to the condenser, causing reduced thermal performance.

Frequency spectrum analysis

The Fast Fourier Transform (FFT) of all the temperature and pressure sensors have been computed in order to determine specific frequencies of oscillations during the reference test. The frequency peak at 2.10^{-3} Hz (exemplified in Fig. 3.15) corresponding to the temperature controller of the condenser is found in all the FFT of the sensors signals located in the condenser and the adiabatic parts, with different intensity depending on their location in the PHP, and undetectable in the evaporator part.

Besides that, sensors of the adiabatic part show a predominant group of specific frequencies of oscillations with different intensities depending on their location and the power step. As examples, in Fig. 3.16, 3.17 and 3.18, the power spectrums of temperature oscillations of three sensors of the adiabatic part are shown. It can be observed that a predominant group of frequencies appear during stable phases of oscillations at the power steps with higher thermal performance, indicating an optimum oscillating mode at each power step. Nevertheless, these groups of predominant frequencies are less appreciable on pressure sensors signals, where the intensities of power spectrums are much lower, indicating a thermally driven system where temperature variations are more noticeable

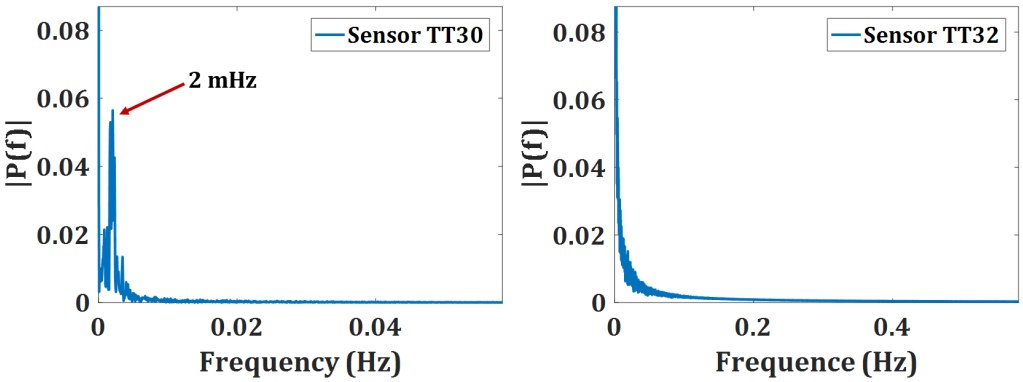

Figure 3.15: Power spectrum of temperature oscillations on sensors TT30 (condenser) and TT32 (evaporator) during the entire reference test.

than pressure variations due to the surrounding liquid film in vapor plugs.

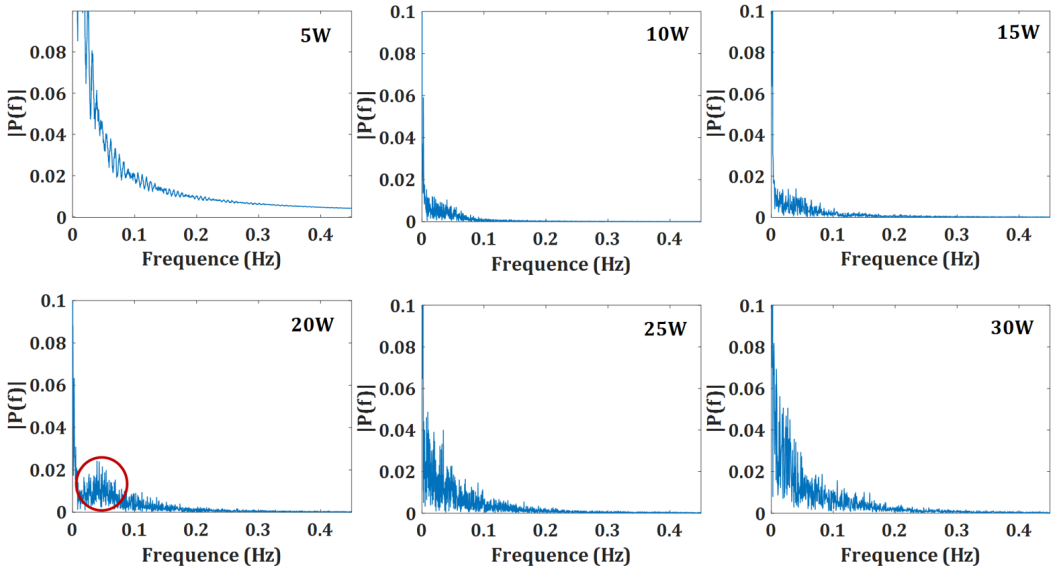

Figure 3.16: Power spectrum of temperature oscillations on sensor TT43 at different power steps.

3.2.5 Dry-out and limits

As mentioned before, at 30 W, the temperature of the evaporator increases continually and the dry-out phase takes place. It can be seen on Fig. 3.13 that during this phase, numerous temperature peaks are measured mainly by sensor TT49, exceeding the saturation temperature and indicating superheated vapor parts in the adiabatic part, known as local dry-outs. Some authors, such as [18] in their numerical studies, have suggested that in this cases, the increasing number of local dry-outs is responsible of the dry-out at the surface of the evaporator. At this point, it becomes more difficult for the liquid slugs, which carry the heat, to reach the evaporator, due to the presence of superheated vapor parts.

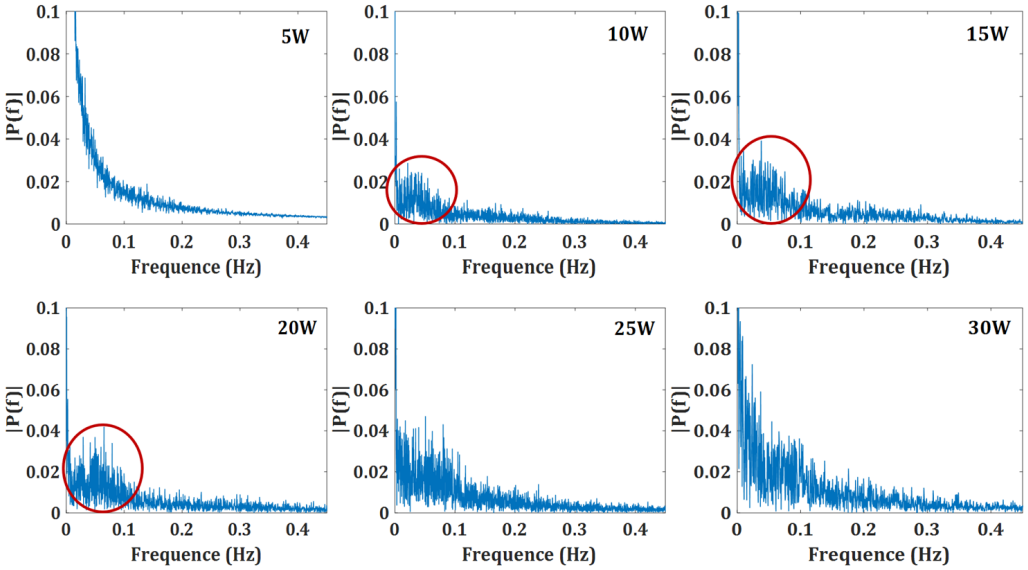

Figure 3.17: Power spectrum of temperature oscillations on sensor TT44 at different power steps.

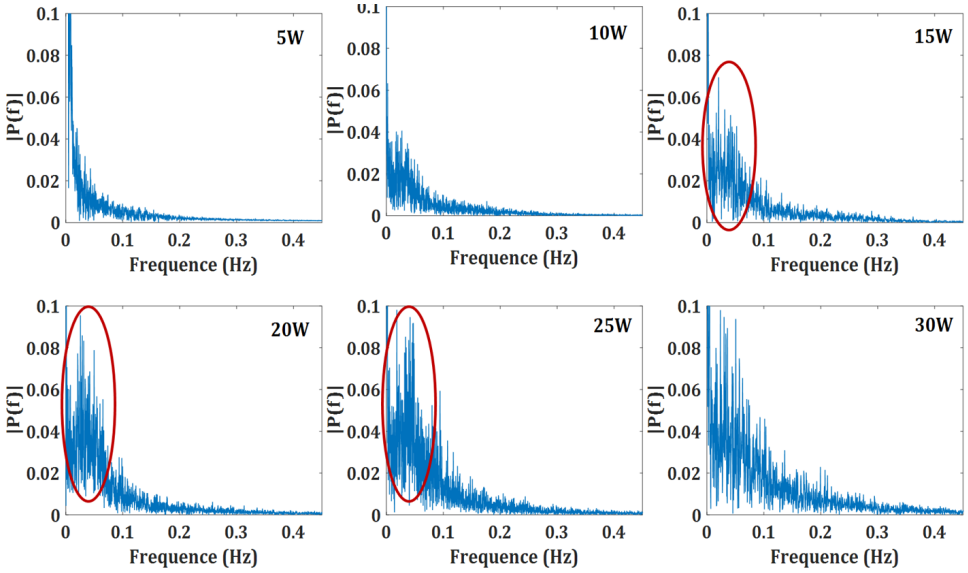

Figure 3.18: Power spectrum of temperature oscillations on sensor TT46 at different power steps.

During the dry-out phase, the PHP can be divided into two independent thermodynamic systems: the evaporator system and the PHP system itself. In the first one, the temperature increases, the fluid is completely evaporated and the heat is not transferred anymore. The fluid in the evaporator is then in superheated state. In the second one, the temperatures of the adiabatic part decrease because the cryocooler is not receiving heat load from the evaporator and the fluid liquefies. The global pressure also decreases during this phase because of the mentioned liquefactions, as noticed by [45]. At this point, it becomes more difficult to determine if the pressure is equal everywhere in the PHP and if it is or not the saturation pressure. Consequently the calculated saturation temperature

cannot be considered and the filling ratio calculations are more inaccurate.

3.3 Conclusions

In this chapter, experimental results of a progressive heat load test performed in the PHP with 36 turns and using nitrogen as working fluid have been analyzed in detail. Hypotheses about the thermodynamic state of the fluid have been presented, the evolution of the temperature and fluid distribution of the different parts has been analyzed and the dry-out phase has been defined. Additional experimental results will be compared to this reference test in the next chapters.

Tests under different heat load conditions and using other cryogenic working fluids (neon and argon) have also been performed in the 36-turns PHP. In the following chapter, experimental results of these tests will be analyzed and compared, in order to determine the influence of the physical properties of the working fluids on thermal performance.

Chapter 4

Comparison between different working fluids

In the previous chapter, experimental results of a progressive heat load test in the PHP with 36 turns using nitrogen as working fluid have been presented, and the thermal performance and the thermohydraulic behavior of the working fluid during the reference test have been analyzed. In this chapter, experimental results of similar tests using neon and argon as working fluids will be presented. The main objective is to compare the thermal performance of the PHP using different cryogenic fluids and to evaluate the influence of the physical properties of these working fluids on the thermal performance.

Neon and argon have been chosen in order to test the same PHP at a different range of temperatures. The working temperatures as well as the critical and boiling points of each fluid are presented in table 4.1 (values have been obtained from GASPAK database [123]).

Table 4.1: Ranges of working temperatures.

Working fluid	Nitrogen	Neon	Argon
Range of working temperatures	74 - 90 K	26 - 42 K	88 - 110 K
Boiling point at 1.10^5 Pa	77.3 K	27.1 K	87.3 K
Triple point	63.15 K 1.25×10^4 Pa	24.55 4.33×10^4 Pa	83.8 K 6.89×10^4 Pa
Critical point	126.2 K 3.39×10^6 Pa	44.5 K 2.66×10^6 Pa	150.7 K 4.9×10^6 Pa

4.1 Comparison with the reference test

4.1.1 General experimental results

In this section, experimental results of a progressive heat load test in the PHP with 36 turns are presented. Firstly with neon as working fluid and secondly with argon as working fluid.

Neon

Fig. 4.1 shows the evolution of the PHP pressure, the corresponding saturation temperature, the average temperatures of the evaporator and the condenser, and the temperatures of the adiabatic part of a progressive heat load test using neon as working fluid. In this test, the filling ratio is initially calculated to be at 40 % and the fluid insertion process is exactly the same as in the reference test described in chapter 3. This time, at the beginning of the test the evaporator is heated from 27 K to 32 K while the temperature of the condenser is maintained at 27 K using the temperature controller. After 17 minutes, when the temperature of the evaporator is stable at 29.2 K, the valve V7 is closed isolating the PHP from the inlet system and the buffer volume. The experiment has been performed increasing gradually the input power at the heater fixed on the surface of the evaporator in 5-watts steps from 5 to 55 W. Each step lasts around 30 minutes. It can be observed in Fig. 4.1 that, as in the reference test, the temperature of the evaporator, as well as the pressure, increases at each power step attaining rapidly a stable average value while the temperature of the condenser is fixed at 27 K all along the test without oscillations. Consequently, the temperature difference between the evaporator and the condenser is greater at each power step, going from 2.2 K at 5 W to 10.8 K at 50 W.

In this case, between 10 and 50 W, the saturation temperature corresponds to the higher values of the temperature measurements of the adiabatic part, indicating the sub-cooled state of the liquid slugs and liquid films (see appendix D), as during the reference test. Nevertheless, intermittent temperature peaks higher than the saturation temperature can be observed, indicating local superheated vapor plugs, known as local dry-outs. Those temperature peaks become more frequent at higher heat loads. At 50 W, the temperature of the condenser increases from 27 K to 28.2 K. This is because we approach the limits of the cold head (the temperature controller indicates 0% of input power), but it is not due to the limits of the PHP system itself, as indicated in [91]. At 55 W, it can be observed that the temperature of the condenser continues to increase (reaching almost 30 K) and the evaporator's temperature is not stable (oscillating between 41.2 and 42.4 K). Furthermore, at this point pressure oscillations are considerably high, oscillating between 4.2 and 5.2×10^5 Pa (pressure sensors stop to measure at 7×10^5 Pa). Due to the instability signs of the system and for security reasons, the experiment was stopped after 5.6 hours,

Table 4.2: Maximum inner diameters.

Working fluid	Nitrogen	Neon	Argon
Range of working temperatures	74 - 90 K	26 - 42 K	88 - 110 K
$\emptyset_{inner}$ at working temperatures (mm)	2.2 - 1.8	1.3 - 0.52	1.9 - 1.6
$\emptyset_{inner}$ at $1{\times}10^5$ Pa (mm)	2.1	1.3	1.9

without reaching clearly the dry-out phase.

The calculated real filling ratio in saturation conditions (R_{sat}) goes from 24.9 to 25.2% during the test. Thus, the average filling ratio of this test is 25%.

We can then conclude that, under these experimental conditions, the PHP is able to transfer a maximum of 50 W of heat load in stable conditions using neon as working fluid.

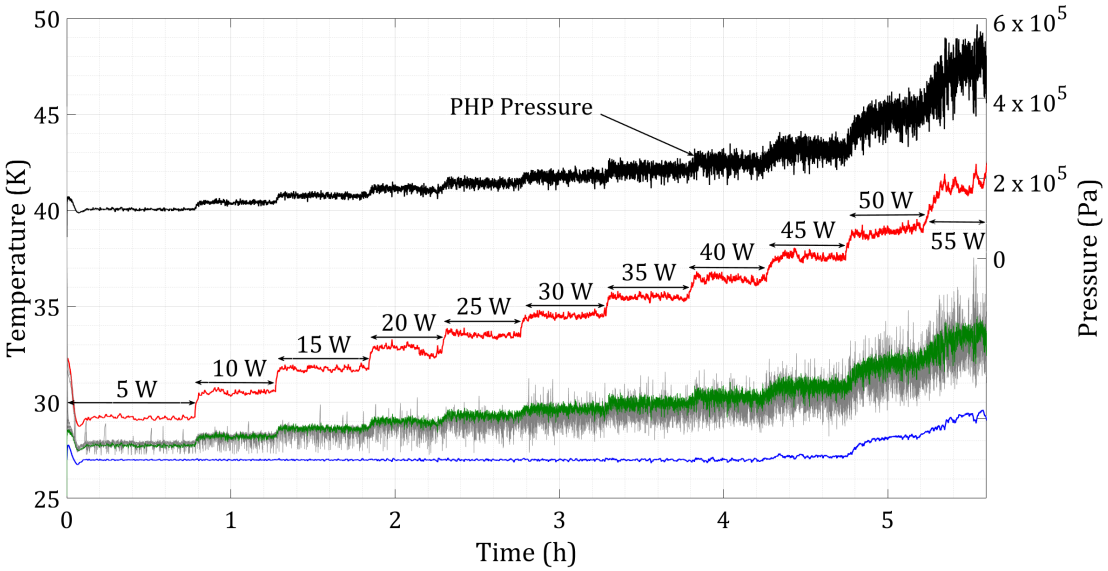

Figure 4.1: Evolution of the PHP pressure (—), the saturation temperature (—), the average temperature of the evaporator (—) and the condenser (—) and the temperatures of the adiabatic part (—) of a progressive heat load experiment using neon as working fluid.

An interesting point is that, in this particular case with neon, the maximum inner diameter for neon was supposed to be around 1.3 mm following the Bond criterion, as indicated in chapter 1, however the inner diameter of the tubes of the PHP is 1.5 mm. In table 4.2 the maximum inner diameters of the different working fluids using the Bond criterion are provided. For these calculations, in order to obtain the maximum possible values, all the physical properties are considered at saturation conditions and have been obtained from NIST Refprop Database [2]. The coefficient A is chosen to be 2 (the most-often used value in open literature [25]).

Argon

Fig. 4.2 shows the evolution of the PHP pressure, the corresponding saturation temperature, the average temperatures of the evaporator and the condenser, and the temperatures of the adiabatic part of a progressive heat load test using argon as working fluid. In this test, the filling ratio is initially calculated to be at 40 % and the fluid insertion process is exactly the same as in the reference test described in chapter 3. This time, at the beginning of the test the evaporator is heated from 89 K to 94 K while the temperature of the condenser is maintained at 89 K using the temperature controller. After 15 minutes, when the temperature of the evaporator is stable at 90.3 K, the PHP is closed and isolated from the inlet system and the buffer volume. The experiment has been performed increasing gradually the input power at the heater fixed on the surface of the evaporator in 5-watts steps from 5 to 40 W. Each step lasts between 45 minutes and 1 hour. It can be observed in Fig. 4.2 that, as in the reference test too, the temperature of the evaporator, as well as the pressure, increases at each power step attaining rapidly a stable average value, while the temperature of the condenser oscillates around 89 K all along the test due mainly to the temperature controller. Consequently, the temperature difference between the evaporator and the condenser is greater at each power step, going from 1.4 K at 5 W to 7.9 K at 30 W.

It can also be observed that during the entire test, the saturation temperature corresponds to the higher values of the temperature measurements of the adiabatic part, indicating too the subcooled state of the liquid slugs and liquid films (see appendix D), as during the reference test. In this case, comparing to the reference test, no temperature peak exceeding the saturation temperature is measured. At 35 and 40 W, the temperature of the evaporator increases continually, indicating the dry-out phase, and the experiment is stopped when the temperature attains 110 K in the evaporator, after 6.1 hours. This time, it can be observed a division into two thermodynamic systems, already mentioned in chapter 3 and suggested in [39], during the dry-out phase. In the evaporator the temperature continues to increase while in the rest of the PHP the temperatures of the adiabatic part and the pressure decrease because the cryocooler is not receiving heat load from the evaporator. The overall heat transfer in the PHP is stopped.

The calculated real filling ratio in saturation conditions (R_{sat}) goes from 29.4 to 29.1% during the test. Thus, the average filling ratio of this test is 29.25%.

We can then conclude that, under these experimental conditions, the PHP is able to transfer a maximum of 30 W of heat load in stable conditions using argon as working fluid.

Remark

At this point, after the general description of progressive heat load tests with the

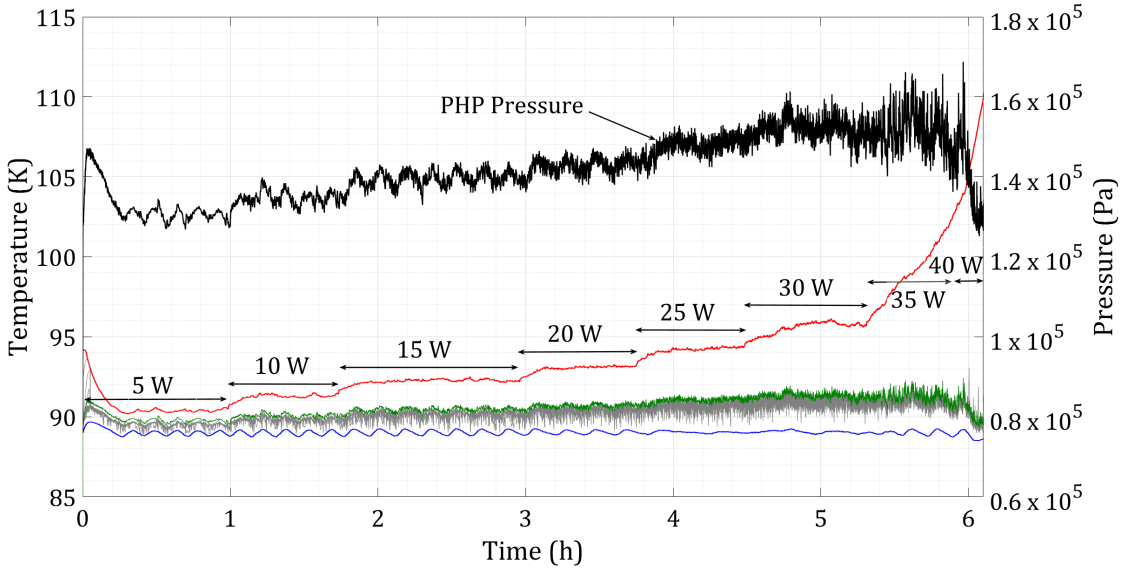

Figure 4.2: Evolution of the PHP pressure (—), the saturation temperature (—), the average temperature of the evaporator (—) and the condenser (—) and the temperatures of the adiabatic part (—) of a progressive heat load experiment using argon as working fluid.

three different working fluids, it can be noticed that the duration of the power steps are different with each working fluid. When using nitrogen, each power step lasts between 40 and 60 minutes, with neon around 30 minutes and with argon between 45 and 60 minutes. This is because, previous progressive heat load tests have been performed to find the maximum heat load transferred by the PHP with each fluid. Then, the duration of the power steps have been determined to be able to perform an entire progressive heat load test in the same day.

4.1.2 Temperature distributions and fluid oscillations

Neon

Fig. 4.3 represents the evolution of the temperatures of the fluid inside the capillary tube located in the center of the PHP (sensors TT46, TT44 and TT49) as well as the calculated saturation temperature at 20 W and 45 W respectively. Analyzing the evolution of these temperatures, we can also see that, when using neon, sensors TT46 and TT44 follow the same tendency while intermittent temperature peaks higher than the saturation temperature are measured by TT49, indicating local dry-outs. In this case, temperature fluctuations (including local dry-outs) become more frequent as the heat load is increased and occur faster than in the reference test with nitrogen.

In addition, comparing the three monitored tubes of the adiabatic section, local dry-outs are only measured by sensor TT49 in the central tube. On contrary to the

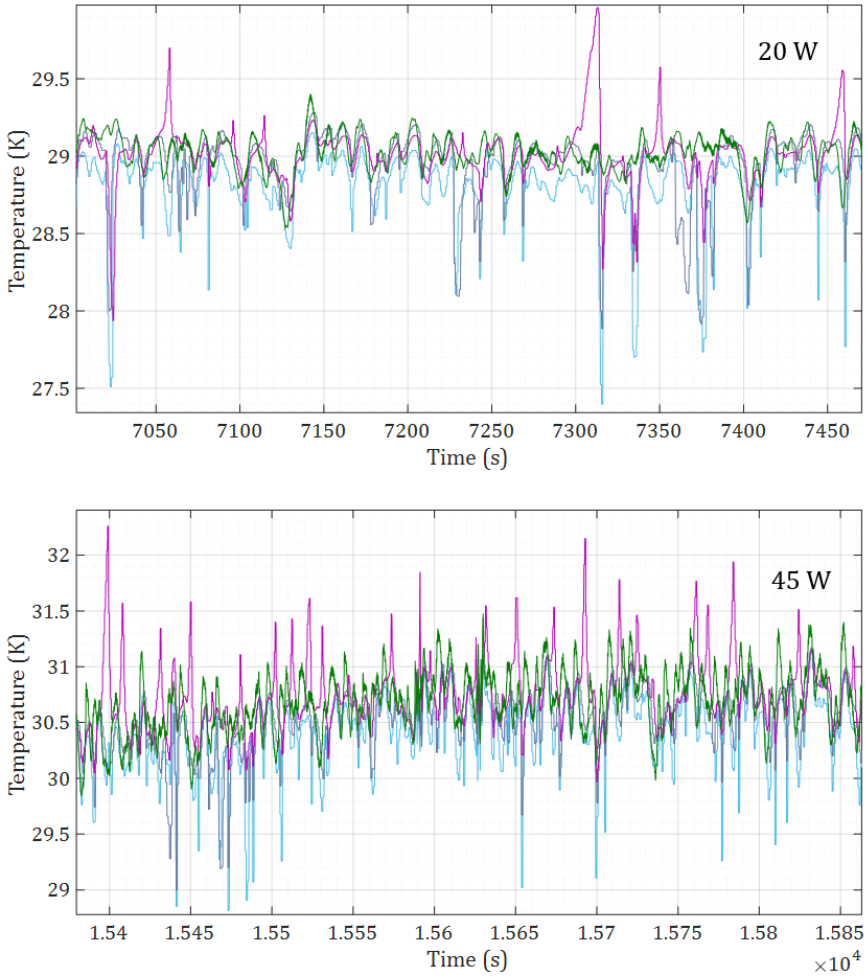

Figure 4.3: Evolution of the temperatures of the fluid inside the capillary tube located in the center of the PHP (sensors TT46 (—), TT44 (—) and TT49 (—)) and the saturation temperature (—) at 20 and 45 W of input power respectively.

reference test, the external tube does not present any specific behavior due to the PHP inlet. Furthermore, after computing a FFT on all the sensors signals, no predominant frequency of oscillations can be noticed. Only in a few power spectrum graphs it can be observed small predominant zones of frequency oscillations, as exemplified in Fig. E.1 in appendix E.

Argon

Fig. 4.4 represents the evolution of the temperatures of the fluid inside the capillary tube located in the center of the PHP (sensors TT46, TT44 and TT49) as well as the calculated saturation temperature at 15 W and 30 W respectively. In this case, no temperature peak indicating a local dry-out is measured during the test but temperature oscillations become more frequent with increasing heat load. The highest temperature is always measured by TT49 but without exceeding the saturation temperature, while the lowest temperature is often measured by TT46 and sometimes TT44. Only when dry-out

takes place, it can be clearly noticed at 40 W that sensor TT49 presents local dry-outs exceeding the saturation temperature, as shown in Fig. 4.5.

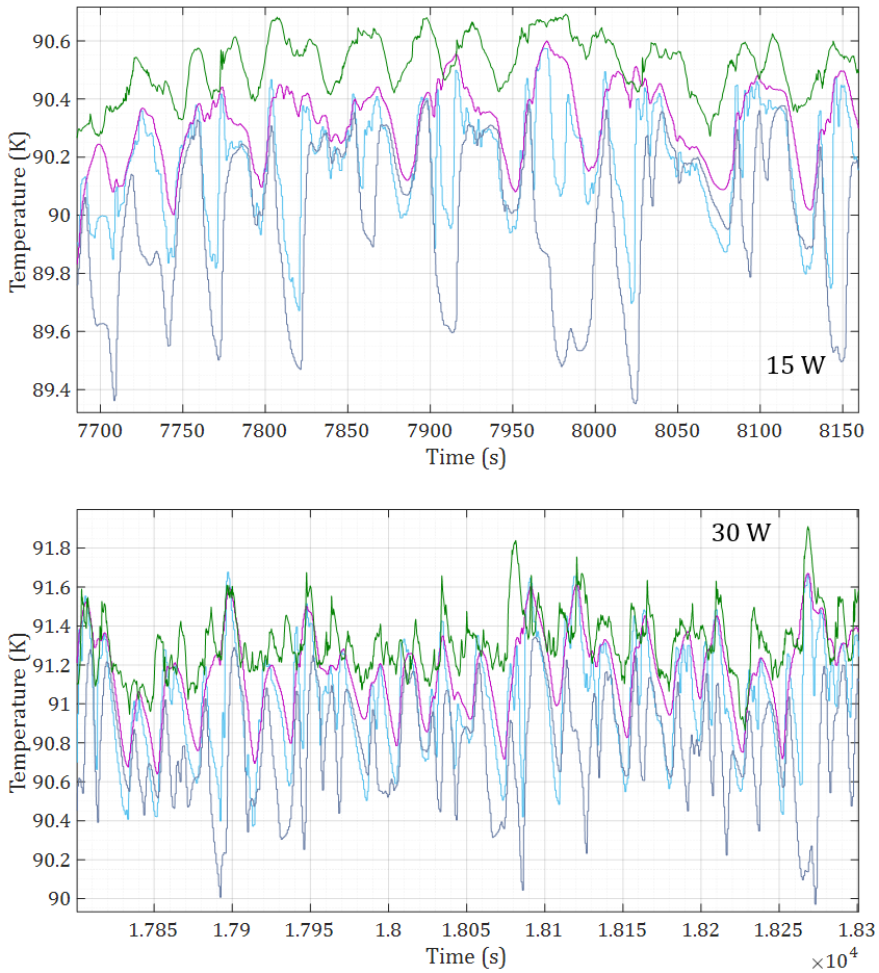

Figure 4.4: Evolution of the temperatures of the fluid inside the capillary tube located in the center of the PHP (sensors TT46 (—), TT44 (—) and TT49 (—)) and the saturation temperature (—) at 15 and 30 W of input power respectively.

None of the two other monitored tubes present local dry-outs during the test or any specific behavior, meaning that either in this test the external tube seems to be affected by the PHP inlet. Furthermore, after computing the FFT of all the sensors, no predominant frequency of oscillations can be noticed in the sensors of the adiabatic and evaporator parts. Only power spectrums of the sensors of the condenser part show a predominant frequency corresponding to the oscillations of the temperature controller, as shown in Fig. E.2 in appendix E.

4.1.3 Evolution of thermal performances

Fig. 4.6 shows the evolution of the equivalent thermal conductivities during the three progressive heat load tests performed using nitrogen, neon and argon.

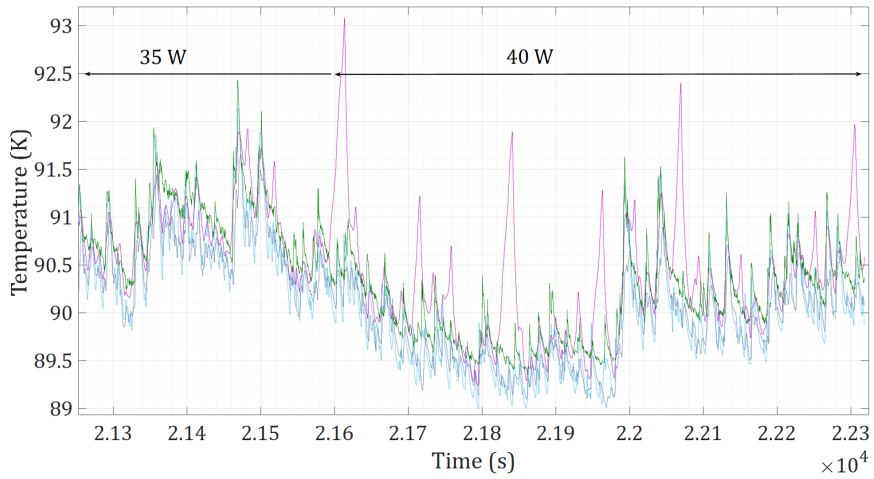

Figure 4.5: Evolution of the temperatures of the fluid inside the capillary tube located in the center of the PHP (sensors TT46 (—), TT44 (—) and TT49 (—))) and the saturation temperature (—) during the dry-out phase (at 35 and 40 W of input power).

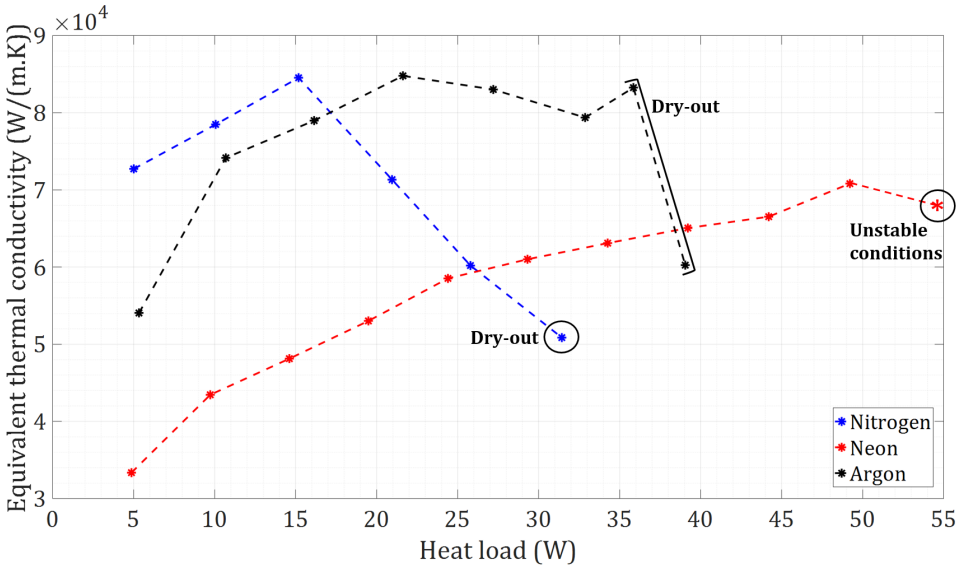

Figure 4.6: Evolution of the equivalent thermal conductivity of the same type of test using different cryogenic fluids: nitrogen (referent test) (—), neon (—) and argon (—).

These three tests have been chosen to be compared due to their similar experimental conditions and because they show the maximum heat transfer capacity (in watts) with each fluid.

It can be seen from Fig. 4.6 that the highest thermal conductivity is achieved when using nitrogen or argon as working fluid, followed by neon, being 85 kW/(m.K), 85 kW/(m.K) and 70kW/(m.K) respectively. As an example, pure copper (RRR=500) at similar ranges of working temperatures presents the following equivalent thermal conductivities: 590 kW/(m.K) at 75 K, 4610 kW/(m.K) at 27 K and 509 kW/(m.K) at 89 K. This represents between 16 and 170 times less than the PHP, which reflects the interest of developing the technology. In addition, with nitrogen and argon, it can be noticed

that a maximum peak of equivalent thermal conductivity is attained at 15 and 20 W, respectively. Nevertheless, when using neon, the maximum heat transfer capacity of the PHP is higher and its equivalent thermal conductivity increases at each power step. It is not clear if at 50 W the PHP in neon attains its real maximum thermal performance. As mentioned in previous section 4.1, the cold head is saturated at 50 W. After, at 55 W, the system becomes unstable decreasing the equivalent thermal conductivity. At this point it is difficult to determine if the limiting factor is the saturated cold head or the PHP itself.

4.2 The influence of the buffer volume

As described in chapter 2, there is a buffer volume in the experimental setup used for the filling process and establishing the initial filling ratio. Progressive heat load tests have been performed at numerous initial filling ratios going from 10 to 90% with the three cryogenic working fluids: neon, argon and nitrogen. Each test have been performed at least two times: once closing the PHP at the beginning of the test as in the reference test, called the closed configuration, and a second time leaving the PHP connected to the buffer volume without closing the valve V7, called the open configuration. In Fig.4.7, 4.9 and 4.11 are represented the equivalent thermal conductivities and liquid filling ratios of tests in open configuration during stable oscillating phases (without including the start-up and the dry-out phases). In Fig. 4.8, 4.10 and 4.12 are represented the equivalent thermal conductivities and liquid filling ratios of tests in closed configuration during stable oscillating phases.

Analyzing the global tendencies of each working fluid, it can be noticed that, in open configuration, at low heat loads the higher conductivities are achieved with low filling ratios, while at high heat loads, the higher conductivities are achieved with high filling ratios. In fact, at low filling ratios the performances rapidly deteriorates with increasing heat load, while at high filling ratios performances increases with increasing heat load. In progressive heat load experiments, the working temperatures increase with the input power at the evaporator, and consequently, the working pressure too. Due to this, considerable amounts of working fluid are transferred to the buffer volume as a response of changes in the working temperatures and pressure. Consequently, at lower filling ratios, the performance is rapidly degraded because there is not enough working fluid in the PHP but, at higher filling ratios, the buffer volume can "absorb" this excess of fluid decreasing the filling ratio and the PHP is able to continue to work in stable conditions. In this configuration, the buffer volume acts as an autoregulation system.

In the closed configuration, the behavior of the fluids and the thermal performances are considerably different. Firstly, it is important to note that, after the filling process, the PHP is closed when the temperature of the evaporator is stable with a heat load of

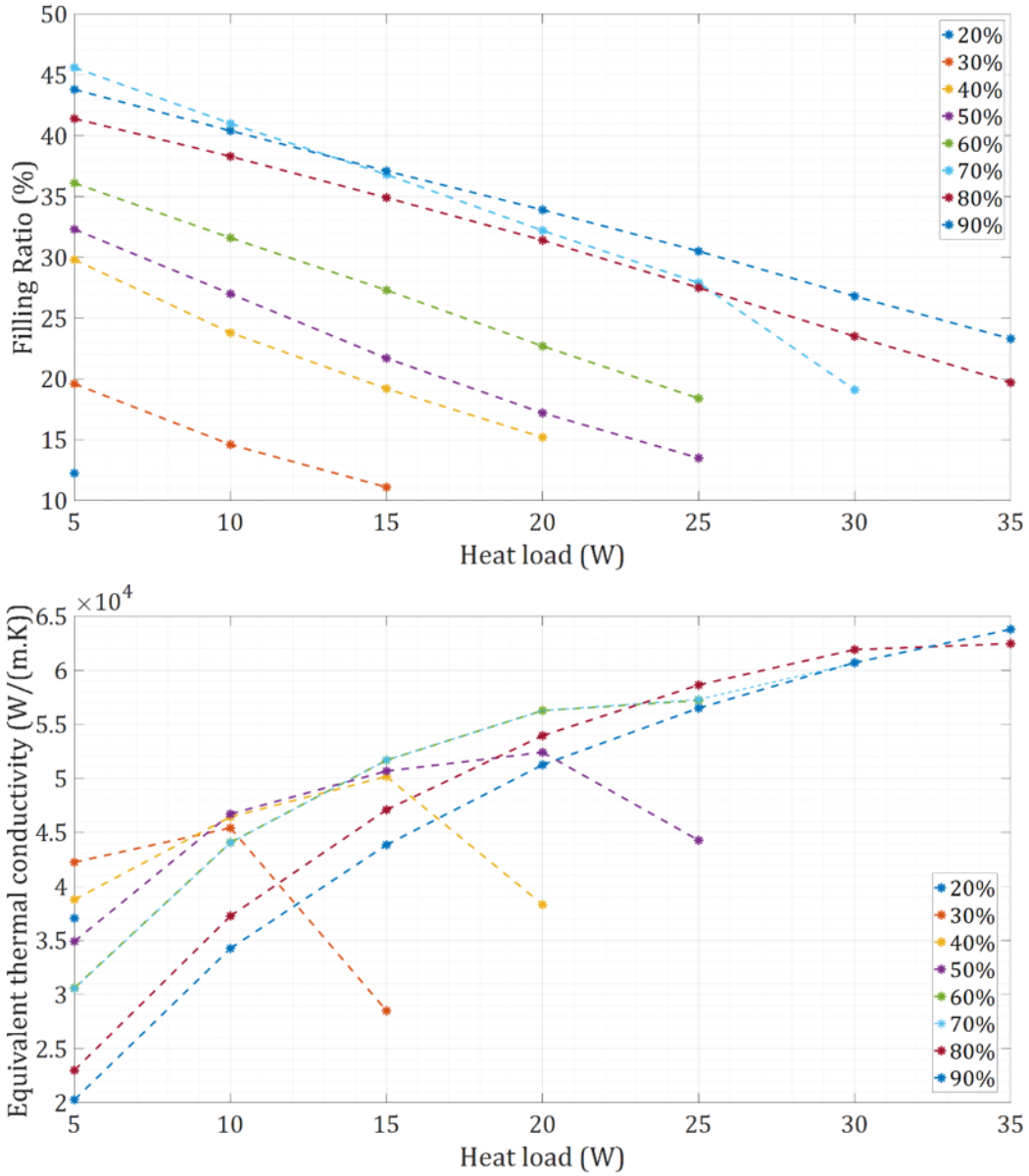

Figure 4.7: Evolution of the equivalent thermal conductivity and liquid filling ratio of progressive heat load tests in the open configuration using neon as working fluid at different initial filling ratios in the open configuration.

5 W. This affects the results of the entire test because when the PHP is closed at 5 W and in stable operating conditions, this filling ratio, at this precise moment, comes from the equilibrium between the buffer volume and the energy given by the 5 W of heat load to the PHP system. Closing the PHP at a different power step would probably give different experimental results, being another parameter to evaluate in future tests. In this case, closing the PHP always at 5 W of heat load, it can be observed that in the closed configuration filling ratios are stable and the highest thermal conductivities are achieved at lower filling ratios.

So, we can then conclude that at a lower heat load, in open or closed configurations,

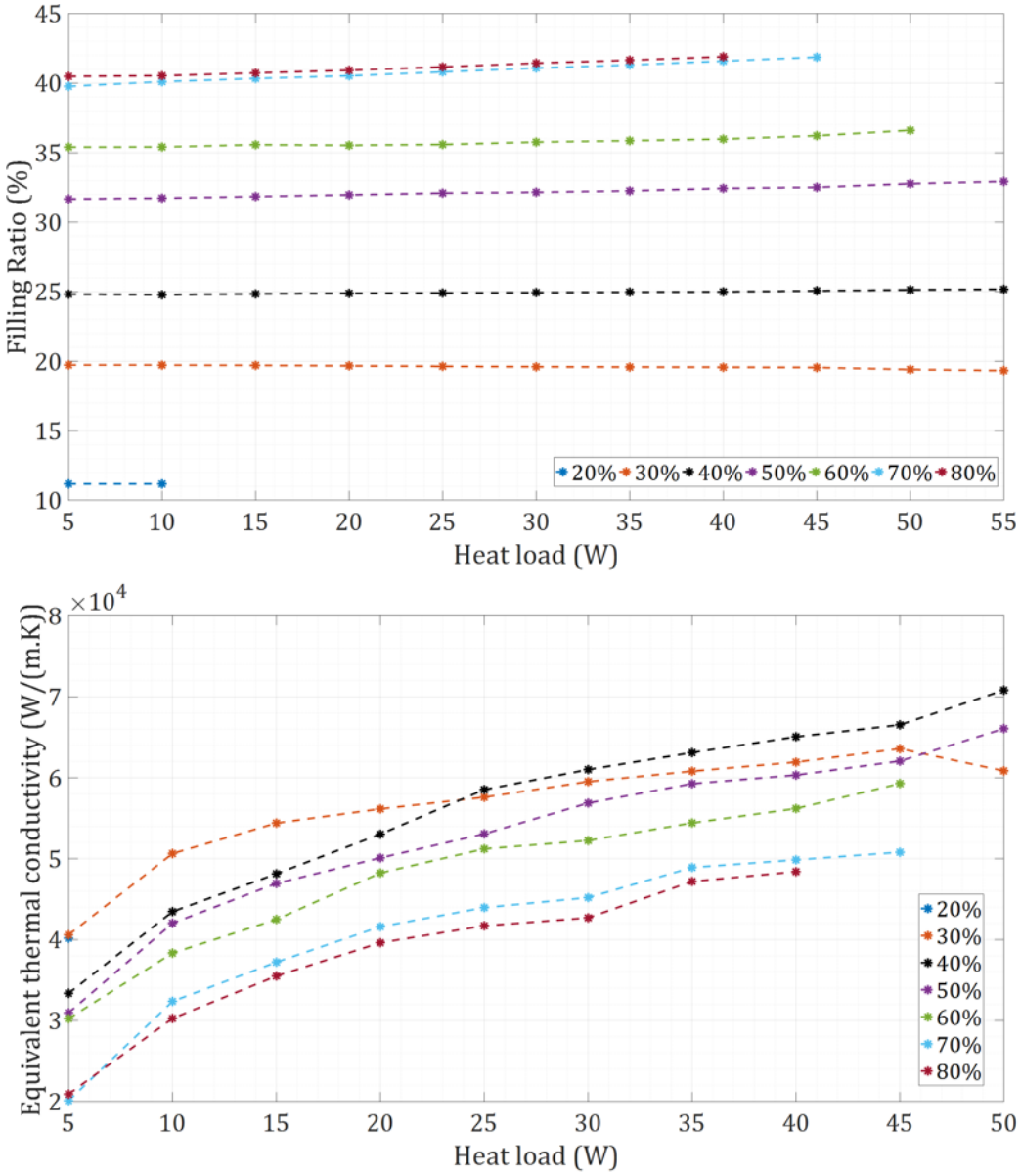

Figure 4.8: Evolution of the equivalent thermal conductivity and liquid filling ratio of progressive heat load tests in the closed configuration using neon as working fluid at different initial filling ratios.

lower filling ratios (around 20 %) are desirable to attain the highest thermal performance. Nevertheless, when increasing the input power, low filling ratios are still desirable in closed configuration but high (initial) filling ratios are desirable in open configuration because the buffer volume reduces the pressure when heat load increases by transfer of fluid, reducing considerably the filling ratio inside the PHP.

In the three cases in closed configuration it can be noticed that the maximum equivalent thermal conductivities are obtained at filling ratios between 20 and 42% (we will call them "optimum filling ratios"), meaning that the PHP attains its maximal performance with less amount of liquid than vapor. More precisely, these optimum filling ratios are

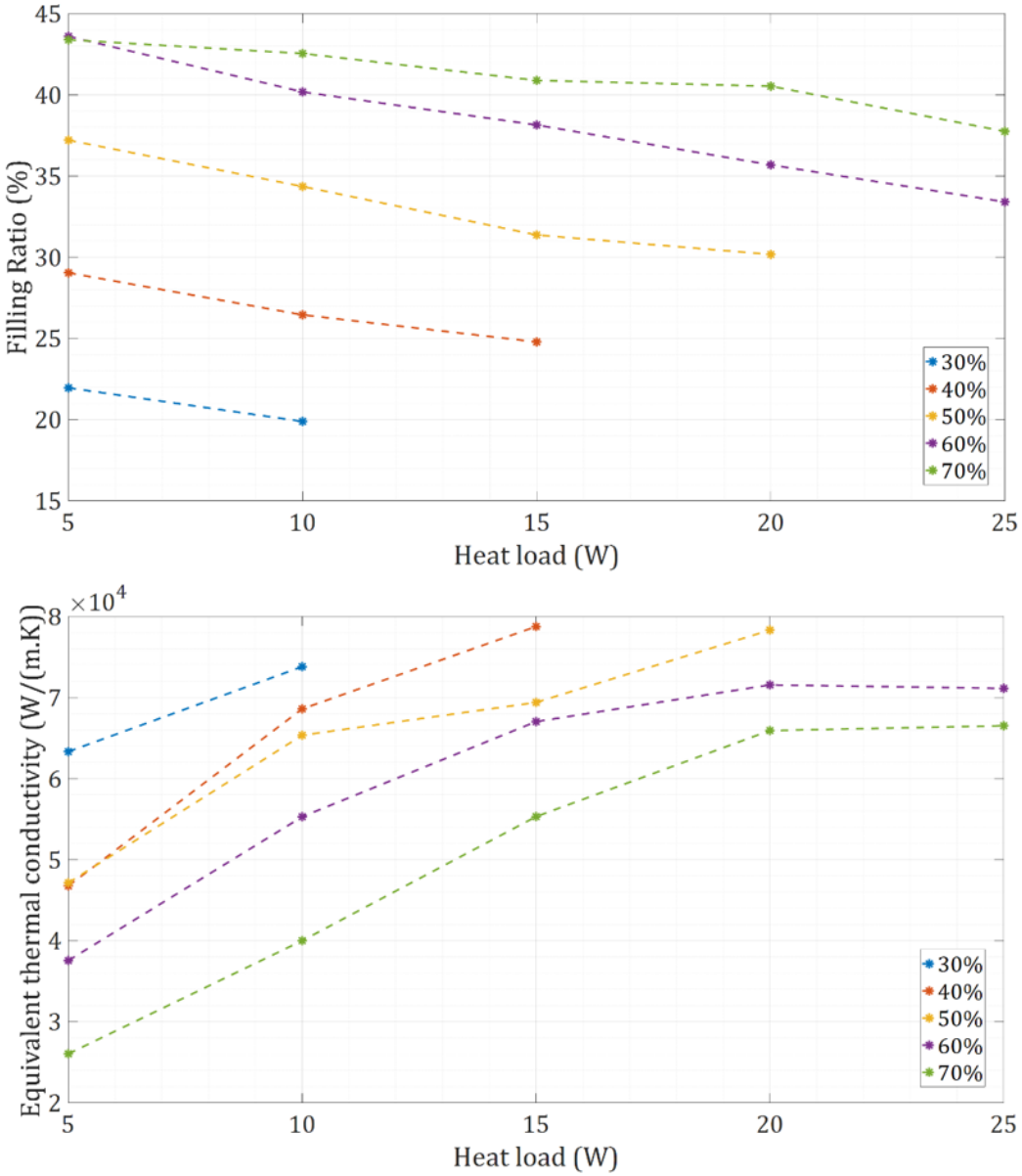

Figure 4.9: Evolution of the equivalent thermal conductivity and liquid filling ratio of progressive heat load tests in the open configuration using argon as working fluid at different initial filling ratios in the open configuration.

between 29 and 42% when using nitrogen, between 22 and 38% when using argon, and between 20 and 25% when using neon. Very similar results in cryogenic PHPs have been found by [9] and [47]. This reveals the importance of the movement of the fluid in the PHP and the oscillations given by the expansion and contractions of the vapor plugs while the liquid parts keep mainly responsible of carrying the heat. Furthermore, at high filling ratios in closed configuration, experimental stable results are not always repeatable when using nitrogen and argon as working fluids. Stop flows, also noticed by [20] in horizontal PHPs, can be observed in Fig. 4.13, revealing that an excessive amount of liquid prevents the stable working operation.

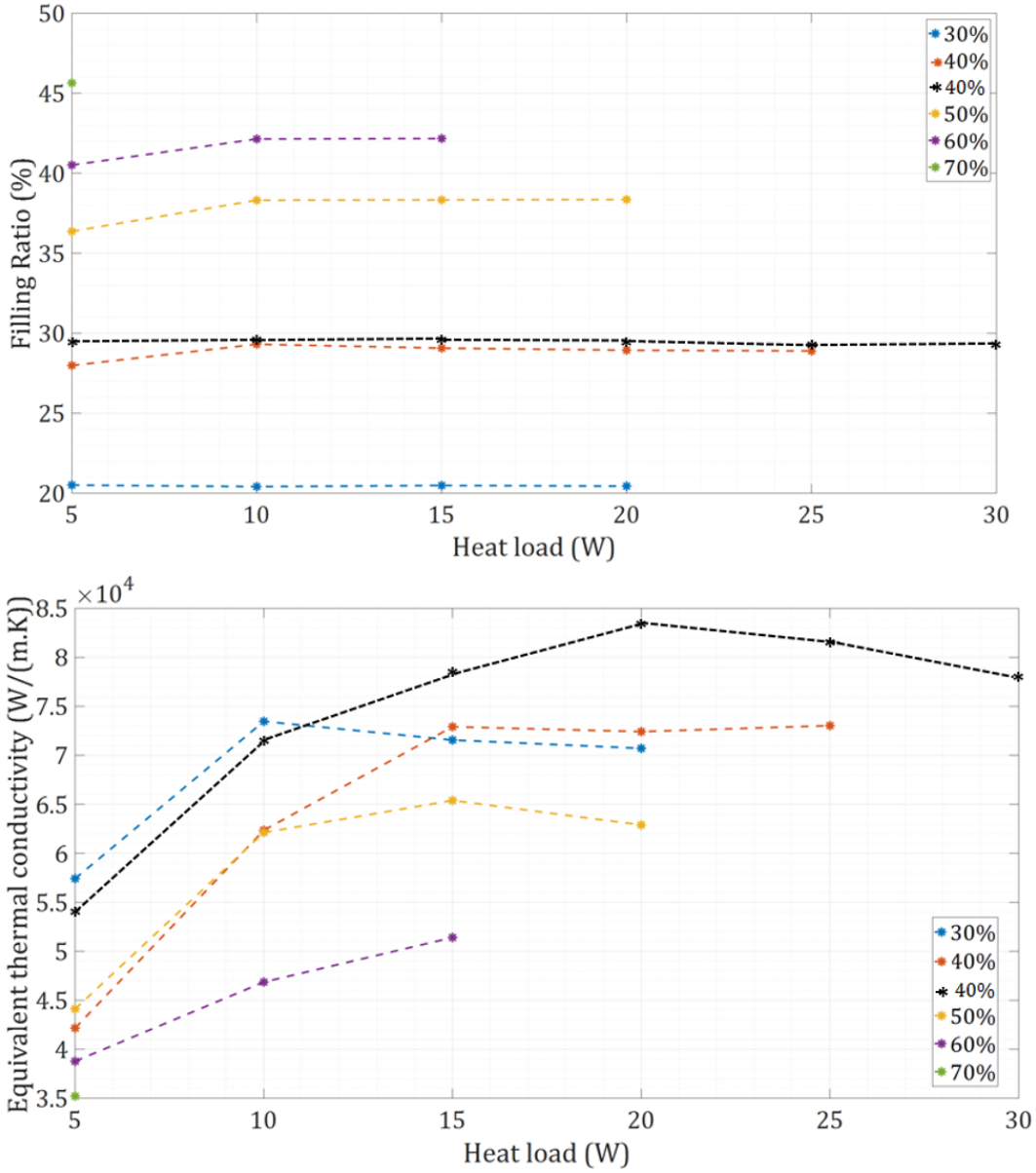

Figure 4.10: Evolution of the equivalent thermal conductivity and liquid filling ratio of progressive heat load tests in the closed configuration using argon as working fluid at different initial filling ratios.

4.3 Differences in fluids' behavior

In the previous sections, several differences in progressive heat load tests using the three different working fluids have been observed and can be summarized as follows:

First of all, it has been observed in the three cases, that the difference between the temperatures of the adiabatic part and the calculated saturation temperature seems to indicate the subcooled state of the liquid parts, as concluded by other authors [31, 62]. Temperature peaks exceeding the saturation temperature (local dry-outs) occur in the central and the external tubes when using nitrogen, only in the central tube when using

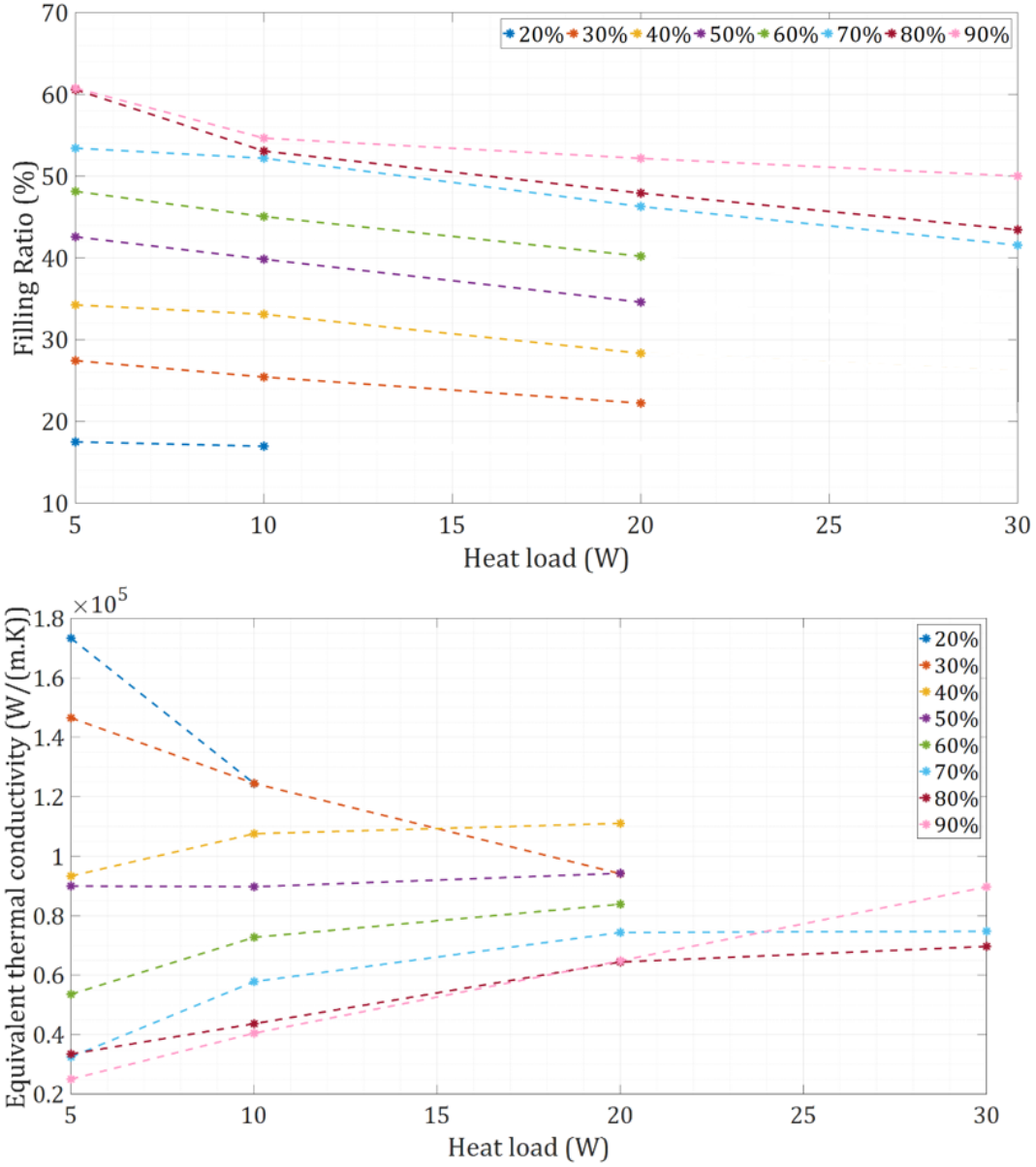

Figure 4.11: Evolution of the equivalent thermal conductivity and liquid filling ratio of progressive heat load tests in the open configuration using nitrogen as working fluid at different initial filling ratios in the open configuration.

neon and no peaks have been measured when using argon as working fluid. With nitrogen, these temperature peaks are more significant and frequent at lower heat load. With neon, the frequency of these temperature peaks increases with the heat load but they are always shorter in duration compared to nitrogen. In addition to that, observing different type of oscillations for each fluid in the adiabatic tubing parts proves the influence of the thermophysical properties of the fluid on the working conditions of the PHP. An example of this is the influence of the PHP inlet in the fluid of the external tube when using nitrogen, which is inexistent with the two other fluids.

Secondly, it has been confirmed that the thermal performance of the same PHP

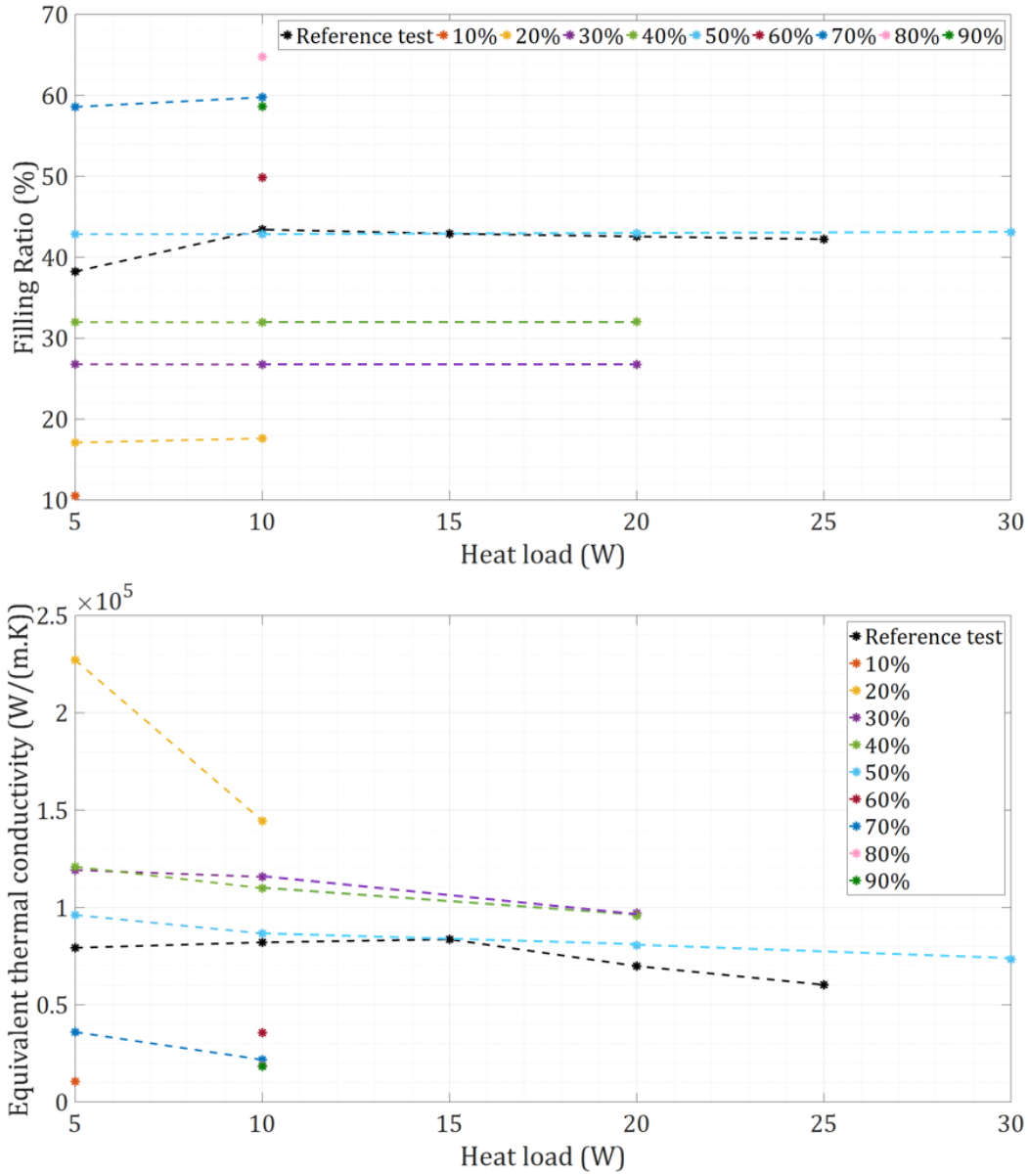

Figure 4.12: Evolution of the equivalent thermal conductivity and liquid filling ratio of progressive heat load tests in the closed configuration using nitrogen as working fluid at different initial filling ratios.

device depends on the fluid tested, as found in the past in cryogenic and ambient temperature pulsating heat pipes [9, 38, 72, 124]. In our study, the highest equivalent thermal conductivities are reached using nitrogen and argon. When using neon, the system is able to transfer a larger power in stable conditions but with considerably lower performance (i.e. higher temperature difference between the evaporator and the condenser at each power step). With nitrogen and argon, a peak of maximum thermal performance is reached at 15 and 20 W, but with neon, the maximum thermal performance was not reached and the cryocooler cold head saturated before that.

Thirdly, it can be observed that when using nitrogen and argon as working fluid, the

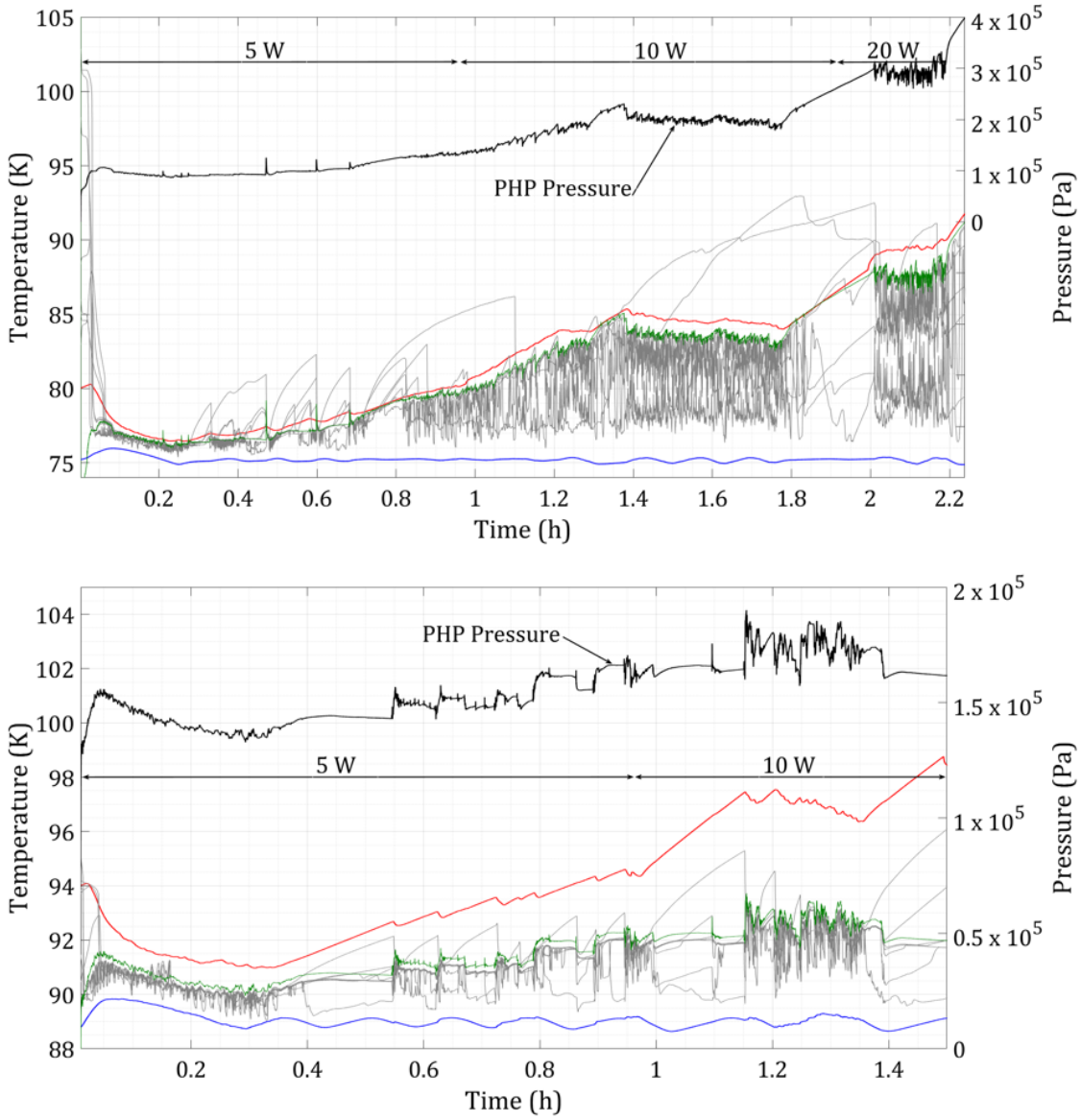

Figure 4.13: Evolution of the PHP pressure (—), the saturation temperature (—), the average temperatures of the evaporator (—) and the condenser (—) and the temperatures of the adiabatic part (—) of a progressive heat load experiment in closed configuration using nitrogen as working fluid with a filling ratio R_{sat} of 66.5% (80% initially). Evolution of the PHP pressure (—), the saturation temperature (—), the average temperatures of the evaporator (—) and the condenser (—) and the temperatures of the adiabatic part (—) of a progressive heat load experiment in closed configuration using argon as working fluid with a filling ratio R_{sat} of 43.8% (60% initially).

dry-out phenomena at the evaporator takes place. In both cases, when the dry-out occurs, the PHP system seems to be divided into two thermal systems. This can be observed with the temperatures distribution of the adiabatic part and the decreasing pressure during that phase. In the case of neon, at 55 W signs of instability appear in the evaporator and condenser parts, but the dry-out phenomena is not initiated.

Comparing the physical properties of the three cryogenic fluids can give us potential

explanations for the different behaviors of the fluids and the performance in the same PHP. The evolution of these physical properties is leaded by the range of working conditions (temperatures and pressure) of each fluid. As mentioned in chapter 1, physical properties are organized by groups depending on their main effect and some of them can even have a dual effect. The surface tension (σ) and the dynamic viscosity (μ_l) of the liquid parts, will be analyzed to understand the ability to flow of each fluid. The specific heat (Cp_l) and the thermal conductivity (λ_l) of the liquid fluid, will be used to analyze the heat transfer. In this way of reasoning, we assumed that the liquid parts are responsible of "carrying" the heat while the movement is leaded by compressions and expansions in the vapor parts and permanent phases changes, as suggested by [72]. In addition, the latent heats of the different fluids (Lv) and the Jacob number (Ja) will be compared to determine the heat transfer between the two phases and the roles of the latent and sensible heats in the overall heat transfer process. Finally, the rates dp/dT at saturation conditions will also be analyzed to determine how important the changes of properties are. The evolutions of the mentioned physical properties have been plotted and are detailed in appendix F (see Fig. F.1, F.2, F.3, F.4, F.5, F.6, F.7, F.8, F.9, and F.10).

Considering the properties related to the movement of the fluid, neon has the lowest surface tension and dynamic viscosity (followed by nitrogen and after, argon), which results in the lowest resistance to the movement (i.e. shear stress) [5, 72, 75]. Regarding the heat transport, on one hand nitrogen has the highest specific heat, followed by neon and argon, but on the other hand nitrogen has the lowest liquid density, followed by neon and argon. If we consider the combination of both properties through the product of $\rho_l \times Cp_l$, neon has the highest result. Respecting the latent heats of the different fluids (Lv), nitrogen has the highest one, followed by argon and neon. On one hand, a lower latent heat makes the fluid easy to boil and to change its phase, and on the other hand, a higher latent heat demands more energy absorbed or released during the phase change [72, 73].

Therefore, it is possible to understand the behavior of the PHP when using neon as working fluid comparing to the two other fluids. Neon is very dynamic and has the lowest flow resistance, due to its low surface tension and dynamic viscosity, its high coefficient $(dp/dT)_{sat}$ contributes to the driving force fluid motion [25, 77] and its low latent heat makes the fluid easy to change its phase. This could explain why neon presents temperature fluctuations with higher frequency, contributing to the global movement of the fluid and making it very dynamic. In addition, its high coefficient $\rho_l \times Cp_l$ leads to a heat transfer by sensible heat and thermal advection through the liquid parts. On the contrary, argon and nitrogen have higher latent heats that indicates that the heat is mainly transferred through phase change processes. Their higher surface tensions and dynamic viscosities make them more difficult to flow and can even sometimes create a stop-flow as it have been seen at high filling ratios in closed configuration in section 4.2. All of this can be confirmed analyzing the Jacob numbers: the lowest values are obtained by argon

and nitrogen, indicating a heat transfer mainly due to the latent heat, while the higher value with neon suggests that it is more transferred by sensible heat. These observations could explain why the optimum filling ratios with neon are lower than for the two other fluids. Firstly, a lower filling ratio means considerable amounts of vapor for expansions and compressions to generate the movement. Secondly, this fluid flow is facilitated by weak properties opposing to the movement (mainly the surface tension (σ) and the dynamic viscosity (μ_l)). At the same time, the heat transfer is ensured by the liquid parts which "carry" important amounts of energy due to its product $\rho_l \times Cp_l$. Also, another important property that gives precious information is the coefficient dp/dT at saturation conditions. Neon has the highest coefficient, meaning that a local temperature difference would generate a considerable local pressure difference, which is related to the driving force fluid motion.

Finally, it has been noticed that the maximum inner diameter when using neon was supposed to be around 1.3 mm, however, the PHP worked with neon in stable conditions with an inner diameter of 1.5 mm in the capillary tubes. The properties of the fluid used for the calculation of this critical diameter have been analyzed (see Fig. G.1, G.2 and G.3 in appendix G). The density difference between the liquid and the vapor phase ($\Delta\rho$), as well as the surface tension (σ), both decrease during the test. The critical diameter decreases also throughout the test. Therefore, only one parameter has not changed: the acceleration of gravity g. From this observation, it can be suggested that, in horizontal pulsating heat pipes, the effect of the acceleration of gravity could be reduced, giving a higher maximum inner diameter in horizontal position, especially if we consider that, as mentioned in chapter 1, the limit of this critical diameter has been obtained from experimental results of vertical capillary tubes. This could be verified by testing the device under zero-gravity conditions or in vertical position.

4.4 Long stability tests

As mentioned in the previous chapter 3, this experimental facility has operated in the past in a different configuration, achieving stable working conditions only for 35 minutes before a spontaneous dry-out, and transferring at maximum 10 W of heat load from the evaporator to the condenser. After doing progressive heat load tests, to be sure the system was able to operate stably for a long duration, we performed long duration tests with the different working fluids at a fixed heat load for each fluid in a closed configuration. The test with nitrogen as working fluid has been performed fixing the heat load at 20 W and a real filling ratio of 36 %. The test with neon has been performed with a fixed heat load of 50 W and a real filling ratio of 26 %, and the test with argon has been performed fixing the heat load at 20 W and a real filling ratio of 26 %. In Fig. 4.14 we have the evolution pressures, saturation temperatures, the average temperatures of the evaporator and the

condenser, and the temperatures of the adiabatic part.

The three tests were stopped only due to the impossibility of surveillance in the laboratory during the night. Because the system was tested for a significant amount of time, we can conclude that the pulsating heat pipe with 36 turns is able to work in stable conditions during long periods, and can be used as a reliable cooling system.

4.5 Conclusions

In this chapter, experimental results of progressive heat load tests performed in the PHP with 36 turns and using neon and argon as working fluid have been analyzed in detail. Different fluid behaviors (including temperature distribution and oscillations) and performances have been observed depending on the working fluid used. These differences have been partly explained by analyzing the evolution of the fluid physical properties. In addition, the evolution of the equivalent thermal conductivities and the filling ratios of numerous progressive heat load tests in open and closed configuration have been studied. The effect of the buffer volume as an autoregulation system has been demonstrated, as well as the important role of the movement of the fluid generated mainly by the vapor parts in the global working conditions of the PHP. Moreover, long stability tests have been performed to demonstrate that the pulsating heat pipe with 36 turns is able to work in stable conditions during long periods and can be used as a reliable cooling system.

In the following chapter, experimental data corresponding to specific working conditions in the PHP will be presented. In this way, the influence of the start-up conditions, the temperature of the condenser and the number of turns will be studied. Experimental results of high heat inputs imitating a quench situation will also be presented.

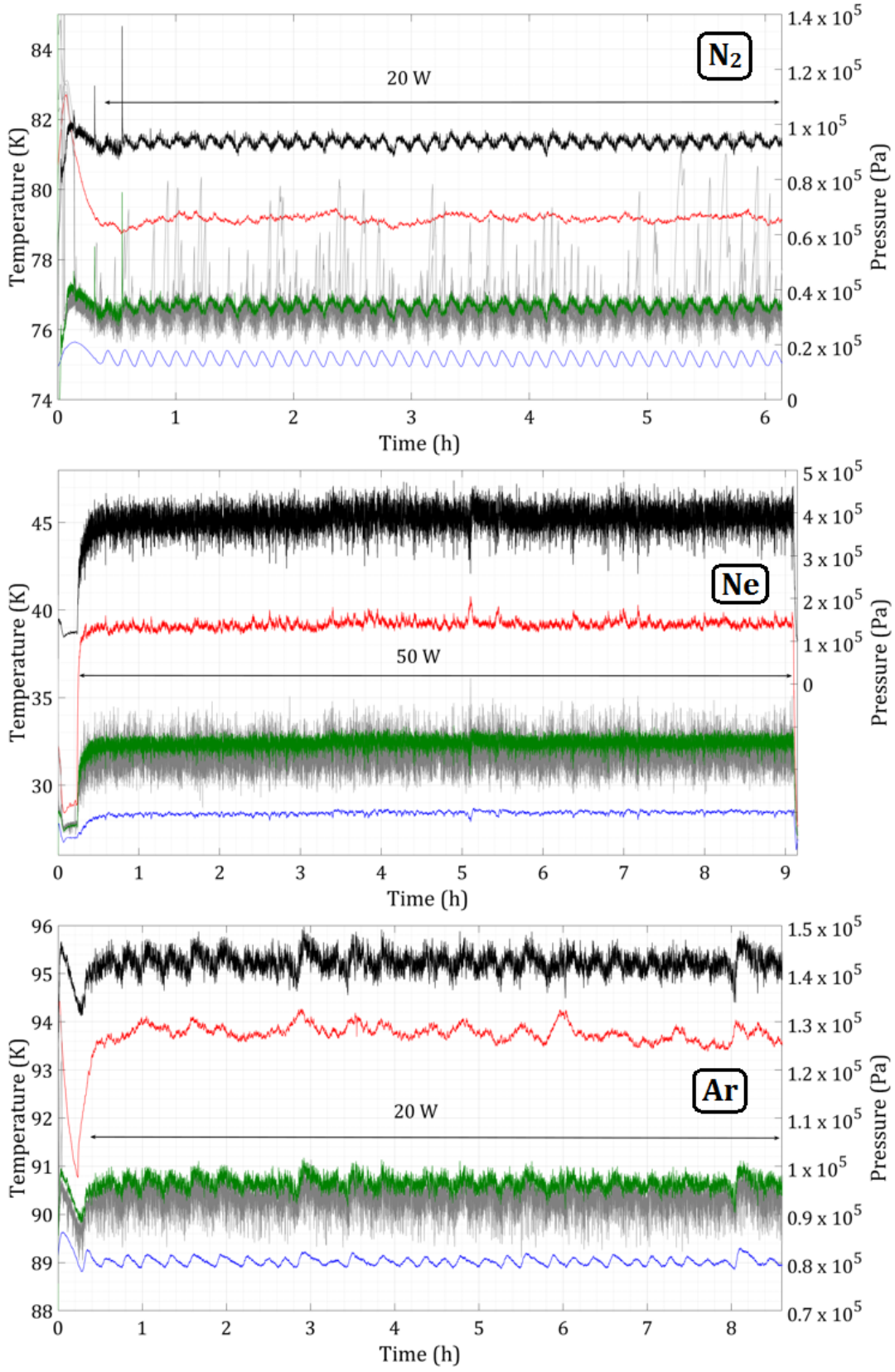

Figure 4.14: Evolution of the PHP pressure (—), the saturation temperature (—), the average temperatures of the evaporator (—) and the condenser (—) and the temperatures of the adiabatic part (—) of fixed heat load experiments in closed configuration using nitrogen, neon and argon as working fluids respectively.

Chapter 5

Specific working conditions and limitations

5.1 Influence of the start-up conditions

Progressive heat load tests described in chapters 3 and 4 are characterized by specific start-up conditions to compensate the absence of gravity assistance. Since the beginning of each test, the temperature controller is fixed to a desired temperature. Then, the evaporator part is heated until a temperature difference of 5 K between the evaporator and the condenser is reached. At this point, the input power of the evaporator is fixed at 5 W and the filling process in the PHP starts. After this phase, if the test takes place in closed configuration, valve V7 is closed when the temperature of the evaporator is stable, isolating the PHP from the buffer volume. If it takes place in open configuration, the PHP is not closed and remains connected to the buffer volume during the entire test.

In order to evaluate their influence in the global performance of the PHP, different start-up conditions have been tested. These tests have been performed in closed configuration to avoid the influence of the buffer volume in the PHP system.

Using nitrogen as working fluid, similar tests to the reference test (closed configuration) have been done imposing different conditions at the beginning of the filling process. A first group of tests have been performed maintaining the same initial filling ratio of 50 % and a heat load of 5 W since the beginning of the test but with different initial temperature differences between the evaporator and the condenser. One test have been done starting with a temperature difference between the evaporator and the condenser of 0 K. Experimental results have demonstrated that thermal performance is lower than in the reference test and, at the beginning of the test at 5 W, the temperature of the evaporator is not stable due to fluid stop phenomena occurring in the PHP that prevent heat from the evaporator to be properly evacuated and increasing its temperature momentarily, as it

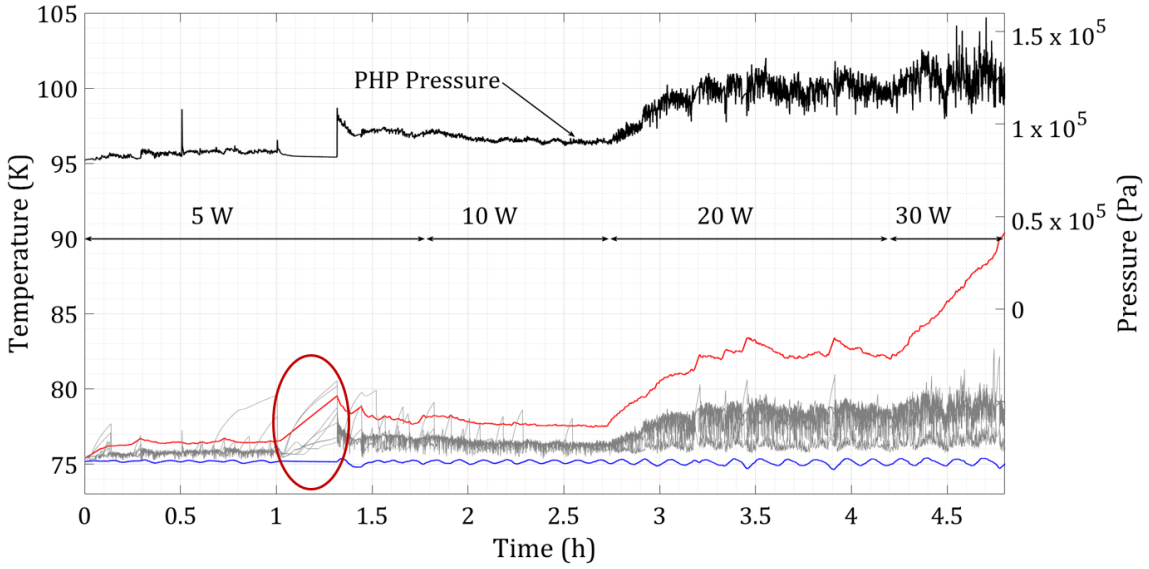

Figure 5.1: Evolution of the PHP pressure (—), the average temperature of the evaporator (—) and the condenser (—) and the temperatures of the adiabatic part (—) of a progressive heat load experiment in closed configuration using nitrogen as working fluid starting with the same temperature in the evaporator and the condenser after the filling process.

can be seen in Fig. 5.1 identified by a red ellipse. This seems to indicate that a minimum initial temperature difference and heat load promotes an appropriate fluid distribution and oscillations in the PHP ensuring a stable temperature at the evaporator part from the beginning of the test. In addition, a second test with an initial temperature difference of 20 K has been performed. Experimental results have shown in this case that there is no difference in terms of thermal performance comparing to the reference test. Apart from that, with a temperature difference of 20 K during the start-up phase, the evaporator took more time (40 minutes) to reach a stable temperature around 76 K, as it can be noticed in Fig. 5.2. This indicates that is not necessary to start a test with such a high temperature difference in the present PHP with 36 turns.

After this first series of initial conditions tests, we decided to fix the temperature difference at the beginning of the test at 5 K and evaluate the initial input power at different filling ratios. Progressive heat load tests with initial filling ratios of 30, 50 and 70 % have been done imposing, during the filling process, input powers at the evaporator of 0, 2 and 5 W. This second group of tests is summarized in the following table 5.1 for nitrogen:

Tests with an initial filling ratio of 30 % presented similar results in the three cases. Real filling ratios were very similar in the three cases, around 28 %, corresponding to the filling ratios giving the highest conductivities in open configuration with nitrogen (see chapter 4). Due to this, thermal performances were very similar and the system worked properly, maintaining a stable temperature at the evaporator in the three cases. Experimental results have been plotted and are detailed in Fig. H.1 in appendix H. In

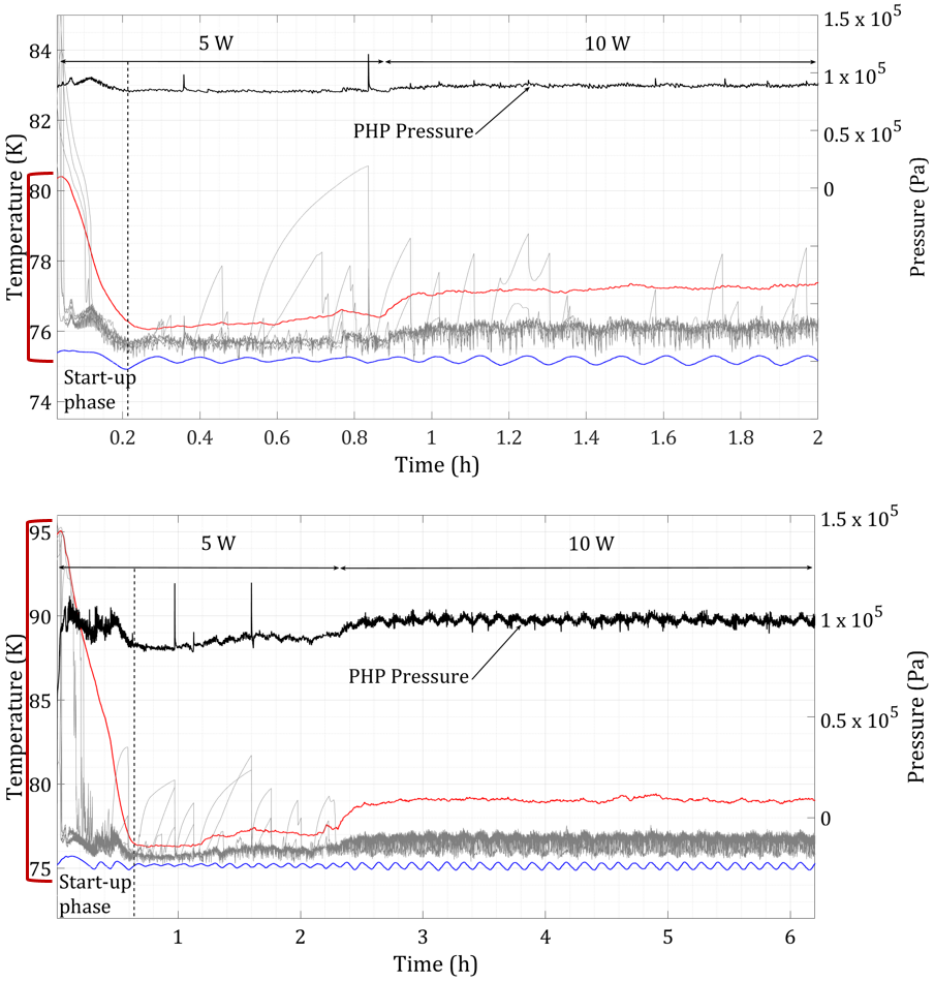

Figure 5.2: Evolution of the PHP pressure (—), the average temperature of the evaporator (—) and the condenser (—) and the temperatures of the adiabatic part (—) of a start-up test in closed configuration using nitrogen as working fluid with different initial temperature difference between the evaporator and the condenser: 5 K and 20 K respectively.

Table 5.1: Start-up variables for nitrogen.

Initial filling ratio (nitrogen)	Input power
30 %	0 W
	2 W
	5 W
50 %	0 W
	2 W
	5 W (reference test)
70 %	0 W
	2 W
	5 W

addition, Fig. 5.3 shows the evolution of the PHP pressure, the average temperatures of the evaporator and the condenser, and the temperatures of the adiabatic part of the three start-up tests with an initial filling ratio of 50%. In this case, it can be identified by a red ellipse on the graph, that start-up conditions have considerable consequences in the PHP behavior. It can be observed that when imposing initial input powers at the evaporator during the start-up phase of 0 and 2 W, fluid stop phenomena occur in the adiabatic part increasing the temperature of the evaporator. This kind of instability tends to disappear when increasing the initial input power, as it can be seen in the test at 5 W, where the temperature of the evaporator remains stable. The working pressures of each case before closing the PHP are 0.8×10^5, 0.815×10^5 and 0.83×10^5 Pa at initial power of 0, 2 and 5 W respectively. This working pressure inside the PHP has a logical consequence in the filling ratio: the real filling ratios (R_{sat}) at 0, 2 and 5 W of initial input power are 48, 45 and 42 % respectively. In fact, higher working pressures prevent more fluid to get inside the PHP (remaining in the buffer volume) during the filling process (or start-up phase) resulting in lower real filling ratios and ensuring more stable results. Furthermore, experimental results of tests performed with an initial filling ratio of 70% (see Fig. H.2 in appendix H) confirms this tendency. After imposing 0 W during the start-up phase, the temperature of the evaporator was completely unstable. It was partially unstable when imposing 2 W during the start-up phase and stable when imposing 5 W during the start-up phase. Working pressures and real filling ratios also followed the same tendency, the lowest real filling ratio was 58% at 5 W and the highest was 61% at 0 W, with temperatures of the adiabatic part and the evaporator very unstable. These experimental results reveal that when the initial filling ratio becomes too important (more than 30%) higher initial input powers create higher working pressures inside the PHP preventing too much fluid to get inside the PHP system. This results in lower real filling ratios and provides higher thermal performances maintaining a stable temperature at the evaporator at each power step.

The same type of start-up tests have been performed using neon as working fluid and are summarized in table 5.2. Fixing a temperature difference between the evaporator and the condenser of 5 K, different initial filling ratios and input powers during the filling process before closing the PHP (start-up phase) have been tested. Experimental results were similar to nitrogen. Also in the case of neon, during tests with an initial filling ratio of 30% the temperature of the evaporator kept stable at each step power without fluid stops occurring at the adiabatic part (see Fig. H.3 in appendix H). In addition, tests with an initial filling ratio of 50% also presented an unstable evaporator's temperature evolution and fluid stop conditions at the adiabatic part after applying 0 and 2 W of input power during the filling process (or start-up phase) (see Fig. H.4 in appendix H). And concerning tests with an initial filling ratio of 70%, after the start-up phase, the evaporator directly dried-out (see Fig. H.5 in appendix H).

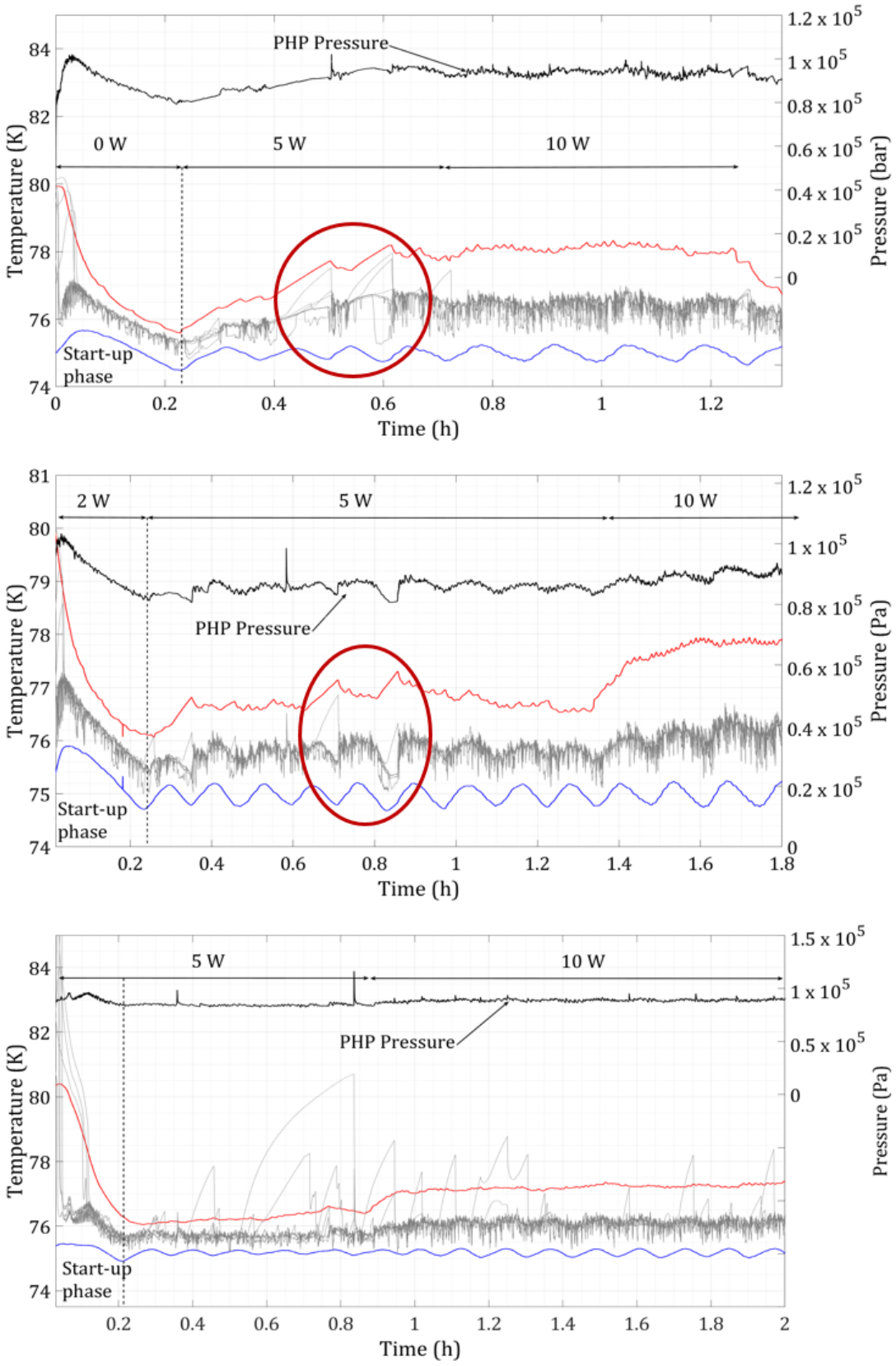

Figure 5.3: Evolution of the PHP pressure (—), the average temperature of the evaporator (—) and the condenser (—) and the temperatures of the adiabatic part (—) of a start-up test in closed configuration using nitrogen as working fluid (initial filling ratio of 50 %) with different initial heat loads during the filling process.

Table 5.2: Start-up variables for neon.

Initial filling ratio (neon)	Input power
30 %	0 W
	2 W
	-
50 %	0 W
	2 W
	5 W
70 %	0 W
	2 W
	-

Start-up tests with an initial temperature difference between the evaporator and the condenser and an initial input power at the evaporator have confirmed that an enthalpy reserve in the evaporator (due to the temperature difference between the evaporator and the condenser) and a constant power as soon as you introduce the fluid are desirable during the filling process, to improve the process itself and contribute to a better distribution of the fluid inside the PHP. Furthermore, the fluids distribution during start-up tests at different input powers an initial filling ratios have shown similar behavior using nitrogen and neon. It has been observed that when the initial filling ratio becomes too important (often more than 30%), higher initial input powers during the filling process (or start-up phase) prevent that too much fluid gets inside the PHP due to higher working pressures in the PHP, giving lower real filling ratios (closer to optimum working conditions) and provides higher thermal performances.

5.2 Influence of the temperature of the condenser

In addition to the start-up conditions, the influence of the temperature of the condenser in the PHP system has also been studied. For this, several tests fixing the condenser at different temperatures have been carried out for a better characterization of the PHP working conditions.

A first group of tests using nitrogen as working fluid in open configuration have been performed. Progressive heat load tests have been done fixing the temperature of the condenser at 75, 80 and 85 K and with initial filling ratios of 20, 50 and 80 %. Experimental results have been summarized in tables 5.3, 5.4 and 5.5. In this tables are indicated the temperature of the condenser during each test, as well as the equivalent thermal conductivity and real filling ratio at each power step.

It is important to notice that during tests with an initial filling ratio of 80 %, temperatures were very unstable in the evaporator at low power steps (mainly 5 and 10 W) as a result of an excessive amount of liquid inside the PHP, as mentioned in the

Table 5.3: Tests in open configuration using nitrogen as working fluid at 20% of initial filling ratio.

	Condenser at 75 K	
Input power (W)	5	10
Equivalent thermal conductivity (kW/(m.K))	100	100
Real filling ratio FR_{sat} (%)	18	17
	Condenser at 80 K	
Input power (W)	5	10
Equivalent thermal conductivity (kW/(m.K))	120	120
Real filling ratio FR_{sat} (%)	13	13
	Condenser at 85 K	
Input power (W)	5	10
Equivalent thermal conductivity (kW/(m.K))	15	22
Real filling ratio FR_{sat} (%)	10	10

Table 5.4: Tests in open configuration using nitrogen as working fluid at 50% of initial filling ratio.

	Condenser at 75 K		
Input power (W)	5	10	20
Equivalent thermal conductivity (kW/(m.K))	70	90	100
Real filling ratio FR_{sat} (%)	40	35	33
	Condenser at 80 K		
Input Power (W)	5	10	20
Equivalent thermal conductivity (kW/(m.K))	70	100	100
Real filling ratio FR_{sat} (%)	35	33	25
	Condenser at 85 K		
Input power (W)	5	10	20
Equivalent thermal conductivity (kW/(m.K))	70	100	Dry-out
Real filling ratio FR_{sat} (%)	30	29	Dry-out

Table 5.5: Tests in open configuration using nitrogen as working fluid at 80% of initial filling ratio.

	Condenser at 75 K			
Input power (W)	5	10	20	30
Equivalent thermal conductivity (kW/(m.K))	35	45	68	73
Real filling ratio FR_{sat} (%)	65	55	49	45
	Condenser at 80 K			
Input power (W)	5	10	20	30
Equivalent thermal conductivity (kW/(m.K))	40	50	80	Dry-out
Real filling ratio FR_{sat} (%)	50	45	41	Dry-out
	Condenser at 85 K			
Input power (W)	5	10	20	30
Equivalent thermal conductivity (kW/(m.K))	40	70	90	Dry-out
Real filling ratio FR_{sat} (%)	42	39	35	Dry-out

Table 5.6: Tests in closed configuration using nitrogen as working fluid at 20% of initial filling ratio.

	Condenser at 75 K	
Input power (W)	5	10
Equivalent thermal conductivity (kW/(m.K))	130	125
Real filling ratio FR_{sat} (average) (%)	18.25	
	Condenser at 80 K	
Input power (W)	5	10
Equivalent thermal conductivity (kW/(m.K))	unstable	unstable
Real filling ratio FR_{sat} (average) (%)	14.5	
	Condenser at 85 K	
Input power (W)	5	10
Equivalent thermal conductivity (kW/(m.K))	unstable	unstable
Real filling ratio FR_{sat} (average) (%)	11.6	

previous chapter 4. The average values of the equivalent thermal conductivity and the real filling ratio have been calculated and included in table 5.5.

Analyzing data from tables, it can be noticed that the highest equivalent thermal conductivities are achieved when real filling ratios are closer to the optimum values (between 20 and 40 %) defined in chapter 4. These maximum conductivities are attained with the condenser at 85 K and initial filling ratios of 50 and 80 % and with the condenser at 75 K with and an initial filling ratio of 20 %. This could be interpreted as follows: the temperature of the condenser determines the range of working temperatures and pressures inside the PHP, in this way, a higher temperature at the condenser will originate higher working pressures that, as it has been seen in the previous section 5.1, will affect the real filling ratio during the filling process and the rest of the test. In this case, experimental results are highly conditioned by the range of working temperatures and the real filling ratios. In the same way, when the filling ratio is too low, the evaporator dries-out at very low power steps, as it can been noticed with tests having an initial filling ratio of 20 % in table 5.3.

A second group of tests using nitrogen as working fluid but this time in closed configuration have also been performed. Progressive heat load tests have been done fixing the temperature of the condenser at 75, 80 and 85 K and with initial filling ratios of 20, 50 and 80 %. In this case, experimental results with an initial filling ratio of 80 % were too unstable to compare the thermal performances and conclude, probably due to an excessive amount of fluid inside the PHP system, as mentioned in chapter 4. Experimental results with initial filling ratios of 20 and 50 % have been summarized in tables 5.6 and 5.7. In this tables are indicated the temperature of the condenser during each test, as well as the equivalent thermal conductivity and real filling ratio at each power step.

It can be noticed that real filling ratios in the tests with an initial filling ratio of 20 % were too low to make the PHP work. These real filling ratios were 18.25, 14.5 and

Table 5.7: Tests in closed configuration using nitrogen as working fluid at 50% of initial filling ratio.

	Condenser at 75 K			
Input power (W)	5	10	20	30
Equivalent thermal conductivity (kW/(m.K))	75	80	80	79
Real filling ratio FR_{sat} (average) (%)	42.25			
	Condenser at 80 K			
Input power (W)	5	10	20	30
Equivalent thermal conductivity (kW/(m.K))	75	90	87	Dry-out
Real filling ratio FR_{sat} (average) (%)	39			Dry-out
	Condenser at 85 K			
Input power (W)	5	10	20	30
Equivalent thermal conductivity (kW/(m.K))	78	87	90	Dry-out
Real filling ratio FR_{sat} (average) (%)	30.4			Dry-out

11,6 % with the condenser at 75, 80 and 85 K respectively. The test with the condenser at 75 K and a real filling ratio of 18.25 % was the only one able to work at 5 and 10 W of heat load. In addition to that, tests with an initial filling ratio of 80 % achieved real filling ratios of 66, 56 and 50 % with the condenser at 75, 80 and 85 K respectively, but in the three tests the temperature of the evaporator never reached a stable value, as mentioned before. At this point, mostly tests with an initial filling ratio of 50 % were taken into consideration for the analysis. From these experimental data, we can noticed that, as in closed configuration, the maximum conductivities are attained with the condenser at 85 K and a real filling ratio of 30.4 %, followed by the condenser at 80 K and a real filling ratio of 39 % and the condenser at 75 K and a real filling ratio of 42.25 %. This confirms once again that the temperature of the condenser determines the range of working temperatures and pressures inside the PHP. A higher temperature at the condenser will originate higher working pressures achieving in this case the lowest real filling ratio (close to optimum working conditions) during the filling process before closing the PHP. Complementary to that, it is important to note that even if the maximum conductivities are achieved with the lowest filling ratio at 85 K in the condenser, the PHP system is able to work up to 30 W when the condenser is at 75 K and this is due to a higher real filling ratio of 42.25 %.

In order to verify this trends in the behavior of the PHP at different condenser's temperatures, another group of tests using neon as working fluid in closed configuration have been performed. Progressive heat load tests have been done fixing the temperature of the condenser at 27, 30 and 32 K and with initial filling ratios of 30, 50 and 80 %. Experimental results have been summarized in tables 5.8, 5.9 and 5.10. In this tables are indicated the temperature of the condenser during each test, as well as the equivalent thermal conductivity and real filling ratio at each power step.

Experimental data from tests using neon as working fluid reveal similar global behavior of the PHP at different condenser's temperatures. Tests with an initial filling ratio

Table 5.8: Tests in closed configuration using neon as working fluid at 30% of initial filling ratio.

	Condenser at 27 K	
Input power (W)	from 5 to 50	
Equivalent thermal conductivity (kW/(m.K))	from 47 to 66	
Real filling ratio FR_{sat} (average) (%)	19.75	
	Condenser at 30 K	
Input power (W)	5	10
Equivalent thermal conductivity (kW/(m.K))	40	Dry-out
Real filling ratio FR_{sat} (average) (%)	12.5	
	Condenser at 32 K	
Input power (W)	not tested	
Equivalent thermal conductivity (kW/(m.K))	not tested	
Real filling ratio FR_{sat} (average) (%)	not tested	

Table 5.9: Tests in closed configuration using neon as working fluid at 50% of initial filling ratio.

	Condenser at 27 K
Input power (W)	from 5 to 50
Equivalent thermal conductivity (kW/(m.K))	from 34 to 65
Real filling ratio FR_{sat} (average) (%)	32.5
	Condenser at 30 K
Input power (W)	from 5 to 45
Equivalent thermal conductivity (kW/(m.K))	from 38 to 69
Real filling ratio FR_{sat} (average) (%)	26.4
	Condenser at 32 K
Input power (W)	unstable
Equivalent thermal conductivity (kW/(m.K))	unstable
Real filling ratio FR_{sat} (average) (%)	18

Table 5.10: Tests in closed configuration using neon as working fluid at 80% of initial filling ratio.

	Condenser at 27 K
Input power (W)	from 5 to 40
Equivalent thermal conductivity (kW/(m.K))	from 20 to 49
Real filling ratio FR_{sat} (average) (%)	41.25
	Condenser at 30 K
Input power (W)	from 5 to 40
Equivalent thermal conductivity (kW/(m.K))	from 30 to 62
Real filling ratio FR_{sat} (average) (%)	35.5
	Condenser at 32 K
Input power (W)	from 5 to 30
Equivalent thermal conductivity (kW/(m.K))	from 38 to 62
Real filling ratio FR_{sat} (average) (%)	26.75

of 30 % obtained the best results in terms of thermal performance (or equivalent thermal conductivity) when the temperature of the condenser was fixed at 27 K, because lower working pressures gave a higher filling ratio of 19.75 %, enough to be able to work and transfer the heat in a PHP mode. At a higher temperature at the condenser (30 K), the real filling ratio was too low to make the PHP to work. For the same reason, the system was not even tested at 32 K at the condenser. With an initial filling ratio of 50 %, the highest thermal conductivities were attained with the condenser fixed at 30 K, achieving a real filling ratio of 26.4 %, closer to optimum conditions on closed configuration with neon (around 20-25 %, see chapter 4). At 27 K at the condenser, the real filling ratio was higher (32.5 %) and the thermal performance lower and, at 32 K at the condenser the real filling ratio was too low (18 %) and the PHP never reached a stable value at the evaporator during the test. As mentioned in the previous chapter 4, neon is more dynamic but also "reactive" due to its rate dp/dT at saturation conditions. In addition, the slope of the $(dp/dT)_{sat}$ curve is more steep and changes in the range of working temperatures leads to higher ranges of working pressures. Thus, differences between initial and real filling ratios are more important. Due to this, going from 30 to 32 at the condenser, we achieve a real filling ratio of 26.4 in one case and 18 in the other case. In the first case the PHP system worked properly while in the second case the PHP system was completely unstable at the evaporator. In experimental results with an initial filling ratio of 80 %, we can find that the best conductivity is achieved with the condenser at 32 K, where the real filling ratio is the lowest one (26.75 %) and the closest one to optimum working conditions.

We can then conclude that, using neon or nitrogen as working fluid, we can find globally the same trends in the behavior of the PHP testing different temperatures at the condenser. It is remarkable that with neon differences between real filling ratios in tests starting with the same initial filling ratio but different temperatures at the condenser are more important than for nitrogen, because of higher differences in the working pressures at each temperature increase. Due to higher rate dp/dT at saturation conditions. In any case, we can conclude that the temperature of the condenser determines the range of working temperatures and pressures inside the PHP. In this way, a higher temperature at the condenser originates higher working pressures in the PHP that affects the real filling ratio during the filling process and, consequently, during the rest of the test, influencing the global thermal performances.

5.3 Effect of the number of turns

As mentioned in chapter 2, the experimental facility of the present research project is composed of three horizontal pulsating heat pipes that differ in the number of parallel capillary tubes (or U-turns). One PHP has 36 turns, where the majority of tests have been performed. The second PHP has 24 turns and the third one has 12 turns.

At the beginning of the project, the three PHPs have been tested to determine the limits of each device. After analyzing the first experimental results and to notice that the PHP having 36 turns gives from far the best thermal performances and stable results, it has been decided to test the different fluids and specific working conditions in this PHP. Nevertheless, it is interesting to present and compare experimental results of the two other PHPs in order to determine the influence of the number of parallel turns in a one meter long horizontal PHPs.

Several tests have been performed in the PHP with 24 turns using nitrogen as working fluid. Since the beginning of the series of tests, it has been more difficult to attain a stable temperature at the evaporator in operating conditions. No test worked in a PHP mode in closed configuration, where the evaporator dried-out since the beginning of each test. In open configuration it was either impossible to reach a stable temperature at the evaporator imposing standard start-up conditions, with a temperature difference of 5 K between the evaporator and the condenser and an input power of 5 W at the evaporator during the filling process. The only way to attain a certain stability at the evaporator was to start with a temperature difference of 20 K and an input power of 5 W at the evaporator since the beginning of the test. It is necessary a higher temperature difference between both ends (the evaporator and the condenser), which implies a higher pressure difference during the filling process when testing the PHP having 24 turns. With a higher number of U-turns (36), small pressure drops when the fluid flows through each turn could contribute to the global pressure oscillations helping in the filling process, as suggested by [17]. Due to this, with the PHP having 36 turns, the initial temperature difference to start oscillations is lower than with the PHP having 24 turns.

Since start-up conditions have been defined for the PHP having 24 turns, progressive heat load tests with different initial filling ratios in open configuration have been performed in order to determine the maximum heat transfer capacity of this PHP. It appears that maximum heat load transferred in stable conditions with this PHP is 7.5 W. Fig. 5.4 shows the evolution of the PHP pressure, the corresponding saturation temperature, the average temperatures of the evaporator and the condenser, and the temperatures of the adiabatic part of a fixed heat load test of 7.5 W using nitrogen as working fluid. In this test, the filling ratio is initially calculated to be at 70 % and the test was performed in open configuration. This time, at the beginning of the test the evaporator is heated from 75 K to 95 K while the temperature of the condenser is maintained at 75 K. It can be observed in Fig. 5.4 that during the entire test the temperature difference between the evaporator and the condenser stays relatively high (around 19 K), and pressure peaks are more frequent and important than the same type of test with nitrogen in the PHP with 36 turns. In addition, fluid stops can be clearly distinguished and are considerable frequent comparing to the PHP with 36 turns, where the higher number of turns could contribute to internal flow perturbations reducing the probability of fluid stops, as suggested by [85].

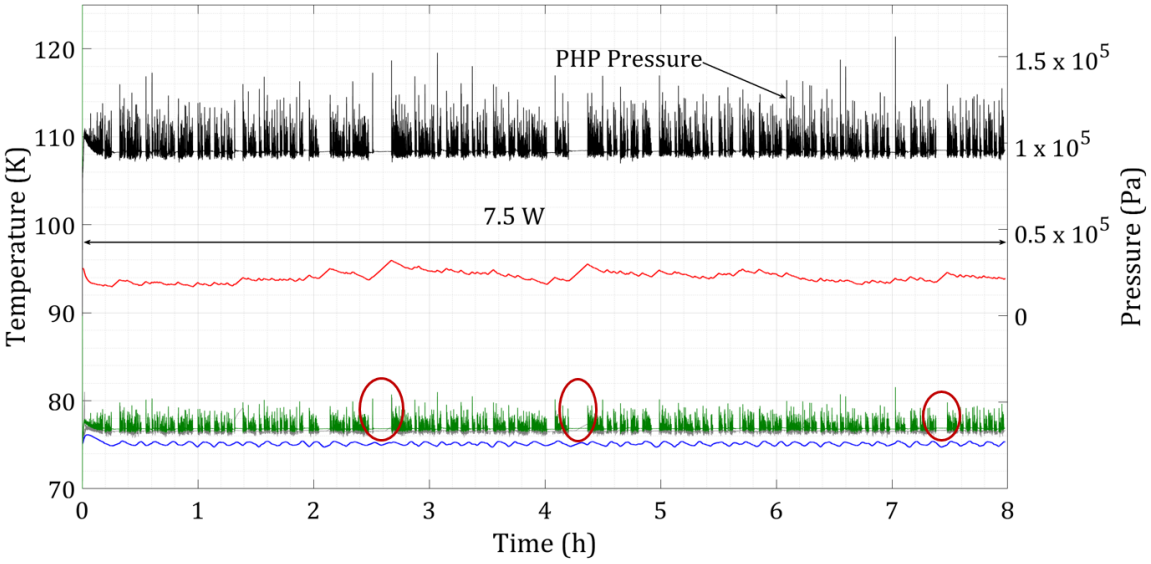

Figure 5.4: Evolution of the PHP pressure (—), the saturation temperature (—), the average temperature of the evaporator (—) and the condenser (—) and the temperatures of the adiabatic part (—) of a fixed heat load experiment in open configuration using nitrogen as working fluid in the PHP with 24 turns.

During this test, the equivalent thermal conductivity achieved is 9.2 kW/(m.K) and the calculated real filling ratio in saturation conditions (FR_{sat}) is 45.5 % on average. For comparison, a similar test in the PHP with 36 turns in open configuration and starting with a temperature difference of 5 K, an input power of 5 W and an initial filling ratio of 70 % too, attains an equivalent thermal conductivity of 29 kW/(m.K) at 5 W and 54 % of real filling ratio, and 56 kW/(m.K) at 10 W and 53 % of real filling ratio, with temperature differences in operating conditions between the evaporator and the condenser only of 2.6 and 2.8 K, respectively. Thus, it can globally be noticed that the PHP with 24 turns exhibits a lower thermal performance and heat transfer capacity, and these differences are not proportional to the number of turns.

Tests at different condenser's temperatures have also been performed in the PHP with 24 turns in open configuration, using nitrogen as working fluid and fixing the input power at the maximum heat capacity of the PHP: 7.5 W. These tests have been done fixing the temperature of the condenser at 75, 80 and 85 K and with an initial filling ratio of 50 %. Experimental results have been summarized in table 5.11, where the temperature of the condenser, as well as the equivalent thermal conductivity and real filling ratio are indicated. Also in this case, higher temperatures at the condenser generate higher working pressures and lower real filling ratios. In this case, the test performed with the condenser at 80 K gives the highest equivalent thermal conductivity with an real filling ratio of 34 %.

The PHP with 24 turns has also been tested using neon as working fluid in open configuration and the maximum heat capacity of the PHP appears to be also 7.5 W, maintaining a stable temperature at the evaporator. Fig. 5.5 shows the evolution of the

Table 5.11: Tests in open configuration in the PHP with 24 turns using nitrogen as working fluid at 50% of initial filling ratio.

	Condenser at 75 K
Input power (W)	7.5
Equivalent thermal conductivity (kW/(m.K))	8.9
Real filling ratio FR_{sat} (%)	38
	Condenser at 80 K
Input power (W)	7.5
Equivalent thermal conductivity (kW/(m.K))	9
Real filling ratio FR_{sat} (%)	34
	Condenser at 85 K
Input power (W)	7.5
Equivalent thermal conductivity (kW/(m.K))	8.2
Real filling ratio FR_{sat} (%)	29

PHP pressure, the corresponding saturation temperature, the average temperatures of the evaporator and the condenser, and the temperatures of the adiabatic part of a fixed heat load test of 7.5 W using neon as working fluid. In this test, the filling ratio is initially calculated to be at 50 %. At the beginning of the test the evaporator is heated from 27 K to 32 K while the temperature of the condenser is maintained at 27 K using the temperature controller. This time, the temperature difference between the evaporator and the condenser was 5 K and the initial input power during the filling process was 5 W. Comparing with the previous test performed with nitrogen in the same PHP, the temperature of the evaporator is less stable, furthermore, temperature peaks at the adiabatic part exceeding the saturation temperature appear and, no fluid stop seems to take place. These differences confirms once again differences in the PHP behavior associate to the working fluid. We can see again characteristics of a very dynamic fluid, easy to flow but that suffers important thermodynamic changes at each temperature variation.

The same test has also been performed with the condenser fixed at 30 and 32 K, as indicated in table 5.12. In the first case, the PHP worked stably at 5 W of heat load but dried-out at 7.5 W. In the second case, the PHP never reached a stable value at the evaporator. Comparing results between the test with the condenser at 27 K and the test with the condenser at 30 K, it can be noticed again the relation between the working temperatures and pressures and the real filling ratio. In this case, the highest thermal performance (22 kW/(m.K)) was achieved with the condenser at 27 K and a real filling ratio of 24 %.

As mentioned at the beginning of this section, the PHP having 12 parallel capillary tubes (or U-turns) has also been tested. This latter was able to transfer a maximum of 2 W and 5 W of heat load using respectively nitrogen and neon as working fluids. Nevertheless, it is important to remark that stable conditions at the evaporator were achieved during tests with a very specific start-up conditions, revealing the fragile stability of the PHP

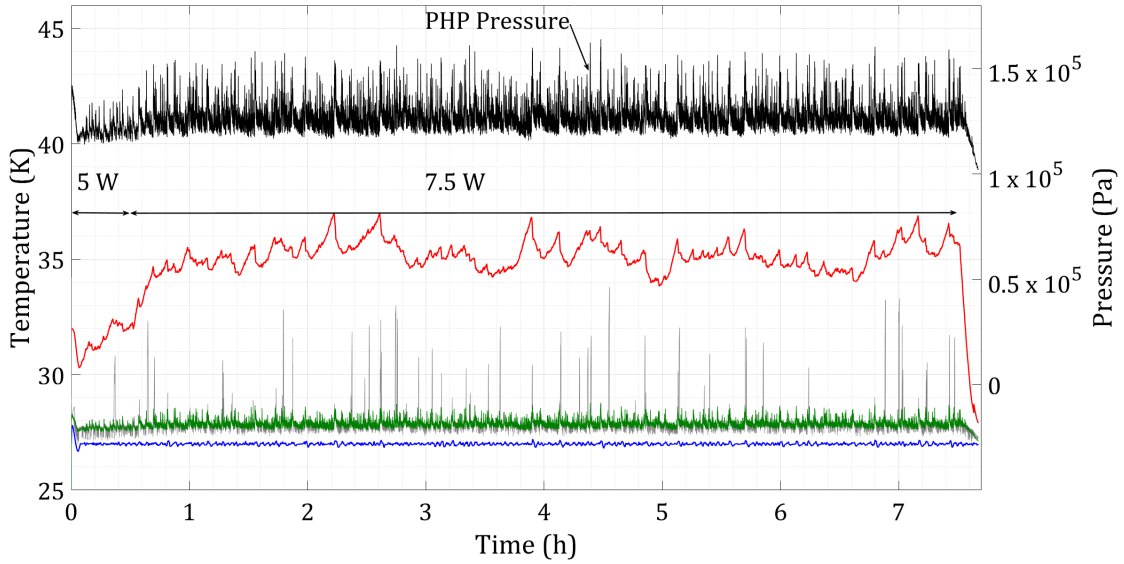

Figure 5.5: Evolution of the PHP pressure (—), the saturation temperature (—), the average temperature of the evaporator (—) and the condenser (—) and the temperatures of the adiabatic part (—) of a fixed heat load experiment in open configuration using neon as working fluid in the PHP with 24 turns.

Table 5.12: Tests in open configuration in the PHP with 24 turns using neon as working fluid at 50% of initial filling ratio.

	Condenser at 27 K	
Input power (W)	5	7.5
Equivalent thermal conductivity (kW/(m.K))	17.5	Dry-out
Real filling ratio FR_{sat} (%)	20	Dry-out
	Condenser at 30 K	
Input power (W)	5	7.5
Equivalent thermal conductivity (kW/(m.K))	25	22
Real filling ratio FR_{sat} (%)	26	24
	Condenser at 32 K	
Input power (W)	unstable	unstable
Equivalent thermal conductivity (kW/(m.K))	unstable	unstable
Real filling ratio FR_{sat} (%)	unstable	unstable

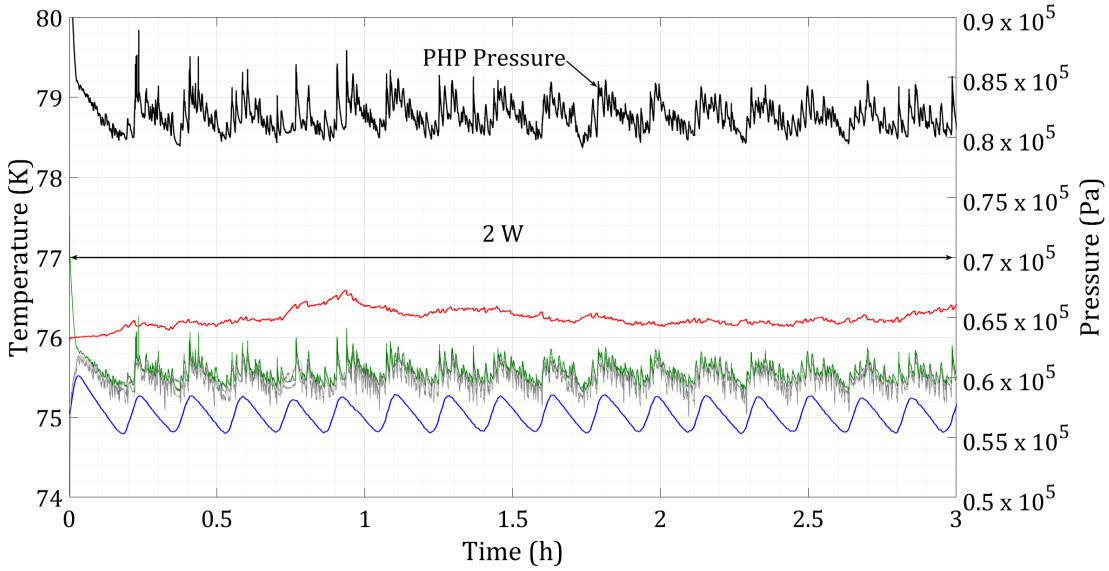

Figure 5.6: Evolution of the PHP pressure (—), the saturation temperature (—), the average temperature of the evaporator (—) and the condenser (—) and the temperatures of the adiabatic part (—) of a fixed heat load experiment in open configuration using nitrogen as working fluid in the PHP with 12 turns.

comparing to the two other PHPs. The PHP has also been tested at different temperatures at the condenser with nitrogen in open configuration. Experimental results are plotted in Fig. 5.6, Fig. 5.7 and table 5.13. Fig. 5.6 shows the evolution of the PHP pressure, the corresponding saturation temperature, the average temperatures of the evaporator and the condenser, and the temperatures of the adiabatic part of a fixed heat load test of 2 W using nitrogen as working fluid. In this test, the filling ratio is initially calculated to be at 50 %. The temperature difference between the evaporator and the condenser is 1 K, the initial input power during the filling process is 2 W and the condenser is fixed at 75 K. The calculated real filling ratio (R_{sat}) is 41 %. Fig. 5.7 shows the evolution of the PHP pressure, the corresponding saturation temperature, the average temperatures of the evaporator and the condenser, and the temperatures of the adiabatic part of a progressive heat load test using neon as working fluid. In this test, the initial filling ratio is 100 %. The calculated real filling ratio (R_{sat}) goes from 37 to 24 %. The temperature difference between the evaporator and the condenser is 5 K, the initial input power during the filling process is 2.5 W and the condenser is fixed at 27 K. Globally, experimental results present the same trends in the fluid behavior that we have been describing in this section. Nevertheless, these results should be treated with great caution especially considering that parasite heat inputs arriving into the PHP have been estimated to be 1.015 W (see chapter 2). Even if not all of these parasite heat inputs go necessarily on the PHP with 12 turns, it represents a considerable part of the heat capacity of the PHP, being not possible to determine with accuracy its real maximum heat capacity.

In this section, experimental results of tests performed in the two other PHPs com-

Table 5.13: Tests in open configuration in the PHP with 12 turns using neon as working fluid at 50% of initial filling ratio.

	Condenser at 75 K
Input power (W)	2
Equivalent thermal conductivity (kW/(m.K))	80
Real filling ratio FR_{sat} (%)	41
	Condenser at 80 K
Input power (W)	2
Equivalent thermal conductivity (kW/(m.K))	120
Real filling ratio FR_{sat} (%)	37
	Condenser at 85 K
Input power (W)	2
Equivalent thermal conductivity (kW/(m.K))	140
Real filling ratio FR_{sat} (%)	24

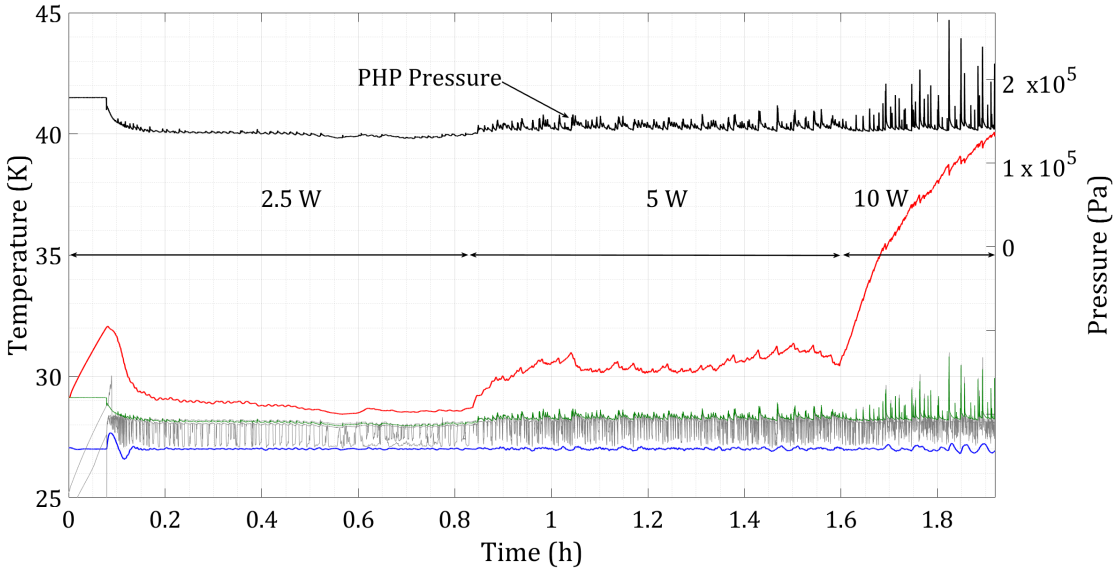

Figure 5.7: Evolution of the PHP pressure (—), the saturation temperature (—), the average temperature of the evaporator (—) and the condenser (—) and the temperatures of the adiabatic part (—) of a fixed heat load experiment in open configuration using neon as working fluid in the PHP with 12 turns.

posing the experimental facility have been presented. It has been observed that the more the number of tubes decreases it becomes more difficult to attain stable operating conditions. It appears to be necessary to impose very specific start-up conditions for the filling process when the number of turns in the PHP is reduced. Not only the initial conditions but also the maximum heat load and the thermal performance seems to be affected by the number of turns. Actually, the maximum heat load drops drastically as the number of tubes decreases. It appears that in horizontal PHPs, not only a minimum number of turns is necessary to start the fluid oscillations as indicated by [17, 25], but also that increasing the number of turns the heat transfer capacity increases as in [125]. On the other hand, it is also important to remark that, as mentioned in chapter 2, the copper plates which constitute the evaporators have the same size and are not proportional to the number of turns. This could explain why the reduction of the heat capacity and the thermal performance is not proportional to the number of turns. To verify this hypothesis, important changes in the experimental facility need to be done. Furthermore, same global trends in the behavior of the fluid in the PHP working at different temperatures at the condenser have been confirmed. Experimental results and thermal performance are leaded by the real filling ratio which depends on the working temperatures and pressures especially during the filling process.

5.4 Quench tests for magnet applications

Focusing on superconducting magnets applications, a final series of tests have been done with a sudden extra heat load at the surface of the evaporator when the PHP is operating in stable conditions, simulating a quench situation of a superconducting magnet, which we will call from now "quench test". This information is necessary to foresee the transient thermal behavior and operating limits of this kind of device during transient heat loads like quench situations.

All the tests have been performed in closed configuration, where the PHP is not connected to the buffer volume. These "quench situations" have been tested in the PHP having 36 turns with nitrogen and neon as working fluids and following the same filling process than during the reference test: with an initial temperature difference between the evaporator and the condenser of 5 K, initial heat load of 5 W at the evaporator and the condenser always fixed at a desired temperature. After the start-up phase, when the PHP is closed and working at 5 W with a stable temperature at the evaporator, the input power at the evaporator is switched from 5 to 20, 40, 60, 80 or 100 W during a certain time corresponding to a desire energy that represents the energy released in a quench situation. At the end of the quench test, the input power at the evaporator is switched back to 5 W. The equivalent energies dissipated by the heating system are 10, 50 and 100 kJ.

Table 5.14: List of quench tests with nitrogen.

Initial filling ratio	Energy
50 %	10 kJ
	50 kJ
	100 kJ

Table 5.15: List of quench tests with neon.

Initial filling ratio	Energy
30 %	10 kJ
	50 kJ
	100 kJ
Energy	**Initial filling ratio**
10 kJ	30 %
	50 %
	70 %

In tables 5.14 and 5.15 are listed all the quench tests performed with nitrogen and neon, respectively. Some tests have been performed several times to verify the reproducibility of the experimental results.

Fig. 5.8 shows the evolution of the temperature difference between the evaporator and the condenser during quench tests of an equivalent energy of 10 kJ at different input powers and an initial filling ratio of 50 % using nitrogen and neon as working fluids. The average real filling ratios (R_{sat}) are 43 and 32.3 %, respectively. The temperature difference represents what is happening in the evaporator because the condenser always keeps stable thanks to the temperature controller. It can be observed that for the same amount of heat load, temperature differences are more important when using neon, but the time durations to recover stable conditions (at 5 W) are lower. As an example, at 60 W of heat load, using nitrogen the PHP attains a temperature difference of 7.4 K and takes around 1000 s to come back to stable conditions, while when using neon the PHP attains 13.7 K and takes around 500 s to come back to stable conditions. This is mainly due to neon's steeper slope of dp/dT at saturation conditions. In addition, this results were expected due to the difference of the specific heat of the copper plates at the ranges of working temperatures of neon and nitrogen. For the same amount of energy, for a lower specific heat, the temperature increase during the quench test is expected to be higher, which is the case of neon (see Fig. I.1 appendix I).

Fig. 5.9 shows the evolution of the temperature difference between the evaporator and the condenser during quench tests using nitrogen as working fluid with an initial ratio of 50 % at different energies: 10 kJ, 50 kJ and 100 kJ, respectively. In this case, the real filling ratios are all the same: 43 % ± 0.5 %. The evolution of the working pressures and the temperatures of the adiabatic part are given in Fig. I.2, I.3 and I.4 in appendix I. During the entire test, excepting punctual local dry-outs, the temperatures of the adiabatic

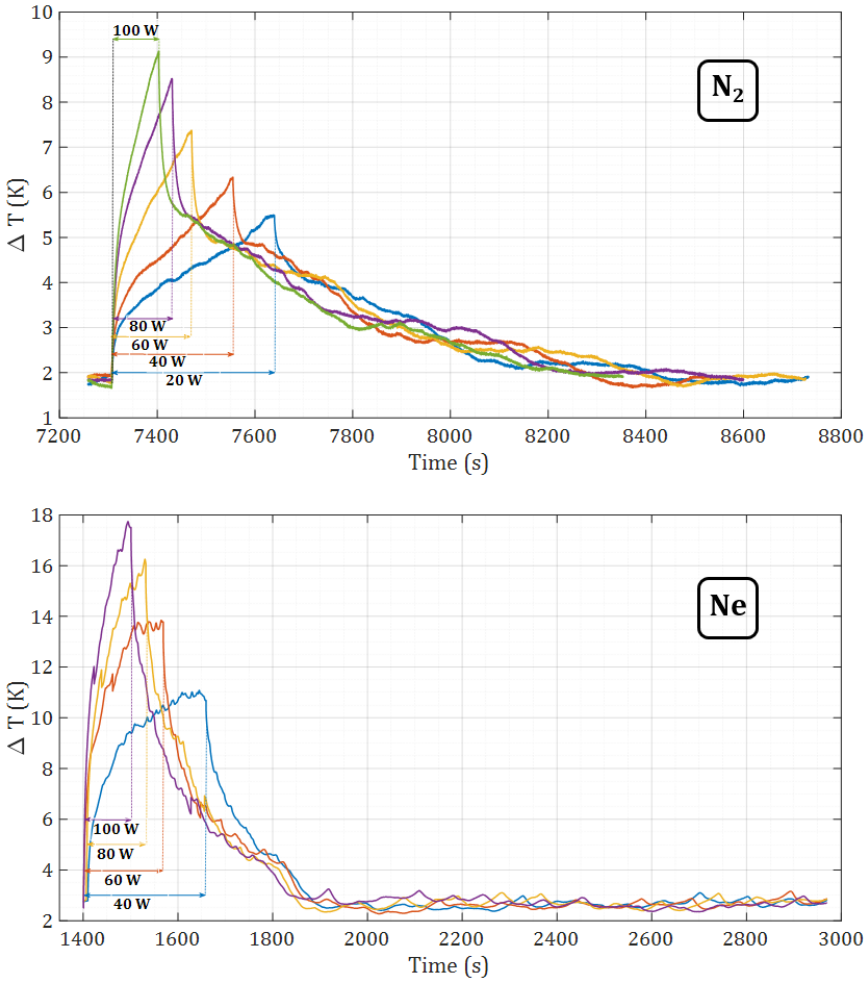

Figure 5.8: Evolution of the temperature difference between the evaporator and the condenser during quench tests of an equivalent energy of 10 kJ at different input powers and an initial filling ratio of 50 % using nitrogen and neon as working fluids, respectively.

section never stop to oscillate. This shows that even if the temperature difference between the evaporator and the condenser increases, the oscillating flow inside the PHP is able to transfer partially the heat. It can be observed that in some cases, at 50 and 100 kJ, after the "quench", the oscillations of the adiabatic part stopped (fluid stop phenomena) and the evaporator was not able to decrease its temperature, it has been necessary to open the PHP to the buffer volume to be able to recover stable working conditions, revealing the irreversibility of the dry-out phenomenon at the evaporator in these conditions, as noticed by [44]. The reduction of pressure generated opening the PHP releases the high pressure reached inside the PHP and contributes to recover fluids oscillations necessary to the flow circulation. When using neon, the PHP system recovers from all type of transient thermal situations and it recovers faster, as it can be seen in Fig. 5.10. This figure shows the evolution of the temperature difference between the evaporator and the condenser during quench tests using neon as working fluid with an initial ratio of 30 % at different energies: 10 kJ, 50 kJ and 100 kJ, respectively, where the real filling ratios are 23 % ± 0.5 %. The evolution of the working pressures and the temperatures of the adiabatic part are given in Fig. I.5, I.6 and I.7 in appendix I, where it can be seen that during the entire test the temperatures of the adiabatic section never stop to oscillate. It has been decided to start with initial filling ratios of 50 % with nitrogen and 30 % with neon in order to attain as much as possible the optimum real filling ratio for each gas in closed configuration (between 25 and 42 % for nitrogen and 20 and 25 % for neon see chapter 4). So, we can globally conclude that, due to its fluid properties, when using neon as working fluid the PHP is able to react faster to heat load changes and recover after a quench situation, while with nitrogen, temperature differences between the evaporator and the condenser are lower. When the working pressures become too important inside the PHP after a quench test, the buffer volume can be connected to the PHP to recover stable working conditions. This solution is more often necessary when using nitrogen as working fluid but can also be necessary with neon in very extreme conditions, such as a high filling ratio, as exemplified in Fig. 5.11. In this case, quench tests with an energy of 10 kJ and with different initial filling ratios (30 %, 50 % and 70 %) have been performed. The real filling ratios are 22, 32 and 47 % respectively. It can be noticed that in the third case, with the higher filling ratio, temperature differences (and the corresponding pressures too) are considerably higher than in the two other cases, and it has been necessary to open the PHP to the buffer volume in all the quench tests to be able to recover a stable temperature at the evaporator.

Moreover, it is interesting to remark that for a given working fluid and energy, the PHP system takes always the same time from the beginning of the quench to recover stable working conditions, no matter the input power inputted at the evaporator, as already noticed by [126].

In this section, experimental results of quench tests performed in the PHP with 36

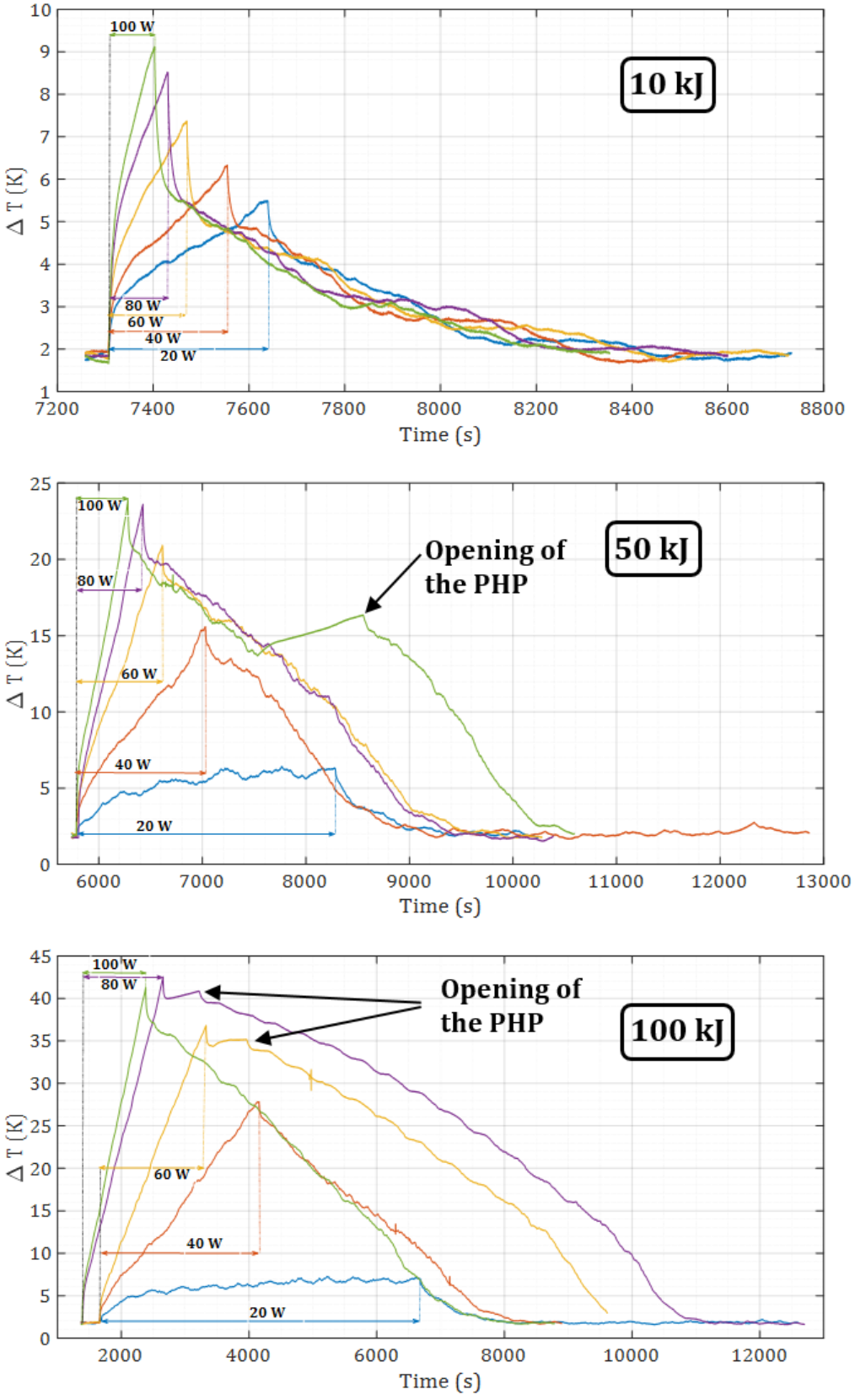

Figure 5.9: Evolution of the temperature difference between the evaporator and the condenser during quench tests using nitrogen as working fluid with an initial ratio of 50 % at different energies: 10 kJ, 50 kJ and 100 kJ, respectively.

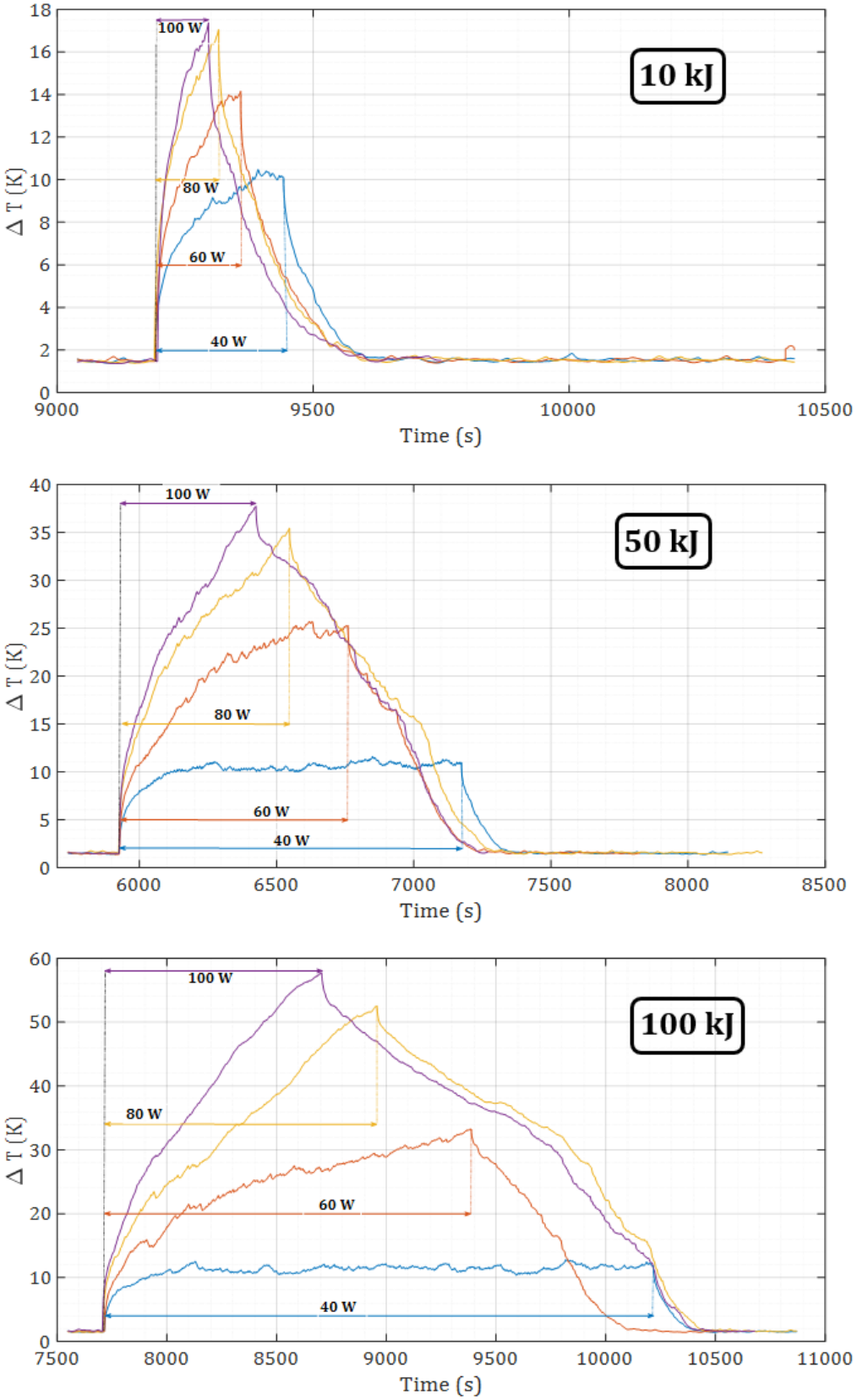

Figure 5.10: Evolution of the temperature difference between the evaporator and the condenser during quench tests using neon as working fluid with an initial ratio of 30 % at different energies: 10 kJ, 50 kJ and 100 kJ, respectively.

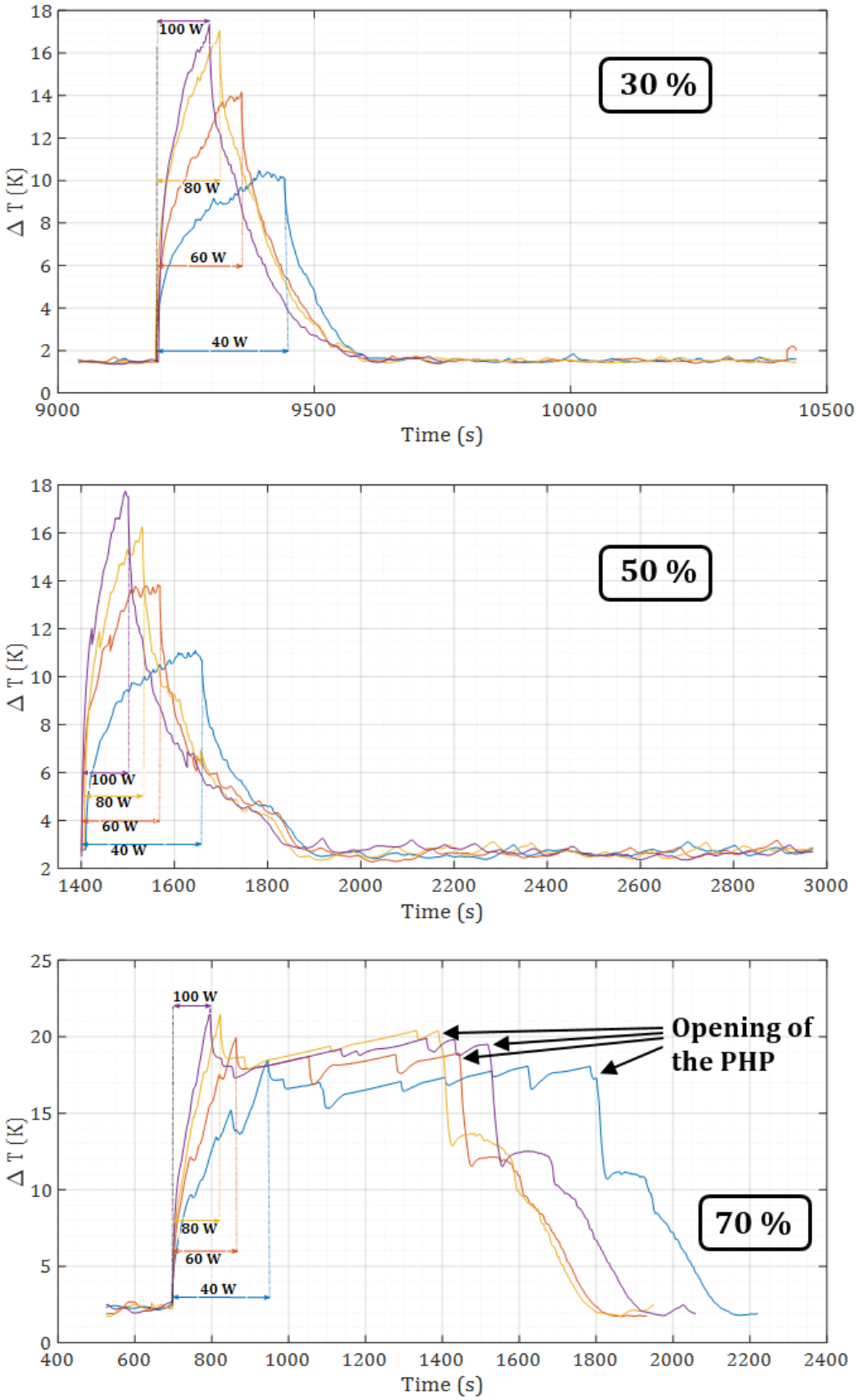

Figure 5.11: Evolution of the temperature difference between the evaporator and the condenser during quench tests at an energy of 10 kJ using neon as working fluid with different initial filling ratios: 30 %, 50 % and 70 %, respectively.

turns and using nitrogen and neon as working fluids have been presented. It has been noticed that, when the working pressures are very high and the fluid has problems to flow and oscillate, opening the PHP to the buffer volume could be a solution to recover stable working conditions. In addition, it has been verified once again that, due to its physical properties, neon suffer more extreme changes in temperature and pressure achieving higher temperature differences during the quench on one hand but recovering faster from transient thermal situations on the other hand. These experimental results give us information about the behavior of the PHP system in case of quench for future magnet applications, nevertheless more tests need to be done to characterize the PHP system in a larger range of heat load extreme situations.

5.5 Conclusions

Specific tests have been performed in order to determine the limits and the specific working conditions of the three pulsating heat pipes composing the experimental facility of the present research project. Nitrogen and neon at different filling ratios have been tested for these purposes.

Firstly, start-up conditions concerning the initial temperature difference between the evaporator and the condenser as well as the initial input power at the evaporator, have been defined depending on the working fluid. It has been confirmed that a minimum amount of energy is desirable for the filling process contributing to a better distribution of the fluid inside the PHP. It has also been observed that when the initial filling ratio is too important (often more than 30%), higher initial input powers during the filling process prevent an excess of fluid to get inside the PHP due to higher working pressures in the PHP, giving lower real filling ratios and providing higher thermal performances maintaining a stable temperature at the evaporator at each power step.

In addition, the influence of the temperature of the condenser has also been studied concluding that, for both fluids, the temperature of the condenser determines the range of working temperatures and pressures inside the PHP as well as the real filling ratio during the filling process and, consequently, during the rest of the test, influencing the global thermal performances.

Furthermore, the two other PHPs have also been tested and the maximum heat load transferred by each PHP have been presented. It appears that it is more difficult to attain stable operating conditions when reducing the number of turns. The maximum heat load and the thermal performance are also considerably reduced when the number of turns decreases.

Moreover, a final series of tests have been done imposing a sudden extra heat load at the surface of the evaporator when the PHP is operating in stable conditions, simulating

a quench situation of a superconducting magnet. When the PHP uses nitrogen as working fluid, the temperature differences between the evaporator and the condenser during quench tests are lower than when using neon, nevertheless, time duration to recover stable working conditions after the quench are lower with neon. It appears also that opening the PHP to the buffer volume to recover stable working conditions could be a solution to reduce the pressure inside the PHP and re-start the oscillating flow. This information is necessary to foresee the behavior of the PHP system in case of quench for future magnet applications.

This chapter represents the last piece of the experimental results. In the following chapter, the numerical part of the present research project will be presented, including the numerical model and the corresponding results.

Chapter 6

Numerical simulation of the fluid's behavior in a capillary tube

6.1 Introduction

In the numerical field several authors have been working on pulsating heat pipes simulations, developing models to predict the behavior of the working fluid and the heat transfer phenomena, as detailed in chapter 1. The most completed numerical models for pulsating heat pipes are 1D models, where the oscillatory phenomenon is predicted by solving mass, momentum, and energy equations for the liquid slugs and vapor plugs, including several assumptions concerning the physical parameters, such as the liquid film thickness, the incompressibility of the liquid phase, the vapor phase pressure evolution (considered as an ideal or real gas), the heat transfer coefficients for solid-fluid heat interactions, etc.

As a reference, Faghri's group [15, 74, 102] has developed one of the first consistent 1D numerical models for looped and unlooped PHPs, complemented by Mameli et al. [17, 59, 60, 87], who have included more physical parameters. In addition, V. Nikolayev et al. have also developed 1D models for multi-branch horizontal PHP simulations [18, 20] and for a single capillary tube [19]. Furthermore, Rao et al. [34, 106] have also performed several simulations to compare with experimental results of a single vertical capillary tube. Moreover, one of the only 2D and 3D numerical models have been developed by Pouryoussefi et al. [86, 90].

As it has been presented in this writing, pulsating heat pipes are simple geometry systems based on numerous and complex mechanisms occurring almost simultaneously, which complicates to include all of them into numerical simulations. This explains why the most completed models have been developed in 1D, and only a few studies consider 2 (or even 3) dimensions. Even if the present research project is mainly an experimental work, we also wanted to contribute to the PHP numerical field by starting to develop a

2D model with an axisymmetric geometry of a single capillary tube in horizontal position, as a first step towards future 2D simulations of horizontal pulsating heat pipes.

6.2 Experimental reference case

The main goal of this simulation work is to develop a 2D numerical model based on a simple geometry but able to represent the fluid's behavior in a capillary tube, considering the different physical parameters and phenomena occurring inside a PHP, for future 2D horizontal pulsating heat pipes simulations.

For this purpose, the physical case represented in this numerical model correspond to the experimental model developed by Gully et al. [52]. Their experimental set-up, detailed in Fig. 6.1, is composed of a single capillary tube in horizontal position with an evaporator, adiabatic and condenser part. The evaporator end of the tube is blind while the condenser end of the tube is connected to a constant pressure reservoir. The capillary tube is made of stainless steel with an inner and outer diameter of 2 and 3 mm, respectively. The evaporator and the condenser are made of 150 mm copper plates. A heater is fixed on the evaporator copper plate on its first third closer to the adiabatic part. The condenser is anchored to the isothermal copper plate of the cold head of a cryocooler and its temperature is fixed with a temperature controller. The reservoir temperature can be adjusted by activating a heater fixed at the reservoir in order to regulate the reservoir pressure. The working fluid is oxygen and the system operates at cryogenic temperatures between 60 and 70 K. The fluid inside the capillary tube is distributed in one liquid slug and one vapor plug, and the interface between both phases (the meniscus) oscillates between both ends. In addition, a temperature sensor is located inside the tube in the evaporator part and another pressure sensor is fixed at the blind end of the evaporator part. In this way, the saturation temperature is calculated from the pressure measurements of the evaporator part. This experimental work have been performed to evaluate the thermodynamic state of the vapor bulk, and it has been demonstrated the deviation of the vapor part from the saturation conditions by compressions and expansions and the superheated state of the vapor part.

Since the heater of the evaporator is activated at 1.5 W, the liquid-vapor interface starts to oscillate entering in the evaporator and condenser parts with a frequency of oscillations of 1.5 Hz. The condenser temperature is fixed at 66.2 K, the reservoir temperature at 70 K and the average temperature of the evaporator is 72.7 K. The experimental results are represented in Fig. 6.2. The saturation temperature $T_{sat}(P_v)$ (calculated from the pressure sensor of the evaporator part) oscillates around the saturation temperature fixed by the reservoir and, the vapor temperature oscillates around the evaporator temperature. The numerical results will be compared with these experimental temperature

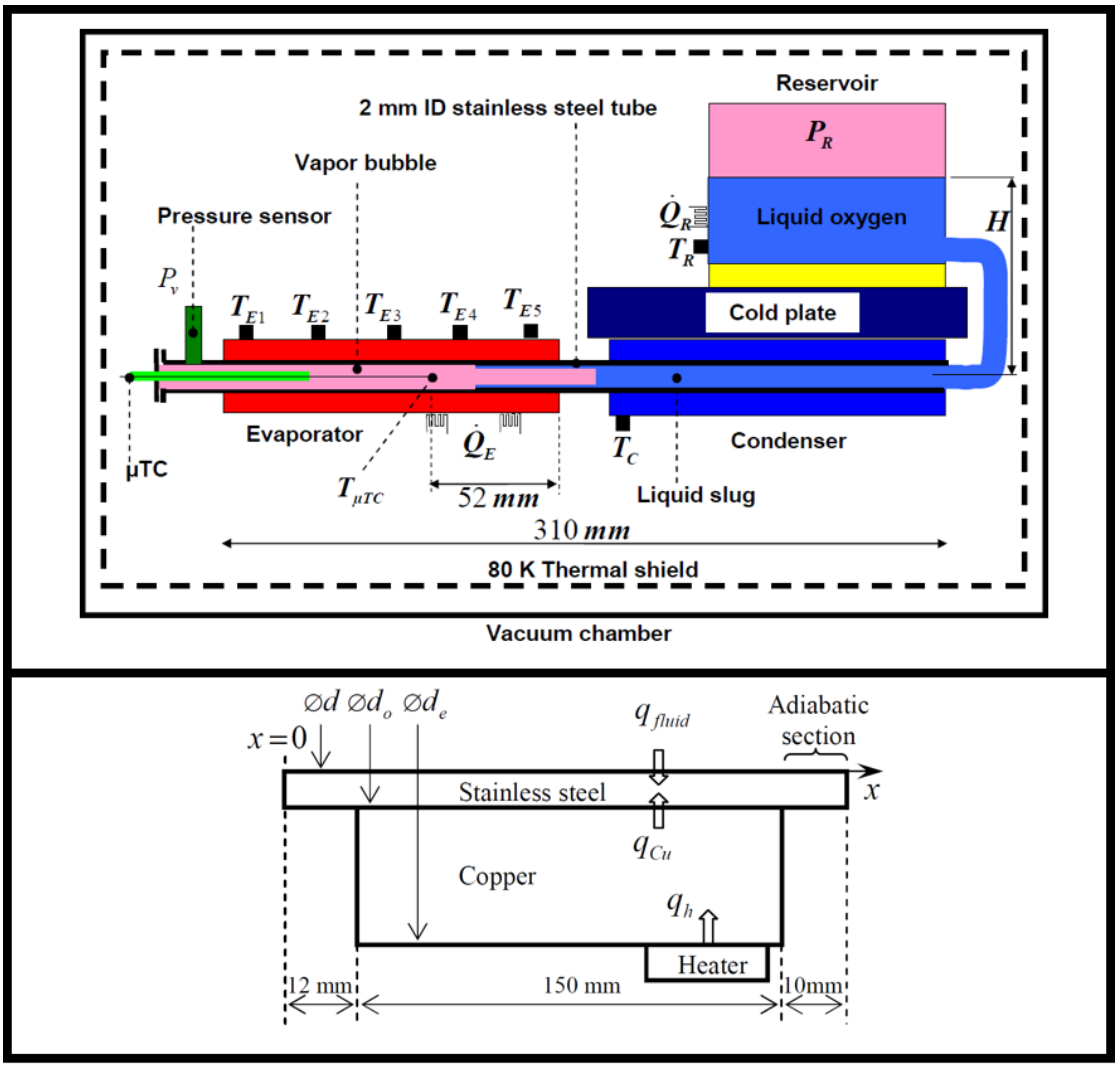

Figure 6.1: Schematic illustration of the experimental set-up of the reference case [52].

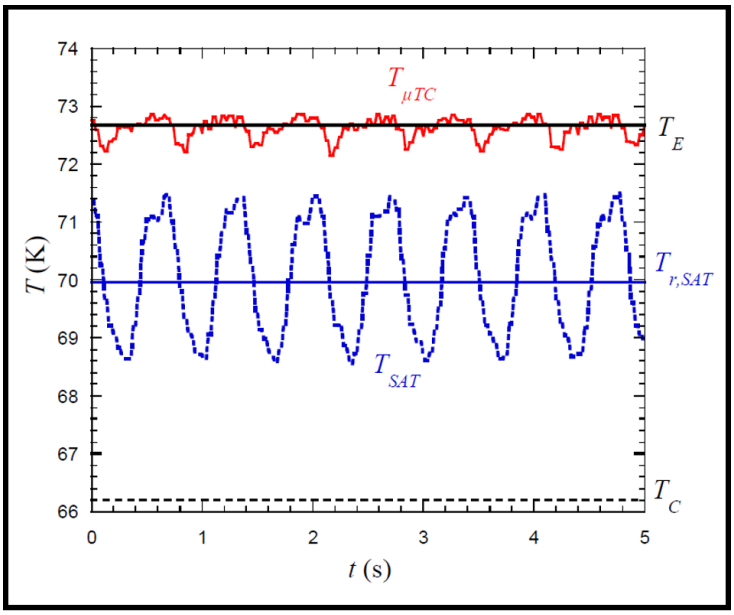

Figure 6.2: Experimental results of the reference case [52]. T_{sat} (— —) corresponds to the calculated saturation temperature, $T_{\mu TC}$ (—) represents the measured temperature in the evaporator part, T_E (—) corresponds to the temperature of the evaporator copper plate and T_C (— —) corresponds to the temperature of the condenser copper plate.

and pressure measurements to validate the model.

Finally, it is important to mention that in the experimental set-up of this reference case [52] it is not possible to visualize the interface position. Due to this, the authors have simulated the oscillations of the interface with the ANSYS CFX® software to determine the Nusselt number (Nu). The simulation has been performed in a 2D axisymmetric geometry of a tube closed at one end and having an oscillating piston at the other end. The imposed oscillations at the piston are given in Fig. 6.3 and will also be used as a reference.

This experimental model has been chosen for our simulation due to its simple geometry and configuration, its horizontal position and cryogenic range of temperatures, always in line with the topic of the present research project on cryogenic horizontal pulsating heat pipes.

6.3 Simulation models

The simulation work of this project has been performed using the ANSYS Fluent® software. This latter allows to perform simulations in general fluid mechanics with the possibility of parallel processing taking advantage of multiprocessor systems in a single machine, as in this study. The mesh of the geometry representing the model has been generated with ANSYS ICEM CFD® software and then imported into ANSYS Fluent®.

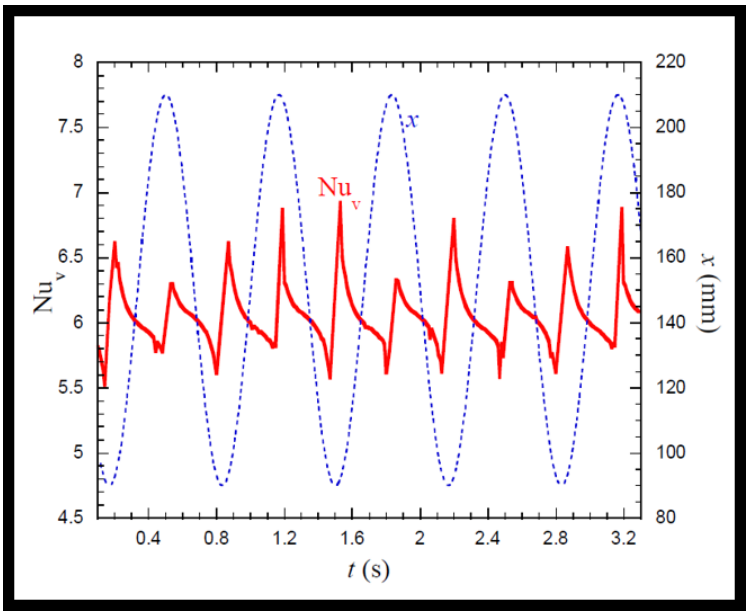

Figure 6.3: Evolution of the imposed oscillations of the piston in the simulation of the reference case [52] (x=0 at the blind tube end).

0.25	0.25	0.12	0	0
1	1	0.9	0.45	0
1	1	1	0.9	0.1
1	1	1	1	0.2
1	1	1	1	0.2

Figure 6.4: Schematic illustration of a fluid interface with the volume fractions.

Transient simulations have been performed with a pressure-based Fluent solver using the Volume of Fluid (VOF) method in a 2D axisymmetric geometry. The flow is assumed laminar and the gravity force is not considered.

In computational fluid dynamics (CFD), the volume of fluid (VOF) method is a free-surface or fluid-fluid interface modelling technique that allows to follow the evolution of the shape and position of the interface. The founding idea of the VOF method is to use a discrete function that represents the volume fraction of one of the phases in each control volume: the fractional function α_q of a given phase q, with $0 \leq \alpha_q \leq 1$. If $\alpha_q = 0$ or $\alpha_q = 1$, the control volume is full of one of the two phases. If $0 < \alpha_q < 1$, the control volume contains both phases and the corresponding interface, represented in Fig. 6.4.

In this way, the free-surface is not defined sharply, instead it is distributed over the height of a cell. The evolution and movement of the interface between the phases is

accomplished by the solution of the continuity equation for the volume fraction of one (or more) of the phases. In the ANSYS Fluent® solver [127], this equation has the following form:

$$\frac{1}{\rho_q}[\frac{\partial \alpha_q \rho_q}{\partial t} + \nabla \cdot (\alpha_q \rho_q \vec{v_q}) = S_{\alpha_q} + \sum_{p=1}^{n}(\dot{m_{pq}} - \dot{m_{qp}})], \tag{6.1}$$

where $\dot{m}_{qp}$ is the rate of mass transfer from phase q to phase p and $\dot{m}_{pq}$ is the mass transfer from phase p to phase q. By default, the source term S_{α_q} is zero.

Where the volume fraction equation respects the following constraint:

$$\sum_{q=1}^{n} \alpha_q = 1. \tag{6.2}$$

In this case, the volume fraction equation is solved through explicit time discretization, where standard finite-difference interpolation schemes are applied to the volume fraction values that were computed at the previous time step,

$$\frac{\alpha_q^{n+1}\rho_q^{n+1} - \alpha_q^n \rho_q^n}{\Delta t} V + \sum_f (\rho_q U_f^n \alpha_{q,f}^n) = [\sum_{p=1}^{n}(\dot{m_{pq}} - \dot{m_{qp}}) + S_{\alpha_q}]V, \tag{6.3}$$

where $n+1$ is the index for current time step, n is the index for previous time step, $\alpha_{q,f}$ is the phase value of the q^{th} volume fraction, V is the volume of cell and U_f is the volume flux through the face, based on normal velocity.

The properties of each phase are determined by the presence of the component phases in each control volume. In this way, for an n-phase system, the volume-fraction-averaged property respects the following constraint:

$$p = \sum_{q=1}^{n} \alpha_q p_q. \tag{6.4}$$

As an example, in a two-phase system, the density in a cell will be calculated as follows:

$$\rho = \alpha_2 \rho_2 + (1 - \alpha_2)\rho_1. \tag{6.5}$$

Concerning the momentum equation, a single one is solved throughout the domain, and the resulting velocity field is shared among the phases. In this case, the external force F is zero. The equation is defined as follows:

$$\frac{\partial(\rho\vec{v})}{\partial t} + \nabla \cdot (\rho\vec{v}\vec{v}) = -\nabla p + \nabla \cdot [\mu(\nabla\vec{v} + \nabla\vec{v}^T)] + \rho\vec{g} + \vec{F}. \tag{6.6}$$

A single energy equation is also solved throughout the domain, and the result is shared among the phases. The equation is defined as follows:

$$\frac{\partial(\rho E)}{\partial t} + \nabla \cdot (\vec{v}(\rho E + p)) = \nabla \cdot (k_{eff}\nabla T) + S_h, \tag{6.7}$$

where E is the energy, k_{eff} is the effective thermal conductivity, also shared by the phases, and S_h is the source term.

In addition, in the VOF model, energy and temperatures are treated as mass average variables, as shown below:

$$E = \frac{\sum_{q=1}^{n} \alpha_q \rho_q E_q}{\sum_{q=1}^{n} \alpha_q \rho_q}, \tag{6.8}$$

$$T = \frac{\sum_{q=1}^{n} \alpha_q \rho_q T_q}{\sum_{q=1}^{n} \alpha_q \rho_q}. \tag{6.9}$$

Finally, concerning the solution methods, the pressure-velocity coupling method follows a SIMPLE algorithm developed by ANSYS Fluent® [127] with a PRESTO! loop having a first order implicit time discretization and second order Upwind spatial discretization.

6.3.1 Dynamic model

For this simulation work, a first model has been developed to study the shape and evolution of the two-phase interface, oscillating between the evaporator and the condenser part. This model will be called the "dynamic model". It is based on a 2D axisymmetric geometry of a horizontal capillary tube with oxygen as working fluid where pressure variations have been imposed at one end to generate the oscillations of the liquid-vapor interface. The mesh used, shown in 6.5, is composed of 117 743 square cells (25 in the y-axis) with minimum and maximum face areas between 5.001667×10^{-5} and 5.26318×10^{-5} m^2. The size of the cells has been defined ensuring the equilibrium between a sharp interface and a Courant number (Cou) below 0.5. For this, different meshes have been tested and are presented in Fig. J.1 and J.2 in appendix J.

The time calculations are 0.5 and 1 s, with a time step of 10^{-5} s and a number of steps of 50 000 and 100 000. The dimensions are given in Fig. 6.6, where are indicated the

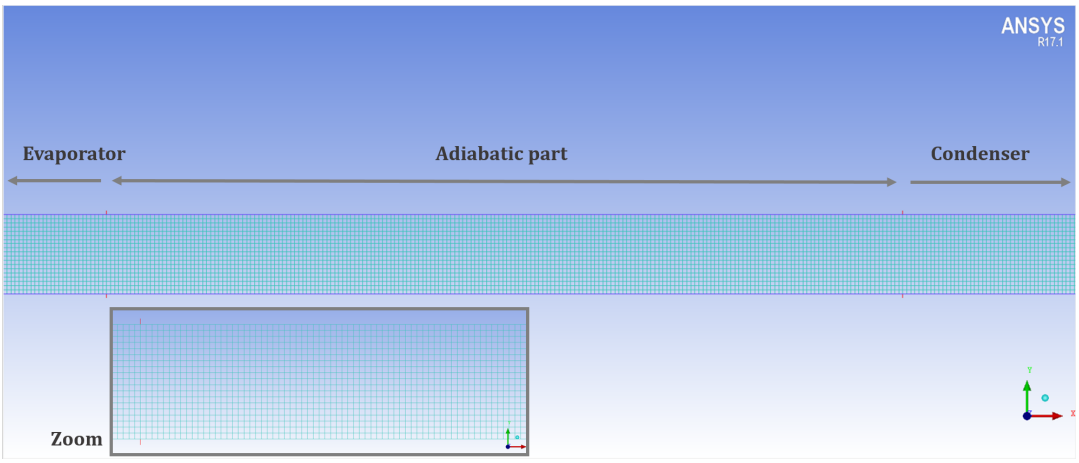

Figure 6.5: Image zoom of the mesh for the dynamic model (the mesh dimensions are identical in the entire figure).

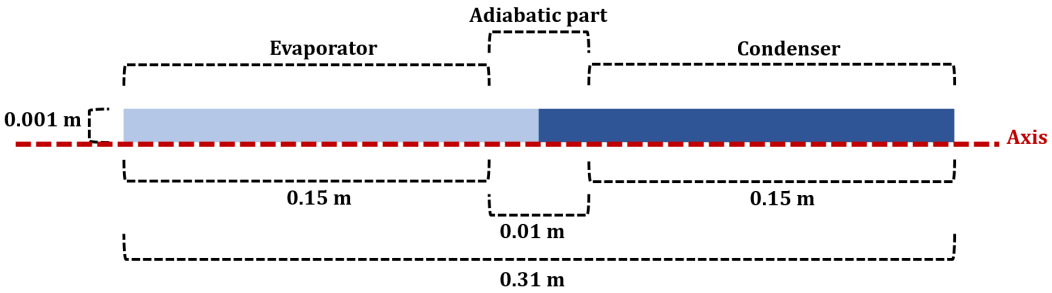

Figure 6.6: Schematic illustration of the dynamic model with the geometry dimensions.

lengths of the evaporator, the condenser, the adiabatic part and half of the inner diameter because this 2D axisymmetric geometry is oriented in the x-axis.

The boundary and initial conditions are indicated in Fig. 6.7. The simulation starts with a single liquid part at 6262.3 Pa and a single vapor part at 6312.5 Pa and the two-phase interface located at the center of the figure. At the condenser end the pressure is fixed at 6262.3 Pa, at the evaporator end a user-defined function (UDF) of pressure is imposed. This UDF is a sinusoidal function that indicates the evolution of pressure as a function of the time. It has been defined in accordance with the experimental results of the reference case [52]. The UDF code, coded in C language, is given as follows:

```
#include "udf.h"
#define PI 3.141592654
DEFINE_PROFILE(unsteady_pressure,thread,position)
{
        face_t f;
```

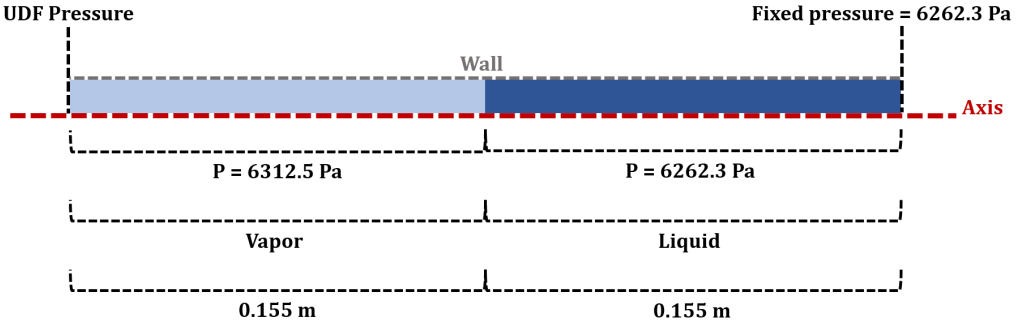

Figure 6.7: Initial and boundary conditions of the dynamic model.

```
        real t = CURRENT_TIME;
        begin_f_loop(f, thread)
        {
                F_PROFILE(f,thread,position) =
                6312.5 + 1687.5*sin(2*PI*1.5*t);
        }
        end_f_loop(f,thread)
}
```

It can be noticed that, in the UDF code, the average pressure value (6312.5 Pa) and the amplitude of oscillations (1687.5 Pa) correspond to the median values between the maximum and minimum experimental pressure oscillations and to the pressure variations from the saturation pression of oxygen at 70 K, as indicated in Fig. 6.8. Those values are obtained from experimental results of the reference case [52]. Even if the temperature oscillations have the same amplitude, the corresponding pressure oscillations in saturation conditions do not have the same amplitude in both directions due to the slope of oxygen's saturation curve (see Fig. J.6 in appendix J). Because of this, the slight initial pressure difference between the vapor and liquid part has been chosen to adapt the initial conditions to the UDF sinusoidal function.

In the model, the wall adhesion option is selected to ensure the formation of a liquid film, as in capillary tubes. The surface tension (σ) is 0.0184 N/m, corresponding to the surface tension of oxygen at saturation conditions at 70 K. To complete this model, a contact angle between the liquid phase and the solid wall must be indicated as a wettability parameter. This contact angle is the result of the equilibrium between surface tension forces in the triple line (solid-liquid-gas), given by Young's equation (6.10) and illustrated in Fig. 6.9. In order to analyze the evolution and shape of the liquid-vapor interface, several contact angles have been tested and will be presented in section 6.4.

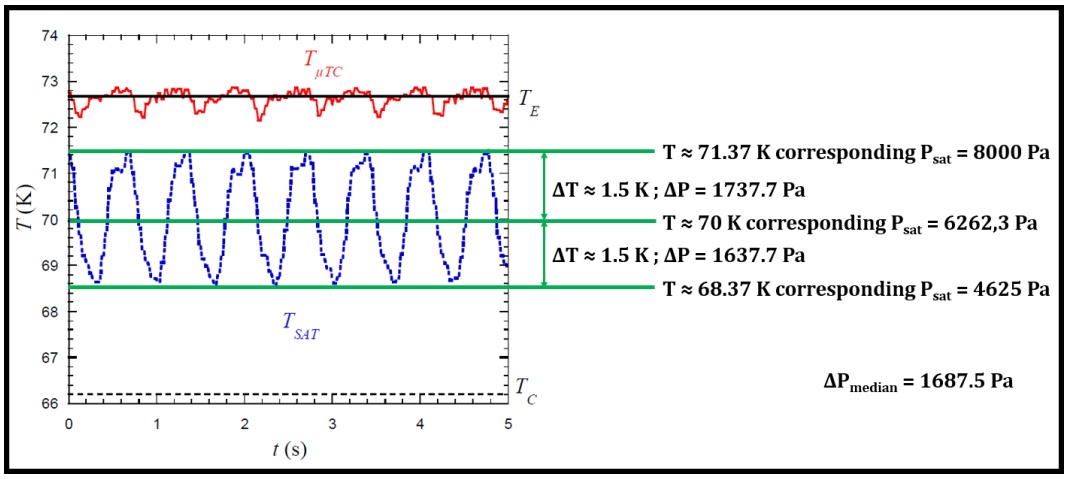

Figure 6.8: Evolution of the saturation pressure and saturation temperature from the experimental reference case.

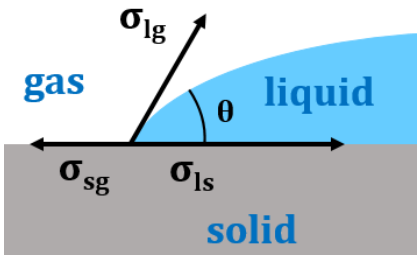

Figure 6.9: Schematic illustration of the equilibrium between surface tension forces in the triple line.

$$\sigma_{sl} + \sigma_{lg}\cos(\theta) = \sigma_{sg} \tag{6.10}$$

6.3.2 Thermal model

After analyzing the behavior of the two-phase interface, the numerical model has been updated and completed including the thermal equations and components of the VOF method. This second model, called the "thermal model" has a more completed geometry with a solid part representing the copper evaporator, and the heat transfer from the evaporator to the condenser through the fluid oscillations is studied.

In this thermal model, evaporation and condensation processes are simulated using the Lee model of the Fluent solver [127], typically used for VOF modelling. Depending on the range of temperatures, the mass transfer is given by:

$$\dot{m_{lv}} = Coef_l \alpha_l \rho_l \frac{T_l - T_{sat}}{T_{sat}}, \tag{6.11}$$

during the evaporation process, when $T_l > T_{sat}$, and given by:

$$\dot{m_{vl}} = Coef_v \alpha_v \rho_v \frac{T_{sat} - T_v}{T_{sat}}, \tag{6.12}$$

during the condensation process, when $T_{sat} > T_v$.

Generally, the evaporation and condensation coefficients, $Coef_l$ and $Coef_v$, can be interpreted as a relaxation times, but more precisely, the concept of time appears during temperature changes, leading the mass transfer process, which can be interpreted as $\frac{\alpha_l \rho_l T_l - T_{sat}}{\Delta t}$. In this case, to define these coefficients, a few assumptions have been made: during the evaporation and condensation process in a cell the temperature of the cell is equal to the saturation temperature and constant. This is acceptable due to the small size of the cells (described below), which means that the temperature variation between two cells close to each other is not significant. In addition to that, we consider that all the "excess of energy" of the cell making possible to exceed the saturation temperature will be used in the evaporation process (the inverse reasoning is considered for the condensation process). These assumptions have already been used in the past by [128] based on [129], and give the following general formulation of the mass transfer:

$$\dot{m} = \frac{(T - T_{sat})\rho\alpha Cp}{L_v}, \tag{6.13}$$

where the T, ρ, α, Cp and L_v are the temperature, density, volume fraction, specific heat and latent heat of each phase. In this way considering equations 6.11, 6.12 and 6.13 for the same Δt, the evaporation and condensation coefficients can be defined as follows:

$$Coef_l = \frac{Cp_l T_{sat}}{L_v}, \tag{6.14}$$

and

$$Coef_v = \frac{Cp_v T_{sat}}{L_v}. \tag{6.15}$$

In this case, the evaporation and condensation coefficients are 0.5085 and 0.2963. They have been calculated with T_{sat} at 70 K and the latent heat (L_v) and specific heats (Cp_l and Cp_v) at this saturation temperature.

Furthermore, phase-change phenomena are leaded by variations of the saturation temperature, obtained from pressure variations. The polynomial law relating the pressure to the saturation temperature has been obtained from Refprop database [2] and is given as follows:

$$T_{sat}(p) = 1 \times 10^{-11} p^3 - 2 \times 10^{-7} p^2 + 0.0027p + 59.914. \tag{6.16}$$

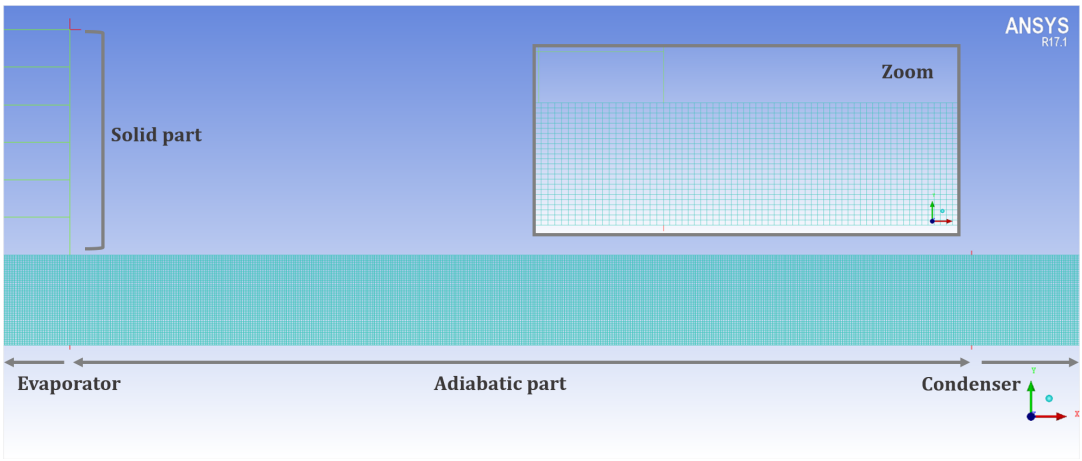

Figure 6.10: Image zoom of the mesh for the thermal model.

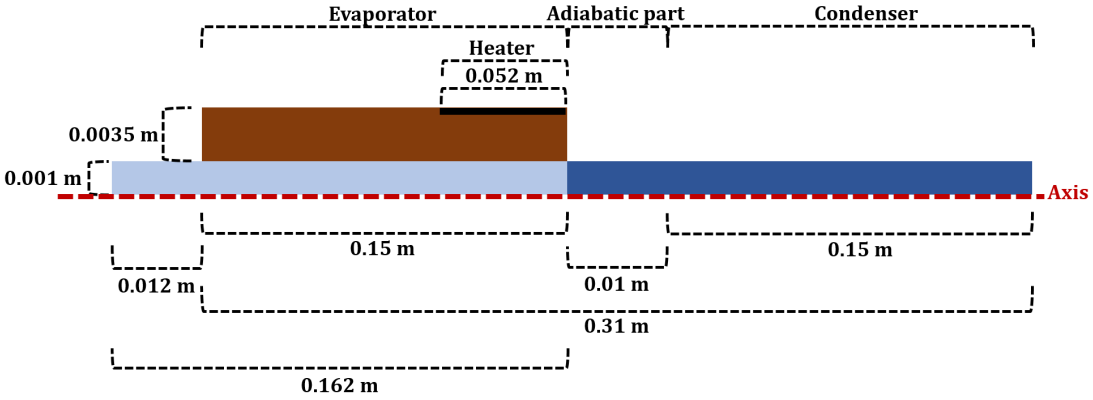

Figure 6.11: Schematic illustration of the thermal model.

Concerning the geometry, the mesh used for this model is detailed in Fig. 6.10. It is composed of 145 080 square cells with minimum face area of $4.166667 \times 10^{-5}\ m^2$ and a maximum face area of $1.020408 \times 10^{-3}\ m^2$, corresponding to the evaporator solid part. The size of the cells are in the same order of magnitude as in the dynamic model, nevertheless, a second mesh with smaller cells has also been tested to verify that any information is lost after adding the thermal component. Details about this second mesh are given in Fig. J.3, J.4 and J.5 in appendix J.

The total time calculation is 2.5 s, with a time step of 10^{-5} s and a number of steps of 250 000. The dimensions of the geometry are given in Fig. 6.11, including the new component representing the solid copper plate of the evaporator.

The boundary and initial conditions are indicated in Fig. 6.12, as well as the positions of the temperature sensor in the evaporator part, as in the reference case [52]. The simulation starts with a single liquid part and a single vapor part, with the liquid part in subcooled state (at 6262.3 Pa and 66.2 K) and the vapor part at the same starting con-

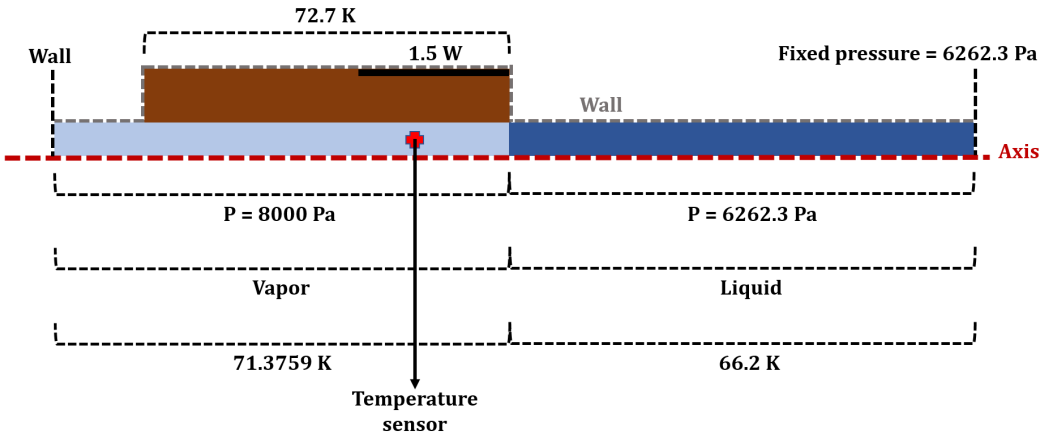

Figure 6.12: Initial and boundary conditions of the thermal model.

ditions than in the reference case (at 8000 Pa and 71.37 K) to ensure thermal instability since the beginning of the test to generate fluid oscillations. Comparing to the dynamic model, this time the evaporator end is indicated as a wall, without UDF, and in the condenser end the pressure is fixed at 6262.3 Pa to observed fluid oscillations only due to thermal instabilities.

After analyzing the numerical results of this simulation (presented in next section 6.4), a second thermal configuration has been tested to analyze the heat transfer between the working fluid and the evaporator and condenser parts. The boundary and initial conditions of this second case are indicated in Fig. 6.13. Where a mass flow UDF has been imposed in the condenser end to force the fluid to enter in the evaporator part and verify the heat transfer between the fluid and the evaporator solid part. The UDF code has been adjusted to obtain the same amplitude of oscillations of the liquid-fluid interface than in the reference case, indicated in Fig. 6.3 in section 6.2. It is coded in C language as follows:

```
#include "udf.h"
#define PI 3.141592654
DEFINE_PROFILE(inlet_mf,thread,position)
{
  face_t f;
  real t = CURRENT_TIME;
  begin_f_loop(f,thread)
    {
          F_PROFILE(f,thread,position) =
          (-0.0015)*sin(2*PI*t*1.5);
    }
  end_f_loop(f,th);
}
```

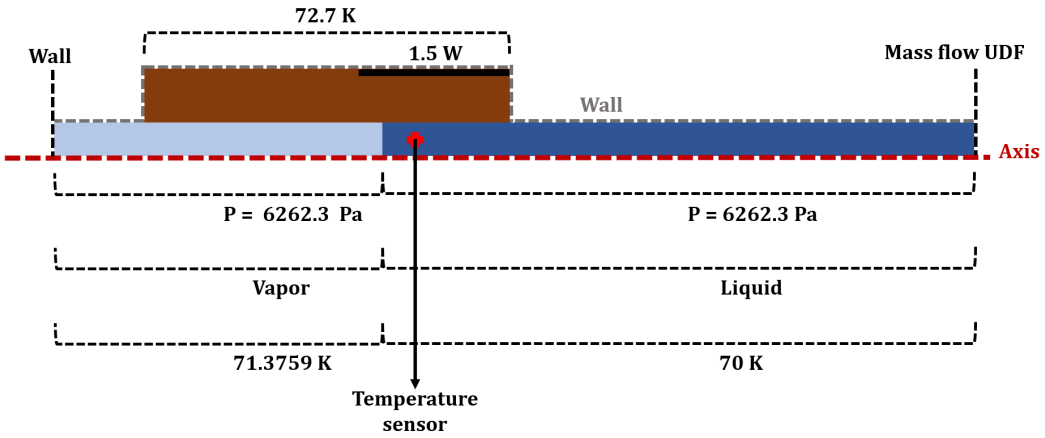

Figure 6.13: Initial and boundary conditions of the second configuration of the thermal model.

In this model, liquid is considered incompressible and vapor follows the Ideal Gas Law given by the Fluent solver [127], where the vapor density is defined as follows:

$$\rho = \frac{p_{op} + p}{\frac{R}{M}T}, \tag{6.17}$$

where p_{op} is the operating pressure, fixed at 0 in this case, and p is the local (or gauge) pressure.

To consider vapor as an ideal gas, as it has been done in [102], [17] and [19], fits very well with the reality when vapor is in superheated state, nevertheless this assumption is less accurate approaching the saturation conditions, where it should better be considered as a real gas. Due to the impossibility to perform simulations with the Fluent solver using the VOF model and the real gas approximation (after several attempts, a mass or energy default appear that crashes the calculation), the ideal gas scheme has been chosen. The vapor density difference at 70 K between the ideal gas law and the real density given by Refprop Database [2] has been calculated to estimated the maximum error due to the approximation. It appears that the ideal gas law gives a vapor density of 0.3449 kg/m^3 (at 70 K and 6262.3 Pa), while Refprop Database gives a vapor density of 0.3386 kg/m^3 (at 70 K and saturation conditions). Thus, the difference is lower than 1.87 %, so this assumption is valid.

Finally, the properties of the different materials used for this thermal model are given in table 6.1.

Table 6.1: Properties of the solid and fluid phases of the thermal model (from CryoComp database [1] and Refprop database [2]).

Copper at 72.7 K		
ρ	8960	kg/m^3
Cp	180	J/(kg.K)
λ	605	W/(m.K)
Steel (SS304) at 70 K		
ρ	7900	kg/m^3
Cp	167	J/(kg.K)
λ	7.59	W/(m.K)
Liquid Oxygen at 66.2 K		
ρ	1254.3	kg/m^3
Cp	1677.6	J/(kg.K)
λ	0.1851	W/(m.K)
μ	0.00043465	Pa.s
Vapor Oxygen at 71.37 K		
ρ	(ideal gas law)	
Cp	979.2609	J/(kg.K)
λ	0.0061	W/(m.K)
μ	5.4653×10^6	Pa.s

Table 6.2: Average thicknesses of the liquid films.

Average thicknesses of the liquid films δ (μm).	
Contact angle = 10°	(only interface)
Contact angle = 20°	≈ 80
Contact angle = 30°	≈ 80
Contact angle = 40°	≈ 110
Contact angle = 50°	≈ 240

6.4 Results

6.4.1 Dynamic model

As mentioned in the previous section, the two-phase interface has been simulated using the dynamic model with different contact angles, in order to determine their influence in the shape of the liquid film and the formation of liquid droplets left behind the advancing liquid film. Nine contact angles have been tested going from 10° to 90° by 10° steps.

In Fig. 6.14 are shown different images of the shape of the liquid film during simulations with the nine different contact angles. It can be observed that with contact angles higher than 60^o (included), the angle is too large and the liquid film is not created, while with contact angles between 10 and 50^o (included), the liquid film is created. This confirms the influence of the contact angle in the liquid film shape. In order to choose a reasonable contact angle in accordance with the reference case, liquid film thicknesses have been analyzed and measured with the ParaView® visualization platform. The average thicknesses of the liquid films are given in table 6.2. With a contact angle of 10^o, there is no clear zone of liquid but a large interface zone, being not possible to determine the thickness of the liquid zone, due to this, it has not been considered. It appears that for contact angles of 20 and 30^o, the average liquid film thickness (around 80 μm) is in the same order of magnitude of what it can be found in literature [18] for the same inner diameter (2 mm). Due to this, the contact angle has been fixed at 30^o for the next simulations.

Once the contact angle has been chosen, the numerical results of the dynamic model with a contact angle of 30° have been analyzed in detail. In Fig. 6.15 are presented different instants of the creation of the liquid film at the beginning of the oscillations. It can be observed that at the end of the advancing liquid film droplets are created and left behind the liquid film. The droplets are created due to what is known as Laplace instabilities. Actually, the shape of an interface is determined by Laplace's Law 6.18, where pressure differences on both sides of an interface are related to the surface tension and the curvature of the film [130], this is because the surface tension tries to minimize the surface energy adopting a circular shape (the minimum energy shape), as explained by

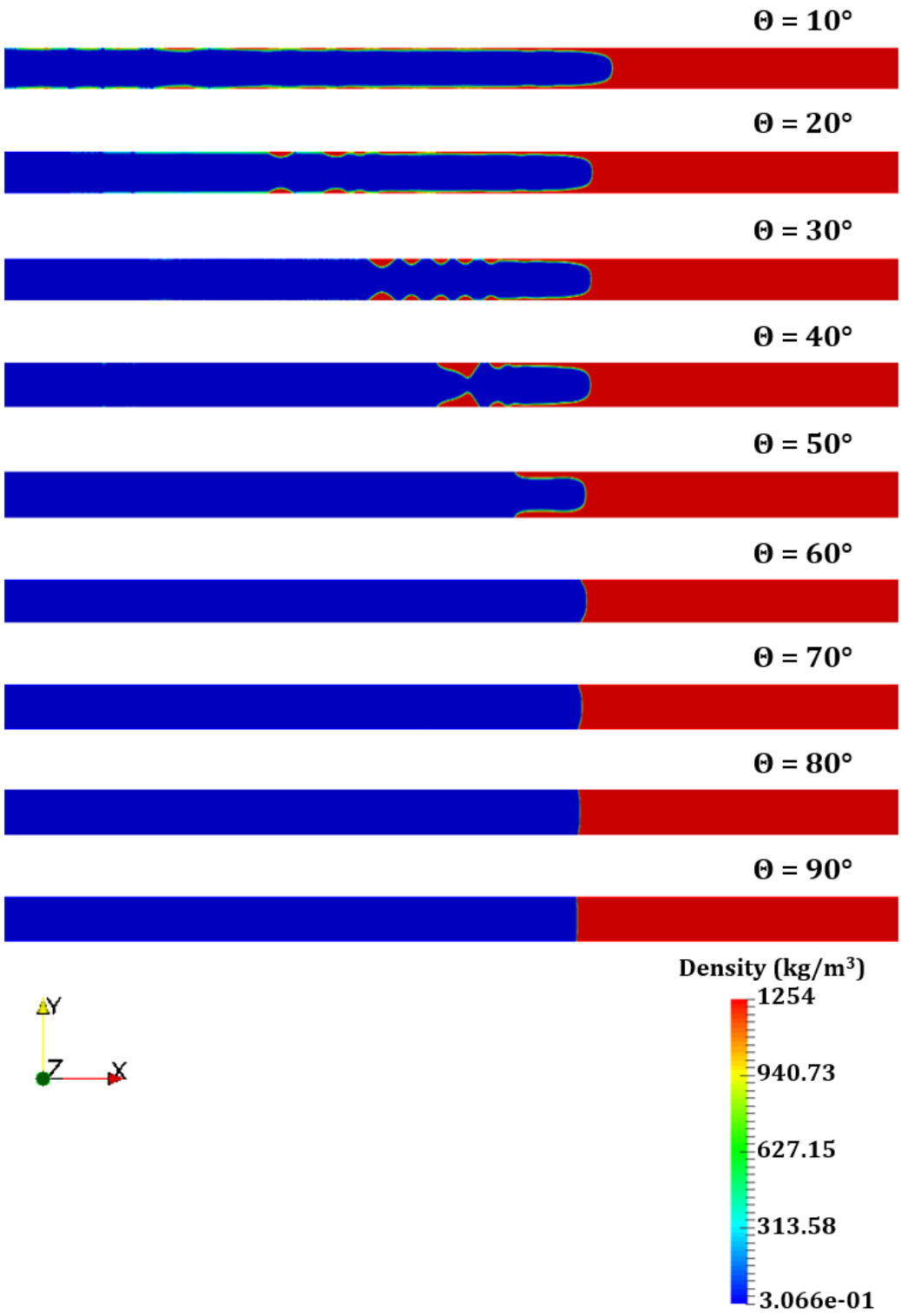

Figure 6.14: Evolution of the fluid-vapor interface as a function of the contact angle.

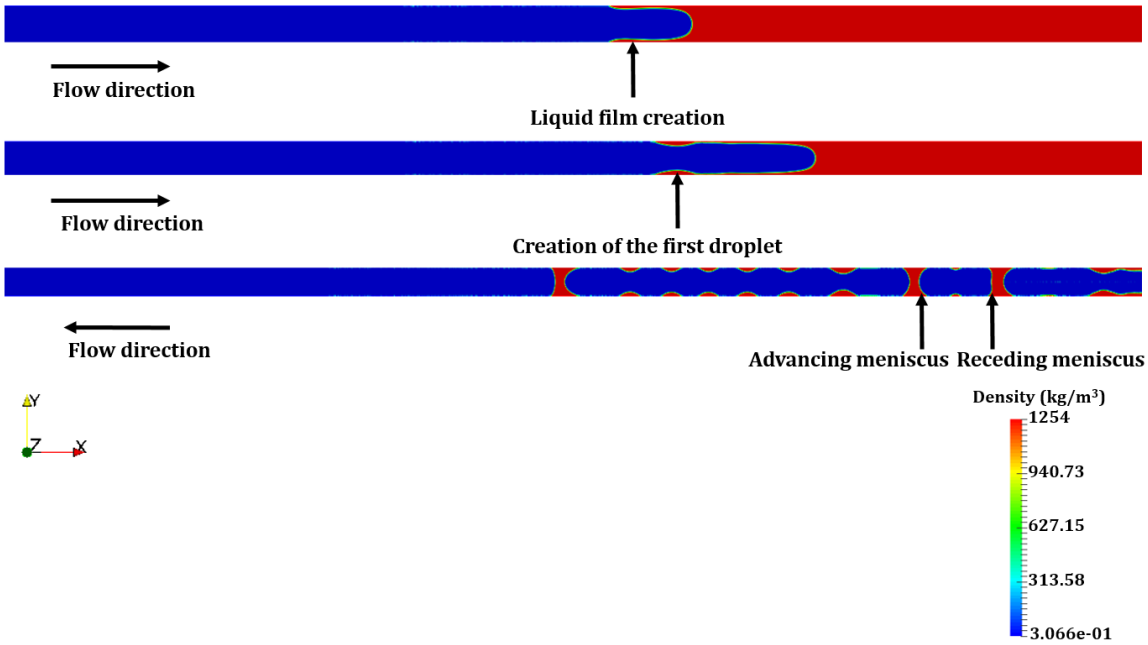

Figure 6.15: Numerical results of the dynamic flow simulation with a fixed contact angle of 30^o.

[131]. In real pulsating heat pipes, these droplets have two possible options: to evaporate contributing to the overall latent heat exchange (usually when they have a very small diameter comparing to the inner tube diameter), or to merge creating a new liquid slug.

$$\Delta p = \sigma(\frac{1}{R_1} + \frac{1}{R_2}) \tag{6.18}$$

where R_1 and R_2 are the radius of curvature.

Furthermore, it can be observed also in Fig. 6.15 that the nose and the tail of a vapor plug adopts a difference shape depending on the direction. It is important to consider that in a real situation, the vapor plug would probably be surrounded entirely by the liquid due to condensation, which is not simulated in this case because the heat equation is not solved in this dynamic model. Nevertheless it is possible to observe the shape adopted by the vapor plug varies depending on the flow direction. This has also been noticed by [78] and by [5] in some fluids.

Simulation results of the dynamic model have revealed the influence of the contact angle in the liquid film thickness and droplets formation due to Laplace instabilities. Moreover, it has been shown that the behavior of a two-phase interface in a capillary tube can be simulated using the VOF method in a 2D geometry, as a new alternative for future PHP simulations. Nevertheless, the model can still be optimized including more information about the triple line evolution, as studied by [132].

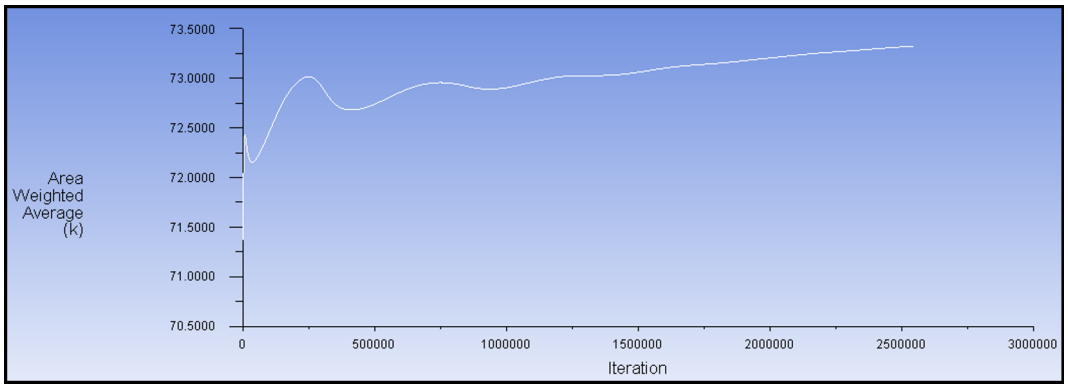

Figure 6.16: Temperature evolution during the thermal simulation with a fixed pressure at the condenser end.

6.4.2 Thermal model

A second group of simulations have been performed with the thermal model in order to complete the previous simulation results, including the thermal component. This thermal model represents the second step for a future completed 2D PHP numerical model.

A first group of thermal simulations have been performed fixing the pressure of the condenser end, as indicated in section 6.3.2. The simulation starts with unstable thermal conditions between the liquid and the vapor parts, as indicated in section 6.3.2. The temperature evolution at the point indicated in Fig. 6.12 in section 6.3.2, that represents the temperature sensor of the reference case, has been plotted and is presented in Fig. 6.16.

It has been observed with the ParaView® visualization platform, that after a few oscillations due to the initial thermal instabilities, the two-phase interface stops to oscillate and stays in the condenser part, maintaining one single liquid part and one single vapor part. Due to this, the liquid part do not enter anymore into the evaporator, which means that the heat from the evaporator solid part is not being transferred to the liquid part. The poor heat transfer to the vapor seems not to be enough to evacuate the heat generated by the heater and the temperature of the evaporator increases.

This reveals the necessity of having additional forces or instabilities, apart from thermodynamic instabilities, to maintain an oscillating two-phase flow in horizontal capillary tubes. It is important to note that in the reference case, the reservoir plays this role changing its pressure gradually and pushing the liquid in the condenser due to gravity force (see Fig. 6.1 in section 6.2). In pulsating heat pipes, one of these additional forces or instabilities could come from the pressure drop in the U-turns, as indicated by [17]. To confirm this hypothesis, future thermal simulations should be performed with another geometry and mesh that includes a U-turn or several alternating evaporator and condenser parts, which correspond to the next step of this simulation work. Unfortunately, there

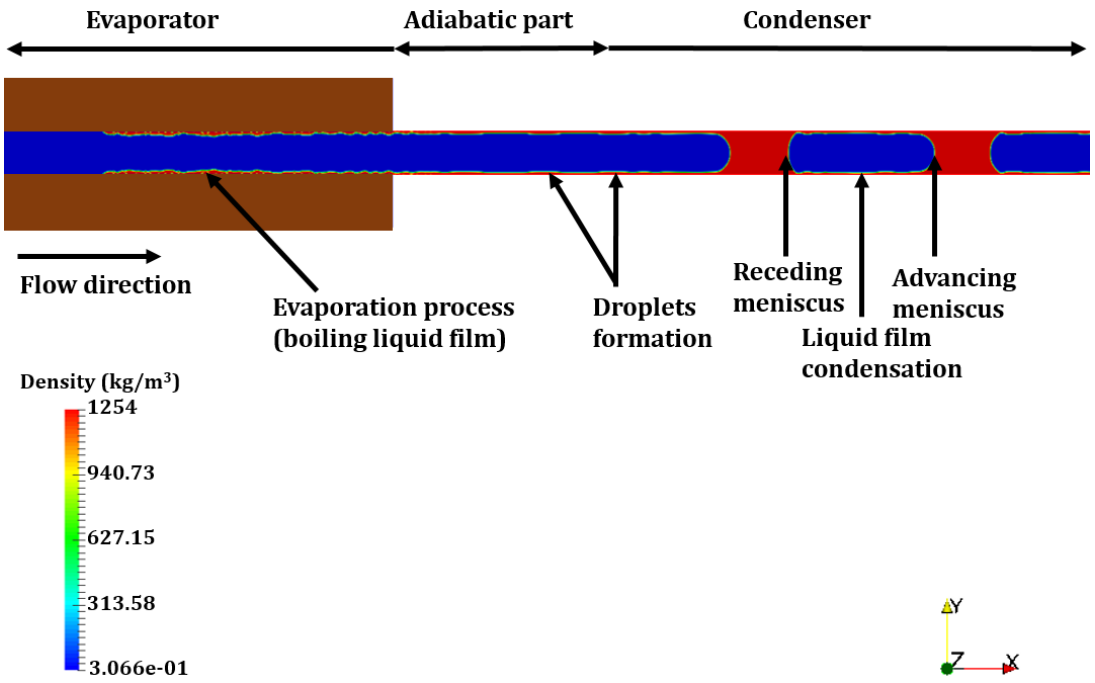

Figure 6.17: Zoom of the capillary tube of an instant of the second thermal simulation.

was no time in this research project to performed and include simulation results of a third geometry.

Nevertheless, it can be observed during the oscillations phases that, comparing to the dynamic simulation results, droplets formation due to Laplace instabilities are less pronounced due to condensation on the condenser part and the shape of the advancing and receding meniscus (or interface) are also different depending on the direction of the flow (see Fig. 6.17).

Furthermore, a last simulation has been performed with the present geometry to verify if the heat transfer between the liquid phase and the evaporator occurs and if it is in accordance with the experimental results of the reference case. For this, the boundary conditions at the end of the condenser have been changed for a mass flow UDF, imposing a sinusoidal evolution of the mass flow in accordance with oscillations of the interface position estimated in the reference case, as indicated in section 6.3.2.

The temperature evolution at the point representing the temperature sensor of the reference case has been plotted and is presented in Fig. 6.18. It can be observed that, after a few unstable oscillations due to the initial conditions, the temperature oscillates between 71 and 73.5 K, due to the penetration of the liquid phase into the evaporator zone and the associated heat transfer. The arrival of the liquid phase into the evaporator part allows a better heat transfer between the evaporator and the liquid, "carrying" the heat to the condenser zone. This confirms the satisfactory heat transfer between the solid and the liquid part, necessary for PHPs simulations. In addition, it has been possible to observe and verify the evaporation and condensation processes of the liquid film in the evaporator

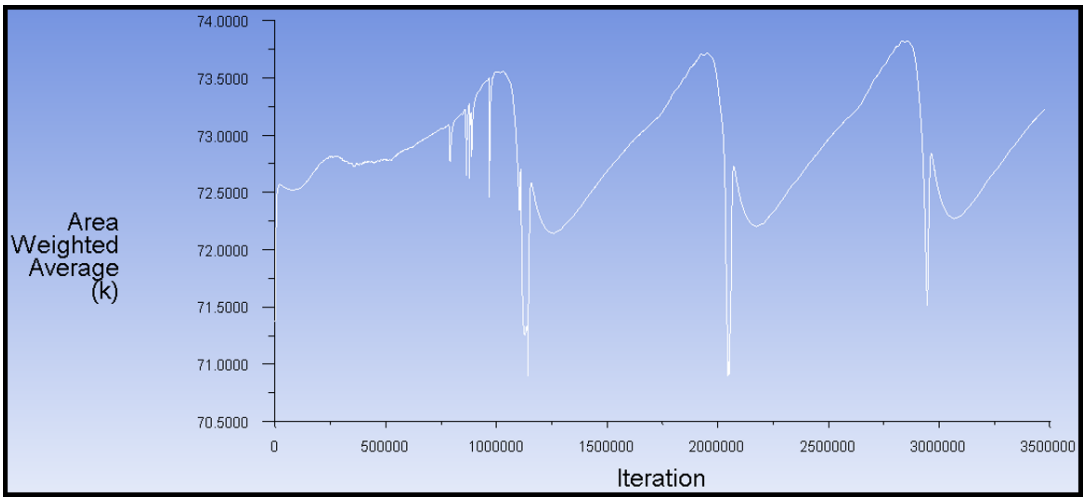

Figure 6.18: Temperature evolution during the thermal simulation with a variable mass flow at the condenser end.

and the condenser (see Fig. 6.17), as well as the specific dynamic flow characteristics of the two-phase interface presented previously in the dynamic simulation results.

Simulation results of the thermal model have shown the necessity of an additional instability (force or pressure variation) that contributes to global flow oscillations in pulsating heat pipes, apart from thermodynamic instabilities. Moreover, it has been verified the heat transfer between the evaporator solid part and the fluid and the condenser part and the fluid.

6.5 Conclusions

Two CFD models have been developed for transient simulations with a pressure-based Fluent solver using the Volume of Fluid (VOF) method in a 2D axisymmetric geometry: a "dynamic model" to analyze the interface shape evolution and a "thermal model" to simulate fluid oscillations due to thermal instabilities in PHPs.

Simulation results of the dynamic model have revealed the influence of the contact angle in the liquid film thickness and droplets formation due to Laplace instabilities, even if the model can still be optimized including more information about the triple line evolution. Simulation results of the thermal model have shown the necessity of an additional instability (force or pressure variation) complementary to thermodynamic instabilities to maintain the oscillating flow in PHPs. It has also been verified the heat transfer between the evaporator solid part and the fluid and the condenser part and the fluid in this type of simulation. Nevertheless, the model needs to be enriched by modifying the geometry to include alternating evaporator and condenser parts or adding a region creating pressure instabilities.

Even if this type of CFD 2D axisymmetric simulation is still at its early stages, it has been shown that transient simulations in CFD with a pressure-based Fluent solver using the Volume of Fluid (VOF) method in a 2D axisymmetric geometry can be developed for future 2D pulsating heat pipes simulations.

Synthesis and comments

The main goal of this research project was to characterize the thermohydraulic behavior of the meter-scale horizontal cryogenic pulsating heat pipes as a cooling solution for space superconducting magnets. To fulfill this objective, several experiments have been conducted in a cryogenic facility composed of three different horizontal pulsating heat pipes. In addition, a numerical 2D model has been proposed for future horizontal pulsating heat pipes simulations.

To characterize the pulsating heat pipes, different types of experiments have been performed:

- Progressive heat load tests (in three PHPs with the three different working fluids).
- Long stability tests (with different working fluids in the PHP with 36 turns).
- Start-up tests (with nitrogen and neon as working fluids in the PHP with 36 turns).
- Tests with a variable temperature at the condenser (with nitrogen and neon as working fluids in the PHP with 36 turns).
- Quench tests (with nitrogen and neon as working fluids in the PHP with 36 turns).

From all of these tests, it has been possible to characterize one of the longest existing meter-scale horizontal pulsating heat pipes. On one hand, certain characteristics of the PHPs already known from literature have been confirmed, on the other hand, new characteristics and specific thermohydraulic behaviors have been found during this project, opening up the debate about certain characteristics only associated to horizontal PHPs or exclusively related to the working fluid.

From experimental results of progressive heat load tests performed in the PHP with 36 turns and using nitrogen, neon and argon as working fluid it has been possible to determine the maximum heat load transfer capacity of the PHP with each different fluid and the corresponding thermal performance. It appears that nitrogen and argon achieved the highest equivalent thermal conductivities, while neon was able to transfer a higher power in stable conditions. In addition, assumptions about the thermodynamic state of the subcooled liquid phase in the PHP in stable operating conditions have been made and

the presence of local dry-outs has been identified.

Furthermore, during progressive heat load tests, each fluid presented its specific behavior. When using nitrogen, numerous local dry-outs at low heat loads have been observed, as well as a gradual temperature distribution along the same tube of the adiabatic part at high heat loads. With neon, the most noticeable characteristic is the increasing frequency of fluid oscillations when increasing the heat load. With argon, the gradual temperature distribution along the same tube of the adiabatic part is more noticeable at low heat loads and reduces with increasing heat load.

Moreover, with nitrogen and argon, the dry-out phase has been observed and characterized by a division of the PHP into two zones, one mainly full of vapor and a the other one mainly full of liquid. In the case of neon, the system never dried out and its maximum heat load transfer capacity was never reached up the cooling capacity of the cryocooler.

Differences between fluid's behaviors have been partly explained by analyzing the evolution of the fluid physical properties related to the movement and the heat transfer capacity. Nevertheless, further investigations need to be done to quantify precisely the influence of each parameter in the overall heat transfer.

In order to conclude about the relation between the liquid filling ratio in the PHP and its thermal performance, numerous progressive heat load tests have been performed at different filling ratios in closed configuration. Analyzing the corresponding equivalent thermal conductivities, it has been possible to determine optimum filling ratios giving the highest thermal performances. It appears that these optimum filling ratios go from 20 to 42% for the three fluids. Working in stable conditions with more vapor than liquid reveals the important role of the movement of the fluid generated mainly by the expansions and compressions of the vapor parts in the global working conditions of the PHP. In addition, the same tests have also been performed in open configuration, leaving the PHP connected to the buffer volume during each entire test. From this, it has been possible to conclude about the regulation made by the buffer volume in case of overpressure in the PHP.

Moreover, to demonstrate that the pulsating heat pipe with 36 turns is able to work in stable conditions during long periods, around 8 hours, and that it can be used as a reliable cooling system, long stability tests have been performed with nitrogen and argon at 20 W of heat load and neon at 50 W of heat load.

Other series of specific tests have been performed to determine the limits and the specific working conditions of the three pulsating heat pipes using nitrogen and neon as working fluids.

Start-up conditions concerning the initial temperature difference between the evaporator and the condenser as well as the initial input power at the evaporator, have been defined depending on the working fluid, confirming that a minimum amount of energy

is necessary for the filling process to attain stable oscillating phases since the beginning of the test. The influence of the temperature of the condenser has also been studied. It appears that the temperature of the condenser determines the range of working temperatures and pressures inside the PHP and, consequently, the real filling ratio during the filling process and the global thermal performances. The two other PHPs have also been tested and their maximum heat transfer capacities have been determined, confirming that it is more difficult to reach stable operating conditions when reducing the number of turns for long horizontal cryogenic PHP. The heat capacity and the thermal performance are also reduced.

From the "quench tests" it has been found that, when the PHP uses nitrogen as working fluid, temperature differences between the evaporator and the condenser during the test are lower than when using neon, nevertheless, time duration to recover stable working conditions after the quench are lower with neon. It also appears that opening the PHP to the buffer volume to recover stable working conditions could be a solution to reduce the pressure inside the PHP and re-start the oscillating flow faster.

Concerning the numerical part, a model has been proposed for transient simulations with a pressure-based Fluent solver using the Volume of Fluid (VOF) method in a 2D axisymmetric geometry. Certain characteristics of fluid dynamics in capillary tubes have been confirmed. It has also been noticed that thermodynamic instabilities are not enough to generate the fluid oscillations in capillary tubes, other phenomena, such as the pressure drop due to the turns have to be considered. Even if this 2D axisymmetric simulation is still at its early stages, several aspects of the models have been validated after analyzing the evolution of different parameters, suggesting that this kind of model can be considered as a new platform for future 2D pulsating heat pipes simulations.

Conclusions and perspectives

The results of the study presented here have allowed to push further the current knowledge of horizontal meter-scale cryogenic pulsating heat pipes.

From all of the experimental results, it has been possible to determine, according to the working fluid, the maximum heat transfer capacity of the PHP system, as well as its thermal performance and behavior. The dry-out phase has also been identified and characterized. It has been possible to determine the range of optimum filling ratios, the start-up conditions and the thermal response to sudden high heat transient inputs. The influence of the range of working temperatures and the number of turns in the PHP system have also been characterized.

Nevertheless, further investigations can still been performed to complete the characterization of horizontal meter-scale cryogenic pulsating heat pipes. These experiments difficult to achieved at these temperatures could enhanced by improving the instrumentation, including visualization. Moreover, several parameters should be tested to increase our understanding of the physics of the PHPs.

Without modifying the existing experimental facility, additional possible studies are listed below:

- Due to the extensive monitorization of the experimental facility, it has been possible to obtain precious information about the PHP operating conditions. The numerous pressure sensors in the PHP have indicated the global pressure of the system during tests. Nevertheless, it is important to note that all the pressure sensors are located close to the evaporator or the condenser but in the adiabatic part. It has been observed that during the dry-out process, the pressure and the temperatures of the adiabatic part decreases because of the condensation of the fluid in this zone due to the annihilation of heat transfer along the PHP. The increasing temperature of the evaporator during this dry-out indicates that there is an extensive evaporation of the fluid in this zone and that the fluid reaches a vapor superheated state. Therefore, a pressure sensor in one of the tubes located in the evaporator part would probably help to verify this.
- Always regarding the thermodynamic state of the fluid during operating conditions,

it should be an interesting option to be able to measure the real temperature and pressure with sensors directly in contact with the fluid. In addition, having both pressure and temperature sensors at the same location it would be possible to verify some specific phenomena such as the adiabatic compressions occurring during local dry-outs or the subcooled state of the liquid parts in operating conditions.

- Same progressive heat load tests could be performed modifying the positions of the temperature sensors. For example, adding temperature sensors in the other external tube could help to determine the influence of the asymmetric inlet of the PHP.

- Also, in order to compare experimental results with another cryogenic fluid, oxygen could be tested (range of working temperatures around 90 K). Analyzing physical properties of oxygen between 85 and 105 K, it appears that the surface tension and dynamic viscosity are in the same order of magnitude than argon. In addition, the latent heat and the rate of $(dp/dT)_{sat}$ are similar to nitrogen's ones. On the other hand, the density and specific heat are in the same order of magnitude than neon. All of this seems to indicate that oxygen as working fluid would probably have a similar fluid circulation than nitrogen and argon on one hand, and heat transfer capacity by advection through the liquid parts similar to neon. Testing oxygen would be an opportunity to verify all of these physical properties interpretation.

In addition, a few modifications of the existing experimental facility could be done for further investigations:

- First of all, changing the cold head, it would be possible to test neon as working fluid in the PHP having 36 turns without saturating the cold head and determine more precisely the maximum heat load transfer capacity of neon.

- Concerning the filling process, another interesting option could be to test the PHP by inserting the fluid through the evaporator phase. In the cryogenic field, PHP are generally filled through the condenser. Introducing the fluid in the PHP through the evaporator could give different results. On one hand, immediate evaporation of the fluid could create a huge vapor zone making difficult to create a good heat transfer. On the other hand, liquid arriving to the evaporator after being cooled in the tube thermalized at the surface of the thermal link could rapidly cool down the evaporator and reach faster stable operating conditions in the PHP.

- It would be also interesting to extend the length of the adiabatic part for future cooling magnet applications, to separate as much as possible the cryocooler from the fringe field. As mentioned in chapter 3, this experimental facility has operated in the past with a 3 m long adiabatic part, obtaining less stable results using nitrogen as working fluid than the existent version. To test a PHP with a total length of 2 m would be a good compromise.

- Also, reducing the parasite heat inputs arriving in the experimental facility (for example reducing the size of the cryostat or testing each PHP one by one in the cryostat), it would be possible to characterized more precisely each PHP, defining the heat transfer capacity to the nearest watt.
- It has been found that, when using neon as working fluid, the PHP system attains the highest heat transfer capacity, even if the inner diameter was larger than the maximum theoretical one. Testing systematically the same geometrical configuration with different tube sizes would give more answers about the limit of the inner diameter in horizontal PHPs.
- Visualization work with transparent tubes should help to confirm several phenomena, such as the liquid film evaporation during dry-outs or to characterize the fluid circulation with respect to the heat load.

More generally, for larger applications, it would be interesting to test and characterize different fluid mixtures to have a larger range of possible phase-change transitions. Furthermore, after notifying that neon presents excellent heat transfer capacity with an inner diameter larger than the critical one. It would be interesting to test the same capillary tubes in vertical position with neon, in order to verify if the existing limit defining the critical diameter has to be reviewed in the case of horizontal PHPs.

Concerning the numerical work, for future simulations, it would be interesting to test a bigger geometry with more number of evaporator and condenser parts, to approach the real PHP configuration. It would also be an interesting option to modify the geometry, including a U-turn and characterize the influence of the pressure drop due to the U-turn, generating pressure instabilities to maintain fluid oscillations. Another interesting study could be to test the fluid behavior under different diameters. This could give us possible answers concerning the larger size of the inner diameter when using neon in collaboration with experimental works. These calculations would probably need a huge capacity calculation of the machine.

Appendix A

Calibration of Pt100 temperature sensors below 60 K

When neon (Ne) is used as working fluid during the experimental tests, the range of working temperatures oscillates between 25 and 50 K. As noted in chapter 2, at these temperatures, the lowest temperature given by the calibration curve is 37 K, therefore an extension of the calibration curve is necessary below 50 K. The procedure of this new calibration is described as follows:

Firstly, the temperature of the empty PHP is fixed at 25 K (measured precisely with the Cernox® SD temperature sensors). Then, using the heaters, the temperature of the PHP is increased slowly to 100 K. During this process, the resistance measurements of the Pt100 Omega® sensors as well as the temperature measurements of one Cernox® SD sensor are registered using the Labview® program. The average of the resistance values of the Pt100 Omega® sensors are calculated in order to have a single array of resistance values. Then, a polynomial equation is obtained for the Pt100 Omega® sensors, relating the resistance to the temperature measurements given by the Cernox® SD sensor. Finally, the coefficients of this new polynomial equation are introduced into the general Labview® program of the PHP. Even if the polynomial equation has been obtained from averaged resistance values, the deviation between temperature measurements given by the Pt100 Omega® sensors after the calibration is lower than 0.2 K.

Appendix B

Calibration of Kulite Pressure sensors

The Kulite® pressure sensors are calibrated before every test period. This calibration is done using as reference the pressure measurements of the MKS Baratron® Absolute Pressure Transducer. Nitrogen (N_2) is the working fluid used for this calibration procedure which is described as follows:

First of all, the temperature of the PHP is fixed in order to have the fluid inside the PHP only in vapor phase. Then, the PHP is filled with nitrogen (N_2) gas in steps of 0.5 bar from 0 to 5 bars. During this filling operation, the voltage measurements given by the Kulite IS® pressure sensors, as well as the pressure measurements of the MKS Baratron® Absolute Pressure Transducer are registered using a specific Labview® program. A new polynomial equation is obtained for each Kulite IS® pressure sensor, relating their voltage measurements to the pressure given by the MKS Baratron® Absolute Pressure Transducer. Finally, the coefficients of these new polynomial equations are introduced into the general Labview® program of the PHP.

Appendix C

Thermal response simulation

A thermal simulation using COMSOL Multiphysics® has been performed to determine the accuracy of temperature measurements when liquid nitrogen is flowing in contact with the inner surface of a capillary tubing part of the adiabatic section in the PHP. A model of a single stainless steel capillary tube with three ceramic temperature sensors on its external surface has been developed with the same dimensions than the experimental setup, as it can be seen in Fig. C.1. To perform the simulation, experimental data from the reference test have been included and several assumptions have been considered.

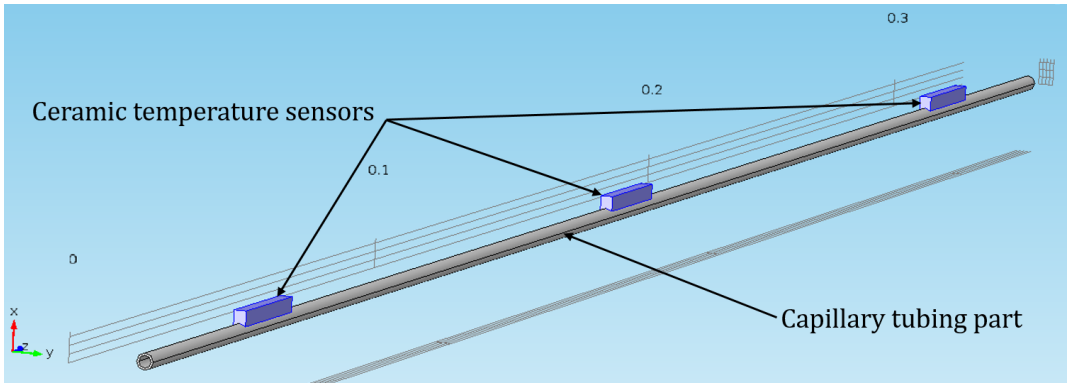

Figure C.1: Schematic illustration of the adiabatic tubing part of the Comsol Multiphysics® thermal simulation.

Firstly, a heat transfer coefficient h has been calculated from the following convective law:

$$Q = Ah(T_{fluid} - T_{surface}), \tag{C.1}$$

where Q is the heat input at the surface of the evaporator, A is the total surface of the U-turns of the evaporator and T_{fluid} and $T_{surface}$ are the temperatures of the fluid and the inner surface of the tube respectively.

The main assumptions to calculate the heat transfer coefficient h are:

- Heat transfer between the fluid and the capillary tube is considered to be mainly

Table C.1: Code input parameters.

Material properties (from CryoComp database [1])	
Stainless Steel (304L) Thermal Conductivity	8 W/(m.K)
Stainless Steel Density	7900 kg/m^3
Stainless Steel Specific Heat Capacity	190 J/kg.K
Ceramic Thermal Conductivity	193 W/(m.K)
Ceramic Density	3255 kg/m^3
Ceramic Specific Heat Capacity	75 J/kg.K
Geometric parameters	
Inner diameter	1.5 mm
Outer diameter	2 mm
Tube length	33 cm

through the liquid phase. Heat transfer between the vapor phase and the tube is considered negligible.

- The filling ratio (FR%) at the evaporator is considered at 50%.
- Values of Q, T_{fluid} and $T_{surface}$ are obtained from experimental data from the reference test, being 10 W, 76 K and 77.4 K, respectively. This values correspond to the condenser and evaporator average temperatures at 10 W of input power.
- The heat exchange surface considers the 36 capillary U-turns of the evaporator.

Considering this, h is calculated to be 280 W/m^2.K. It is important to note that this convective heat transfer coefficient h is calculated considering the evaporator's surface and temperature. The corresponding convective heat transfer coefficient in the adiabatic part would probably be higher due to a lower evaporation rate and cooler liquid slugs.

Secondly, the calculated coefficient h is then included in the model and the thermal simulation using COMSOL Multiphysics® is performed. Boundary conditions at both ends of the tube are fixed at 75 K and 77.4 K, being the experimental measured temperatures of the condenser and the evaporator respectively. In addition, code input parameters are given in Table C.1.

In this simulation, the thermal response to a sudden temperature increase of liquid nitrogen flowing in the capillary tube is evaluated. For this, temperatures at the inner surface of the tube and the difference sensors are calculated. Simulation results including the temperature evolution of one temperature sensor and the inner surface of the tube are plotted in Fig. C.2. It can be observed that, a sudden temperature increase has been imposed to the flowing liquid nitrogen in contact with the inner surface of the capillary tube, going from 76 K to 78 K during 5 s. Numerical results show that all the tempera-

ture sensors follow the same evolution, and the temperature difference between the inner surface of the tube and the ceramic sensors is lower than 0.1 K during the entire thermal response simulation. Furthermore, it can be observed that after 5 s, the difference between the imposed temperature of the fluid (78 K) and the simulated temperatures is 0.2 K, meaning that the temperature indicated by sensors of the adiabatic section and the fluid temperature are almost the same (less than 0.2 K difference). A thermal response of 5 s is in the order of magnitude (or even lower) of temperature oscillations in the adiabatic part, as it can be seen, for example, in Fig. 3.7, 3.8, 3.9 and 3.10 in chapter 3.

It is important to note that, if the fluid in contact with the inner surface of the tube were in vapor state, this thermal response could not be so fast and accurate due to the lower thermal conductivity of vapor nitrogen (20 times lower than liquid nitrogen). For that reason, this simulation has been performed considering liquid nitrogen in contact with the inner surface of the tube.

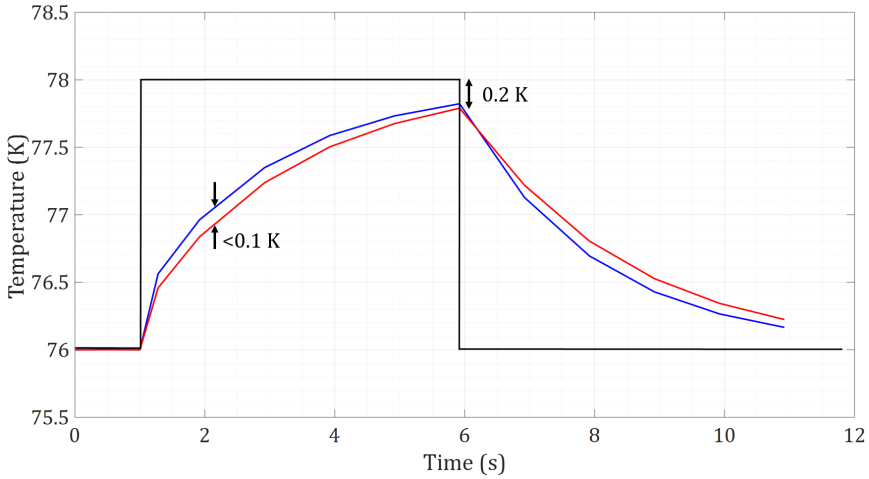

Figure C.2: Imposed temperature increment to the liquid nitrogen in contact with the inner surface of the capillary tube (—), and temperature response at the inner surface of the tube (—) and at one of the sensors (—) (all the sensors show exactly the same tendency).

Appendix D

Extrapolation of the thermal simulation to the other working fluids

In the previous appendix C, are presented the results of a thermal simulation performed to determine the accuracy of temperature measurements when liquid nitrogen is flowing in contact with the inner surface of a capillary tubing part of the adiabatic section in the PHP.

In order to verify if the simulation results can be extrapolated to the two other working fluids, the following reasoning has been done:

The heat transfer coefficient h used for the simulation is calculated from the convective law,

$$Q = Ah(T_{fluid} - T_{surface}), \tag{D.1}$$

where Q is the heat input at the surface of the evaporator, A is the total surface of the U-turns of the evaporator and T_{fluid} and $T_{surface}$ are the temperatures of the fluid and the inner surface of the tube respectively.

Analyzing the experimental results of the progressive heat load tests in chapter 4, it can be seen that, for the same amount of heat load, when using neon as working fluid the temperature difference between the average temperature of the adiabatic part (here considered as T_{fluid}) and the surface of the evaporator (here considered as $T_{surface}$) is 4 K. However, when using nitrogen and argon this temperature differences are 2 and 2.5 K, respectively. Due to this, the heat transfer coefficient h when using neon should be 2 times lower because the temperature difference is 2 times higher. Nevertheless, apart from the temperature difference, it is important to know that the total heat exchange surface of the U-turns of the evaporator (A) has been calculated considering a liquid filling ratio

of 50%, which is a very constraining hypothesis. Actually, the real average real filling ratios of nitrogen and neon during the progressive heat load tests are 42.6% and 25%, respectively. So, the heat exchange surface when using neon is 1.7 times smaller. From this, we can conclude that, the heat transfer coefficient h is finally considerably similar in both cases (nitrogen and neon), because the high temperature difference obtained with neon is compensated by the lower filling ratio and, consequently, the small heat exchange surface, for the same amount of heat load.

Then, we can consider that the numerical results of the thermal simulation described in appendix C can be extrapolated to the other fluids, neon and argon, being possible to conclude that we are also able to measure the presence of liquid neon or argon in contact with the inner surface of a capillary tubing part of the adiabatic section in the PHP.

Appendix E

Power spectrums of temperature oscillations

Examples of power spectrums of temperature sensors during progressive heat load tests using neon and argon as working fluids.

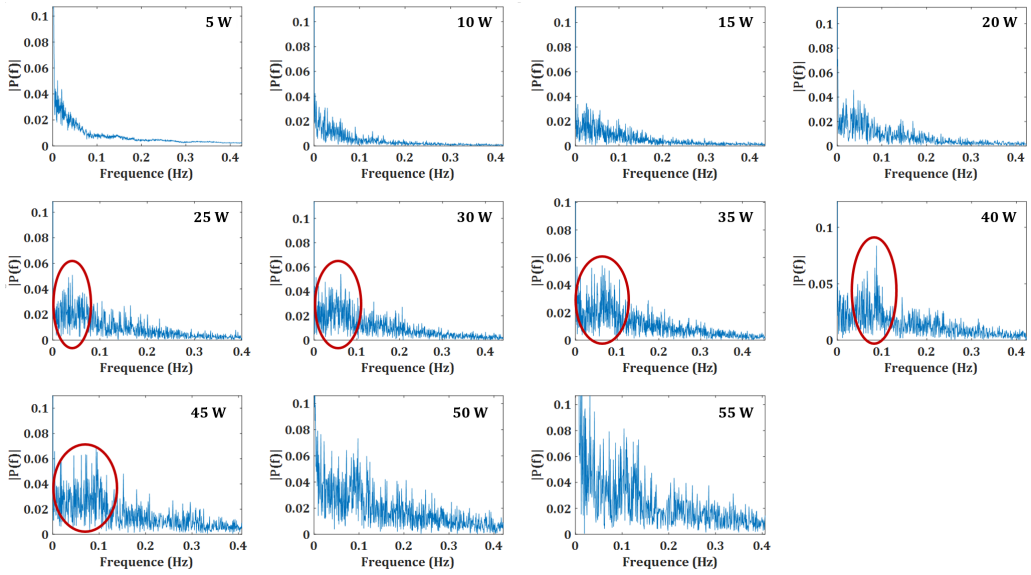

Figure E.1: Power spectrum evolution of temperature oscillations on sensor TT45 during a progressive heat load test using neon as working fluid.

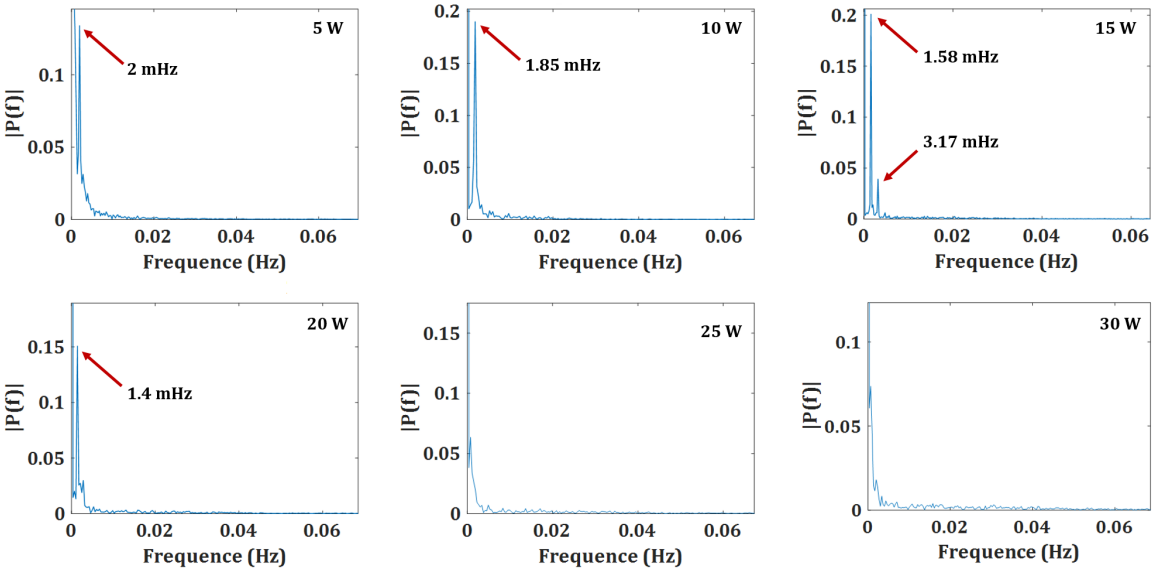

Figure E.2: Power spectrum evolution of temperature oscillations on sensor TT30 during stable phases of a progressive heat load test using argon as working fluid.

Appendix F

Fluid properties

The evolution of physical properties of the three cryogenic working fluids tested during the research project are presented in this section. These properties have been obtained using NIST Refprop Database [2] from temperature and pressure evolutions during progressive heat load tests.

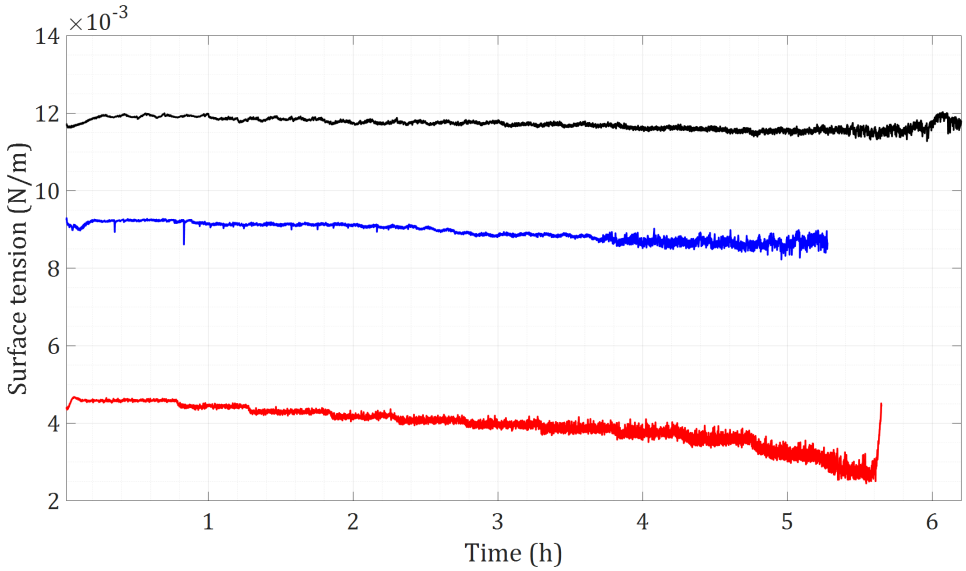

Figure F.1: Evolution of the surface tension during progressive heat load tests of the three working fluids: nitrogen (—), neon (—) and argon (—).

The Jacob number represents the ratio of the sensible heat for a given volume of liquid to heat or cool through the temperature difference in arriving to its saturation temperature, to the latent heat required in evaporating the same volume of vapor [133] and is defined as follows:

$$Ja = \frac{Cp \cdot \Delta T}{Lv},$$

where Cp is the specific heat, Lv is the latent heat and ΔT is the temperature difference between the saturation temperature and the temperature of the condenser.

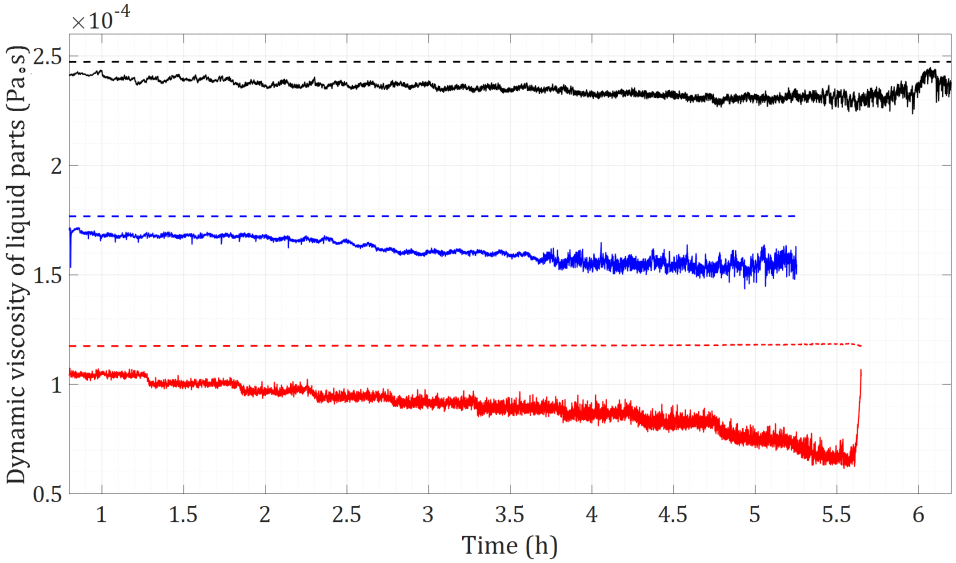

Figure F.2: Evolution of the dynamic viscosity of the liquid phase during progressive heat load tests of the three working fluids: nitrogen at saturation temperature (—), nitrogen at condenser's temperature (— —), neon at saturation conditions (—), neon at condenser's temperature (— —), argon at saturation conditions (—) and argon at condenser's temperature (— —).

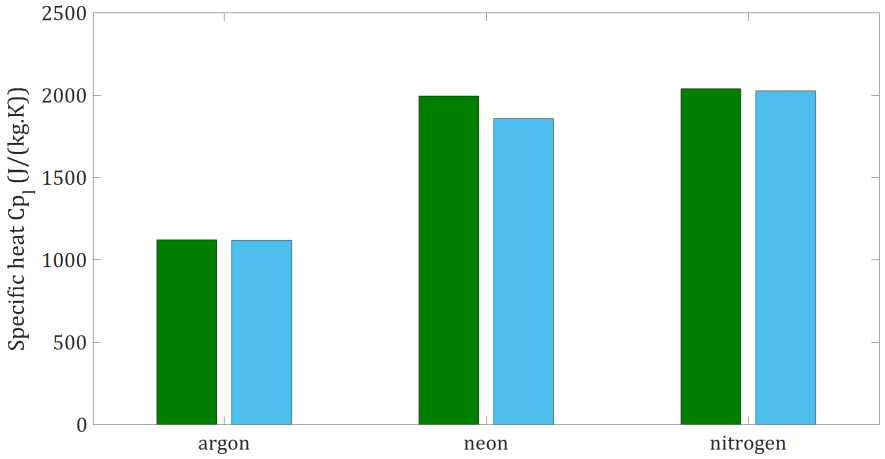

Figure F.3: Average values of the specific heat of the liquid parts during progressive heat load tests of the three working fluids: nitrogen, neon and argon. The specific heat is calculated considering the liquid parts at saturation temperature (—) and at the temperature of the condenser (—).

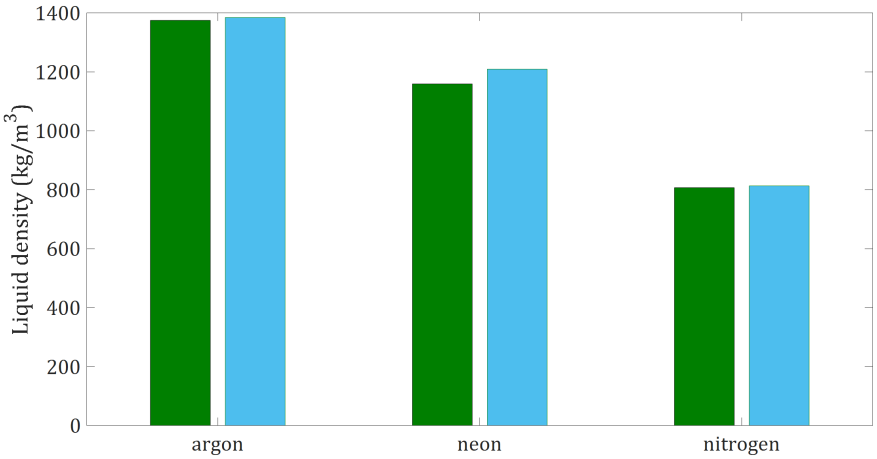

Figure F.4: Average values of the liquid density during progressive heat load tests of the three working fluids: nitrogen, neon and argon. The liquid density is calculated at saturation temperature (—) and at the temperature of the condenser (—).

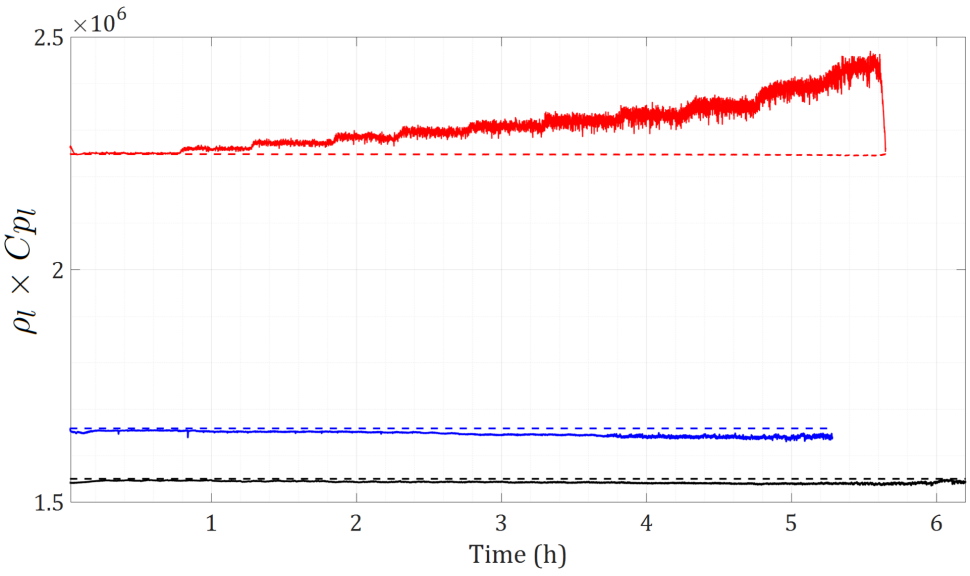

Figure F.5: Evolution of the product $\rho_l \times Cp_l$ during progressive heat load tests of the three working fluids: nitrogen at saturation temperature (—), nitrogen at condenser's temperature (— —), neon at saturation conditions (—), neon at condenser's temperature (— —), argon at saturation conditions (—) and argon at condenser's temperature (— —).

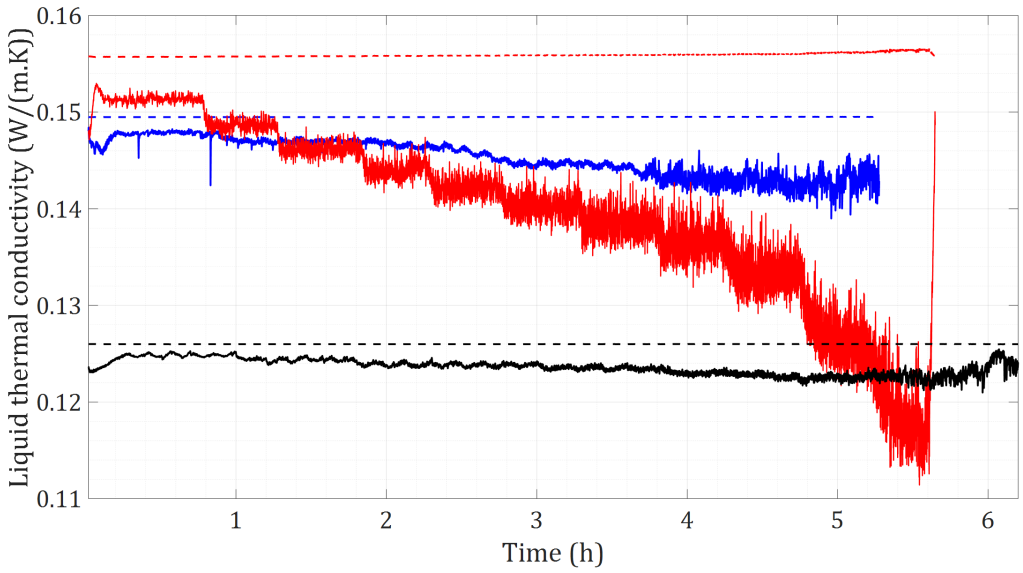

Figure F.6: Evolution of the liquid thermal conductivity during progressive heat load tests of the three working fluids: nitrogen at saturation temperature (—), nitrogen at condenser's temperature (— —), neon at saturation conditions (—), neon at condenser's temperature (— —), argon at saturation conditions (—) and argon at condenser's temperature (— —).

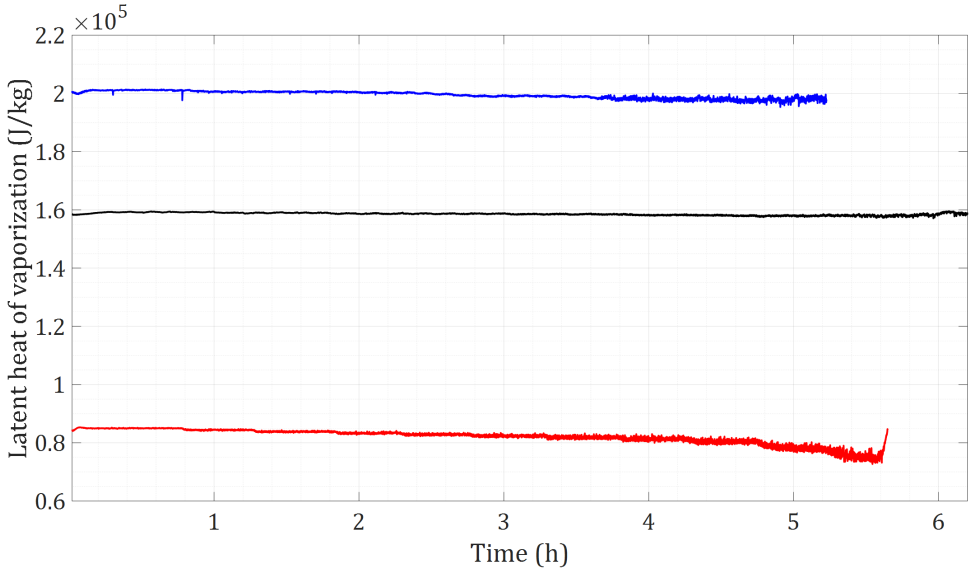

Figure F.7: Evolution of the latent heat during progressive heat load tests of the three working fluids: nitrogen (—), neon (—) and argon (—).

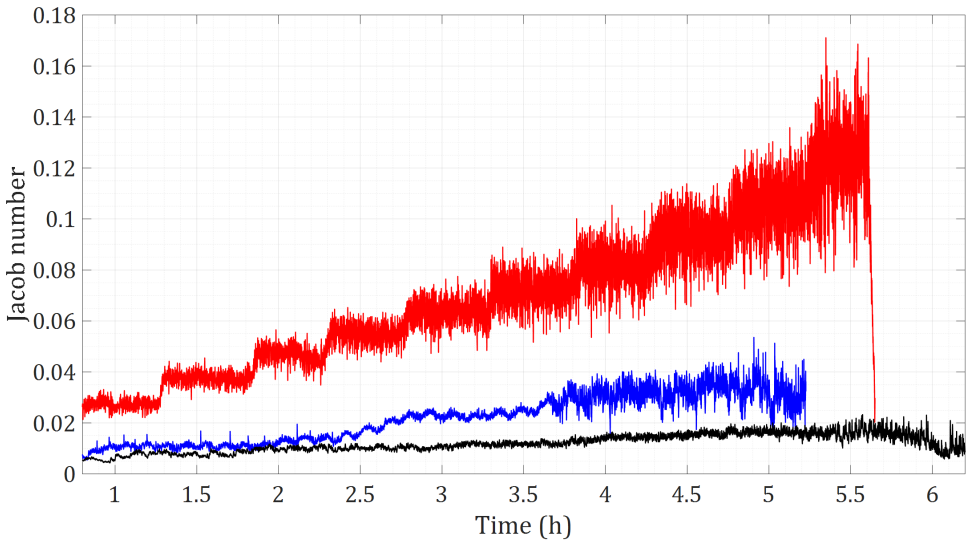

Figure F.8: Evolution of the Jacob number during progressive heat load tests of the three working fluids: nitrogen (—), neon (—) and argon (—).

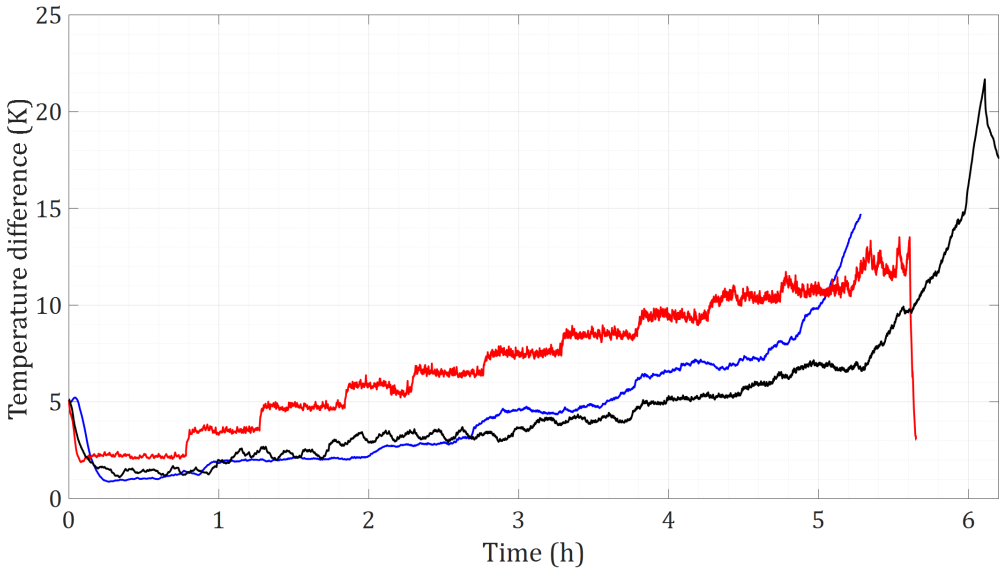

Figure F.9: Evolution of the temperature difference between the evaporator and the condenser during progressive heat load tests of the three working fluids: nitrogen (—), neon (—) and argon (—).

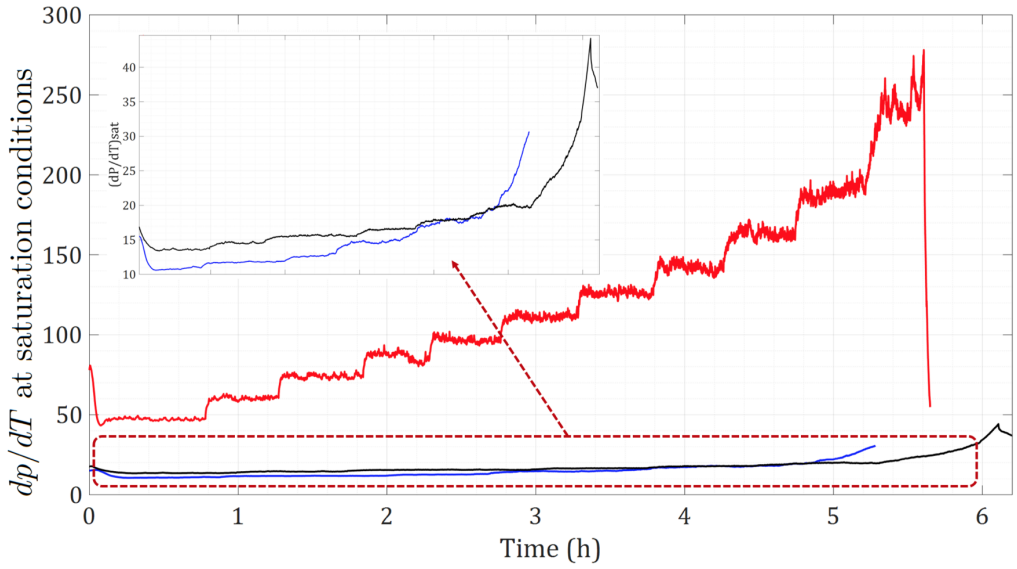

Figure F.10: Evolution of the rate dp/dT at saturation conditions during progressive heat load tests of the three working fluids: nitrogen (—), neon (—) and argon (—).

Appendix G

Neon's critical diameter

The evolution of the properties of neon to determine its maximum critical diameter during a progressive heat load test have been calculated using NIST Refprop Database [2].

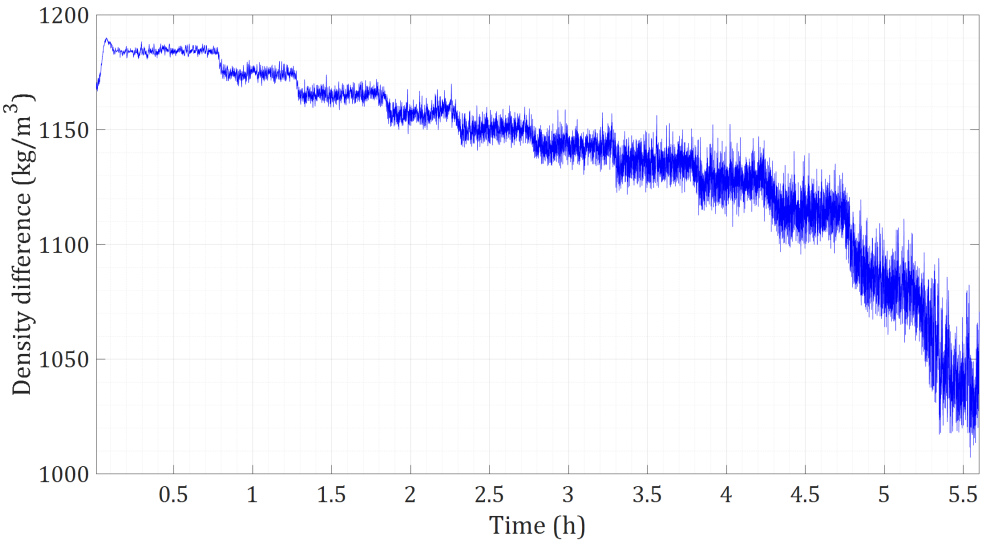

Figure G.1: Evolution of the density difference between the liquid and the vapor phase during a progressive heat load test with neon as working fluid.

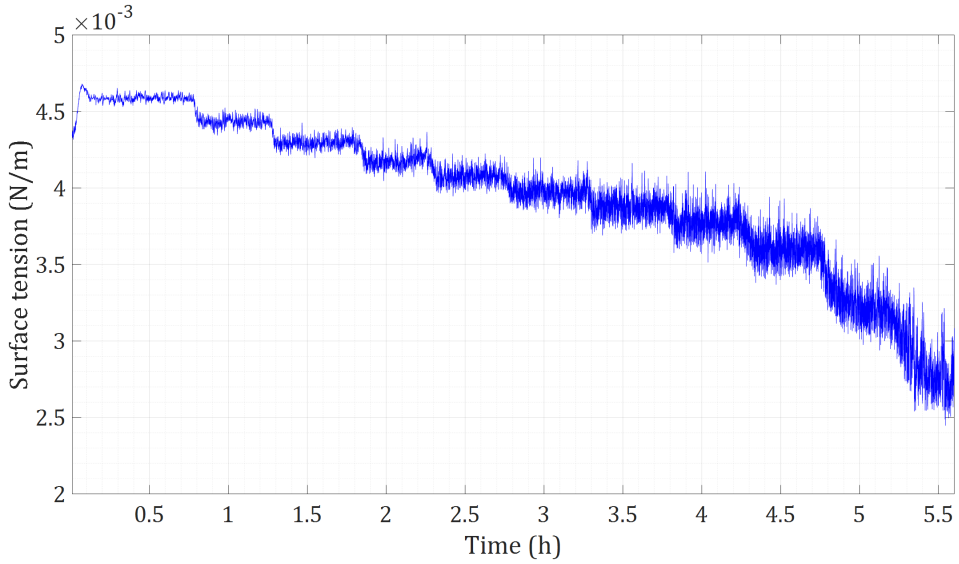

Figure G.2: Evolution of the surface tension during a progressive heat load test with neon as working fluid.

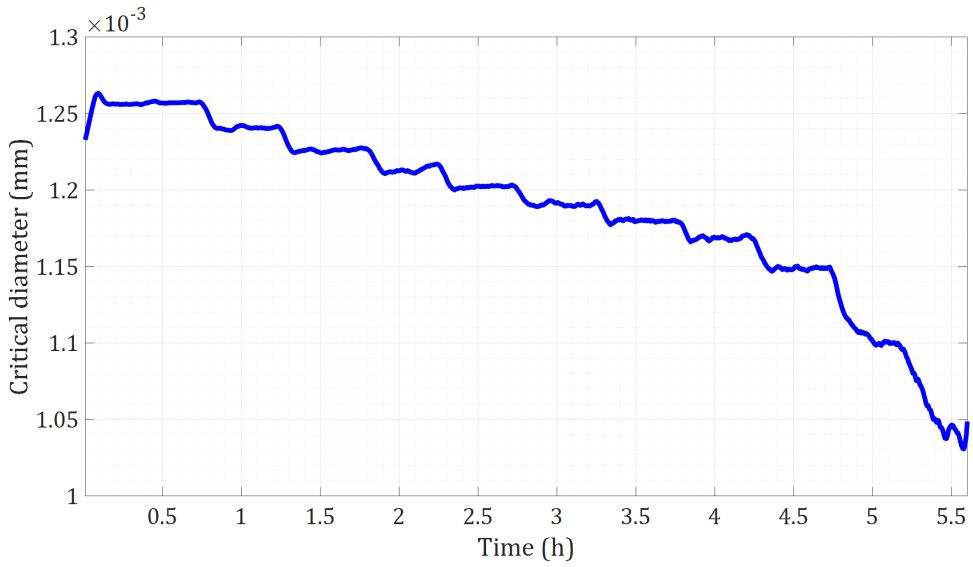

Figure G.3: Evolution of the critical diameter during a progressive heat load test with neon as working fluid.

Appendix H

Example of experimental results at different start-up conditions

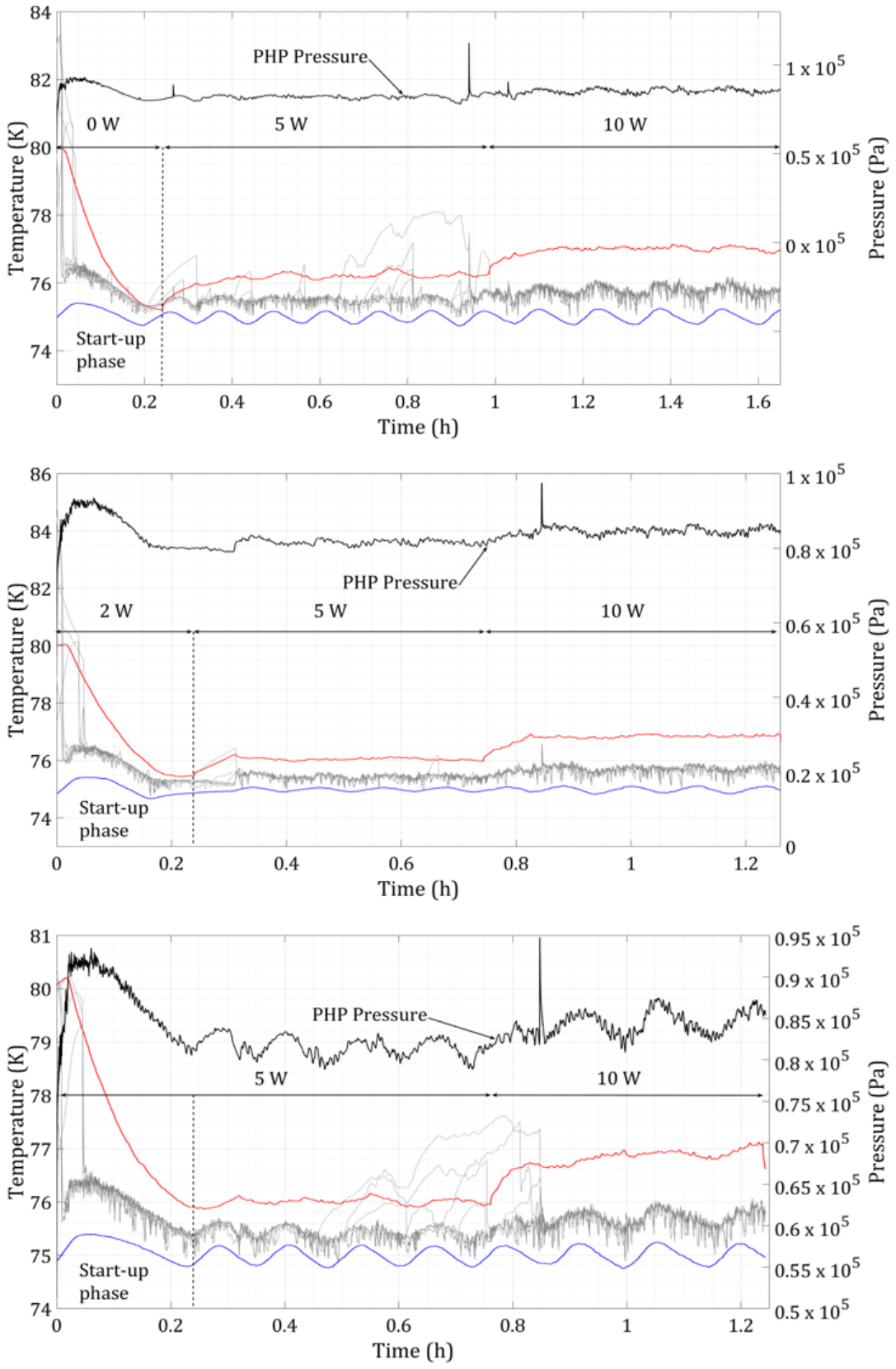

Figure H.1: Evolution of the PHP pressure (—), the average temperature of the evaporator (—) and the condenser (—) and the temperatures of the adiabatic part (—) of a start-up test in closed configuration using nitrogen as working fluid (initial filling ratio of 30 %) with different initial heat loads during the filling process in the PHP with 36 turns.

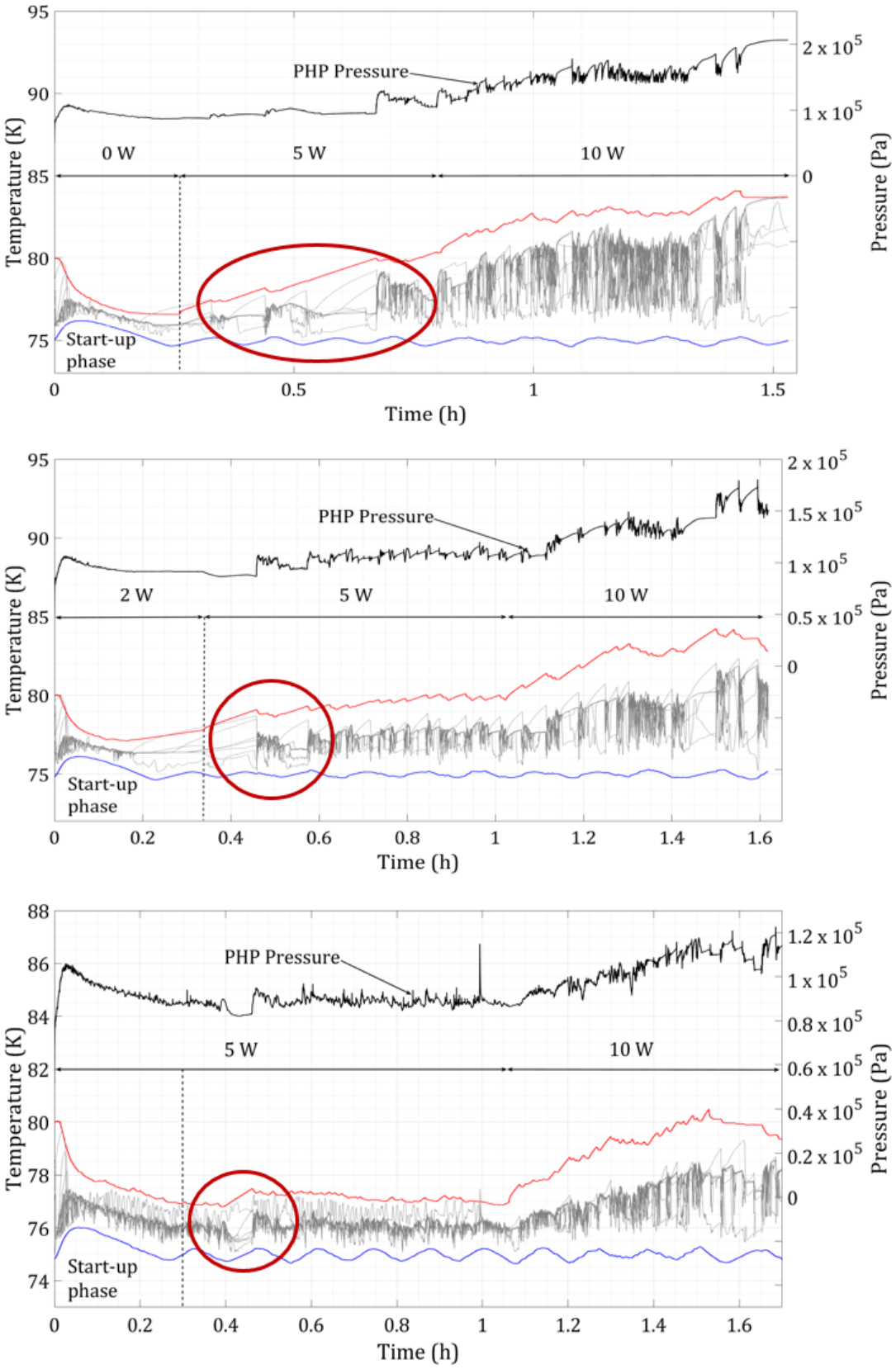

Figure H.2: Evolution of the PHP pressure (—), the average temperature of the evaporator (—) and the condenser (—) and the temperatures of the adiabatic part (—) of a start-up test in closed configuration using nitrogen as working fluid (initial filling ratio of 70 %) with different initial heat loads during the filling process in the PHP with 36 turns. The fluid stop phenomena are identified by a red ellipse.

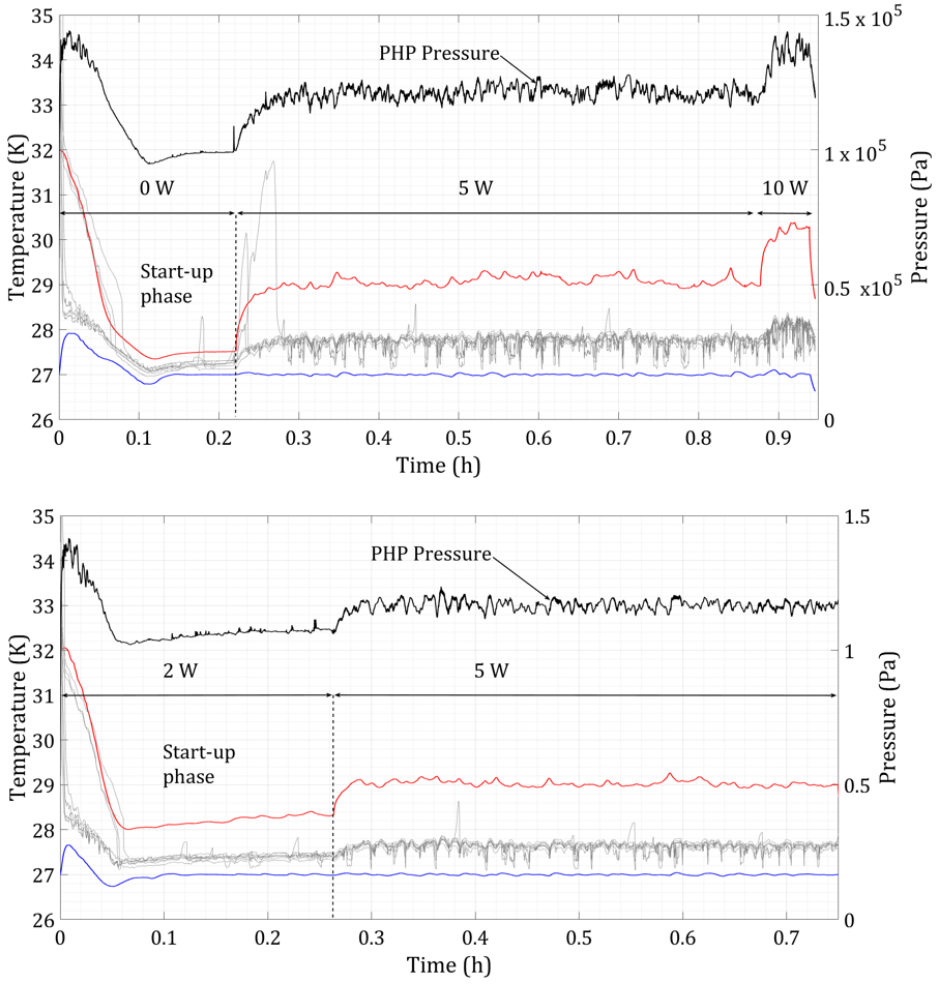

Figure H.3: Evolution of the PHP pressure (—), the average temperature of the evaporator (—) and the condenser (—) and the temperatures of the adiabatic part (—) of a start-up test in closed configuration using neon as working fluid (initial filling ratio of 30 %) with different initial heat loads during the filling process in the PHP with 36 turns.

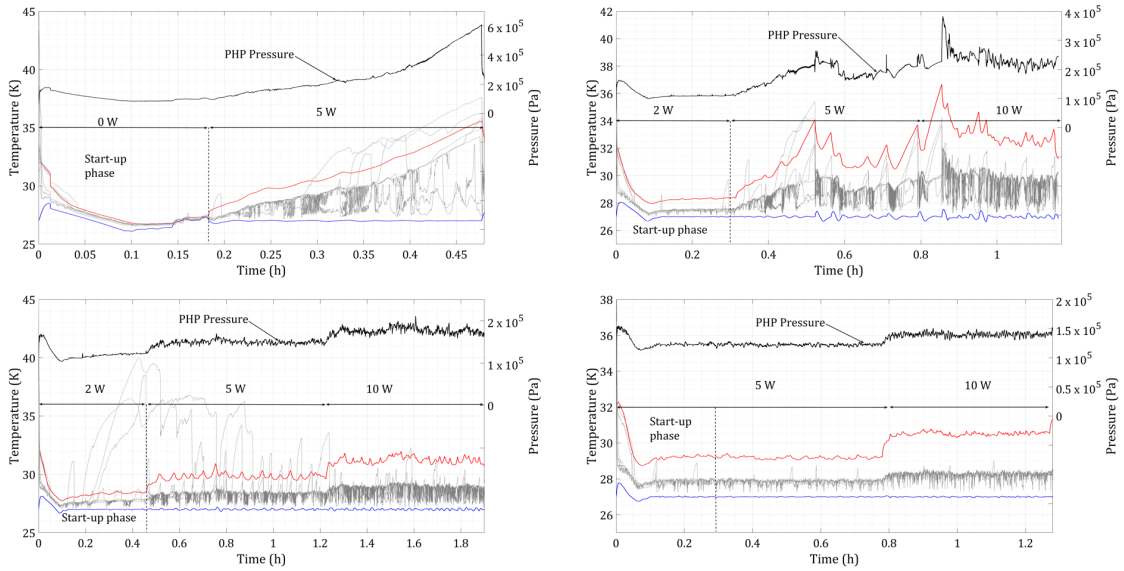

Figure H.4: Evolution of the PHP pressure (—), the average temperature of the evaporator (—) and the condenser (—) and the temperatures of the adiabatic part (—) of a start-up test in closed configuration using neon as working fluid (initial filling ratio of 50 %) with different initial heat loads during the filling process in the PHP with 36 turns.

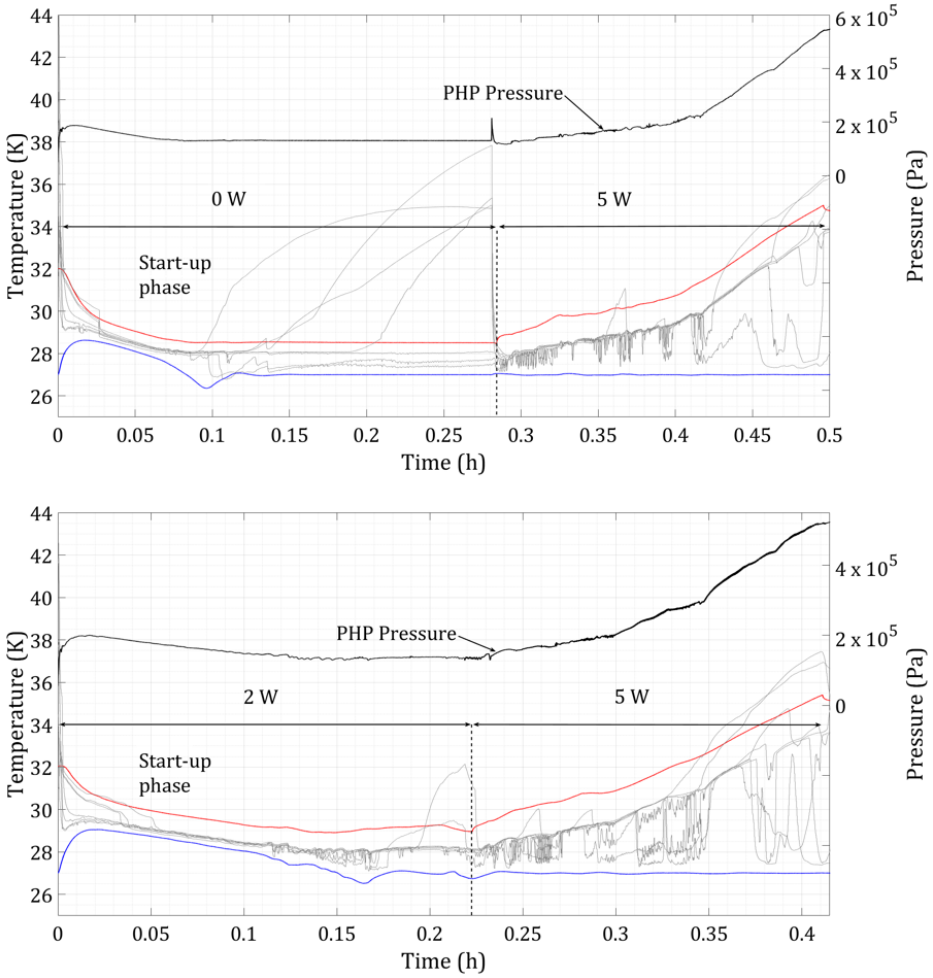

Figure H.5: Evolution of the PHP pressure (—), the average temperature of the evaporator (—) and the condenser (—) and the temperatures of the adiabatic part (—) of a start-up test in closed configuration using neon as working fluid (initial filling ratio of 70 %) with different initial heat loads during the filling process in the PHP with 36 turns.

Appendix I

Complementary experimental results of quench tests

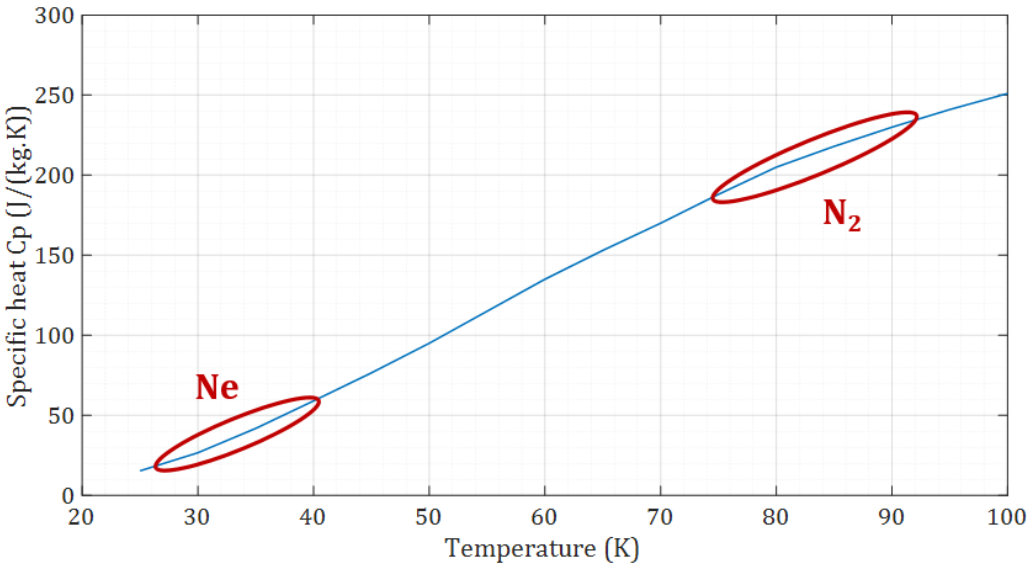

Figure I.1: Evolution of the specific heat of copper (RRR=50) with temperature (from CryoComp database [1]). Ranges of working temperatures of the PHP using neon and nitrogen as working fluids are indicated.

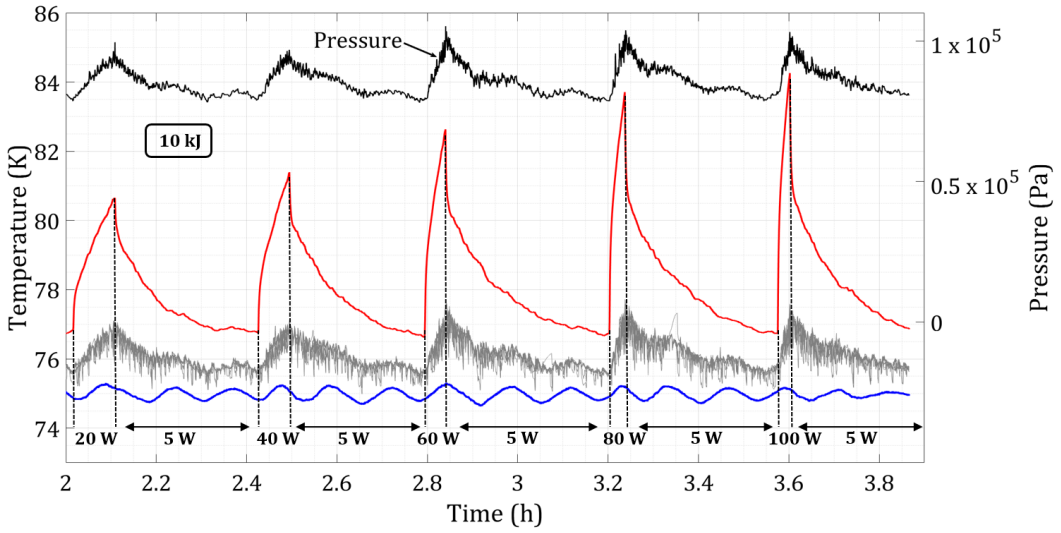

Figure I.2: Evolution of the PHP pressure (—), the average temperature of the evaporator (—) and the condenser (—) and the temperatures of the adiabatic part (—) of several quench tests of 10 kJ using nitrogen as working fluid (initial filling ratio of 50 %).

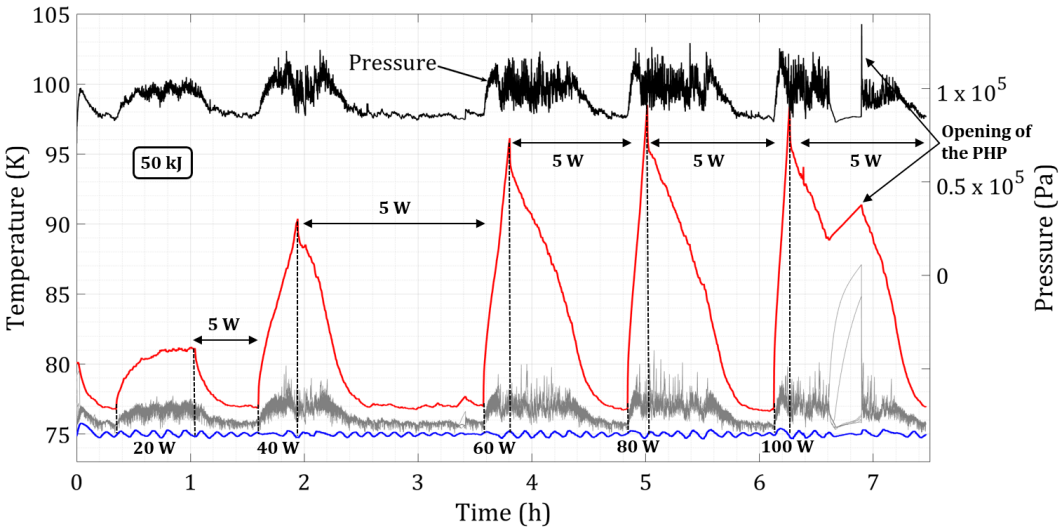

Figure I.3: Evolution of the PHP pressure (—), the average temperature of the evaporator (—) and the condenser (—) and the temperatures of the adiabatic part (—) of several quench tests of 50 kJ using nitrogen as working fluid (initial filling ratio of 50 %).

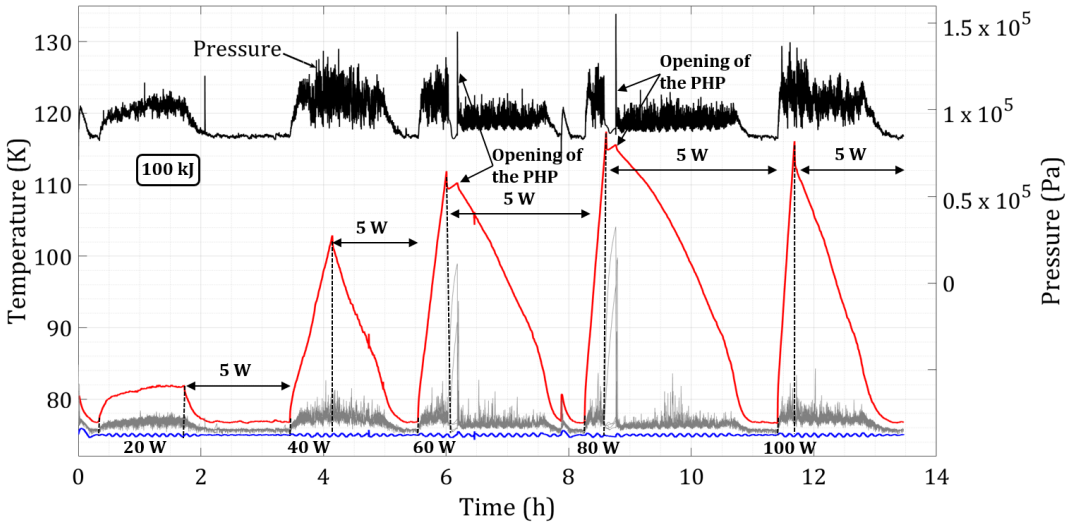

Figure I.4: Evolution of the PHP pressure (—), the average temperature of the evaporator (—) and the condenser (—) and the temperatures of the adiabatic part (—) of several quench tests of 100 kJ using nitrogen as working fluid (initial filling ratio of 50 %).

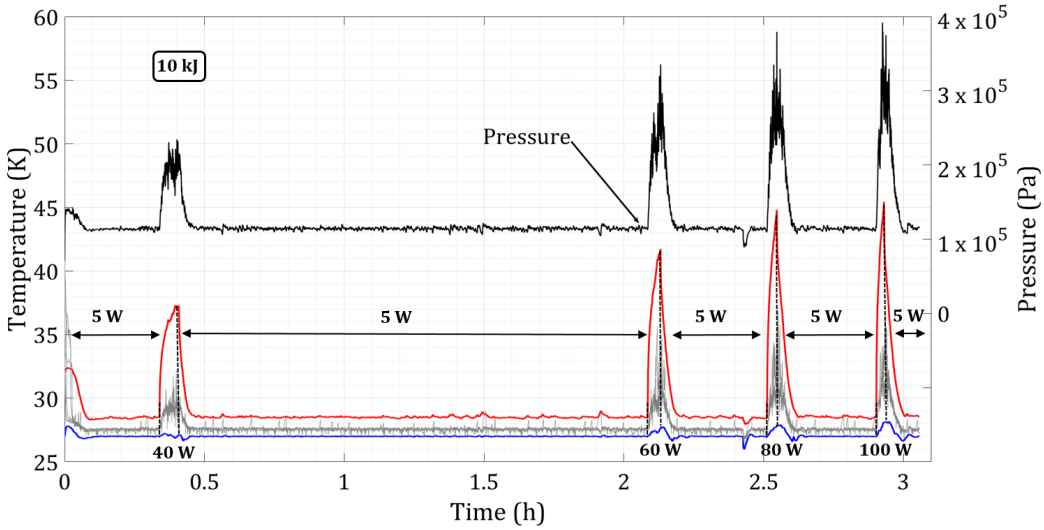

Figure I.5: Evolution of the PHP pressure (—), the average temperature of the evaporator (—) and the condenser (—) and the temperatures of the adiabatic part (—) of several quench tests of 10 kJ using neon as working fluid (initial filling ratio of 30 %).

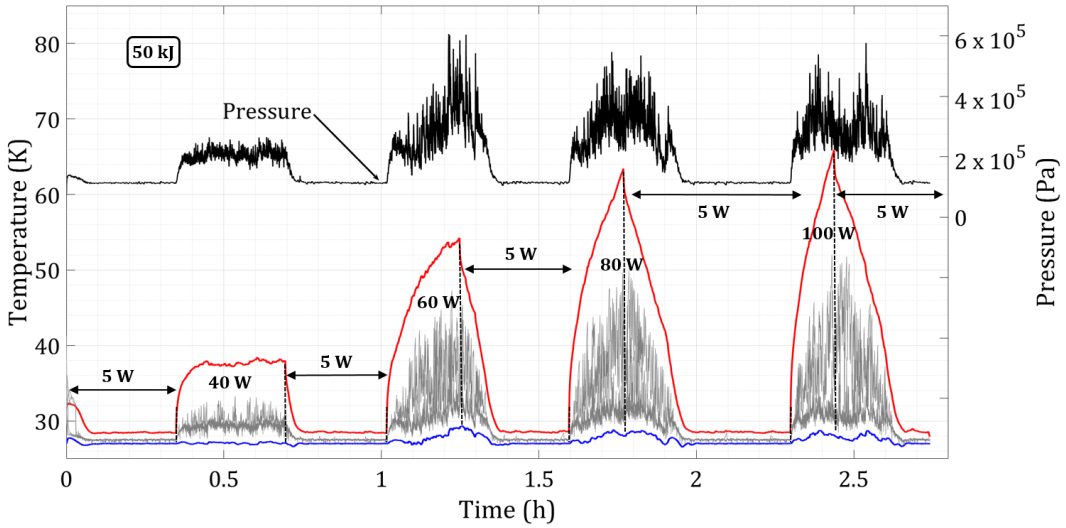

Figure I.6: Evolution of the PHP pressure (—), the average temperature of the evaporator (—) and the condenser (—) and the temperatures of the adiabatic part (—) of several quench tests of 50 kJ using neon as working fluid (initial filling ratio of 30 %).

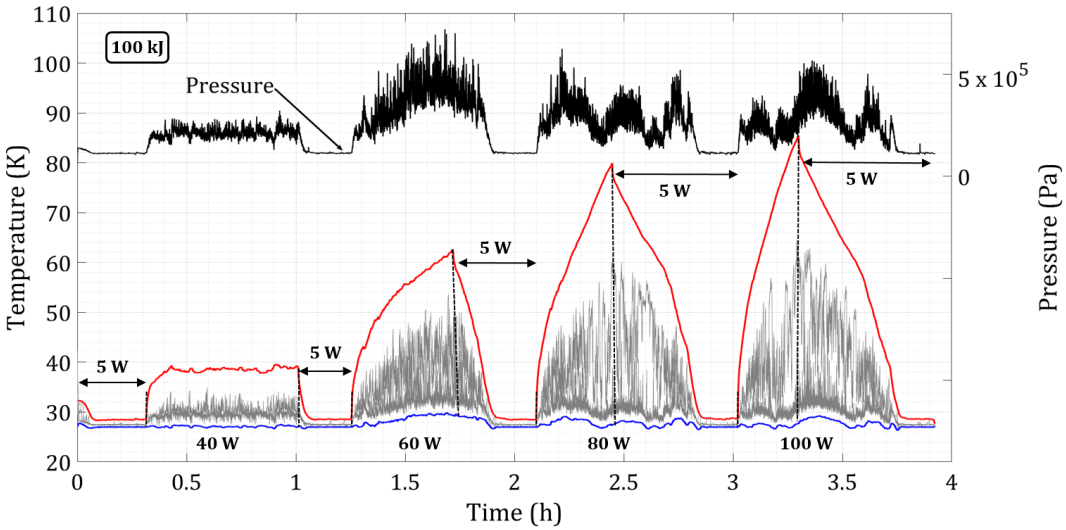

Figure I.7: Evolution of the PHP pressure (—), the average temperature of the evaporator (—) and the condenser (—) and the temperatures of the adiabatic part (—) of several quench tests of 100 kJ using neon as working fluid (initial filling ratio of 30 %).

Appendix J

Complementary information of the simulation work

A second mesh with larger cells has been tested with the dynamic model to compare the sharpness of the liquid-vapor interface. This second mesh is composed of 27 873 square cells with a minimum and maximum face areas between 1.000667×10^{-4} and 1.111111×10^{-4} m^2. Images of this second mesh are given in Fig. J.1 and J.2. This mesh has not been selected because it has been observed from the simulation results that the liquid film was very large not clearly defined, the cells were too large in this case.

In the case of the thermal model, a second mesh with smaller cells has also been tested to verify that we do not lose information after including a thermal component to the previous dynamic model. This second mesh is composed of 592 655 square cells with a minimum face area of 2.040816×10^{-5} m^2 and a maximum face area of 1.020408×10^{-3} m^2 corresponding to the solid part. Images of this second mesh are given in Fig. J.3, J.4 and J.5. This mesh has not been selected because it has been observed from the simulation results that simulation defaults appear indicating a sudden phase change of the total volume of a cell from one step to the other due to slight temperature changes. The cells were probably too small in that case.

The liquid-vapor saturation curve of Oxygen is given in Fig. J.6.

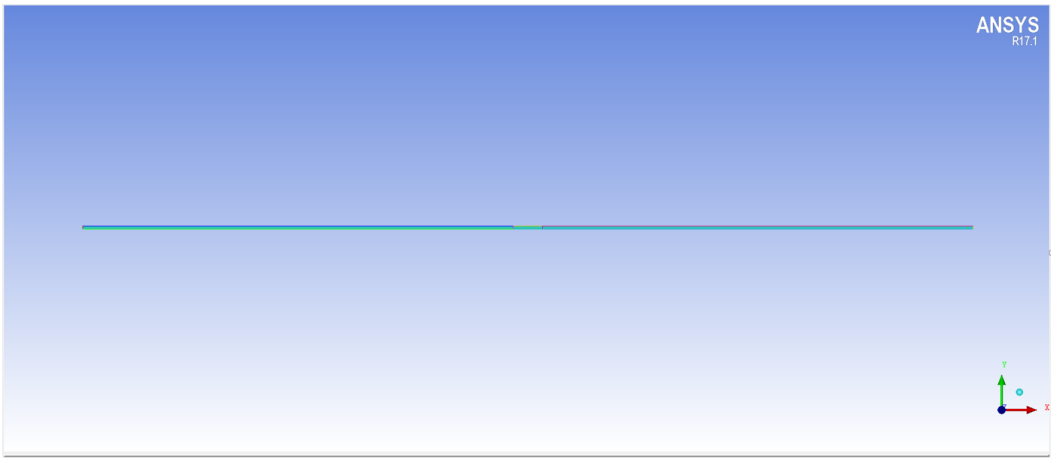

Figure J.1: Second mesh tested with the dynamic model.

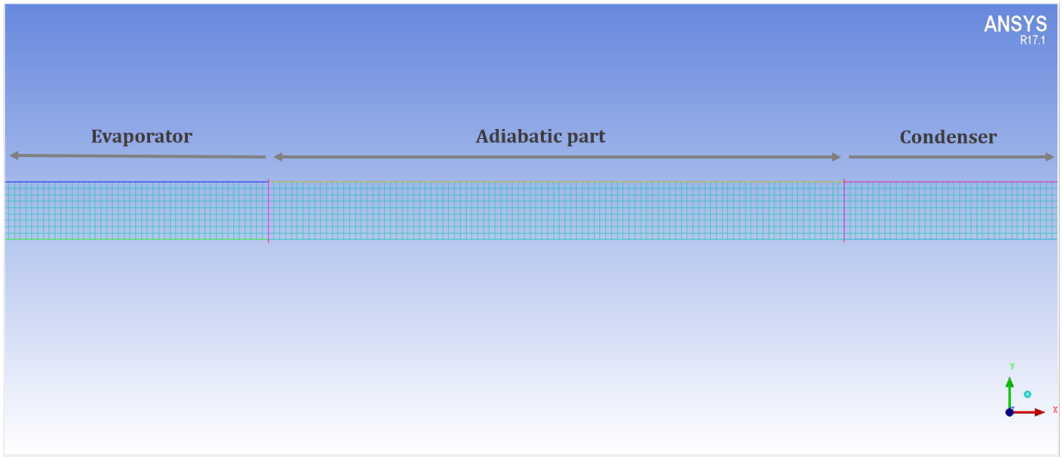

Figure J.2: Image zoom of the second mesh tested with the dynamic model.

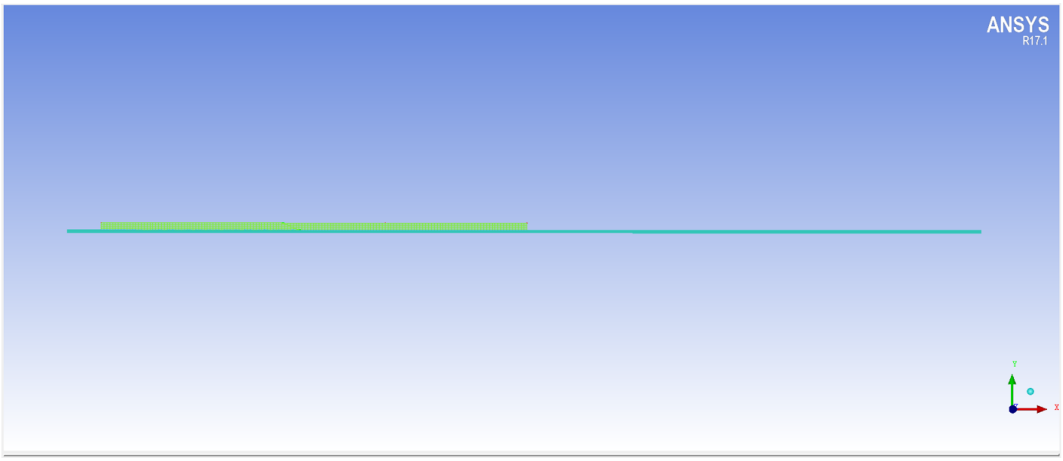

Figure J.3: Second mesh tested with the thermal model.

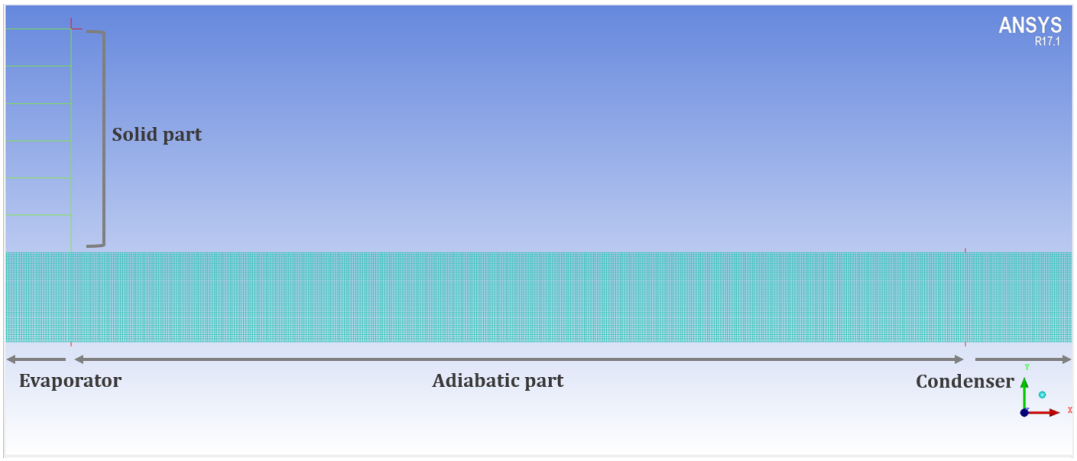

Figure J.4: Image zoom of the second mesh tested with the thermal model.

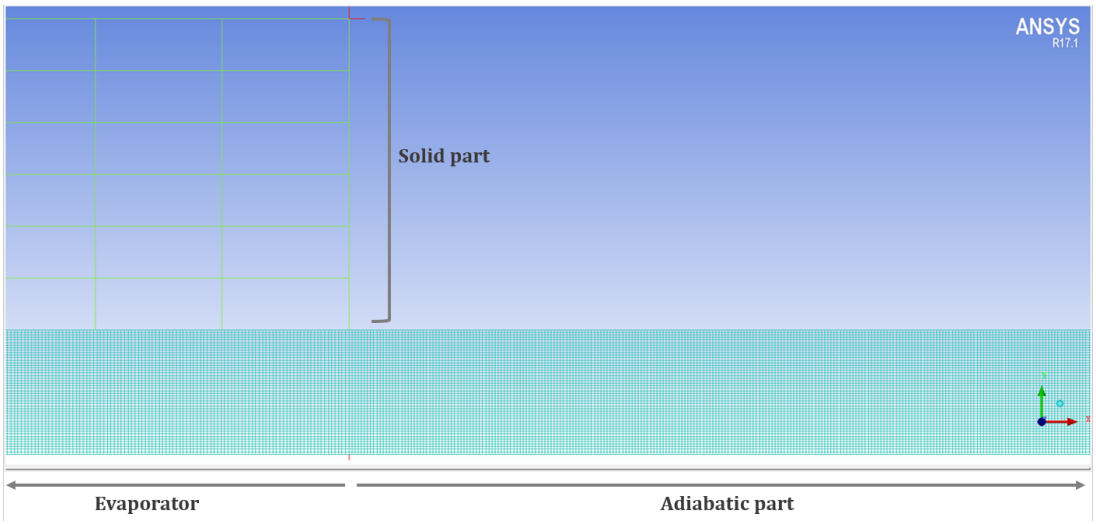

Figure J.5: Detailed image zoom of the second mesh tested with the thermal model.

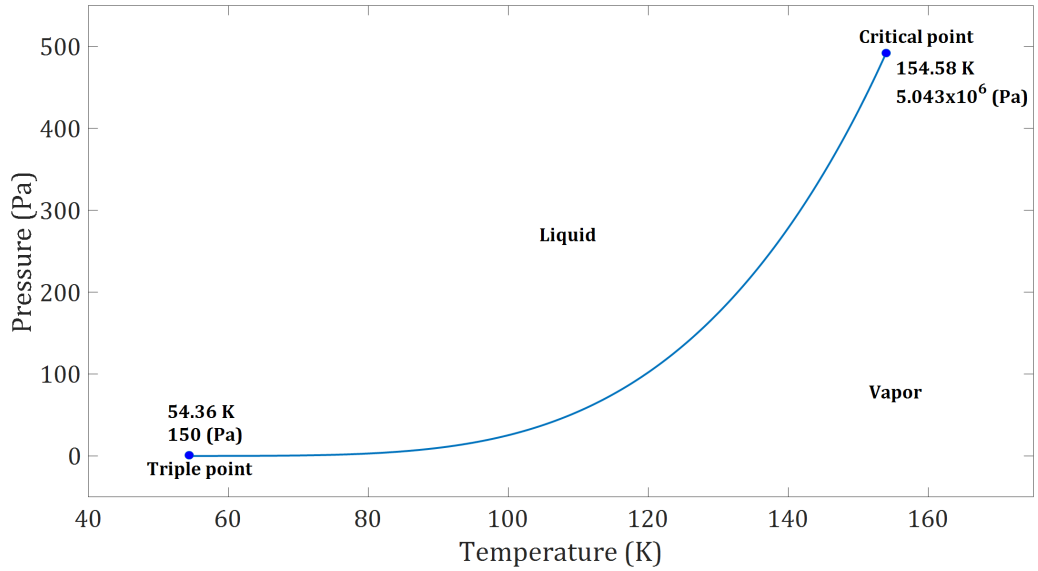

Figure J.6: Saturation curve of Oxygen.

Appendix K

Résumé en français: Étude des caloducs cryogéniques pulsés diphasiques d'un mètre de longueur

K.1 Introduction

La cryogénie est à l'origine de la production des basses températures et de l'étude des phénomènes physiques qui se manifestent à ces températures. Elle est utilisée pour un vaste domaine d'applications, comprenant l'électronique, la médecine, le transport et la physique des accélérateurs.

La supraconductivité est un phénomène qui se manifeste dans certains matériaux dits supraconducteurs à des températures cryogéniques, au-dessous d'une certaine valeur critique. À l'état supraconducteur, le courant électrique peut circuler sans aucune résistance ni perte d'énergie. Dans le cas des aimants supraconducteurs, il devient donc possible de faire circuler des courant électriques très importants et de générer ainsi des champs magnétiques très puissants, utilisés dans les IRM pour le médical ou pour dévier les faisceaux des particules dans les accélérateurs, par exemple.

De nos jours, dans le domaine de la supraconductivité, beaucoup d'efforts se focalisent dans le développement des supraconducteurs à haute température critique, dits hauts-Tc. Cela permet de remplacer l'hélium dans le processus de refroidissement par d'autres fluides cryogéniques, à plus haute température de changement de phase, présents en plus grandes quantités sur terre et d'éviter ainsi les successives pénuries d'hélium.

Un caloduc pulsé diphasique (*Pulsating Heat Pipe* (PHP) en anglais) est un lien

thermique diphasique composé d'un tube lisse capillaire sous forme de serpentin reliant un évaporateur (ou partie à refroidir) avec un condenseur (ou partie froide), séparés tous les deux par une zone adiabatique au milieu. Le fluide de travail à l'intérieur du tube capillaire se trouve à une pression et température proches du changement de phase. Du à cela, et aux dimensions capillaires du tube, le fluide à l'intérieur se distribue de façon alternée en parties liquides et parties vapeurs entourées par un film liquide. Des instabilités thermo-hydrauliques permanentes sont à l'origine d'un écoulement oscillant du fluide permettant de transférer la chaleur de l'évaporateur au condenseur. Les différents paramètres liés à la géométrie et au fluide de travail du PHP peuvent avoir une influence sur les performances thermiques du système et sont à l'origine de nombreuses études.

Inventés par Akachi dans les années 90, les PHP ont été largement étudiés à température ambiante par Khandekar [5] et développés pour des différentes applications telles que le refroidissement des composants électroniques [6] ou le stockage de chaleur [7, 8]. Dans le domaine de la cryogénie, les PHPs ont été principalement développés pour le refroidissement d'aimants supraconducteurs. Par exemple, des PHPs d'une dizaine de centimètres ont été testés par Mito et Natsume [9–12] avec différents fluides cryogéniques. À l'échelle du mètre, des PHPs verticaux ont été étudiés par Fonseca [13] en utilisant de l'hélium comme fluide caloporteur. Selon la littérature sur le sujet, il s'avère que les PHPs fonctionnant en position horizontale ont un comportement comparable à un fonctionnement sans gravité [14]. Néanmoins, aucun PHP cryogénique horizontal de un mètre de longueur fonctionnant avec différents fluides de travail a été développé et testé jusqu'à présent. Concernant les simulations numériques, les codes les plus complets ont été principalement développés dans une seule dimension par Shafii et Zhang [15, 16], Mameli [17] et Nikolayev [18–20], du fait de la complexité des phénomènes physiques intervenant simultanément dans le PHP. Néanmoins, il n'existe pas de nos jours un modèle numérique simulant correctement le comportement des PHPs. Le développement de simulations à deux dimensions représente donc un véritable pas en avant pour des futures modélisations des PHPs.

L'objectif du présent projet de recherche consiste à étudier et caractériser le comportement thermo-hydraulique des caloducs cryogéniques pulsés horizontaux en tant que système de refroidissement pour les aimants supraconducteurs. Ce projet comprend une partie expérimentale dans laquelle sont présentés les résultats issus de nombreux tests cryogéniques avec différents fluides, et une partie numérique représentant le comportement du fluide diphasique dans un tube capillaire.

K.2 Descriptif expérimental

Tous les tests expérimentaux ont été réalisés dans un environnement cryogénique. Pour cela, les caloducs pulsés à tester sont introduits dans cryostat sous vide et entourés de plusieurs écrans thermiques, afin de réduire au maximum les apports thermiques extérieurs.

Le banc expérimental est composé de trois PHPs en position horizontale et configuration fermée. Les tubes lisses capillaires sont en acier inox avec des diamètres interne et externe de 1,5 et 2 mm, respectivement. La seule différence entre chaque PHP est le nombre de tours formant le serpentin: 36, 24 et 12. Les parties évaporatrices, condensatrices et adiabatiques mesurent 33 cm chacune, donnant lieu à une longueur totale de 1m par PHP. Chaque partie évaporatrice et condensatrice est composée d'une plaque en cuivre usinée pour incorporer les tubes capillaires en acier inox. Sur la superficie de chaque plaque évaporatrice, un chauffeur est fixé pour imposer une puissance thermique souhaitée et ainsi évaluer la capacité de transfert thermique du système. Du côté des condenseurs, ceux-ci sont reliés thermiquement formant un seul bloc. Au-dessus, une plaque en cuivre assure une bonne liaison thermique entre la tête froide du cryo-générateur et le bloc de condenseurs. Sur celle-ci, trois tubes en cuivre sont thermalisés et relient l'entrée de chaque PHP au circuit d'insertion de gaz à l'extérieur du cryostat. De cette façon, le fluide de travail provenant de l'extérieur du cryostat est refroidit avant d'être introduit dans le PHP. De plus, sur la plaque en cuivre sont fixés plusieurs chauffeurs à fin de pouvoir contrôler la température du bloc de condenseurs. Concernant l'instrumentation, les trois PHPs disposent de nombreux capteurs de température et pression distribués dans les parties évaporatrices, condensatrices et adiabatiques, ainsi qu'un capteur de vide permettant de contrôler le vide à l'intérieur du cryostat.

Le dispositif expérimental comprends aussi un système d'insertion du fluide de travail dans les PHPs. Ce dernier est composé de plusieurs bouteilles de gaz contenant les différents fluides de travail ainsi que leur volume tampon correspondant, une pompe à vide pour évacuer toute impureté du PHP avant chaque test et un circuit d'insertion avec de nombreuses vannes et tuyaux relient les bouteilles avec les fluides de travail à l'extérieur du cryostat avec l'entrée des PHP à l'intérieur du cryostat.

Par ailleurs, le système d'acquisition est relié à un programme Labview permettant d'envoyer les différentes instructions au système, de contrôler et monitorer les PHPs et d'enregistrer les données brutes issues des tests. Toutes ces données sont par la suite traitées avec des programmes codés sous Matlab.

Avant chaque période de tests, toutes les connections électriques sont vérifiées et des nombreux tests de fuites sont réalisés. Une fois que le cryostat est complètement fermé, le pompage démarre pour atteindre un vide "cryogénique", entre 10^{-4} et 10^{-6} mbar.

Ensuite, avant de démarrer chaque test, le PHP à tester ainsi que le circuit d'insertion sont pompés pour éviter des impuretés à l'intérieur.

Au début de chaque test, le PHP est rempli avec le volume tampon qui contient le fluide travail sous forme gazeuse. Lors de l'insertion, le gaz se refroidit et se condense dans le tube d'insertion thermalisé sur la plaque en cuivre. La différence de pression dans le volume tampon entre le début et la fin de l'insertion déterminera la quantité de fluide introduite dans le PHP.

K.3 Analyse des résultats expérimentaux à l'azote

Dans un premier lieu, le PHP avec 36 tubes en parallèle a été testé à l'azote. En fixant la température du condenseur à 75 K et en augmentant progressivement la charge thermique dans l'évaporateur par paliers de 5 W, il a été possible d'évaluer les performances thermiques du système.

Il s'avère que le système est capable de transférer jusqu'à 25 W de façon stable (avec des températures stables au niveau du condenseur et de l'évaporateur) et d'atteindre une conductivité thermique équivalente maximale de 85 kW/(m.K) à 15 W. L'évolution des oscillations de pression et de température de la partie adiabatique tout au long du test permettent de conclure sur l'état thermodynamique du système en fonction de la charge thermique imposée dans l'évaporateur. Tous les capteurs de pression indiquent que celle-ci est identique, au moins, dans la partie adiabatique. En faisant l'hypothèse que le fluide dans le tube est à saturation on en déduit sa température. De plus, les mesures de température de la partie adiabatique semblent indiquer que les parties liquides se trouvent dans un état sous-refroidi, à l'exception de quelques pics de température excédant la température de saturation voir même celle de l'évaporateur. Ce phénomène ponctuel peut s'expliquer par des compressions adiabatiques exercées par deux parties liquides autour d'une partie vapeur déjà surchauffée.

Ajouté à cela, l'analyse détaillée de l'évolution des températures dans le tube central de la partie adiabatique nous montre un comportement différent des oscillations de température en fonction de la puissance thermique imposée à l'évaporateur. À bas flux thermique, 5 et 10 W, la distribution des températures est assez chaotique avec, d'un côté, des pics excédant la température de saturation, et de l'autre, la température la plus basse est à chaque fois mesurée par un capteur différent. Lorsqu'on augmente la puissance thermique, à 15, 20 et 25 W, la distribution des températures devient plus ordonnée avec la température la plus basse généralement mesurée par le capteur le plus proche du condenseur, suivie de celui situé au centre du tube puis celui situé près de l'évaporateur, et toujours au-dessous de la température de saturation. Finalement, à 30 W, les pics de températures excédant la température de saturation réapparaissent, révélant la perte

de stabilité dans le système. En effet, à cet instant, la température de l'évaporateur augmente sans arrêt en évaporant tout son fluide à l'intérieur (vapeur surchauffée), la phase de "séchage" est atteinte, le système n'est plus stable, le transfert thermique du condenseur à l'évaporateur n'est plus assuré.

De plus, l'analyse des FFT des oscillations de température à chaque palier de puissance ne révèlent pas de fréquence d'oscillation spécifique.

K.4 Comparaison des résultats expérimentaux avec différents fluides de travail

Dans le but de comparer les performances thermiques d'un même PHP avec différents fluides de travail, de nombreux tests expérimentaux ont été réalisés en utilisant du néon et de l'argon comme fluides de travail. Lors de ces tests, la température du condenseur est fixée pendant que la charge thermique de l'évaporateur augmente progressivement par paliers de 5 W. Dans le cas du néon, la température du condenseur est fixée à 27 K, dans le cas de l'argon, celle-ci est fixée à 89 K.

En utilisant du néon comme fluide de travail, le système est capable de transférer jusqu'à 50 W de façon stable et d'atteindre une conductivité thermique équivalente de 70 kW/(m.K) à 50 W. De plus, les mesures de température de la partie adiabatique semblent indiquer aussi que les parties liquides se trouvent dans un état sous-refroidi et on constate aussi la présence de pics de température excédant la température de saturation, mais jamais celle de l'évaporateur. L'analyse de l'évolution des températures du tube central de la partie adiabatique nous indique que la fréquence des oscillations augmente avec la puissance thermique. À partir de 50 W la température du condenseur augmente aussi à cause de la limite en puissance du cryo-générateur. À ce stade, la limite thermique du PHP n'est pas atteinte mais la tête froide ne peut plus absorber la puissance thermique envoyée par le chauffeur de l'évaporateur et le test est arrêté par sécurité. Il est intéressant de remarquer que pour le néon, le diamètre interne des tubes capillaires (ici 1,5 mm) défini dans la littérature par le critère de Bond pour ce type dispositif PHP est légèrement supérieur au maximum théorique (environ 1,25 mm) est le système fonctionne néanmoins avec des excellentes performances thermiques.

En utilisant de l'argon comme fluide de travail, le système est capable de transférer jusqu'à 30 W de façon stable et d'atteindre une conductivité thermique équivalente de 85 kW/(m.K) à 20 W. Les mesures de température de la partie adiabatique semblent indiquer aussi que les parties liquides se trouvent dans un état sous-refroidi, mais cette fois-ci on ne constate pas des pics de température excédant la température de saturation. En analysant l'évolution des températures du tube central de la partie adiabatique on constate une distribution claire des température tout le long du tube, avec la température

la plus basse mesurée par le capteur le plus proche du condenseur, suivie de celui situé au centre du tube puis celui situé près de l'évaporateur. De plus, à partir de 35 W, la température de l'évaporateur augmente sans arrêt, la phase de "séchage" est de nouveau atteinte, le transfert thermique du condenseur à l'évaporateur n'est plus assuré.

On peut donc constater que les performances thermiques, en termes de conductivité thermique équivalente, sont plus élevées pour l'azote et l'argon mais il est possible de transférer un plus grand nombre de watts de façon stable en utilisant du néon comme fluide de travail. Ajouté à cela, on remarque aussi qu'avec l'azote et l'argon on atteint les phases de séchage dans l'évaporateur lorsque la puissance thermique imposée est trop importante, alors que avec le néon, la capacité maximale de transfert thermique du PHP n'a jamais été atteinte.

Par la suite, de nombreux tests d'augmentation progressive de charge thermique dans l'évaporateur ont été réalisés avec les trois fluides de travail présentés (azote, néon et argon) et des quantités de liquide et gaz variables, ce que l'on appelle le taux de remplissage. Ce dernier considère le rapport entre le volume de liquide à l'intérieur du PHP divisé par le volume total du PHP. Il s'avère que pour les trois fluides, les conductivités thermiques maximales sont atteintes à des taux de remplissage entre 20 et 42 %, concrètement, entre 29 et 42 % pour l'azote, entre 22 et 38 % pour l'argon et entre 20 et 25% pour le néon.

Les nombreux résultats expérimentaux ainsi que l'analyse des différents paramètres physiques des fluides de travail nous permettent de comprendre le comportement du système PHP en fonction du fluide caloporteur:

Premièrement, concernant les propriétés physiques liées au mouvement du fluide, on constante que le néon a les plus faibles tension superficielle et viscosité dynamique, ce qui est à l'origine d'une faible résistance au mouvement. Par rapport au pur transport de chaleur, si l'on considère le produit de la densité liquide multiplié par la chaleur spécifique ($\rho_l \times Cp_l$), on retrouve que le néon obtient le plus grand résultat. Par ailleurs, c'est l'azote suivi de l'argon puis du néon qui a la plus grande chaleur latente. En effet, une chaleur latente importante demande un échange d'énergie plus important lors du changement de phase, alors qu'une chaleur latente faible facilite l'ébullition et le changement de phase.

À partir de cela, il devient possible de mieux comprendre le comportement du PHP en utilisant du néon comme fluide de travail par rapport aux deux autres. De par ses propriétés physiques, le néon est très dynamique avec une faible résistance au mouvement, qui se prête facilement au changement de phase et avec un coefficient $(dp/dT)_{sat}$ très élevé, ce qui contribue au oscillations du fluide diphasique dans les tubes capillaires du PHP. Cela peut expliquer pourquoi le néon présente des fréquences d'oscillations de température plus importantes qui reflètent le mouvement du fluide. De plus, son coefficient $\rho_l \times Cp_l$ permet un transfert de chaleur important par chaleur sensible des parties liquides. Au contraire, les fortes chaleurs latentes de l'azote et l'argon reflètent un transfert de chaleur

plus important par changement de phase pour ces deux fluides. Ces observations peuvent ainsi expliquer les valeurs des taux de remplissage optimum que l'on trouve pour les différents fluides: pour le néon le taux de remplissage optimum est beaucoup plus faible que pour les deux autres fluides. En effet, un faible taux de remplissage révèle d'un volume total de vapeur plus important que de liquide dans le PHP, sachant que les expansions et compressions de vapeurs contribuent aux oscillations totales du mouvement du fluide. Si on ajoute à cela les faibles propriétés du fluide opposant le mouvement, ainsi que son élevé coefficient $(dp/dT)_{sat}$ et l'important transport de chaleur des parties liquides, il devient logique d'obtenir un transfert thermique maximal du PHP avec des petits taux de remplissages.

Finalement, la stabilité sur le long terme du système PHP est vérifiée avec la réalisation de tests à température fixe dans le condenseur et puissance fixe dans l'évaporateur pendant plusieurs heures. La puissance imposée à l'évaporateur étant la puissance maximale (ou presque) de fonctionnement stable du PHP pour chaque fluide de travail, à savoir, 20 W pour l'azote et l'argon et 50 W pour le néon.

K.5 Comportements spécifiques et limites du système PHP

En plus des tests de montée en puissance dans l'évaporateur pour définir les capacités de transfert thermique maximales du PHP, d'autres tests spécifiques ont été réalisés pour caractériser ces PHP cryogéniques, cette fois-ci avec de l'azote et du néon comme fluides de travail.

En premier lieu, différentes conditions de démarrage ont été testées avec des différentes puissances et températures initiales sur l'évaporateur lors de l'insertion du fluide dans le PHP. Il s'avère qu'un minimum d'énergie (réserve d'enthalpie) dans l'évaporateur est désirable au début de chaque test pour faciliter le processus de remplissage de fluide dans le PHP.

Deuxièmement, le PHP a aussi été testé en fixant différentes températures dans le condenseur et forçant ainsi le système à travailler à des gammes de températures différentes pour un même fluide (toujours en restant aux alentours du changement de phase, donc près de la ligne de saturation). Il a été possible ainsi de remarquer que la gamme de températures, et donc pressions, de fonctionnement conditionne le taux de remplissage dans le PHP et, par conséquent, ses performances thermiques.

Troisièmement, les deux autres PHP avec 24 et 12 tubes en parallèle ont aussi été testés à fin de déterminer l'influence du nombre de tubes dans les performances thermiques du système PHP. Il a été possible de confirmer ce que la littérature indique, il devient en effet plus difficile d'atteindre un fonctionnement stable lorsque l'on réduit le nombre de tubes et la capacité de transfert thermique est considérablement réduite.

Finalement, un dernier groupe de tests ont été réalisés dans le but d'imiter une situation de "quench" d'un aimant supraconducteur pour observer le comportement thermodynamique transitoire dans le PHP. En imposant une puissance thermique très importante (allant de 20 à 100 W) dans l'évaporateur lorsque le PHP est en fonctionnement stable, il a été possible de déterminer la capacité de récupération du PHP après imposer une énergie si importante. Par exemple, en utilisant du néon comme fluide de travail, les temps de récupération sont beaucoup moins importants qu'avec l'azote. Néanmoins, plus de tests seront nécessaires dans le futur pour bien caractériser le PHP lors de ces situations extrêmes.

K.6 Simulation numérique du comportement du fluide dans un tube capillaire

Un modèle numérique a été développé pour simuler le comportement du fluide diphasique à l'intérieur d'un tube capillaire en position horizontale. Il s'agit d'un modèle CFD développé avec le solveur Fluent qui utilise la méthode VOF (*Volume Of Fluid*) pour définir l'interface diphasique ainsi que les propriétés des deux phases du fluide, tout cela dans une géométrie 2D axisymétrique. La géométrie du modèle, ainsi que les températures de fonctionnement et le fluide de travail (oxygène diphasique), sont basés sur un modèle expérimental existant.

Des simulations sur la dynamique du fluide ont premièrement été réalisées pour analyser la formation du film liquide et l'interface diphasique, et étudier les paramètres reliés à cela, tels que l'angle de contact et les différentes formes des bulles de vapeur en fonction du sens de circulation du fluide. Ensuite, des simulations thermiques ont été réalisés à fin de vérifier le transfert de chaleur entre l'évaporateur et le condenseur grâce aux oscillations du fluide diphasique. Ainsi, il a été aussi possible de vérifier certains phénomènes thermiques typiques des PHP, tels que l'ébullition et la condensation du film liquide et d'autres caractéristiques de la dynamique du fluide diphasique.

Ce model numérique est dans ces premiers stades de développement et peut être encore amélioré, néanmoins il s'avère prometteur pour les futures simulations de PHP en 2D.

K.7 Conclusions et Perspectives

Les résultats expérimentaux et numériques obtenus durant le présent projet de recherche apportent à la communauté scientifique des nouvelles données et pistes sur le comportement des caloducs cryogéniques pulsés diphasiques (PHP) de un mètre de longueur fonctionnant en position horizontale.

Il a été ainsi possible de déterminer la capacité maximale de transfert thermique d'un PHP de un mètre de longueur en fonction du fluide de travail, ainsi que de mieux comprendre son comportement thermo-hydraulique durant les phases de fonctionnement stable et de séchage. Il a été possible de déterminer de conditions optimales de démarrage (avec une température et puissance thermique initiales) et des conditions optimales de fonctionnement (en identifiant les taux de remplissage qui donnent les meilleures conductivités thermiques équivalentes). De plus, l'influence de la gamme de pressions et températures de fonctionnement ainsi que le nombre de tubes en parallèle ont aussi été déterminées. Les PHP cryogéniques ont été initialement développés comme possible solution au refroidissement des aimants supraconducteurs, pour cela, des tests spécifiques imitant une situation de quench dans un aimant ont été réalisés en imposant une très importante quantité d'énergie dans l'évaporateur à fin de vérifier la capacité du PHP à récupérer des conditions stables de fonctionnement. Pour finir, le modèle numérique a permis de vérifier et d'étudier certaines caractéristiques du comportement du fluide dans les tubes capillaires des PHP et représente un premier pas pour le développement de futurs codes numériques en 2D pour le caloducs pulsés diphasiques.

Il est néanmoins nécessaire de continuer les recherches sur les caloducs pulsés diphasiques pour finir de comprendre et caractériser les nombreuses instabilités thermo-hydrauliques qui ont lieu dans ces derniers. En effet, certains paramètres peuvent encore être testés et étudiés pour mieux comprendre la physique des PHP. Par exemple, déterminer la différence de pression locale entre une partie vapeur et une partie liquide qui est à l'origine du mouvement du fluide permettra de mieux connaître l'état thermodynamique du fluide ainsi que d'obtenir plus d'information sur la dynamique locale de l'écoulement. De plus, toujours dans l'idée de comparer les performances thermiques d'un même PHP avec différents fluides de travail, il pourrait être intéressant de tester le PHP avec de l'oxygène comme fluide de travail. Par ailleurs, changer la méthode d'insertion du fluide pourrait être aussi une piste à développer dans l'idée d'optimiser les temps de remplissage et la distribution du fluide à l'intérieur du PHP. Au niveau du travail numérique, modifier la géométrie du modèle existant et incorporer plus d'information sur l'évolution de l'angle de contact pourrait fournir des résultats plus réalistes sur la formation des zones de vapeur et du film liquide. Finalement, des travaux de visualisation pourrait confirmer beaucoup d'hypothèses sur l'état du fluide et la forme des bulles de vapeur dans les tubes capillaires des PHP.

Bibliography

[1] CryoComp Rapid Cryogenic Design. 88 Materials in the Properties Database. Thermal Analysis Software. Version 5.2.

[2] NIST Reference Fluid Thermodynamic and Transport Properties Database (REFPROP): Version 9.1.

[3] Département des Accélérateurs, de Cryogénie et de Magnétisme - Institut de recherche sur les lois fondamentales de l'Univers - CEA Saclay. Un bouclier magnétique pour les futurs vols spatiaux: le projet SR2S. http://irfu.cea.fr/dacm/Phocea/Vie_des_labos/Ast/ast.php?t=fait_marquant&id_ast=3595, 2015. Online; accessed 4 November 2015.

[4] Community Research and Development Information Service (CORDIS) - European Commission. Space Radiation Superconductive Shield. https://cordis.europa.eu/project/rcn/106623/factsheet/en, 2016. Online; accessed 1 April 2016.

[5] Sameer Khandekar. *Thermo-Hydrodynamics of Closed Loop Pulsating Heat Pipes*. PhD thesis, Institut für Kernenergetik und Energiesysteme der Universität Stuttgart, 2004.

[6] Shun Okazaki, Hideyuki Fuke, Hiroyuki Ogawa, and Yoshiro Miyazaki. Development of Meter-Scale O-Shaped and U-shaped Oscillating Heat Pipes for GAPS. In *IEEE Aerospace Conference*, 2014.

[7] Jiateng Zhao, Zhonghao Rao, Chenzhen Liu, and Yimin Li. Experiment Study of Oscillating Heat Pipe and Phase Change Materials Coupled for Thermal Energy Storage and Thermal Management. *International Journal of Heat and Mass Transfer*, 99:252–260, 2016.

[8] Jiateng Zhao, Jie Qu, and Zhonghao Rao. Experiment investigation on thermal performance of a large-scale oscillating heat pipe with self-rewetting fluid used for thermal energy storage. *International Journal of Heat and Mass Transfer*, 111:999, 2017.

[9] Toshiyuki Mito, Kyohei Natsume, Nagato Yanagi, Hitoshi Tamura, Tsutomu

Tamada, Koji Shikimachi, Naoki Hirano, and Shigeo Nagaya. Development of Highly Effective Cooling Technology for a Superconducting Magnet Using Cryogenic OHP. *IEEE Transactions on Applied Superconductivity*, 20(3):2023–2026, 2010.

[10] Toshiyuki Mito, Kyohei Natsume, Nagato Yanagi, Hitoshi Tamura, Tsutomu Tamada, Koji Shikimachi, Naoki Hirano, and Shigeo Nagaya. Achievement of High Heat Removal Characteristics of Superconducting Magnets With Imbedded Oscillating Heat Pipes. *IEEE Transactions on Applied Superconductivity*, 21(3, 2):2470–2473, 2011.

[11] K. Natsume, T. Mito, N. Yanagi, H. Tamura, T. Tamada, K. Shikimachi, N. Hirano, and S. Nagaya. Development of cryogenic oscillating heat pipe as a new device for indirect/conduction cooled superconducting magnets. *IEEE Transactions on Applied Superconductivity*, 22(3):4703904–4703904, 2012.

[12] Toshiyuki Mito, Kyohei Natsume, Nagato Yanagi, Hitoshi Tamura, and Yoshiro Terazaki. Enhancement of thermal properties of hts magnets using built-in cryogenic oscillating heat pipes. *IEEE Transactions on Applied Superconductivity*, 23 (3):4602905–4602905, 2013.

[13] Luis Diego Fonseca, John Pfotenhauer, and Franklin Miller. Results of a three evaporator cryogenic helium Pulsating Heat Pipe. *International Journal of Heat and Mass Transfer*, 120:1275–1286, 2018.

[14] M. Mameli, L. Araneo, S. Filippeschi, L. Marelli, R. Testa, and M. Marengo. Thermal Response of a Closed Loop Pulsating Heat Pipe Under a Varying Gravity Force. *International Journal of Thermal Sciences*, 80:11–22, 2014.

[15] MB Shafii, A Faghri, and YW Zhang. Thermal modeling of unlooped and looped pulsating heat pipes. *Journal of Heat Transfer - Transactions of the Asme*, 123(6): 1159–1172, 2001.

[16] YW Zhang and A Faghri. Oscillatory flow in pulsating heat pipes with arbitrary numbers of turns. *Journal of Thermophysics and Heat Transfer*, 17(3):340–347, 2003.

[17] M. Mameli, M. Marengo, and S. Zinna. Numerical model of a multi-turn Closed Loop Pulsating Heat Pipe: Effects of the local pressure losses due to meanderings. *International Journal of Heat and Mass Transfer*, 55(4):1036–1047, 2012.

[18] Iaroslav Nekrashevych and Vadim S. Nikolayev. Effect of tube heat conduction on the pulsating heat pipe start-up. *Applied Thermal Engineering*, 117:24–29, 2017.

[19] S. P. Das, V. S. Nikolayev, F. Lefevre, B. Pottier, S. Khandekar, and J. Bonjour. Thermally induced two-phase oscillating flow inside a capillary tube. *International Journal of Heat and Mass Transfer*, 53(19-20):3905–3913, 2010.

[20] Iaroslav Nekrashevych and Vadim Nikolayev. Pulsating heat pipe simulations: Impact of php orientation. *Microgravity Science and Technology*, 2 2019.

[21] Randall F. Barron. *Cryogenic Systems*. McGraw-Hill series in mechanical engineering. McGraw-Hill, 1966.

[22] Michael Tinkham. *Introduction to Superconductivity: Second Edition*. Dover Books on Physics. Dover Publications; Second edition, 2004.

[23] B. Baudouy. Heat transfer and cooling techniques at low temperature, 2013.

[24] H. Godfrin and C. Gianèse. Crise de l'hélium: l'inquiétude persiste. *Reflets de la physique*, 39:19–21, 2014.

[25] Yuwen Zhang and Amir Faghri. Advances and Unsolved Issues in Pulsating Heat Pipes. *Heat Transfer Engineering*, 29(1):20–44, 2008.

[26] S. Rittidech, N. Pipatpaiboon, and S. Thongdaeng. Thermal Performance of Horizontal Closed-Loop Oscillating Heat-Pipe with Check Valves. *Journal of Mechanical Science and Technology*, 24(2):545–550, 2010.

[27] Keiyo Gi, Fumiaki Sato, and Saburo Maezawa. Flow Visualization Experiment on Oscillating Heat Pipe. pages 373–377, 1999.

[28] M Hosoda, S Nishio, and R Shirakashi. Study of meandering closed-loop heat-transport device (vapor-plug propagation phenomena). *International Journal Series B-Fluids and Thermal Engineering*, 42:737–744, 1999.

[29] S. Khandekar, P.K. Pnigrahi, F. Lefevre, and J. Bonjour. Local hydrodynamics of flow in a pulsating heat pipe: a review. *Frontiers in Heat Pipes*, 1(2):1–20, 2010.

[30] Romain Bruce, Maria Barba, Antoine Bonelli, and Bertrand Baudouy. Thermal performance of a meter-scale horizontal nitrogen pulsating heat pipe. *Cryogenics*, 93:66–74, 2018.

[31] Vadim Nikolayev and Iaroslav Nekrashevych. Vapor thermodynamics and fluid merit for pulsating heat pipe. *Preprint submitted to Applied Thermal Engineering*, 2019.

[32] Sameer Khandekar, Anant Prasad Gautam, and Pavan K. Sharma. Multiple quasi-steady states in a closed loop pulsating heat pipe. *International Journal of Thermal Sciences*, 48(3):535–546, 2009.

[33] M Groll and S Khandekar. Pulsating heat pipes: Progress and prospects. In *Energy and Environment, Vols 1 and 2*, pages 723–730, 2003.

[34] Manoj Rao, Frederic Lefevre, Pierre-Clement Czujko, Sameer Khandekar, and Jocelyn Bonjour. Numerical and experimental investigations of thermally induced

oscillating flow inside a capillary tube. *International Journal of Thermal Science*, 115:29–42, 2017.

[35] Aejung Yoon and Sung Jin Kim. Experimental and theoretical studies on oscillation frequencies of liquid slugs in micro pulsating heat pipes. *Energy Conversion and Management*, 181:48–58, 2019.

[36] H. Akachi. Structure of a heat pipe, 1990. US Patent 4,921,041.

[37] H. Akachi. Structure of micro-heat pipe, 1993. US Patent 5,219,020.

[38] Luis Diego Fonseca, Franklin Miller, and John Pfotenhauer. A Helium Based Pulsating Heat Pipe For Superconducting Magnets. In *Advances in Cryogenic Engineering*, volume 1573, pages 28–35, 2014.

[39] Maria Barba, Romain Bruce, Antoine Bonelli, and Bertrand Baudouy. Experimental study of Large-scale cryogenic Pulsating Heat Pipe. *IOP Conf. Ser.: Mater. Sci. Eng. 278 012156*, 2017.

[40] Xu Han, Hongbin Ma, Anjun Jiao, and John K. Critser. Investigations on the Heat Transport Capability of a Cryogenic Oscillating Heat Pipe and its Application in Achieving Ultra-Fast Cooling Rates for Cell Vitrification Cryopreservation. *Cryobiology*, 56(3):195–203, 2008.

[41] Kyohei Natsume, Toshiyuki Mito, Nagato Yanagi, Hitoshi Tamura, Tsutomu Tamada, Koji Shikimachi, Naoki Hirano, and Shigeo Nagaya. Heat Transfer Performance of Cryogenic Oscillating Heat Pipes for Effective Cooling of Superconducting Magnets. *Cryogenics*, 51(6, SI):309–314, 2011.

[42] Luis Diego Fonseca. *Experimental Characterization of Cryogenic Helium Pulsating Heat Pipes*. PhD thesis, University of Wisconsin-Madison, 2017.

[43] Dong Xu, Laifeng Li, and Huiming Liu. Experimental Investigation on the Thermal Performance of Helium Based Cryogenic Pulsating Heat Pipe. *Experimental Thermal and Fluid Science*, 70:61–68, 2016.

[44] Yi Li, Qiuliang Wang, Shunzhong Chen, Baozhi Zhao, and Yinming Dai. Experimental Investigation of the Characteristics of Cryogenic Oscillating Heat Pipe. *International Journal of Heat and Mass Transfer*, 79:713–719, 2014.

[45] Qing Liang, Yi Li, and Qiuliang Wang. Experimental investigation on the performance of a neon cryogenic oscillating heat pipe. *Cryogenics*, 84:7–12, 2017.

[46] Qing Liang, Yi Li, and Qiuliang Wang. Cryogenic Oscillating Heat Pipe for Conduction-Cooled Superconducting Magnets. *IEEE Transactions on Applied Superconductivity*, 28, 2018.

[47] Qing Liang, Yi Li, and Qiuliang Wang. Effects of filling ratio and condenser temperature on the thermal performance of a neon cryogenic oscillating heat pipe. *Cryogenics*, 89:102–106, 2018.

[48] Qing Liang, Yi Li, and Qiuliang Wang. Study on a neon cryogenic oscillating heat pipe with long heat transport distance. *Heat and Mass Transfer*, 54:1721–1727, 2018.

[49] A. J. Jiao, H. B. Ma, and J. K. Critser. Experimental Investigation of Cryogenic Oscillating Heat Pipes. *International Journal of Heat and Mass Transfer*, 52(15-16): 3504–3509, 2009.

[50] Luis Diego Fonseca, Franklin Miller, and John Pfotenhauer. Experimental heat transfer analysis of a cryogenic nitrogen pulsating heat Pipe at various liquid fill ratios. *Applied Thermal Engineering*, 130:343–353, 2018.

[51] Xiao Sun, Sizhuo Li, Bo Jiao, Zhihua Gan, and John Pfotenhauer. Experimental study on a hydrogen closed-loop pulsating heat pipe with two turns. *Cryogenics*, 97: 63–69, 2019.

[52] Philippe Gully, Fabien Bonnet, Vadim Nikolayev, N Luchier, and Trung Quan Tran. Evaluation of the Vapor Thermodynamic State in PHP. *Heat Pipe Science and Technology*, 5:369–376, 2013.

[53] F. Bonnet, P. Gully, and V. Nikolayev. Development and Test of a Cryogenic Pulsating Heat Pipe and a Pre-Cooling System. In *Advances in Cryogenic Engineering*, volume 1434, pages 607–614, 2012.

[54] H. R. Deng, Y. M. Liu, R. F. Ma, D. Y. Han, Z. H. Gan, and J. M. Pfotenhauer. Experimental Investigation on a Pulsating Heat Pipe with Hydrogen. In *Advances in Cryogenic Engineering*, volume 101, 2015.

[55] Xiao Sun, John Pfotenhauer, Bo Jiao, Luis Diego Fonseca, Dongyang Han, and Zhihua Gan. Investigation on the temperature dependence of filling ratio in cryogenic pulsating heat pipes. *International Journal of Heat and Mass Transfer*, 126:237–244, 2018.

[56] JJ Gu, M Kawaji, and R Futamata. Effects of Gravity on the Performance of Pulsating Heat Pipes. *Journal of Thermophysics and Heat Transfer*, 18(3):370–378, 2004.

[57] Junjie Gu, Masahiro Kawaji, and Ryosuke Futamata. Microgravity Performance of Micro Pulsating Heat Pipes. *Microgravity Science and Technology*, 16:181–185, 2005.

[58] Kleber Vieira de Pavia, Marcia B. H. Mantelli, Raul Gohr, and Marcelo de As-

sis Corrêa. Wire Mini Heat Pipe under Microgravity Conditions. *14th International Heat Pipe Conference*, 2007.

[59] Mauro Mameli, Marco Marengo, and Stefano Zinna. Numerical Investigation of the Effects of Orientation and Gravity in a Closed Loop Pulsating Heat Pipe. *Microgravity Science and Technology*, 24:79–92, 2012.

[60] M. Manzoni, M. Mameli, C. de Falco, L. Araneo, S. Filippeschi, and M. Marengo. Advanced numerical method for a thermally induced slug flow: application to a capillary closed loop pulsating heat pipe. *International Journal for Numerical Methods in Fluids*, 82:375–397, 2016.

[61] D. Mangini, M. Mameli, A. Georgoulas, L. Araneo, S. Filippeschi, and M. Marengo. A Pulsating Heat Pipe for Space Applications: Ground and Microgravity Experiments. *International Journal of Thermal Sciences*, 95:53–63, 2015.

[62] D. Mangini, M. Mameli, D. Fioriti, S. Filippeschi, L. Araneo, and M. Marengo. Hybrid Pulsating Heat Pipe for space applications with non-uniform heating patterns: Ground and microgravity experiments. *Applied Thermal Engineering*, 126: 1029–1043, 2017.

[63] Mauro Mameli, Andrea Catarsi, Daniele Mangini, Luca Pietrasanta, Davide Fioriti, Marco La Foresta, Lorenzo Caporale, Nicolas Miché, Marco Marengo, Paolo Di Marco, and Sauro Filippeschi. Large Diameter Pulsating Heat Pipe for Future Experiments on the International Space Station: Ground and Microgravity Thermal Response. *19th International Heat Pipe Conference and 13th International Heat Pipe Symposium*, 2018.

[64] Qin Sun, Jian Qu, Qian Wang, and Jianping Yuan. Operational characteristics of oscillating heat pipes under micro-gravity condition. *International Communications in Heat and Mass Transfer*, 88:28–36, 2017.

[65] V Ayel, Cyril Romestant, Yves Bertin, Vincenzo Manno, and Sauro Filippeschi. Visualisation of flow patterns in flat plate pulsating heat pipe: influence of hydraulic behaviour on thermal performances. *17th International Heat Pipe Conference*, 2013.

[66] V. Ayel, L. Araneo, A. Scalambra, M. Mameli, C. Romestant, A. Piteau, M. Marengo, S. Filippeschi, and Y. Bertin. Experimental study of a closed loop flat plate pulsating heat pipe under a varying gravity force. *International Journal of Thermal Sciences*, 96:23–34, 2015.

[67] H. Akachi, F. Polasek, and P. Stulc. Experimental heat transfer analysis of a cryogenic nitrogen pulsating heat Pipe at various liquid fill ratios. *Proceedings of the 5th International Heat Pipe Symposium*, 1996.

[68] L. Lin, R. Ponnappan, and J. Leland. Experimental Investigation of Oscillating Heat Pipes. *Journal of Thermophysics and Heat Transfer*, 15:395–400, 2001.

[69] Qingjun Cai and Chung-lung Chen. Operating characteristic investigations in pulsating heat pipe. *Journal of Heat Transfer - Transactions of the Asme*, 128:1329–1334, 2006.

[70] P Charoensawan, S Khandekar, M Groll, and P Terdtoon. Closed Loop Pulsating Heat Pipes - Part A: Parametric Experimental Investigations. *Applied Thermal Engineering*, 23(16):2009–2020, 2003.

[71] Piyanun Charoensawan and Pradit Terdtoon. Thermal Performance of Horizontal Closed-Loop Oscillating Heat Pipes. *Applied Thermal Engineering*, 28(5-6):460–466, 2008.

[72] Hua Han, Xiaoyu Cui, Yue Zhu, and Shende Sun. A comparative study of the behavior of working fluids and their properties on the performance of pulsating heat pipes (PHP). *Internal Journal of Thermal Sciences*, 82:138–147, 2014.

[73] XM Zhang, JL Xu, and ZQ Zhou. Experimental study of a pulsating heat pipe using FC-72, ethanol, and water as working fluids. *Experimental Heat Transfer*, 17 (1):47–67, 2004.

[74] YW Zhang and A Faghri. Heat transfer in a pulsating heat pipe with open end. *International Journal of Heat and Mass Transfer*, 45(4):755–764, 2002.

[75] Niti Kammuang-Lue, Phrut Sakulchangsatjatai, and Pradit Terdtoon. Effect of Working Fluids and Internal Diameters on Thermal Performance of Vertical and Horizontal Closed-Loop Pulsating Heat Pipes with Multiple Heat Sources. *Thermal Science*, 20(1):77–87, 2016.

[76] Xiaohong Han, Xuehui Wang, Haoce Zheng, Xiangguo Xu, and Guangming Chen. Review of the Development of Pulsating Heat Pipe for Heat Dissipation. *Renewable and Sustainable Energy Reviews*, 59:692–709, 2016.

[77] Remi Bertossi, Vincent Ayel, Balkrishna Mehta, Cyril Romestant, Yves Bertin, and Sameer Khandekar. Motion of liquid plugs between vapor bubbles in capillary tubes: a comparison between fluids. *Heat and Mass Transfer*, 53(11, SI):3315–3327, 2017.

[78] BY Tong, TN Wong, and KT Ooi. Closed-loop pulsating heat pipe. *Applied Thermal Engineering*, 21:1845–1862, 2001.

[79] Wook Hyun Lee, Hyun Suck Jung, Jeung Hoon Kim, and Jong Soon Kim. Flow Visualization of Oscillating Capillary Tube Heat Pipe. pages 355–360, 1999.

[80] Steve Cai, Reh-Lin Chen, and Chung-lung Chen. An Investigation of Evaporation,

Boiling, and Heat Transport Performance in Pulstating Heat Pipe. pages 99–104, 2002.

[81] Giulia Spinato, Navid Borhani, and John R. Thome. Operational Regimes in a Closed Loop Pulsating Heat Pipe. *International Journal of Thermal Sciences*, 102: 78–88, 2016.

[82] Zhi Hu Xue and Wei Qu. Experimental and theoretical research on a ammonia pulsating heat pipe: New full visualization of flow pattern and operating mechanism study. *International Journal of Heat and Mass Transfer*, 106:149–166, 2017.

[83] A Ilinca, D Mangini, M Mameli, D Fioriti, S Filippeschi, L Araneo, N Roth, and M Marengo. Fluid-flow pressure measurements and thermo-fluid characterization of a single loop two-phase passive heat transfer device. *Journal of Physics: Conference Series*, 923:012–022, 2017.

[84] Xiaoyu Cui, Yue Zhu, Zhihua Li, and Shende Shun. Combination study of operation characteristics and heat transfer mechanism for pulsating heat pipe. *Applied Thermal Engineering*, 65(1-2):394–402, 2014.

[85] Mauro Mameli, Marco Marengo, and Sameer Khandekar. Local heat transfer measurement and thermo-fluid characterization of a pulsating heat pipe. *International Journal of Thermal Sciences*, 75:140–152, 2014.

[86] S. M. Pouryoussefi and Yuwen Zhang. Analysis of chaotic flow in a 2D multi-turn closed-loop pulsating heat pipe. *Applied Thermal Engineering*, 126:1069–1076, 2017.

[87] Miriam Manzoni, Mauro Mameli, Carlo de Falco, Lucio Araneo, Sauro Filippeschi, and Marco Marengo. Non equilibrium lumped parameter model for Pulsating Heat Pipes: validation in normal and hyper-gravity conditions. *International Journal of Heat and Mass Transfer*, 97:473–485, 2016.

[88] Dong Soo Jang, Hyun Joon Chung, Yongseok Jeon, and Yongchan Kim. Thermal performance characteristics of a pulsating heat pipe at various nonuniform heating conditions. *International Journal of Heat and Mass Transfer*, 126(B):855–863, 2018.

[89] JL Xu and XM Zhang. Start-up and steady thermal oscillation of a pulsating heat pipe. *Heat and Mass Transfer*, 41(8):685–694, 2005.

[90] S. M. Pouryoussefi and Yuwen Zhang. Nonlinear Analysis of Chaotic Flow in a Three-Dimensional Closed-Loop Pulsating Heat Pipe. *Journal of Heat Transfer - Transactions of the Asme*, 138(12), 2016.

[91] Maria Barba, Romain Bruce, Florent Bouchet, Antoine Bonelli, and Bertrand Baudouy. Thermal Study of a one-meter long Neon Cryogenic Pulsating Heat Pipe. *Accepted for publication.*, 2018.

[92] R Wunenburger, Y Garrabos, C Lecoutre-Chabot, D Beysens, and J Hegseth. Thermalization of a two-phase fluid in low gravity: Heat transferred from cold to hot. *Physical Review Letters*, 84:4100–4103, 2000.

[93] Mauro Mameli, Vincenzo Manno, Sauro Filippeschi, and Marco Marengo. Thermal instability of a Closed Loop Pulsating Heat Pipe: Combined effect of orientation and filling ratio. *Experimental Thermal and Fluid Science*, 59:222–229, 2014.

[94] R. K. Sarangi and M. V. Rane. Experimental Investigations for Start Up and Maximum Heat Load of Closed Loop Pulsating Heat Pipe. In *Chemical, Civil and Mechanical Engineering Tracks of 3rd Nirma University International Conference on Engineering (NUiCONE 2012)*, volume 51, pages 683–687, 2013.

[95] Xun Wang, Tong Han, Lei Wang, Xinxin Mao, and Chengsi Yang. Experimental Study on Start-Up Characteristics of Pulsating Heat Pipe. In *Progress in Power and Electrical Engineering*, volume 354-355, pages 87–91, 2012.

[96] Xiangdong Liu, Yongping Chen, and Mingheng Shi. Dynamic Performance Analysis on Start-Up of Closed-Loop Pulsating Heat Pipes (CLPHPs). *International Journal of Thermal Sciences*, 65:224–233, 2013.

[97] E. T. White and R. H. Beardmore. The Velocity of Rise of Single Cylindrical Air Bubbles through Liquids Contained in Vertical Tubes. *Chemical Engineering Science*, 17(5):351–361, 1962.

[98] Jian Qu, Qian Wang, and Qin Sun. Lower limit of internal diameter for oscillating heat pipes: A theoretical model. *International Journal of Thermal Sciences*, 110: 174–185, 2016.

[99] Lucang Lv, Ji Li, and Guohui Zhou. A robust pulsating heat pipe cooler for integrated high power LED chips. *Heat and Mass Transfer*, 53(11, SI):3305–3313, 2017.

[100] Shuangfeng Wang, Jinjian Chen, Yanxin Hu, and Wei Zhang. Effect of Evaporation Section and Condensation Section Length on Thermal Performance of Flat Plate Heat Pipe. *Applied Thermal Engineering*, 31(14-15):2367–2373, 2011.

[101] Chih-Yung Tseng, Kai-Shing Yang, Kuo-Hsiang Chien, Ming-Shan Jeng, and Chi-Chuan Wang. Investigation of the Performance of Pulsating Heat Pipe Subject to Uniform/Alternating Tube Diameters. *Experimental Thermal and Fluid Science*, 54: 85–92, 2014.

[102] B Holley and A Faghri. Analysis of pulsating heat pipe with capillary wick and varying channel diameter. *International Journal of Heat and Mass Transfer*, 48(13): 2635–2651, 2005.

[103] D. Yin, H. Wang, H. B. Ma, and Y. L. Ji. Operation limitation of an oscillating heat pipe. *International Journal of Heat and Mass Transfer*, 94:366–372, 2016.

[104] Takurou Daimaru, Shuhei Yoshida, and Hiroki Nagai. Study on thermal cycle in oscillating heat pipes by numerical analysis. *Applied Thermal Engineering*, 113: 1219–1227, 2017.

[105] Raffles Senjaya and Takayoshi Inoue. Oscillating heat pipe simulation considering dryout phenomena. *Heat and Mass Transfer*, 50(10):1429–1441, 2014.

[106] Manoj Rao, Frederic Lefevre, Sameer Khandekar, and Jocelyn Bonjour. Heat and mass transfer mechanisms of a self-sustained thermally driven oscillating liquid-vapour meniscus. *International Journal of Heat and Mass Transfer*, 86:519–530, 2015.

[107] Ali Jokar, Ali Abbasi Godarzi, Mohammad Saber, and Mohammad Behshad Shafii. Simulation and optimization of a pulsating heat pipe using artificial neural network and genetic algorithm. *Heat and Mass Transfer*, 52(11):2437–2445, 2016.

[108] Phrut Sakulchangsatjatai, Niti Kammuang-Lue, Kritsada On-Ai, and Pradit Terdtoon. Correlations to Predict Thermal Performance Affected by Working Fluid's Properties of Vertical and Horizontal Closed-Loop Pulsating Heat Pipe. *Thermal Science*, 20(5):1555–1564, 2016.

[109] S Rittidech, P Terdtoon, M Murakami, P Kamonpet, and W Jompakdee. Correlation to predict heat transfer characteristics of a closed-end oscillating heat pipe at normal operating condition. *Applied Thermal Engineering*, 23(4):497–510, 2003.

[110] T Katpradit, T Wongratanaphisan, P Terdtoon, P Kamonpet, A Polchai, and A Akbarzadeh. Correlation to predict heat transfer characteristics of a closed end oscillating heat pipe at critical state. *Applied Thermal Engineering*, 25(14-15):2138–2151, 2005.

[111] Piyanun Charoensawan and Pradit Terdtoon. Thermal performance correlation of horizontal closed-loop oscillating heat pipes. *9th Electronics Packaging Technology Conference*, page 906, 2007.

[112] S Khandekar, P Charoensawan, M Groll, and P Terdtoon. Closed loop pulsating heat pipes - Part B: visualization and semi-empirical modeling. *Applied Thermal Engineering*, 23(16):2021–2033, 2003.

[113] G. Gursel, A. J. H. Frijns, F. G. A. Homburg, and A. A. van Steenhoven. A mass-spring-damper model of a pulsating heat pipe with a non-uniform and asymmetric filling. *Applied Thermal Engineering*, 91:80–90, 2015.

[114] Giulia Spinato, Navid Borhani, and John R. Thome. Understanding the self-

sustained oscillating two-phase flow motion in a closed loop pulsating heat pipe. *Energy*, 90(1):889–899, 2015.

[115] Chao Dang, Li Jia, and Qianyi Lu. Investigation on Thermal Design of a Rack with the Pulsating Heat Pipe for Cooling CPUs. *Applied Thermal Engineering*, 110: 390–398, 2017.

[116] Rong Ji Xu, Xiao Hui Zhang, Rui Xiang Wang, Shu Hui Xu, and Hua Sheng Wang. Experimental investigation of a solar collector integrated with a pulsating heat pipe and a compound parabolic concentrator. *Energy Conversion and Management*, 148: 68–77, 2017.

[117] Zilong Deng, Yi Zheng, Xiangdong Liu, Bingpeng Zhu, and Yongping Chen. Experimental study on thermal performance of an anti-gravity pulsating heat pipe and its application on heat recovery utilization. *Applied Thermal Engineering*, 125: 1368–1378, 2017.

[118] J. Gabriel Monroe, Omar T. Ibrahim, Scott M. Thompson, and Nima Shamsaei. Energy harvesting via fluidic agitation of a magnet within an oscillating heat pipe. *Applied Thermal Engineering*, 129:884–892, 2018.

[119] Mohammad Alhuyi Nazari, Mohammad H. Ahmadi, Roghayeh Ghasempour, Mohammad Behshad Shafii, Omid Mahian, Soteris Kalogirou, and Somchai Wongwises. A review on pulsating heat pipes: From solar to cryogenic applications. *Applied Energy*, 222:475–484, 2018.

[120] E. Kostrov, A. Bagdinov, E. Demikhov, T. Demikhov, V. Lysenko, and N. Piskunov. Performance test of a G-M cooler in magnetic field. 67:440–444, 2015.

[121] Evgeny Kostrov, Evgeny Demikhov, Anton Bagdinov, Timofey Demikhov, Valeriy Lysenko, and Yuri Tysyachnykh. Magnetic Field Operation and Shielding of a G-M Cryocooler. *IEEE Transactions on Applied Superconductivity*, 26, 2016.

[122] Takaaki Morie, Taisuke Shiraishi, and Mingyao Xu. Experimental investigation of cooling capacity of 4K GM cryocoolers in magnetic fields. 67:474–478, 2015.

[123] Gaspak. Thermophysical and transport properties for 33 fluids. Version 3.35.

[124] Luis Diego Fonseca, Franklin Miller, and John Pfotenhauer. Design and Operation of a Cryogenic Nitrogen Pulsating Heat Pipe. In *Advances in Cryogenic Engineering*, volume 101, 2015.

[125] Monan Li, Laifeng Li, and Dong Xu. Effect of number of turns and configurations on the heat transfer performance of helium cryogenic pulsating heat pipe. *Cryogenics*, 96:159–165, 2018.

[126] Romain Bruce, Maria Barba, Florent Bouchet, Antoine Bonelli, and Bertrand Bau-

douy. Transient thermal behavior of a neon Pulsating Heat Pipe (PHP). *Accepted for publication.*, 2019.

[127] ANSYS Inc. *ANSYS Fluent Theory Guide.* ANSYS Inc., 2013.

[128] R. Bruce, S. Pascali, C. Vendramini, and B. Baudouy. Implementation of the thermodynamic and phase transition equations of superfluid helium in CFD software. *IOP Conference Series-Materials Science and Engineering*, 101, 2015.

[129] K. M. Wrobel. *Modelling and Numerical Simulation of Flows with Evaporation and Condensation.* PhD thesis, University of Twente, 2006.

[130] Harold Erbin. *Hydrodynamique-L3.* Art Libre, 2011.

[131] Gounsti Pare. *Cration et jection des gouttes de l'atomisation.* PhD thesis, Universit Pierre et Marie Curie, 2015.

[132] Laura Fourgeaud, Vadim S. Nikolayev, Eric Ercolani, Jerome Duplat, and Philippe Gully. In situ investigation of liquid films in pulsating heat pipe. *Applied Thermal Engineering*, 126:1023–1028, 2017.

[133] M. M.l Awad. *An Overview of Heat Transfer Phenomena.* InTech, 2012.

université PARIS-SACLAY | ÉCOLE DOCTORALE PHENIICS

Titre : Étude des caloducs cryogéniques pulsés diphasiques d'un mètre de longueur

Mots clés : caloducs pulsés, écoulement diphasique, transfert thermique, cryogénie

Résumé : Un caloduc pulsé diphasique est un lien thermique composé d'un tube capillaire lisse sous forme de serpentin reliant un évaporateur à un condenseur, séparés par une partie adiabatique. Les conditions de température et de pression du fluide à l'intérieur du caloduc sont proches des conditions de changement de phase. De ce fait, et grâce aux dimensions capillaires du tube, le fluide se distribue en différentes parties liquide et vapeur distribuées de manière alternée. Les instabilités thermo-hydrauliques permanentes sont à l'origine d'un écoulement oscillant qui permet le transfert de chaleur de l'évaporateur jusqu'au condenseur.

L'objectif du présent projet de recherche consiste à étudier le comportement thermo-hydraulique de trois caloducs cryogéniques pulsés diphasiques testés avec différents fluides cryogéniques (azote, néon et argon) pour le refroidissement d'aimants à haute température critique. De plus, un code numérique a été développé pour les futures simulations 2D des caloducs pulsés diphasiques.

Au cours de ce projet de recherche, de nombreux tests expérimentaux ont été réalisés avec trois fluides cryogéniques différents: azote, néon et argon. Les résultats expérimentaux des tests avec une augmentation de puissance progressive dans l'évaporateur ont révélé des capacités de transfert thermiques très différentes en fonction du fluide, chaque fluide présentant un comportement thermo-hydraulique différent. L'état thermodynamique du fluide lors du fonctionnement stable du PHP et la phase d'assèchement (dry-out) ont été étudiés. Les différences dans le comportement des différents fluides ont été expliquées après l'analyse de leurs propriétés physiques. De plus, les taux de remplissage de fluide dans le PHP donnant les meilleures performances thermiques ont été définis. Ajouté à cela, de nombreux tests réalisés en configuration ouverte (avec le PHP connecté au volume tampon) et en configuration fermé (avec le PHP isolé du volume tampon) ont permis de conclure sur la capacité de régulation du volume tampon en cas de surpression dans le PHP. Aussi, les résultats expérimentaux des longs tests de stabilité ont permis de vérifier la stabilité du système PHP pendant des longues périodes de fonctionnement. Par ailleurs, des tests spécifiques ont été réalisés pour déterminer des conditions optimales de démarrage, l'influence de la température du condenseur dans les performances thermiques du système et l'influence du nombre de tubes en parallèle dans la capacité de transfert thermique du système. Finalement, une série de tests avec une forte puissance thermique imposée au niveau de l'évaporateur imitant une situation de quench dans un aimant supraconducteur ont données des précieuses informations sur les limites thermiques du système. Concernant les simulations numériques, un modèle a été développé avec le solveur Fluent pour des simulations dans une géométrie 2D axisymétrique en utilisant la méthode VOF. La dynamique du fluide dans un tube capillaire a été modélisée et les simulations thermiques ont permis de conclure que les instabilités thermodynamiques restent insuffisantes pour maintenir les oscillations du fluide. Ce modèle est présenté comme une nouvelle plateforme pour de futures modélisations 2D des caloducs pulsés diphasiques.

Université Paris-Saclay
Espace Technologique / Immeuble Discovery
Route de l'Orme aux Merisiers RD 128 / 91190 Saint-Aubin, France

université PARIS-SACLAY | ÉCOLE DOCTORALE PHENIICS

Title : Study of Meter-scale Horizontal Cryogenic Pulsating Heat Pipes

Keywords : pulsating heat pipes, two-phase flow, heat transfer, cryogenics

Abstract : A pulsating (or oscillating) heat pipe (PHP or OHP) is a heat transfer device composed of a single capillary tube bent in many U-turns, connecting an evaporator to a condenser, separated by an adiabatic part. In the PHP, temperature and pressure conditions of the working fluid are close to phase-change conditions. Due to this and to the capillary dimensions of the tube, the fluid is distributed in alternating liquid slugs and vapor plugs. Permanent thermal instabilities in the PHP create the oscillating flow which allows the transfer of heat from one end (the evaporator) to the other (the condenser).

The objective of the present work consists in characterizing the thermo-hydraulic behavior of the meter-scale horizontal cryogenic pulsating heat pipes as a cooling solution for space superconducting magnets. To this, several experiments have been conducted in a cryogenic facility containing three different horizontal pulsating heat pipes. In addition, a numerical 2D model has been proposed for future horizontal pulsating heat pipes simulations.

During the research project, numerous tests have been performed using three different working fluids: nitrogen, neon and argon. From experimental results of progressive heat load tests it has been possible to compare the maximum heat load transfer capacity of the PHP with each fluid and the corresponding thermal performance. It has also been noticed that each fluid presents a specific behavior concerning the fluid oscillations. In addition, the thermodynamic state of the fluid in operating conditions and the dry-out process have been characterized. Differences between fluid's behaviors have been partly explained by analyzing the evolution of the fluid physical properties related to the movement and the heat transfer capacity. Furthermore, it has been possible to conclude about the relation between the liquid filling ratio in the PHP and its thermal performance, determining the filling ratios giving the highest thermal performances. Moreover, similar tests have been performed in open configuration (with the PHP connected to the buffer volume) and closed configuration (with the PHP isolated from the buffer volume). From this, it has been possible to conclude about the regulation made by the buffer volume in case of overpressure in the PHP. Also, experimental results from long stability tests have confirmed that these pulsating heat pipe are able to work in stable conditions during long periods as a reliable cooling system. In addition to that, specific tests have been done to determine the optimum start-tup conditions, the influence of the temperature of the condenser in the thermal performance and the influence of the number of turns in the global heat transfer capacity. A final series of tests have been achieved with a sudden extra heat load at the surface of the evaporator while the PHP is operating in stable conditions, simulating a quench event of a superconducting magnet. Experimental results gave us precious information about the transient thermal behavior and operating limits of this kind of device during transient heat loads like quench situations. Concerning the numerical part, a numerical model has been proposed for transient simulations with a pressure-based Fluent solver using the Volume of Fluid (VOF) method in a 2D axisymmetric geometry. Certain characteristics of fluid dynamics in capillary tubes have been confirmed. It has also been noticed that thermodynamic instabilities are not enough to generate the fluid oscillations in capillary tubes. Even if the 2D axisymmetric simulation is still at its early stages, several aspects of the models have been validated after analyzing the evolution of different parameters, suggesting that this kind of model can be considered as a new platform for future 2D pulsating heat pipes simulations.

Université Paris-Saclay
Espace Technologique / Immeuble Discovery
Route de l'Orme aux Merisiers RD 128 / 91190 Saint-Aubin, France